Earth pressures against- and stability of retaining structures

Sigurður Már Valsson

Earth pressures against- and stability of retaining structures

Sigurður Már Valsson

30 ECTS thesis submitted in partial fulfillment of a
Magister Scientiarum degree in Civil Engineering

Advisors
Arne Kavli
Dr. Arne Åsmund Skotheim
Dr. Sigurður Erlingsson
Dr. Torgeir Døssland

Faculty Representative
Dr. Bjarni Bessason

Faculty of Civil and Environmental Engineering
School of Engineering and Natural Sciences
University of Iceland
Molde, June 2011

Earth pressures against- and stability of retaining structures
30 ECTS thesis submitted in partial fulfillment of a *Magister Scientiarum* degree in Civil Engineering

Abstract

The objective of the presented research is to investigate methods used to calculate earth pressures against- and the stability of retaining structures.

The classical methods of calculating earth pressures are covered in detail. They are named after their creators Charles-Augustin de Coulomb and William John Macquorn Rankine. A special interest is taken in a variant of Rankine's theory developed at Norges teknisk-naturvitenskapelige universitet (NTNU) that incorporates cohesive properties of soils as well as roughness between the structure and the soil material. Both methods are then tested against each other in order to investigate if a clear link exists between the two. The methods are tested against proposed design values of earth pressure coefficients according to the design standard Eurocode 7.

Håndbok 016 is a design handbook published by the Norwegian Road Administration (n. Statens vegvesen). In it is a chapter dedicated to the design of retaining structures and bridge abutments. The methods proposed to design retaining structures are used to design cantilevered structures of various heights and with various foundation- and backfill materials based on a few geometrical constraints.

The structure designs created with methods in Håndbok 016 are modeled in the finite element program PLAXIS to test if the same material factors of safety could be derived that way.

The results from this study are then discussed and commented upon.

Table of Contents

List of Figures

List of Tables

Symbols

a	Attraction
c	Cohesion
f	Mobilization of shear strength
f_ω	Shear plane mobilization
F	Factor of safety
$N^\pm$	Principal stress ratio
N_q	Bearing capacity factor
N_u	Bearing capacity factor
N_γ	Bearing capacity factor
q	Surface load
s_u	Undrained shear strength
u	Porewater pressure
α	Angle of terrain in front of structure
α_a	Angle of critical shear plane for active earth pressures
α_p	Angle of critical shear plane for passive earth pressures
β	Angle of terrain behind structure
γ	Unit weight of soil
γ_M	Material factor of safety
δ	Angle of wall roughness (Coulomb's method)
δ	Inclination of back of wall (stressfield method)
θ	Inclination of back of wall (Coulomb's method)
ρ	Mobilized friction angle
τ	Shear stress
υ	Poisson's ratio
σ	Total stress
σ'	Effective stress
ϕ	Friction angle
ω	Opening angle of Prandtl zone

Abbreviations

HB016	Håndbok 016
MFS	Material factor of safety
MC	Mohr-Coulomb
NTNU	Norges teknisk-naturvitenskapelige universitet
NGI	Norges Geotekniske Institutt
NRA	Norwegian Road Administration
NTH	Norges Tekniske Høgskole
OCR	Overconsolidation ratio
PLAXIS	Plasticity Axi-Symmetry (program)
SVV	Statens Vegvesen
EC	Eurocode

Acknowledgements

1 Introduction

During development of land, one is often confronted with the challenge of creating a difference in terrain elevation over an arbitrary horizontal distance. This can often be done by creating slopes but when the proposed slope can no longer support itself, another kind of solution is required. Retaining structures are manmade structures with the purpose of supporting earth masses for practical or esthetic reasons, solving the above problem up to a point. Some common types of retaining structures are shown in Figure 1.1; they are a) a cantilevered wall b) a dry stone wall and c) a sheet pile wall (anchored).

Figure 1.1: Shows common types of retaining structures in urban development.

In this thesis some common methods used to estimate forces acting on these structures are discussed and analyzed. A special interest is taken in the method recommended by the Norwegian Road Administration (n. Statens vegvesen) in its design handbook named Håndbok 016 (HB016), which is widely used in Norway. The handbook proposes a method to calculate both the lateral pressures against structures as well as a method to estimate the bearing capacity of the foundation under them.

The geometry of a cantilever retaining wall is chosen as a benchmark and a limit design is calculated for varying soil types in both backfill and foundation according to methods proposed in HB016. This process is repeated for various cases in geometry and loading and the effect of changes between cases are studied. Figure 1.2 shows some common failure modes of cantilevered retaining walls, they are discussed in more detail later in this thesis; they are a) bearing capacity failure in foundation b) structure sliding foundation c) overturning d) larger failure mechanisms.
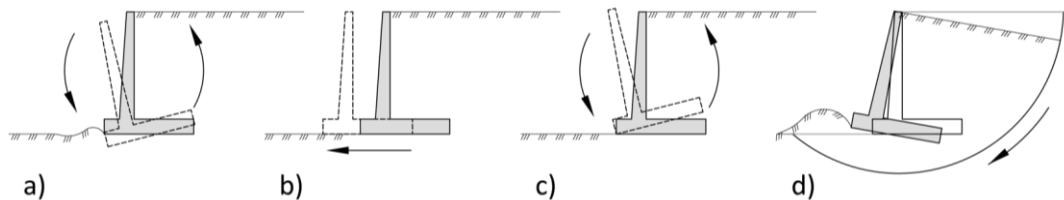
Figure 1.2: Shows common failure modes of cantilevered retaining walls

The finite element method provides an alternative way to design retaining structures. The method is generally used with the aid of computer programs as the calculations usually involve large matrix operations. The program used in this study is PLAXIS; a program that has in the last decades gained high acclaim in finite element analysis of geotechnical problems. The limit designs calculated with conventional hand calculation methods will be evaluated with PLAXIS and the results studied.

2 Theory

2.1 Vertical pressures

2.1.1 In situ vertical stresses

Soil materials have weight and as a result internal stresses are created in all soil masses. The magnitude of these stresses at any location is dependent on the properties of the soil masses, the surrounding geometry, and any external loading. If we take the simplest case of a uniform soil profile with a flat surface and no external loading, the vertical stresses acting on a soil particle at a certain depth is created only by the gravitational forces acting on the soil mass that rests on top of it. It can be calculated in the following manner

$$\sigma_v = \gamma \cdot h \tag{1}$$

where σ_v is the vertical stress component, γ is the unit weight of the soil resting on top of the particle and h is the depth to the particle. Groundwater is often present in real life situations and it creates stresses of its own. Assuming that the groundwater does not flow in any direction then this stress acts equally in all directions and does not add to the stresses acting between particles of the soil mass.

Equation (1) can be modified for effective stresses, layered soils and water pressures. It is then presented as

$$\sigma_v' = q + \Sigma_i(\gamma_i \cdot h_i) - u \tag{2}$$

where σ_v' is the effective vertical stress, q is a load applied onto the surface, γ_i and h_i are the weight and height of each layer and u is the pore pressure. Total stress is defined as the sum of the water pressure and the stresses carried by the soil skeleton. The term effective stress is a very important one as it represents the part of the stress that is carried by the soil skeleton and therefore has effect on the properties of the soil material. Increase in effective stress will induce the soil to move into a more densely packed form (Das, 2002).

A simple soil profile with layered soil and a groundwater table within the soil mass can be seen in Figure 2.1.
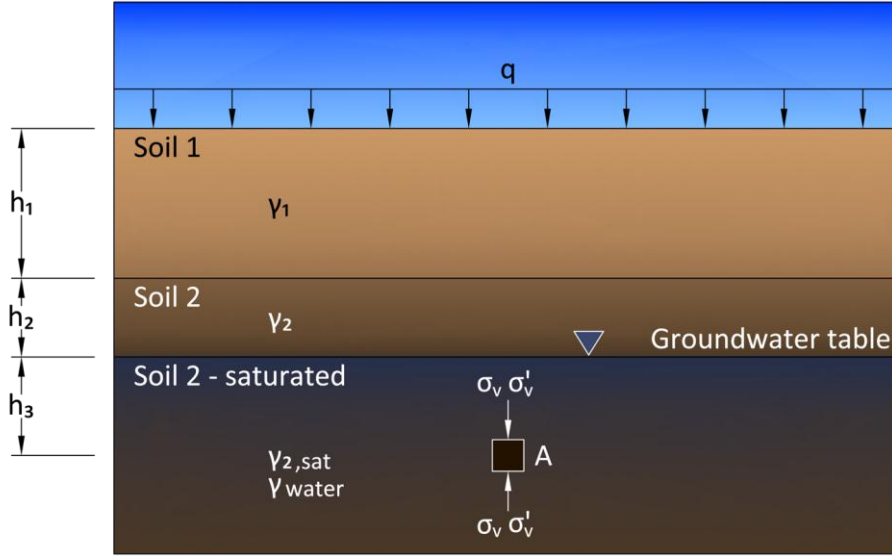
Figure 2.1: A soil profile consisting of layered soil and a groundwater table.

The vertical stress acting on soil element A in Figure 2.1can be described either on a total stress basis using equation (2) as

$$\sigma_v = q + \gamma_1 \cdot h_1 + \gamma_2 \cdot h_2 + \gamma_{2,sat} \cdot h_3$$

or on an effective stress basis as

$$\sigma_v' = q + \gamma_1 \cdot h_1 + \gamma_2 \cdot h_2 + (\gamma_{2,sat} - \gamma_{water}) \cdot h_3$$

Particle A also has horizontal stress acting on it that is not necessarily equal to the vertical stress and methods used to estimate it will be discussed in chapter 2.3.

2.2 Strength parameters of soil

2.2.1 Undrained shear strength, S_u analysis

In a stress situation where the pore water is not allowed to dissipate during loading, strength parameters should be considered on a total stress basis. This is done because any added stress on the soil sample will be carried by porewater between soil particles and not the soil skeleton, hence the effective mean stresses will remain constant during (and immediately after) the loading. As the water cannot escape from the soils pores, its stiffness is added to the equation and so we do not expect any volume change in the soil under these conditions. The strength of soil under these conditions is called undrained shear strength, and is symbolized as S_u (Janbu, et al., 2006).

If we draw the failure criterion with a maximum allowable shear stress in a Mohr diagram we see the special case of the Mohr-Coulomb failure criterion known as the Tresca yield criterion, this can be seen in Figure 2.2 a). The Tresca yield criterion is marked with a striped line indicating that no admissible stress situation can exist above it.
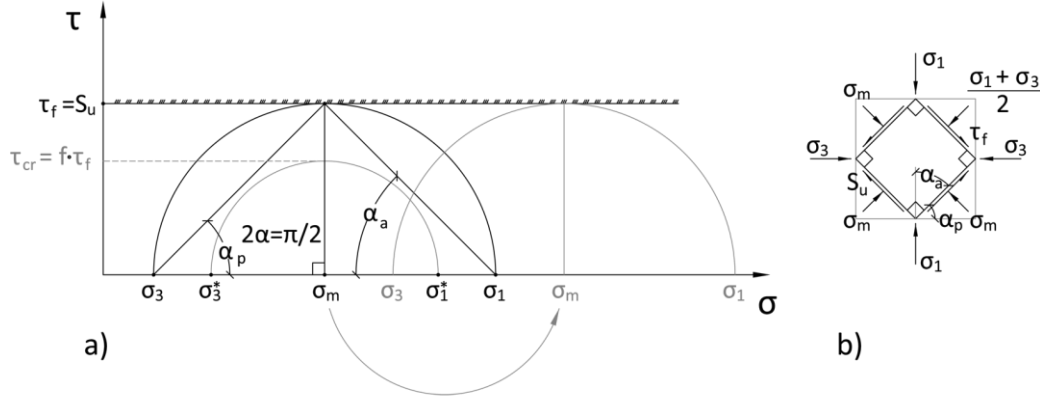
Figure 2.2: a) The Tresca failure criterion. b) The critical failure element.

From the gray circle in Figure 2.2 a), we can see that an increase in the mean total stress does not necessarily mean an increase in the difference between the principal stresses. As the failure criterion Figure 2.2 a) is a horizontal line the maximum allowable shear stress can be defined as the radius of Mohr's circle. In terms of principal stresses this can be written as

$$\tau_f = S_u = \frac{\sigma_1 - \sigma_3}{2} \tag{3}$$

It can be seen in Figure 2.2 a) that the maximum shear stress occurs along a plane with the inclination of $45°$ or $\pi/4$ radians to the principal planes. This stress will be the stress causing failure in an undrained situation and so the shear diamond in the critical shear element, will have right angles as can be seen in Figure 2.2 b). A more detailed explanation of how this is derived can be seen in Appendix A.

Safety factors

Because soil is by no means a homogenous material and its properties vary as a function of its ingredients, it is useful to define a safety margin for the strength parameters. In an undrained analysis this is commonly done by introducing a factor of safety, F, which is the ratio between the maximum allowable shear stress, τ_{cr}, and the failure shear stress τ_f. Another way is to define the ratio so that we decide just how much of the failure shear stress we allow to be mobilized, f. These safety factors are therefore closely connected and are defined as

$$\frac{\tau_f}{\tau_{cr}} = F = \frac{1}{f} \tag{4}$$

F can by definition be greater or equal to $F = 1$ without resulting in failure of the soil material. This means that the degree of mobilization, f, can vary between the no loading value, $f = 0$, and the fully mobilized value of $f = 1$. Values over 1 would mean that the soil carries more shear stress than it can and are therefore inadmissible. It is important to note that this safety factor is applied to the maximum stress the material can withstand and is therefore a material factor independent of load situation.

When designing a slope or a structure in an undrained situation it has to be decided just how close to the failure shear stress, τ_f, it is acceptable that the mobilized shear stress, τ_{cr}, is allowed to reach. In HB016 a material strength safety factor of $F = 1{,}4$ is recommended

4

for the undrained case, when the consequences of failure are estimated as low. This corresponds to a degree of mobilization of $f = 0,714$. If the consequences of failure are estimated as severe, the safety factor should be increased to $F = 1,6$ or $f = 0,625$ (Statens vegvesen, 2010) With soil investigations it is possible to estimate the undrained shear strength of the soil material at hand and using equation (4) the critical design shear stress is calculated as

$$\tau_{cr} = S_u \cdot f \tag{5}$$

This critical design shear stress is illustrated as a gray dashed horizontal line in Figure 2.2-a).

This method of reducing the maximum allowed shear strength is a special case of the *"Phi/c reduction"* method that will be discussed later in this thesis, and can be thought of as having defined the friction angle as $\phi = 0$ and the cohesion as the undrained shear strength.

2.2.2 Drained shear strength, $a - \phi$ analysis

For loading when pore pressures are allowed to dissipate the added stress will eventually be fully carried by the soil skeleton. Hence there will be a change in the effective stresses driving the soil to change its state of compaction, which leads to a change in the strength parameters as a result.

The Mohr-Coulomb failure criterion describes the relationship between the mean stress and the critical shear stress at failure. It is generally presented as

$$\tau_f = c' + \sigma' \tan(\phi') \tag{6}$$

where τ_f is the shear stress at failure, c' is the cohesion of the material, σ' is the effective stress and ϕ' is the friction angle. The line described by equation (6) in Figure 2.3 a) has markings on the top side to indicate that all combinations of principal stresses that create stress circles that cross the line are inadmissible.

As it is experimentally verified that the effective stresses govern the shear strength (Sandven, 2000) the Mohr-Coulomb (MC) criterion described by equation (6) is presented using effective parameters.
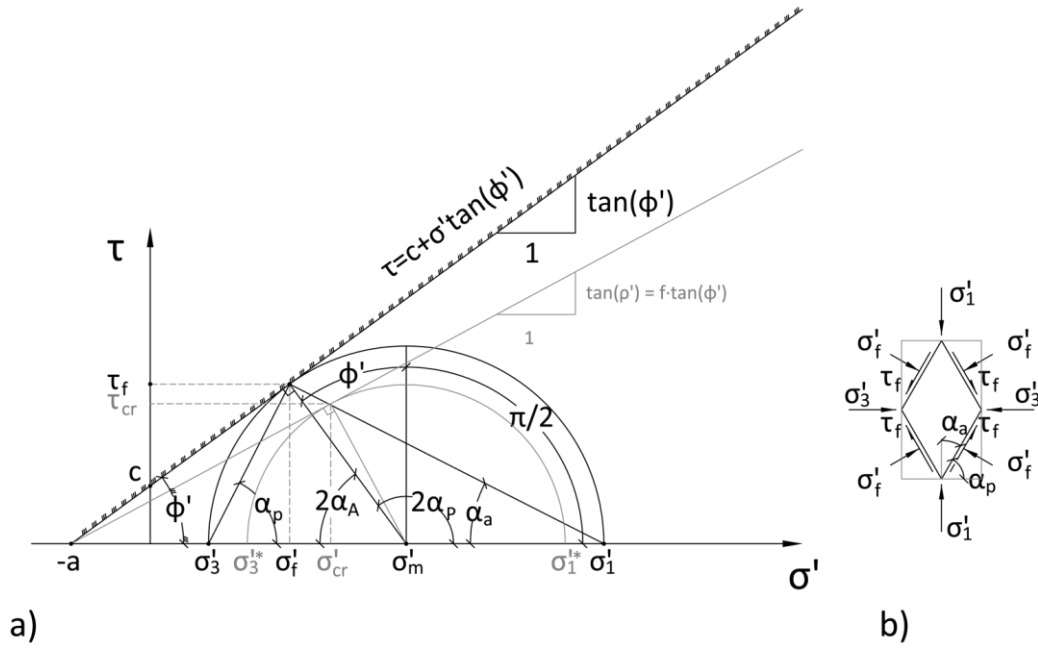
Figure 2.3: a) The Mohr-Coulomb failure criterion. b) The critical failure element.

It is clear from Figure 2.3 a) that it is not only the difference of magnitudes of the principal stresses that decides if the critical shear stress is reached, but rather how unfavorable the combination of the two is. In other words the shear strength is dependent on the stress conditions. In a drained analysis there is always a friction angle. This means that the most critical shear stress plane will never be 45° as it is in the undrained analysis and therefore we never get right angles in the critical stress elements shear diamond as seen in Figure 2.3 b).

Cohesion and the friction angle

The friction angle and cohesion used in the MC-failure envelope are constants used to describe material properties of soils. The model, which was proposed by Coulomb in 1776, assumes a linear relationship between normal and shear stress. More recent studies have shown that the failure envelope is curved and so the MC model will overestimate the strength if it is used to calculate strength at stress levels greatly different than those used to assess its constants (Nordal, 2009). For most practical problems however the approximate results provided by the model are sufficient (Das, 2002).

To get a feeling for these constants it is probably best to take a look at a block resting on an inclined plane. The only driving force acting on the block is gravity pulling at its mass and the resisting force is the friction with the plane. At a certain inclination the driving force will surpass the resisting force and the block will slide. This inclination is defined as the friction angle. In much the same manner soil particles rest on each other and between them are internal frictional forces. If we imagine an inclined surface of a soil mass where the only driving force is the gravitational pull, there will be a certain inclination where the soil mass will slide to find a new state of equilibrium. This angle is approximately the friction angle of the soil mass.

To explain the cohesion it is easy to picture some sort of extra support between the block and the inclined plane, where some shear strength is added independent of normal stresses.

6

As if the block would stick to the plane until that initial bond is broken and the block slides. This extra bond would allow the block to reach higher angles than the friction angle between it and the plane.

Safety factors

As two parameters governing the failure criterion have been introduced, the friction angle and the cohesion, a consistent way to calculate a factor of safety is needed. The MC failure criterion can be presented in many different ways as shown in Appendix B and although the variables change there is one variable that can be found in all of them, and that is the attraction, a. If we hold a constant and reduce the slope of the MC failure line we reduce both ϕ' and c at the same rate thus defining a degree of mobilization. By holding a constant we mathematically only reduce the friction angle and a reduction in the cohesion will follow. The factor of safety in the Phi-C reduction method is defined as

$$F = \frac{1}{f} = \frac{tan(\phi')}{tan(\rho')} \tag{7}$$

where F is the factor of safety, f is the degree of mobilization, ϕ' is the friction angle and ρ' is the mobilized friction angle. We can now turn this formula so it takes the same form as equation (5) as

$$tan(\rho') = tan(\phi') \cdot f \tag{8}$$

This reduced failure envelope can be seen as a gray line in Figure 2.3 a) as well as how the critical stress state with a constant average stress has reduced as a result of the applied material factor of safety. It should be noted that in all the equations in this thesis where the drained friction angle, ϕ', is used it can be interchanged with the reduced friction angle, ρ', to account for the design degree of mobilization in accordance with equation (8). When this is done one must take care to recalculate the cohesion as a result of this safety margin. The link between the attraction and the cohesion is defined with equation (B7) in Appendix B.

2.2.3 Deciding when to use which model

Deciding when to use each method is not an easy task and each situation has to be considered individually. When the material at hand is a granular one and the pore pressures dissipate quickly relative to the speed of loading, the added load is carried by the soil skeleton and not pore pressures. Such a situation is better described as a drained one and effective stresses should be used in the analysis. On the other hand when loading a saturated material that does not allow the porewater to dissipate quickly compared to the speed of loading, the load will be carried by the pore pressures rather than the soil skeleton and the situation is better described using undrained analysis.

The real world is however complicated and a soil mass can be combined of many types of soils with different properties so the situation at hand is often a combination of the two scenarios rather than just one of them. It is therefore not always easy to decide what material model best describes the problem. The key words are the speed of loading and the mediums ability to release porewater and transfer the added stress to its skeleton.

The two methods are different but are connected by a process called consolidation. Consolidation is the time dependent process of pushing the porewater from the soil and thus transferring the excess pore pressures caused by the added loading to the soil skeleton. Because water can be assumed incompressible in comparison with soil, this process will control the rate of the primary settlements after the load has been added.

2.3 Horizontal earth pressures

As was briefly shown in chapter 2.1.1 estimating vertical stresses in soils is a relatively simple task, when we want to investigate the lateral stresses in soils things get more complicated. In the following chapters we will discuss different methods used to estimate lateral earth pressures.

2.3.1 At rest horizontal earth pressures

If we take a look at the situation in Figure 2.1 where we have a soil particle under a flat surface at rest, the horizontal stresses acting on particle A are usually estimated as a function of the vertical stresses. The relationship between the horizontal and vertical stresses can be defined as

$$K = \frac{\sigma_h'}{\sigma_v'} \tag{9}$$

The task of estimating the horizontal stresses becomes a task of estimating the variable K and calculating the vertical stress. When the soil is at rest the ratio K is given an identifying 0, K_0, to indicate that the situation is controlled by static equilibrium.

It is possible to derive the value of K_0 purely by the means of the classical theory of elasticity, and the result is a function of the soils Poisson's ratio. This has been done in Appendix F. This solution is valid for isotropic homogenous materials; most soils are however neither isotropic nor homogenous so this relationship will not be used in this thesis.

Jaky proposed an empirical relationship between the at rest earth pressure coefficient for coarse grained soils and the friction angle of the soil as

$$K_0 = 1 - sin(\phi') \tag{10}$$

It has been shown with laboratory testing that this formula will underestimate K_0 when the soil consists of densely compacted sands (Das, 2002).

Other empirical formulas have been suggested to deal with other types of soils. HB016 proposes the following formula to estimate the at rest earth pressure coefficient for horizontal terrain

$$K_0 = \left(1 - sin(\phi')\right) \cdot \sqrt{OCR} \tag{11}$$

where OCR stands for the overconsolidation ratio. It is defined as

$$OCR = \frac{\sigma_c'}{\sigma_0'} \tag{12}$$

where σ_c' stands for the pre-consolidation pressure, the pressure the soil has encountered previously, and σ_0' stands for the in situ pressure. When no information is available about the over-consolidation ratio it is natural to assume that the current state is the same as the pre-consolidation state and thus equation (11) reduces to equation (10).

When the terrain is sloped at an angle β the at rest earth coefficient can be estimated as

$$K_{0\beta} = K_0 \cdot \left(1 - sin(\beta)\right) \qquad (13)$$

where K_0 is calculated according to equation (10) or equation (11) and the resulting earth pressure force is assumed to be parallel to the inclined terrain (Statens vegvesen, 2010).

When we need to estimate the at rest pressure coefficient where extensive laboratory testing has not been carried out Jaky's formula, equation (10), will provide a good first guess.

Let's say a vertical wall is placed on one side of element A in Figure 2.1 and the soil is excavated from the other side of the wall. As long as the wall does not move we have a case of static equilibrium and the force acting on the wall will be a function of the vertical pressure and the at rest earth pressure coefficient, as is proposed by equation (9). If however the wall starts to move in either direction, the presumption of static equilibrium is broken and thus K_0 no longer applies. We will therefore have to estimate it using different methods.

2.3.2 Smooth vertical walls and stress fields - Rankine zones

Rankine proposed a method for calculating the horizontal earth pressures on a wall that has encountered movement by assuming that the earth mass was equally stressed and thus failing at all points. Using the MC failure envelope and substituting the vertical and horizontal stresses for the major and minor principal stresses, Rankine developed equations to calculate the active and passive earth pressure coefficients. A special notation of Rankine's equations originating from Norges teknisk- naturvitenskapelige universitet (NTNU) is derived in Appendix B. Equation (B10) in Appendix B gives us a direct connection between the major principal stress, σ_1', the minor principal stress, σ_3', the friction angle, ϕ', and the attraction, a. Substituting the vertical stress and horizontal stress for the major- and minor principal stresses in equation (B10) allows us to derive an equation for either the active or passive earth pressure coefficient. By aligning critical stress elements, as seen in Figure 2.3, together we create a stress field that represents the theoretical stress situation in the soil. The orientation and shape of the elements is dependent on whether the main principal stress is horizontal or vertical. In other words it depends on if the wall is being pushed into the soil or if the soil is driving the wall out.
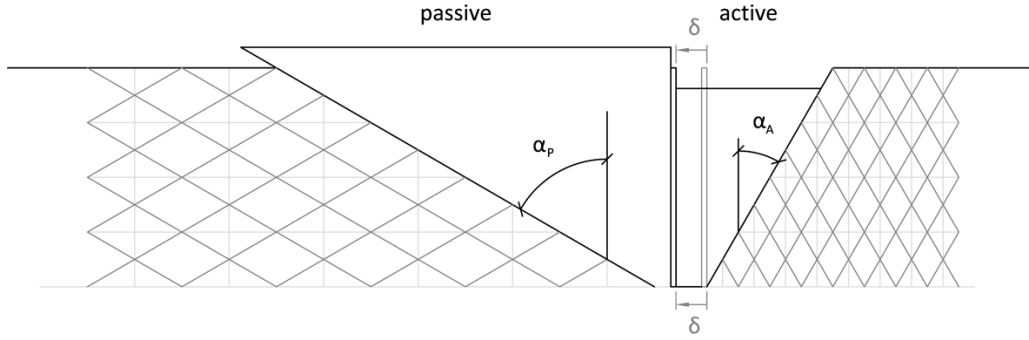
Figure 2.4: The active and passive sides of a wall along with Rankine zones.

The stress fields drawn on either side of the wall in Figure 2.4 are called active and passive Rankine zones. Active Rankine zone develops in the soil mass where the soil pushes the wall out and the passive Rankine zone develops where the soil tries to resist the movement of the wall. Let's first take a look at the stresses in the active stress fields.

Active Rankine zones

Looking at the active (*right*) side of the wall in Figure 2.4 we note that because the wall moves away from the soil mass it cannot maintain large stresses in the horizontal plane so the major principal stress will have to be the vertical one. Using this knowledge σ_v' and σ_h' can be substituted for σ_1' and σ_3' in equation (B10) in Appendix B. By introducing equation (B27) into this the desired equation is derived as

$$(\sigma_h' + a) = (\sigma_v' + a) \cdot N^- \tag{14}$$

where N^- is the minor principal stress ratio given with equation (B27) in Appendix B. The failure wedge that can be seen on the right side of the wall in Figure 2.4 will have the inclination of

$$\alpha_A = \frac{\pi}{4} - \frac{\phi'}{2} \tag{15}$$

to the vertical measured in radians. The angle α_A can be seen schematically in Figure 2.3 b). With equation (14) it is possible to estimate the lateral earth pressure in the active case as a function of the horizontal earth pressure, the friction angle as well as the attraction. This can be used to calculate the magnitude of the force acting on the wall surface on the active side if no shear stress is transferred from the structure to the wall.

Passive Rankine zones

Looking again at the wall in Figure 2.4 and noting that the wall is moving into the soil mass on the passive (*left*) side and as a result the soil wedge is pushed upwards, it can be assumed that the horizontal stresses will in this case be larger than the vertical ones. With similar substitution as before but this time using σ_h' as the major principal stress along with equation (B28) and equation (B10) in appendix B gives the result

$$(\sigma_h' + a) = (\sigma_v' + a) \cdot N^+ \tag{16}$$

where N^+ is the major principal stress ratio given with equation (B28) in Appendix B. This notation of calculating the horizontal earth pressures is not the classical one but the

simplicity of the form is certainly appealing. When comparing equations (14) and (16) we see that the form is remarkably similar and that the only difference are the constants N^+ and N^-. They are however closely related and by comparing equations (B27) and (B28) we see that

$$N^+ = \frac{1+sin(\phi')}{1-sin(\phi')} = \frac{1}{\frac{1-sin(\phi')}{1+sin(\phi')}} = \frac{1}{N^-} \tag{17}$$

As before we can look at the failure wedge in Figure 2.4 and by turning the critical element in Figure 2.3 b), note that the shear surface will have the angle of

$$\alpha_P = \frac{\pi}{4} + \frac{\phi'}{2} \tag{18}$$

to the vertical measured in radians. This angle can be seen in schematically in Figure 2.3 b). With equation (16) it is possible to estimate the passive lateral earth pressures against smooth vertical walls.

Rankine zones are a great tool to approximate horizontal earth pressures but they do not present the whole picture as only critical shear elements oriented in the same direction as the major and minor principal stresses in the soil are used. Because principal stresses act on principal planes which by definition only have normal stresses acting on them, no shear stress is transferred from the soil to the structure. In other words in this idealized model the wall is assumed completely frictionless and the soil can slide effortlessly up and down its sides. As retaining walls are rarely constructed completely smooth it is necessary to take into account the interaction between the wall and the soil.

2.3.3 Rough walls and stress fields - Prandtl zones

The critical soil element and its shear diamond can be seen in Figure 2.3 b), and we note that the one shown in Figure 2.2 b) is merely a special case of the other. The shear elements in Figure 2.4 are rotated so that their major and minor principal stresses are aligned to the vertical and the horizontal, as stated before this would not transfer any shear stresses to the structure. The failure surfaces seen in Figure 2.4 are also a function of the orientation of the critical shear planes and therefore have a planar form.

In reality failure surfaces rarely have a completely planar form and it has been suggested that the most common form is a combination of a straight line and that of a curve in the shape of a logarithmic spiral (Das, 2002). The logarithmic spiral has the equation

$$R_b = R_A \cdot e^{\theta \cdot tan(\phi')} \tag{19}$$

Using the logarithmic spiral it is possible to rotate the stress fields and the critical shear elements along with them. Defining the origin of the logarithmic spiral on the wall at terrain level and initially aligning the critical shear elements so that they have a side that tangents the structure it is possible to rotate the stress field so that it connects to the Rankine zone. This means that by the means of a logarithmic spiral it is possible to transfer all the shear stress in the soil at failure to the structure.
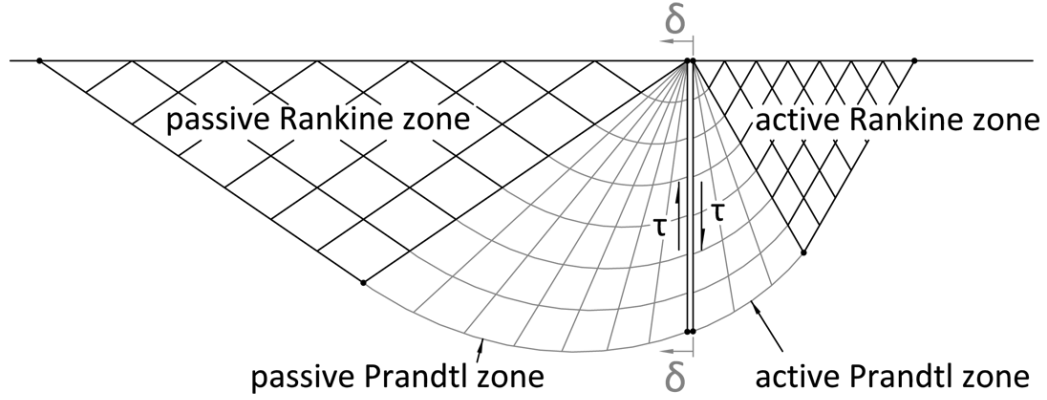
Figure 2.5: The active and passive Rankine and Prandtl zones in a stress field.

In Figure 2.5 it can be seen that the critical stress elements have been rotated so that they have a common side with the structure and thus transferring all the available shear stress to the structure. This implies that the structure is completely rough. In Appendix D it is shown that the relationship between stress acting on either side of the Prandtl zone is described as

$$(\sigma_{c\theta} + a) \cdot e^{2\theta tan(\rho')} = (\sigma_{c0} + a) \tag{20}$$

where $_{c0}$ and $_{c\theta}$ signify the opening and rotated boundary of the Prandtl zone respectively. The equation is consistent in both pressure cases if we define the friction angle to be positive when calculating passive pressures and negative when calculating active pressures.

We have now developed two cases; one where the shear stress in the soil does not affect the structure at all and another where all the shear stress in the soil is transferred to the structure. In reality the amount of shear stress transferred from the soil to the structure will probably lie somewhere in between the two.

2.3.4 Roughness and partially developed stress fields

As was stated above it is not plausible that all retaining structures should either be constructed as completely rough or completely smooth. We therefore introduce a variable called the roughness ratio, r, as a measurement on how much of the shear stress in the soil will be transferred to the structure.

$$r = \frac{\tau}{\tau_{cr}} \tag{21}$$

where τ stands for the shear stress acting on the structure and τ_{cr} stands for the critical shear stress found in the soil mass at failure, shown in Figure 2.3. The roughness ratio will then take the value $r = 0$ when we have a completely smooth wall and the value $r = 1$ when the wall is completely rough. Failure in the soil mass when the roughness is $r = 0$ would create a situation as can be seen in Figure 2.4. Failure in the soil mass when the roughness is $r = 1$ would create a situation as can be seen in Figure 2.5.

When describing a situation where only a part of the shear stress is transferred from the soil to the structure and we have a movement of the wall in respect to the soil as shown in

Figure 2.4, we end up with a combination of two Rankine zones connected by a partially developed Prandtl zone, this can be seen schematically in Figure 2.6 a) and b). The opening angle of the Prandtl zones is then completely governed by the roughness ratio; or how much shear stress is transferred from the soil to the structure.
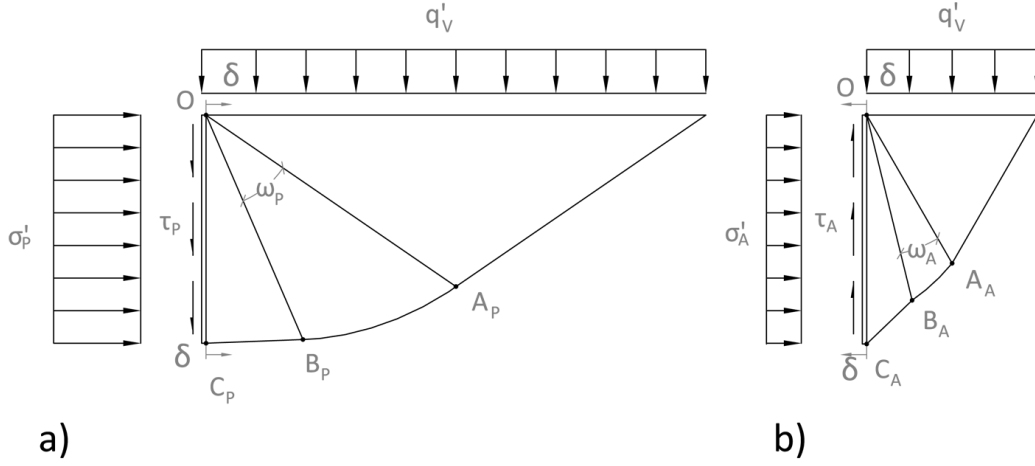
Figure 2.6: Shows the combined stressfields for a) the passive case b) the active case.

If we only have a partially developed Prandtl zone connected to two Rankine zones, the relationship between the vertical and horizontal shear stress can in the passive case be described as

$$(\sigma_h' + a) = \left[\frac{(1+f_\omega^2) \cdot N^+}{1 + f_\omega^2 \cdot N^+} \cdot e^{2 \cdot \omega \cdot tan(\rho')} \right] \cdot (\sigma_v' + a) \tag{22}$$

where f_ω is the shear plane mobilization, ω is the opening angle of the Prandtl zone measured in radians and N^+ is the major principal stress ratio. A derivation of this equation can be found for both the active and passive case in Appendix E. It should be noted that the active pressures can be calculated with equation (22) by shifting the sign of the friction angle.

We can define the factor in the square brackets in equation (22) as a K factor linking the horizontal and vertical stress as the one shown in equation (9) and accept that in our equation we will shift both the horizontal and vertical stress by the attraction, a. It should also be noted that for a roughness of $r = 0$ both f_ω and ω reduce to $f_\omega = \omega = 0$ and the factor K reduces to N^+. Equation 22 is therefore a more general case of equation (16) and is valid for both the active- and the passive earth pressure case. It should be noted that this solution is valid only for roughness on the interval between $r = 0$ and $r = 1$.

To produce a situation with negative roughness we can introduce external forces. This is shown illustratively both for the active and passive state in Figure 2.7.
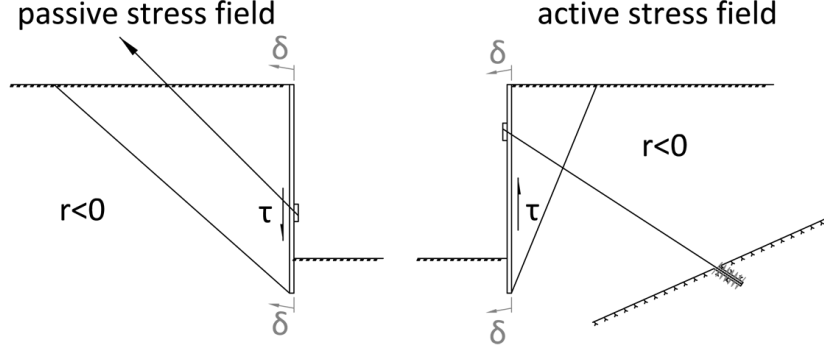
Figure 2.7: Possible scenarios involving negative roughness.

In the passive state a force pulls the wall upward and into the soil and in the active case the wall is anchored to the rock bed below it and is pulled downwards as it moves out. Both cases present an opposite vertical movement of the wall in respect to the soil than the one shown in Figure 2.4.

If we assume a planar shear surface for the active and passive cases involving negative roughness ratios, it can be shown that the connection between the vertical and horizontal earth pressures is governed by the relationship

$$(\sigma_h' + a) = \left(\frac{1}{\sqrt{1+\tan^2(\rho')}-\tan(\rho')\cdot\sqrt{1+r}}\right)^2 \cdot (\sigma_v' + a) \qquad (23)$$

The term involving the second power can be defined as K and as before it is valid for both the active and passive case if we distinguish between them by using a negative friction angle on the active side. It should again be noted that this case is valid only for negative roughness values (Janbu, et al., 2006). Assuming a planar shear surface for negative values of roughness has been shown with different methods to deliver usable approximations of the earth pressure coefficient (Grande, 1976).
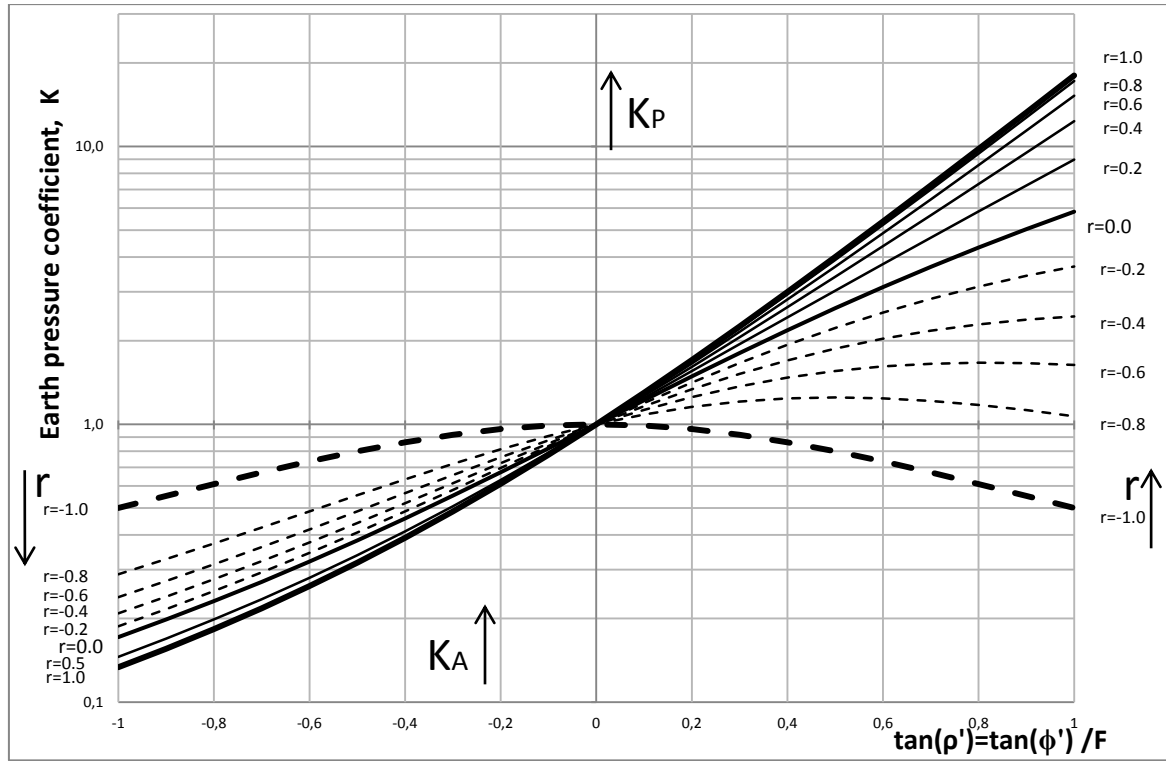
Figure 2.8: Active and passive earth pressure coefficient as a function of tan(ρ') and r.

In Figure 2.8 it should be noted that the dashed lines represent a negative roughness and the continuous lines represent the positive. The active side has a negative friction angle, this is as previously stated only a handy notation introduced in order to generalize equations (22) and (23).

By the means of Figure 2.8 it is now possible to calculate the relationship between vertical and horizontal stress with the equation

$$(\sigma'_h + a) = K_{A/P}(\sigma'_v + a) \tag{24}$$

where a is the attraction and $K_{A/P}$ represents either the passive or active earth pressure coefficient. The required input parameters are $tan(\rho')$ and the roughness, r. This solution is valid for a stress field derived for a horizontal surface and a vertical wall.

The effect of a sloping backfill

When the backfill can be modeled as a continuous slope the theory behind Rankine's stress fields no longer applies in the form already presented. This is because the active and passive pressures are no longer horizontal but have the same inclination as the backfill (Das, 2002). Figure 2.9 shows a sloped terrain and the forces acting on the structure once it has experienced some movement. Note that the active and passive shear stresses have opposite directions.
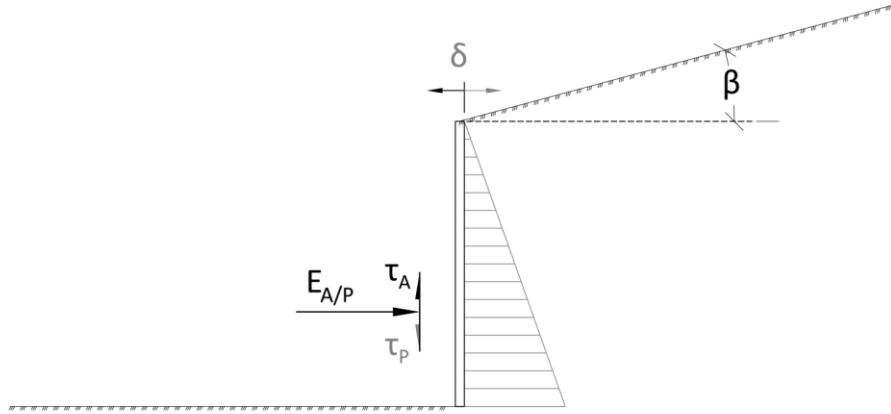
Figure 2.9: Sloped terrain and the retaining forces.

where $E_{A/P}$ is the horizontal force and $\tau_{A/P}$ is the shear stress after the wall has encountered some movement in either direction. In order to generalize the solution of the earth pressure coefficient for the case of a sloping backfill the roughness term, $(1 + r)$, in equation (23) is exchanged with a new variable, t, which is defined as

$$t = (1 + r) \cdot (1 - s) \tag{25}$$

where r is the roughness and s is a new variable defined as

$$s = \frac{tan(\beta)}{tan(\rho')} \tag{26}$$

where β is the angle of inclination of the backfill and ρ' is the mobilized friction angle. There are obvious limitations of application of this approach such as the slope of the backfill cannot be equal or greater than the friction angle. By the definition of the friction angle this would induce a failure in the slope and from a calculation standpoint would mean a negative number under the square root resulting in a complex solution. The variable t, is furthermore not allowed to exceed the value of 4 but recommended maximum value for practical applications is 2 (Statens vegvesen, 2010).
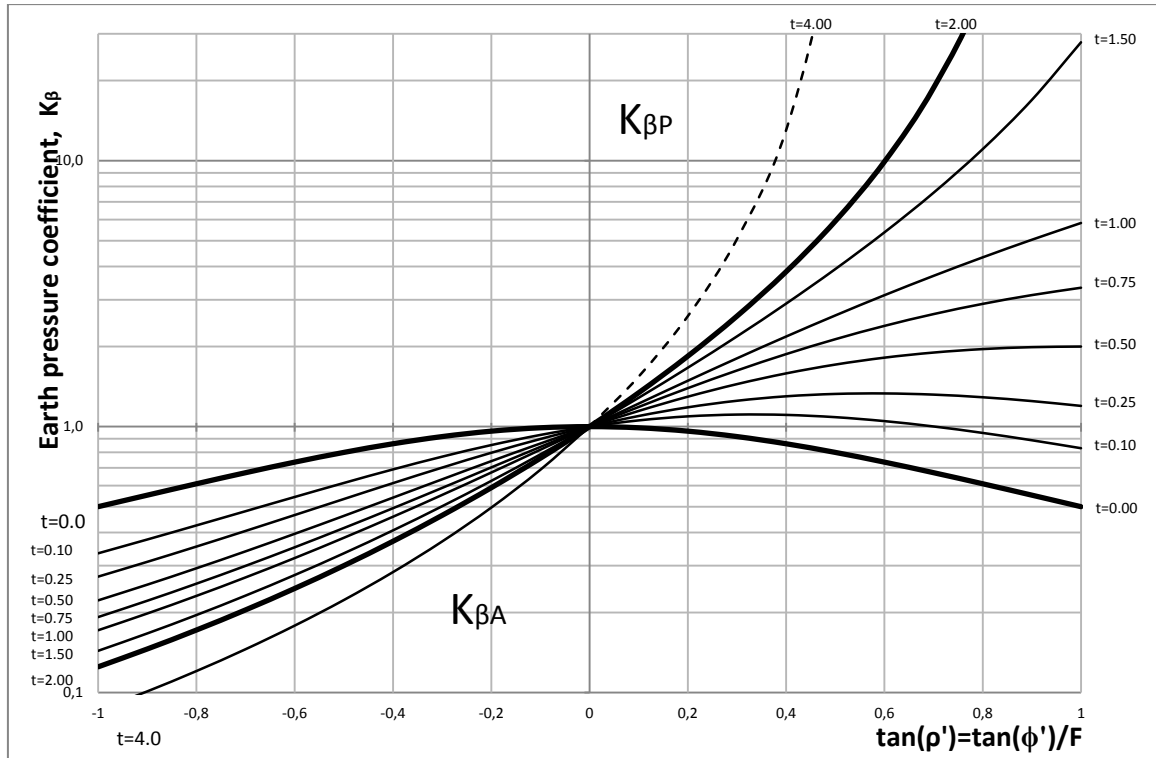
Figure 2.10: Active and passive earth pressure coefficients for sloping terrain.

In addition to the modified version of the earth pressure coefficients the formula used to calculate the earth pressures has been modified as well. The active earth pressures can in this case be calculated as

$$(\sigma_h' + a) = K_{\beta A}(\sigma_v' + a) + \frac{s}{s - \omega_A} \cdot a \tag{27}$$

where s is as defined in equation (26) and

$$\omega_A = \frac{tan(\alpha_A)}{tan(\rho')} = 1 + \frac{1}{sin(\rho')} \cdot \sqrt{\frac{1-s}{1+r}} = 1 + \frac{1}{tan(\rho')} \cdot \sqrt{\frac{(1+tan^2(\rho')) \cdot (1-s)}{1+r}} \tag{28}$$

The passive case can be calculated in a similar manner

$$(\sigma_h' + a) = K_{\beta P}(\sigma_v' + a) + \frac{s}{s - \omega_P} \cdot a \tag{29}$$

where s is again as defined as in equation (26) with the modification that the angle, β, has a positive direction sloping downwards into the backfill and

$$\omega_P = \frac{tan(\alpha_P)}{tan(\rho')} = 1 - \frac{1}{sin(\rho')} \cdot \sqrt{\frac{1-s}{1+r}} = 1 + \frac{1}{tan(\rho')} \cdot \sqrt{\frac{(1+tan^2(\rho')) \cdot (1-s)}{1+r}} \tag{30}$$

This solution assumes a linear failure surface as was done for the case of the negative roughness. This solution assumes that the terrain is sloped upwards for the active case and sloped downwards for the passive case. The coefficients ω_A and ω_P should not be confused with the active and passive openings of the Prandtl zones in equation (22).

17

Rankine´s solution for sloping backfill

Rankine considered the possibility of a sloping backfill and proposed the following earth pressure coefficient for non-cohesive soils in the case of active pressures

$$K_A = cos(\beta) \cdot \frac{cos(\beta) - \sqrt{cos^2(\beta) - cos^2(\phi')}}{cos(\beta) + \sqrt{cos^2(\beta) - cos^2(\phi')}} \tag{31}$$

For the case of passive pressures he proposed the following equation for the earth pressure coefficient

$$K_P = cos(\beta) \cdot \frac{cos(\beta) + \sqrt{cos^2(\beta) - cos^2(\phi')}}{cos(\beta) - \sqrt{cos^2(\beta) - cos^2(\phi')}} \tag{32}$$

where β is the angle of inclination of the backfill and ϕ' is the friction angle. The earth pressure should then be assumed to increase linearly from terrain level to the base of the structure. The force resultant should therefore act at $1/3$ the distance from the base to the top of the structure and be inclined with the same angle as the backfill. (Das, 2002). It has been suggested that Rankine´s solution for passive pressures only gives usable results for values of $\beta \leq 0$. Furthermore it has been stated that the solution should not be used to calculate earth pressures against structures but rather to evaluate forces on vertical planes in soil mass. (State of California Department of Transportation, 1990).

The effect of wall leaning into the backfill

When backside of the wall is sloped into the backfill the stressfield does not develop fully in the same way as has previously been described. HB016 proposes that this be dealt with in the following manner. The active earth pressure coefficient should be calculated as is done in Figure 2.8 or Figure 2.10 and then corrected as

$$K_{A.Corr} = K_\delta \cdot K_A = \frac{cos^2(\delta + \rho')}{cos^3(\delta) \cdot cos(\rho')} \cdot K_A \tag{33}$$

where δ is the angle of the back of the wall. A situation of this sort is shown in Figure 2.11.
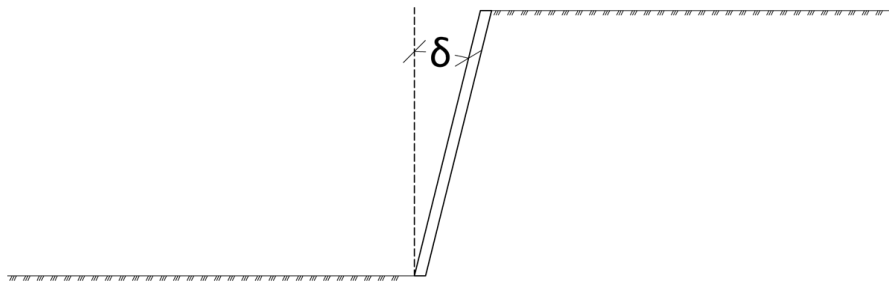
Figure 2.11: Retaining wall sloped into the backfill and the angle δ.

There are noted limitations of application for this reduction method as the mobilized friction angle shall lie in the interval $0 \leq \rho' \leq 40°$ and the angle δ shall lie in the interval $0 \leq \delta \leq 40°$. It is noted that this method was developed for completely smooth walls but the method should give reasonable results when r lies on the interval $-0,5 \leq r \leq 0,7$.

2.3.5 Coulomb's theory of earth pressures against retaining walls

In 1776 Coulomb presented a theory for the active and passive earth pressures against retaining walls. In his formulations he made the assumptions that the failure surface was planar and the soil followed the strength criteria proposed by himself defined by equation (6) with no cohesion. Coulomb also took into consideration the friction between the soil and the back of the wall. The theory is derived by the means of static equilibrium of an assumed linear failure surface as is shown in Figure 2.12.
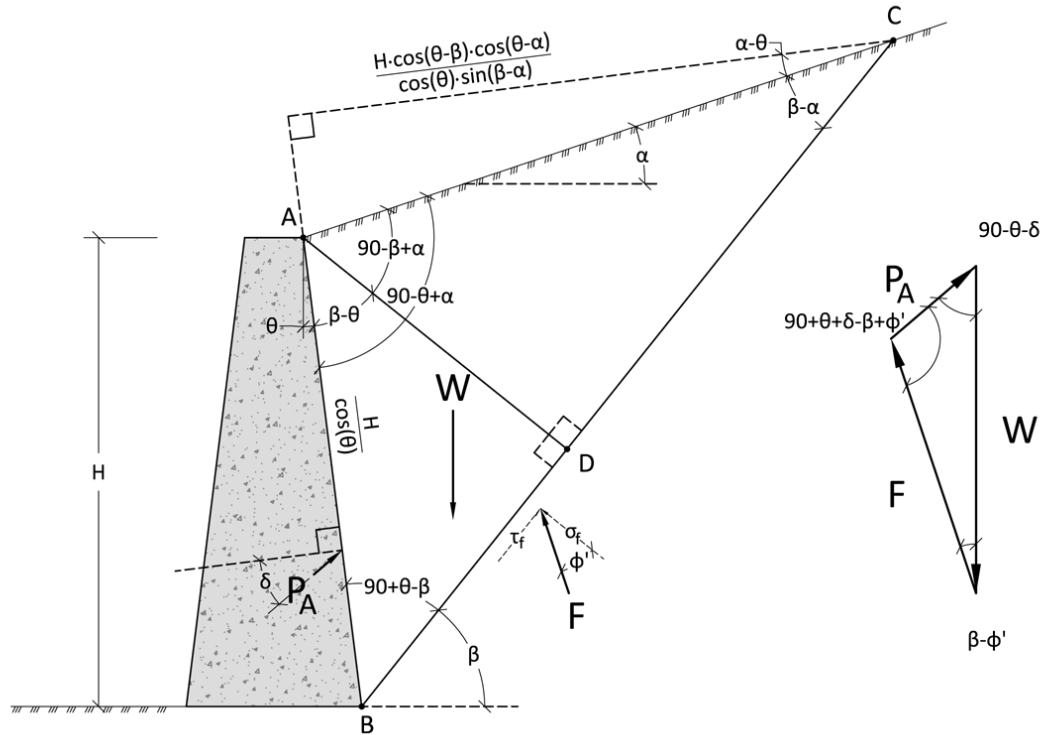
Figure 2.12: Active pressures on a retaining structure along with a force diagram.

The active forces in Figure 2.12 are created by the gravity pulling the soil wedge down and the earth and wall retaining the movement of the wedge along the assumed linear slip surface. The orientation of the forces is derived directly from the geometry of the problem. The relationship between the driving force and the wall force is of a special interest when designing the structure and it can be derived from the geometry alone via the sine rule

$$\frac{P_A}{sin(\beta - \phi')} = \frac{W}{sin(90 + \theta + \delta - \beta + \phi')} \tag{34}$$

where P_A is the force the wall exerts back on the soil wedge, δ is the angle of wall friction, ϕ' is the friction angle of the backfill, θ is the inclination of the back of the wall, β is the angle of the assumed failure surface and W is the weight of the failure wedge. The weight of the failure wedge is a function of the soil density and the area of the wedge which can, with a little help from Figure 2.12, be calculated as

$$W = \frac{\gamma \cdot H^2 \cdot cos(\theta - \alpha) \cdot cos(\theta - \beta)}{2 \cdot cos^2(\theta) \cdot sin(\beta - \alpha)} \tag{35}$$

where α is the angle of the backfill. Putting together equations (34) and (33) we get an equation connecting the lateral active force with the height of wall and assumed angle of the failure surface.

$$P_A = \frac{\gamma \cdot H^2}{2} \cdot \frac{\cos(\theta-\alpha) \cdot \cos(\theta-\beta) \cdot \sin(\beta-\phi')}{\cos^2(\theta) \cdot \sin(\beta-\alpha) \cdot \sin(90+\theta+\delta-\beta+\phi')} \tag{36}$$

where γ is the density of the backfill and H is the height of the structure. If we assume the angle of wall friction, δ, to be constant we have an equation with only one variable; the inclination of the failure surface, β. By differentiation and back substitution it is possible to derive an equation for the active force from the most critical failure plane as

$$P_A = K_a \cdot \frac{\gamma \cdot H^2}{2} \tag{37}$$

where the earth pressure coefficient is independent of the angle β and is given by

$$K_A = \frac{\cos^2(\phi'-\theta)}{\cos^2(\theta) \cdot \cos(\delta+\theta) \cdot \left(1 + \sqrt{\frac{\sin(\delta+\phi') \cdot \sin(\phi'-\alpha)}{\cos(\delta+\theta) \cdot \cos(\theta-\alpha)}}\right)^2} \tag{38}$$

Coulombs passive earth pressure coefficient can be derived in a very similar manner, the angle of the passive force will then be positive as the force points at a downward angle to the wall back and because the failure wedge is now being pushed up the failure surface the shear stress will point in the opposite direction to the active case. This situation is shown in Figure 2.13.
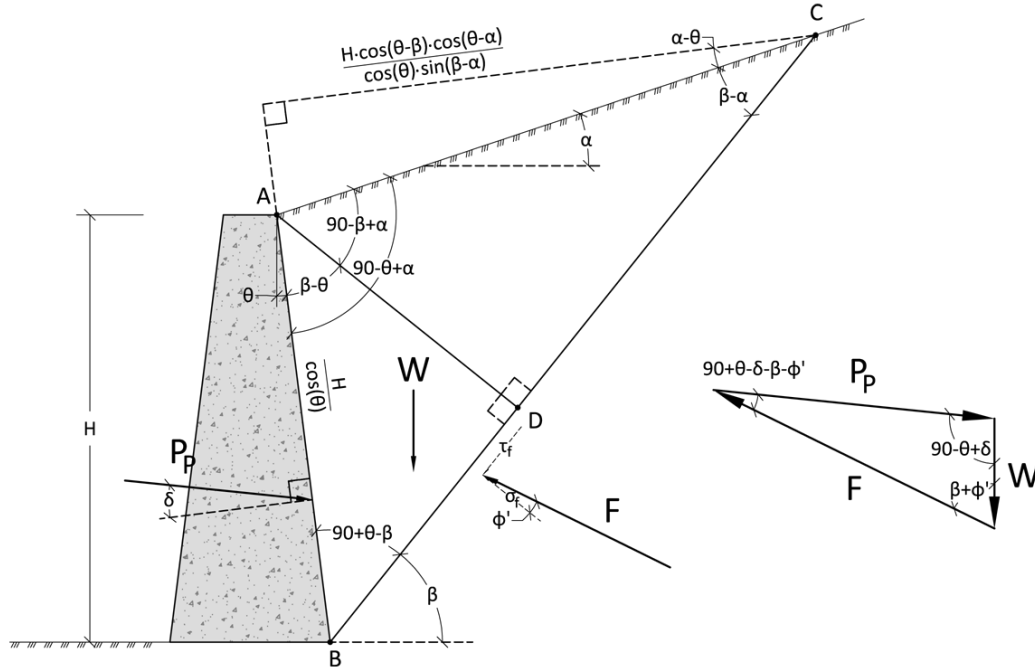
Figure 2.13: Passive pressures on a retaining structure along with a force diagram.

The geometry of the failure wedge in Figure 2.13 has not changed from Figure 2.12, but the orientation of the wall force and frictional force differ from the previous case. Using

the sine rule it is possible to derive a relationship between the driving force and the wall force as

$$\frac{P_P}{sin(\beta+\phi')} = \frac{W}{sin(90+\theta-\delta-\beta-\phi')}$$ (39)

Equation (33) still holds true for this case and by substituting into equation we can derive the equation for Coulombs passive earth pressures as

$$P_P = \frac{\gamma \cdot H^2}{2} \cdot \frac{cos(\theta-\alpha) \cdot cos(\theta-\beta) \cdot sin(\beta+\phi')}{cos^2(\theta) \cdot sin(\beta-\alpha) \cdot sin(90+\theta-\delta-\beta-\phi')}$$ (40)

Using the same methods as described for the active case it is possible to derive the passive pressure for the most critical plane as

$$P_P = K_P \cdot \frac{\gamma \cdot H^2}{2}$$ (41)

where the earth pressure coefficient is given by

$$K_P = \frac{cos^2(\phi'+\theta)}{cos^2(\theta) \cdot cos(\delta-\theta) \cdot \left(1+\sqrt{\frac{sin(\phi'+\delta) \cdot sin(\phi'+\alpha)}{cos(\delta-\theta) \cdot cos(\theta-\alpha)}}\right)^2}$$ (42)

For frictionless, vertical walls retaining cohesionless soils equations (38) and (42) give the same results as equations (14) and (16) (Das, 2002). These derivations are an elegant solution but they do however suffer somewhat as they only apply when calculating non cohesive soils as well as the failure surface is always assumed to be linear, which does not apply in all materials.

2.4 Bearing capacity of foundations

Terzaghi proposed an equation to calculate the ultimate bearing capacity of soils in 1943. His work was based on the principles published by Prandtl 20 years earlier (Das, 2002). According to Terzaghi the ultimate bearing capacity can be calculated with the formula

$$q_u = N_c \cdot c' + N_q \cdot q + N_\gamma \cdot \frac{1}{2} \cdot \gamma \cdot B$$ (43)

where N_c, N_q and N_γ are known as the bearing capacity factors, c' is the cohesion, q is the surcharge, γ is the soil unit weight and B is the width of the footing. Empirical correcting factors are then given to each term to simulate the effect of a certain footing geometry and the depth of embedment.

The factors affecting the bearing capacity the cohesion, surcharge, weight of the soil and geometry of the footing. At NTNU a similar approach has been used to study the bearing capacity of footings. The equation for the average bearing capacity on an effective stress basis proposed by NTNU is given as

$$\overline{\sigma_v} + a = N_q \cdot (z \cdot \gamma'_{over} + a) + N_\gamma \cdot \left(\frac{1}{2} \cdot \gamma'_{under} \cdot B_0\right) - N_u \cdot \Delta\overline{u_b}$$ (44)

An extra term that reduces the bearing capacity has been added to handle excess pore pressures under the footing, as well as the notation has been altered to substitute the cohesion for the attraction.

The bearing capacity factor N_q comes directly from the theory of stress fields, and is calculated in a similar manner as equation (22) is derived. It is given as

$$N_q = \frac{(1+f_\omega^2)\cdot N^+}{1+f_\omega^2\cdot N^+} \cdot e^{(\pi-2\omega)\cdot tan(\rho')} \tag{45}$$

Like the earth pressure coefficient, K, N_q is only dependent on the friction angle and the roughness between the footing and the soil, r_b.
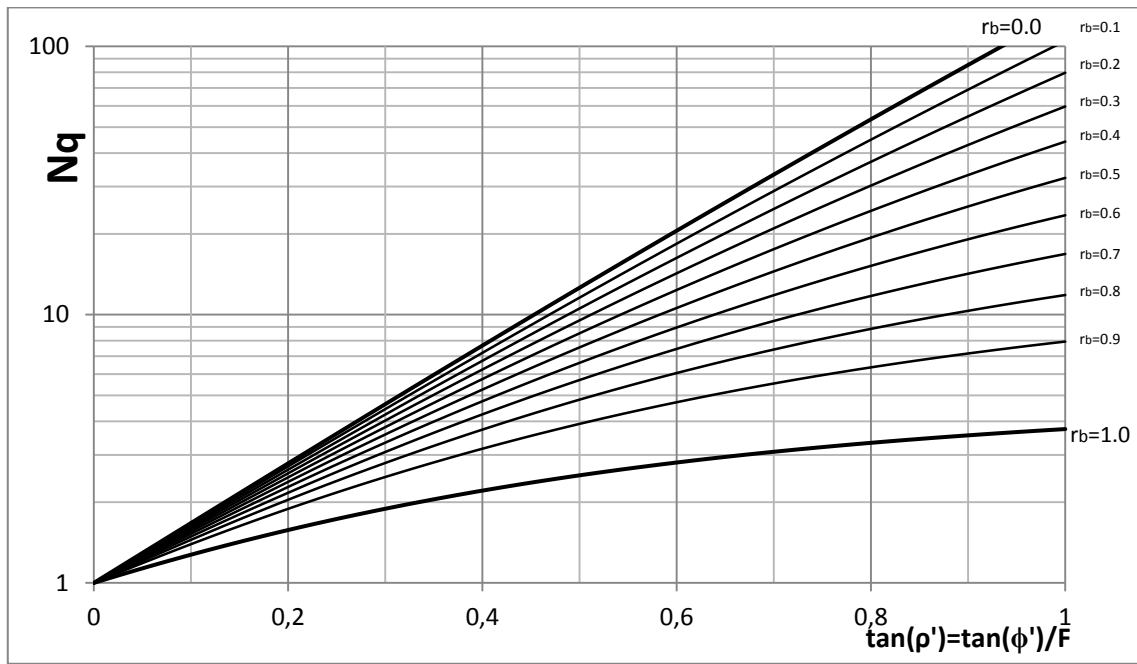
Figure 2.14: The relationship between N_q, tan(ρ') and the roughness, r_b.

It should be noted that the roughness referred to in Figure 2.14 is the roughness acting between soil and foundation and is not connected to the roughness acting between structure and wall as was defined with equation (21).

The factor N_γ is derived from the geometry of the shear surface at failure. This factor is not as easily calculated as the other bearing capacity factors but can be determined with the following iterative process

$$K_p = 2 \cdot sin^2(\alpha_p) \cdot e^{\left(\frac{\pi}{2} + \rho'\right) \cdot tan(\rho')}$$

$$x_0 = 2 \cdot (1 - r) \cdot tan(\rho')$$

loop n times:

$$\psi_{i+1} = atan(x_i - tan(\rho'))$$

$$C_{i+1} = K_p \cdot e^{2 \cdot \psi_{i+1} \cdot tan(\rho')}(1 + tan(\psi_{i+1}) \cdot tan(\rho')) - 1 \qquad (46)$$

$$x_{i+1} = \left((1 + r) + \sqrt{(1 + r)^2 + \frac{(1+r)}{C_{i+1}}}\right) \cdot tan(\rho')$$

next loop:

$$N_\gamma = \frac{2 \cdot C_n \cdot x_n + tan(\rho')}{1 + tan^2(\psi_n)}$$

The convergence is fast and 10-20 iterations should produce good results. This process was developed at NTNU by Professor Nilmar Janbu and the results introduced at a conference about the behavior of offshore structures in Trondheim in 1976, (Janbu, et al., 1976); the method of calculation was however not published on paper. It is referred to here by means of an internal report from his department published years later by a student (Døssland, 1980).
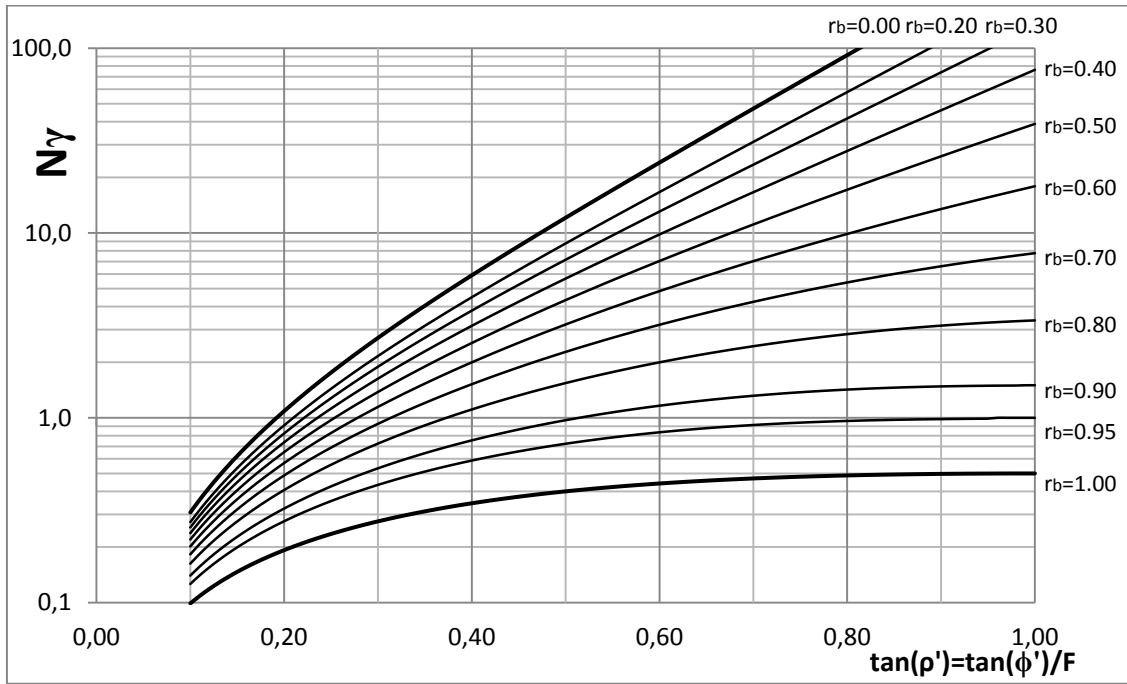
Figure 2.15: The relationship between Nγ, tan(ρ') and the roughness, r_b.

The calculation method does have its limitations and becomes unstable when both the roughness and $tan(\rho')$ approach the value of 1. In Figure 2.15, these side effects have been smoothed out.

The effect of excess pore pressures in the foundation is taken into account via the factor N_u. The parameters that control the behavior of N_u are the same as for the other bearing capacity factors, r and $tan(\rho')$. The effect of excess pore pressures in the foundation will not be discussed in this paper but for the sake of completeness values of N_u can be read from Figure 2.16.
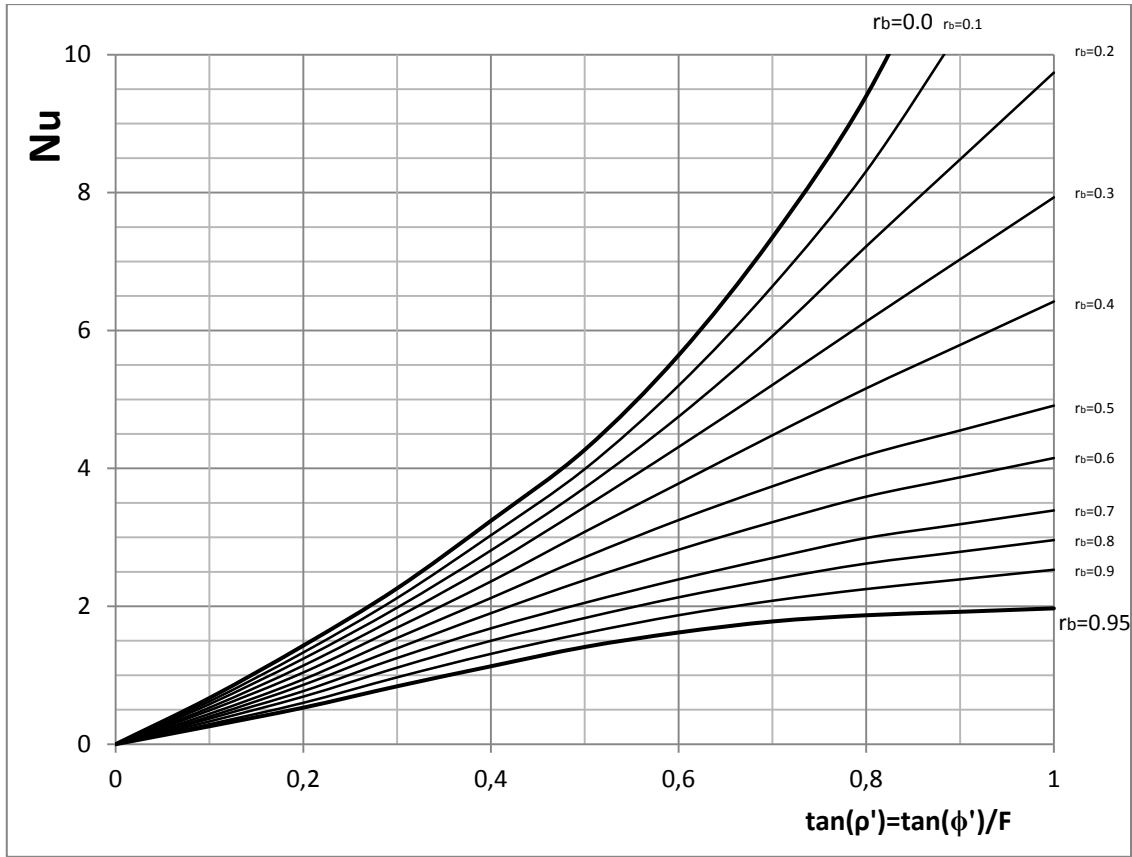
Figure 2.16: The relationship between Nu, tan(ρ') and the roughness, r_b.

The method of calculation behind the values of N_u is unknown to the author of this paper and values presented in Figure 2.16 have therefore not been verified with calculations.

It should again be noted that the roughness referred to in Figure 2.14 - Figure 2.16, r_b, is the roughness between the foundation and soil underneath it and should not be confused with the roughness acting between the wall and soil, r.

The effect of a moment acting on the footing is taken into account with the concept of the effective footing width B_0. The effective footing width is caclulated as

$$B_0 = B - 2 \cdot \left| \frac{M}{F_v} \right| \tag{47}$$

where B is the geometrical width of the footing, M is the moment and F_v is the vertical force acting on the foundation. Figure 2.17 shows illustratively the concept of the effective footing width.
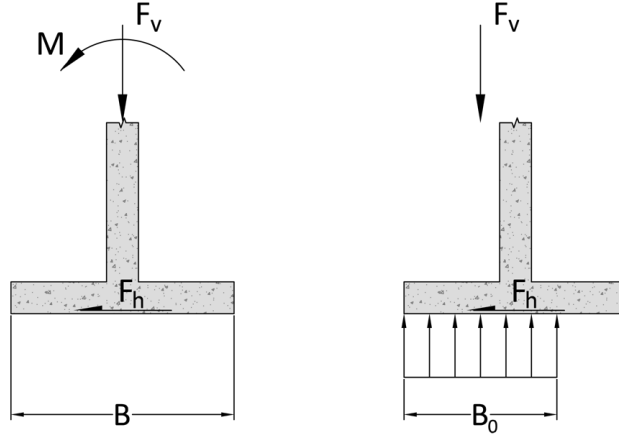
Figure 2.17: The idea behind the effective footing width

Taking the absolute value of the quotient in equation (47) ensures that the effective footing width, B_0, is always equal or less than the geometrical footing with, B (Statens vegvesen, 2010).

Effect of a sloping terrain on bearing capacity

The bearing capacity equation, equation (44), was in part derived by the means of stress fields that develop from a horizontal plate through two Rankine zones and a Prandtl zone to a flat surface on either side of the structure. If the terrain in front of the structure is sloped, the equation no longer applies and some modifications are required.
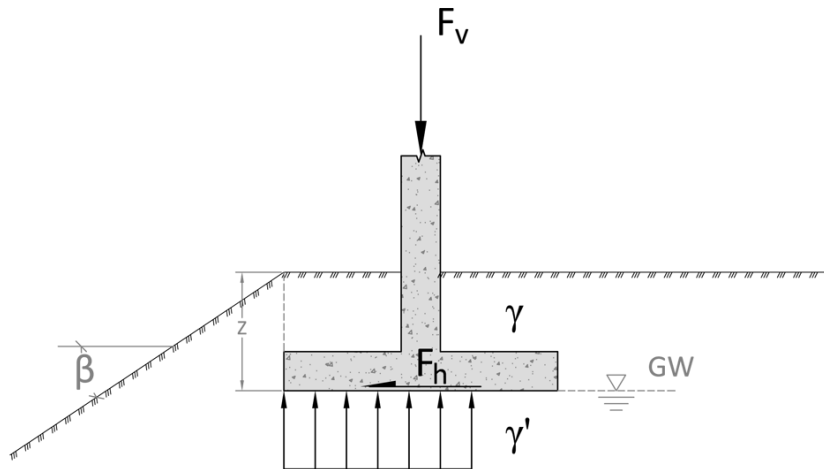
Figure 2.18: An illustrative footing founded near a sloping terrain.

To take care of the reduced bearing capacity two new reduction factors are introduced to equation (44). The equation for the averaged bearing capacity then takes the form

$$\overline{\sigma_v} = f_{sq} \cdot \left(N_q \cdot p' + \frac{1}{2} \cdot N_\gamma \cdot \gamma'_{under} \cdot B_0 \right) + \left(N_q \cdot f_{sa} - 1 \right) \cdot a - N_u \cdot \Delta \overline{u_b} \qquad (48)$$

The two new factors f_{sq} and f_{sa} act as reduction factors for both the loading- and soil weight factors as well as the attraction. They are defined as

$$f_{sq} = \left(1 - 0{,}55 \cdot tan(\beta) \right)^5 \qquad (49)$$

25

and

$$f_{sa} = e^{-2 \cdot \beta \cdot \tan(\rho')} \tag{50}$$

where β is the slope of the terrain and ρ' is the mobilized friction angle of the soil (Statens vegvesen, 2010). The equation for f_{sq} is given as a bounding curve of all results derived for all values of the mobilized friction angle, erring on the safe side (Døssland, 1980). It should be noted that when the terrain inclination is 0 equations (49) and (50) reduce to 1 and equation (48) reduces to equation (44).

Bearing capacity on a total stress basis

The bearing capacity on an undrained, or total stress, basis is somewhat simpler than the one proposed in equation (44). The bearing capacity on a total stress basis for flat terrain can be calculated as

$$\overline{\sigma_v} = N_c \cdot \tau_d + p_v \tag{51}$$

where N_c is the bearing capacity factor, τ_d is the design shear strength and p_v is the surcharge load.

The design shear strength is given as

$$\tau_d = \frac{S_u}{\gamma_M} \tag{52}$$

where S_u is the undrained shear strength and γ_M is the material safety factor. The bearing capacity factor N_c is given as

$$N_{c.strip} = (\pi - 2 \cdot \omega) + \frac{2}{1 + f_\omega^2} \tag{53}$$

where f_ω is calculated with equation (C29) and ω is calculated with equation (C20) noting that in the undrained case $\alpha_A = \alpha_P = \pi/4$. For quadratic and circular foundations it has been proposed that the undrained bearing capacity increases up to 20% depending on the roughness. This is incorporated into the bearing capacity factor with the equation

$$N_{c.quadratic} = N_{c.strip} \cdot (1 + f_a) \tag{54}$$

Values for f_a is can be seen in Figure 2.19.
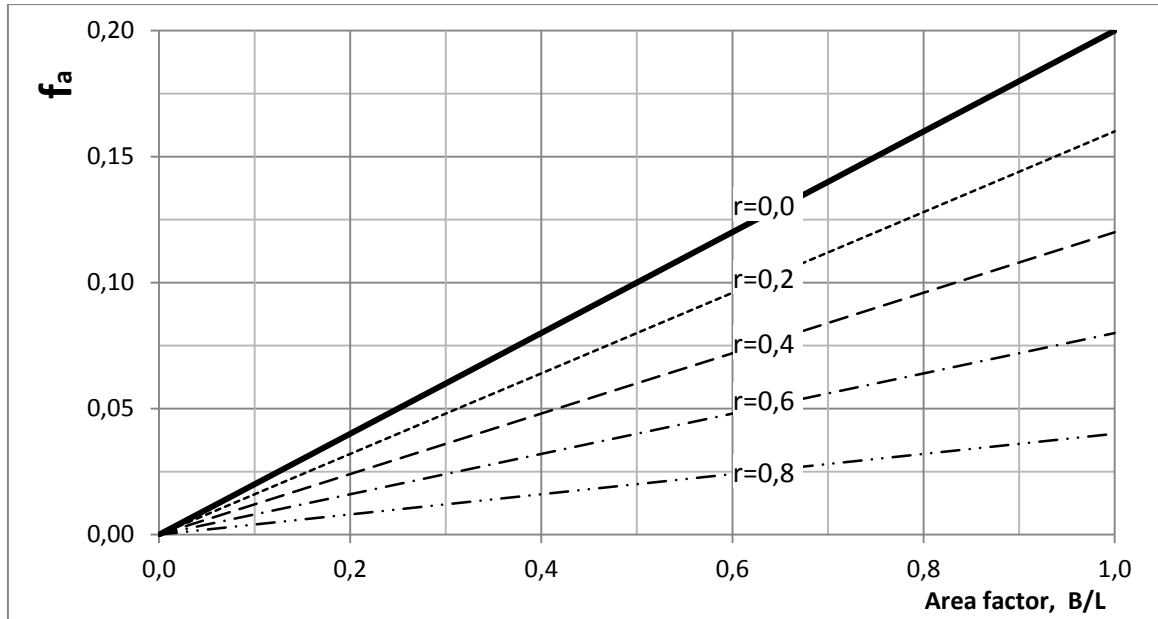
Figure 2.19: The geometrical correction factor f_a.

Using equations (53) and (54) as well as Figure 2.19, a general equation for the bearing capacity factor can be derived as

$$N_c = \left((\pi - 2 \cdot \omega) + \frac{2}{1+f_{\omega}^2}\right) \cdot \left(1 + \frac{0{,}2 \cdot B \cdot (1-r)}{L}\right) \qquad (55)$$

The bearing capacity factor proposed in equation (55) can be seen in Figure 2.20.
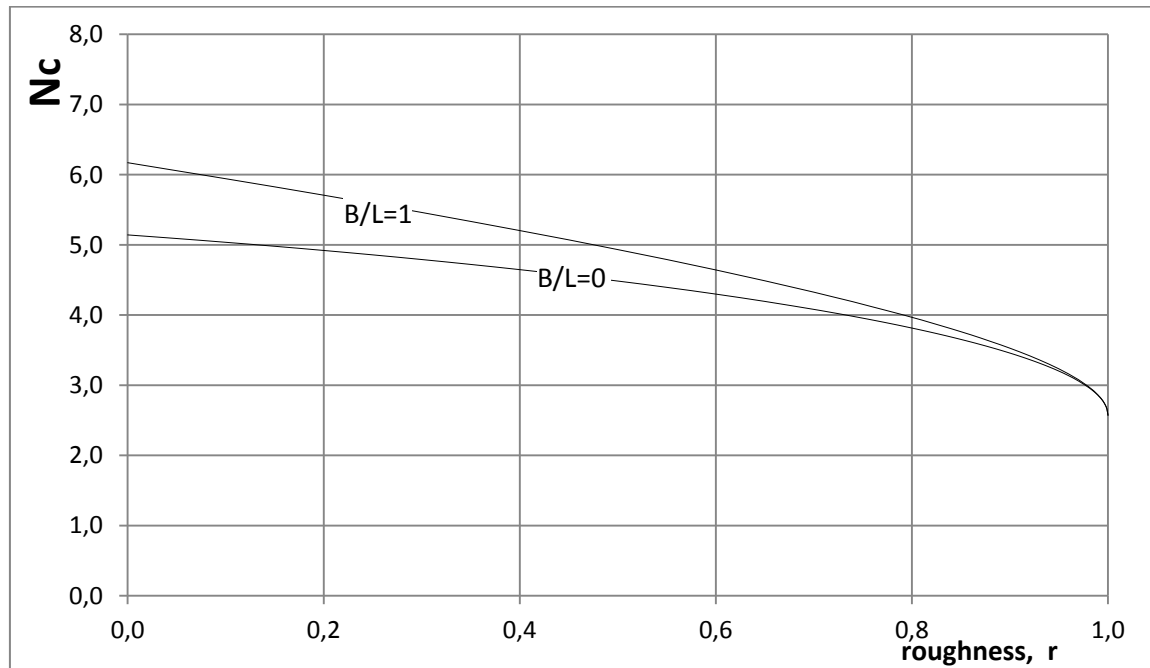
Figure 2.20: The bearing capacity factor N_c as a function of foundation roughness.

The bearing capacity factor N_c in Figure 2.20 only applies as long as the terrain is flat. If it is at an angle another solution is required (Janbu, et al., 2006).

2.5 Failure modes of retaining structures

The stability of a retaining structure is defined by several factors. There are different ways in which a retaining structure can fail and some common ones are shown in Figure 2.21.

a)   b)   c)
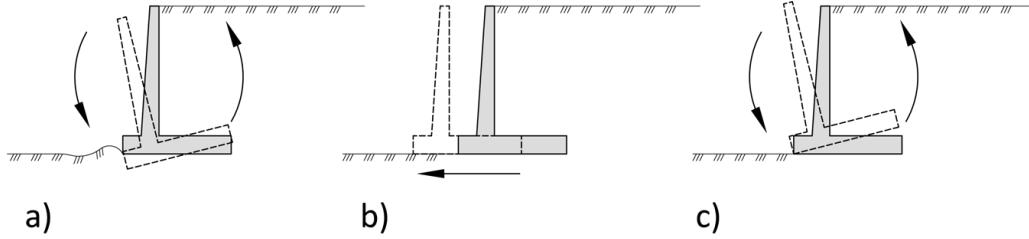
Figure 2.21: Common failure modes; a) bearing capacity failure b) sliding c) overturning

Bearing capacity failure

Failure occurrs when the vertical load exceeds the bearing capacity of the foundation, this can be seen in Figure 2.21 a). This is the most common type of failure found in the calculations done in this paper. In addition to increasing the vertical load the bearing capacity can also be exceeded as a result of variations in the horizontal load. This is due to the fact that changes in the horizontal load affects the effective footing width through the eccentricity of the vertical load and can in some cases be the cause of failure.

Sliding of base

Another failure mode of a designed retaining structure is that the structure slides on its base plate as a result of the lateral forces acting on it, this can be seen in Figure 2.21 b). This failure mode was encountered a few times in the calculations done in this paper.

By summing up all horizontal forces acting on the structure it is easy to check if the shear stresses in the foundation required to act against sliding exceed the shear stresses that can exist in the soil mass. In the method proposed by HB016 the maximum allowed shear stress is reduced from the maximum by a roughness number that varies between the values $r_b = 0,7$ and $r_b = 0,9$ depending on soil type and terrain geometry.

Overturning

If the driving moments acting on the structure are larger than the resisting moments the structure will tip over, this failure mode can be seen in Figure 2.21 c). To check if the earth pressures and design action loads will cause the structure to become unstable is a general requirement when designing retaining structures. By summing up the moments of all forces acting on the structure it is possible to derive an equation for the overturning factor of safety as

$$FS_O = \frac{\sum M_R}{\sum M_D} \tag{56}$$

where M_R are the resisting moments and M_D are the driving moments. If the point of overturning is chosen at the toe, the normal requirement is that $FS_O \geq 3$ (Erlingsson, 2006). The overturning criteria is handled in a different way in the method proposed by HB016 as the overturning moment results in a smaller effective footing reducing the bearing capacity.

Failure in a structure member

Retaining structures are designed to retain masses of earth. After the backfill process is complete a constant load will act on the structure. If the design of the structure itself is not adequate, local structural failures may occur leading to a failure of the structure as a whole.

In the case of a cantilever retaining structure made from concrete, the dimensions at the base of the wall will be a deciding factor whether the structure will collapse or not. It is at the base of the wall that the greatest moment will act and the geometry of the base will have to be able to handle it.

Information on wall base widths and concrete reinforcements can be found in HB100 (Statens vegvesen, 1985) and Eurocode 2 (Eurocode, 2004).

Larger failure mechanisms as a result of the construction

Retaining walls are usually built where a new project requires a larger difference in elevation than the current situation allows. This can as an example be a house or a road constructed in a sloping terrain. In order to get the flat terrain needed to create these structures the existing terrain needs to be cut or a fill be placed on top of it.
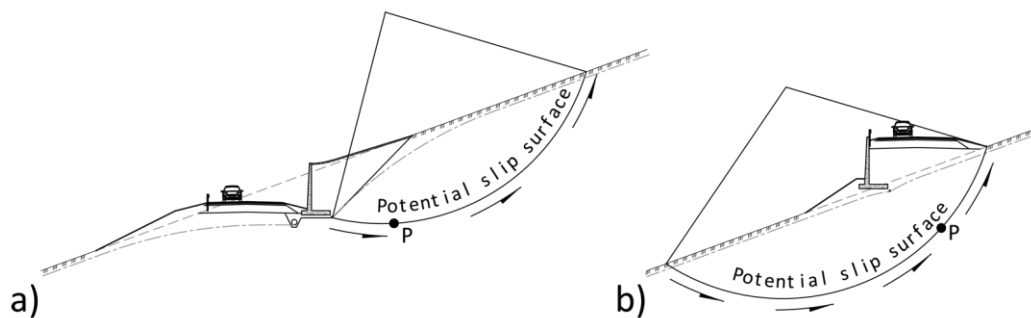
Figure 2.22: Proposed road section in a cut(a) and a fill(b) and resulting failure surfaces.

Figure 2.22 shows two variants of a road construction in the same terrain along with a possible failure mode for each case. The main difference between failures in cuts and fills is that situations involving fills are usually at its most unstable right after construction. The excess pore pressures at point P are then released and the factor of safety gradually rises to a new equilibrium state. In the case of a cut the pore pressures are at their minimum just after construction. The pore pressures build up and the factor of safety gradually decreases to a new equilibrium state. Failure as a result of initial loading in situations involving cuts can occur months or even years after construction.

Evaluation of large failure mechanisms will not be covered in more detail here but more information methods used to calculate slope stability can be found in chapter 4 of HB016. A direct method for calculating slope stability by means of design graphs for simplified geometries is provided (Statens vegvesen, 2010).

Deformations due to settlements

Settlements under a retaining wall mean movement of the wall and its immediate surroundings that change the stress situation around the structure. If the settlements are large enough they can in some cases cause a structure to become unstable and fail.

3 Comparison of methods used to calculate lateral earth pressures

Comparison between Coulomb's methods and the stressfield method is an interesting subject as both methods are approved methods for designing retaining structures according to HB016. The task is interesting as the two have different limitations and use different definitions of soil and structure interaction.

Both methods assume a planar failure surface when the backfill is sloped at an angle. They produce identical results when tested with a frictionless vertical wall retaining a cohesionless soil. This holds true for all admissible inclinations of the backfill.

The stress field method has the great advantage over Coulomb's method that it has been developed with the attraction attached so calculating earth pressures for cohesive backfills is possible. The calculations in this chapter have been done for friction angles that vary from $\phi' = 5°$ to $\phi' \geq 40°$. Although so low friction angles are hard to find in soils the chapter is aimed to compare the methods and therefore a large interval is used.

3.1 Linking the roughness number, r, and the roughness angle, δ.

As both methods produce identical results when there is no friction between wall and soil, it is interesting to investigate if there exists a simple link between the stressfields roughness number, r, and Coulomb's roughness angle, δ.

The roughness angle in theory has a link to the roughness number. By noting that roughness is defined as the percentage of the shear strength available in soil that is transferred to the wall and that Coulomb used his own failure criterion with no cohesion, the roughness number for his method can be defined as

$$r^* = \frac{\tan(\delta)}{tan(\phi')} \tag{57}$$

Assuming angles, δ, that result in a roughness number on the interval $-1 \leq r^* \leq 1$ and calculating the roughness number resulting in the same coefficient of earth pressure in the horizontal direction for various friction angles for the active case and a flat terrain yielded the relationship seen in Figure 3.1. It should be noted that the stressfield method delivers K_A in the horizontal direction but Coulombs method delivers K_A at an angle δ In order to create a clear comparison it is important to account for this so we calculate the horizontal components as

$$K_A^* = K_{A.Coulomb} \cdot cos(\delta) \tag{58}$$

and

$$K_P^* = K_{P.Coulomb} \cdot cos(\delta) \tag{59}$$

For practical considerations the angle of wall friction, δ, should in the active case for the case of loose granular backfill be equal to the friction angle. For the active case with dense

granular backfills it should lie on the interval $\phi'/2 \leq \delta \leq 2\phi'/3$ (Das, 2002). These intervals have been highlighted with dots in Figure 3.1. The choice of negative values of δ for practical applications will not be covered in this thesis but the graph is extended to include those cases as well.

By selecting a wall roughness angle, one manually selects the amount of roughness between the soil and the structure. As the amount of shear stress available in the soil is a strength property of the soil it is important to account for the strength properties when selecting a wall roughness angle to ensure good results.

The roughness number, r, and Coulombs roughness, r^*, can for design purposes assume any values on the interval $-1 \leq r, r^* \leq 1$ as they are defined as a percentage of the maximum shear strength that can exist in the backfill, negative and positive.

Design values for the roughness, r, lie between 0,625 and 0,8 in the ultimate limit state, depending on the failure mechanism and the consequences of failure. For the serviceability limit state, r lies in the interval $0,6 \leq r \leq 0,8$ depending on the flexibility of the structure. The choice of negative values of r for practical applications will not be covered in this thesis as it would introduce external forces to the problem as can be seen in Figure 2.7.
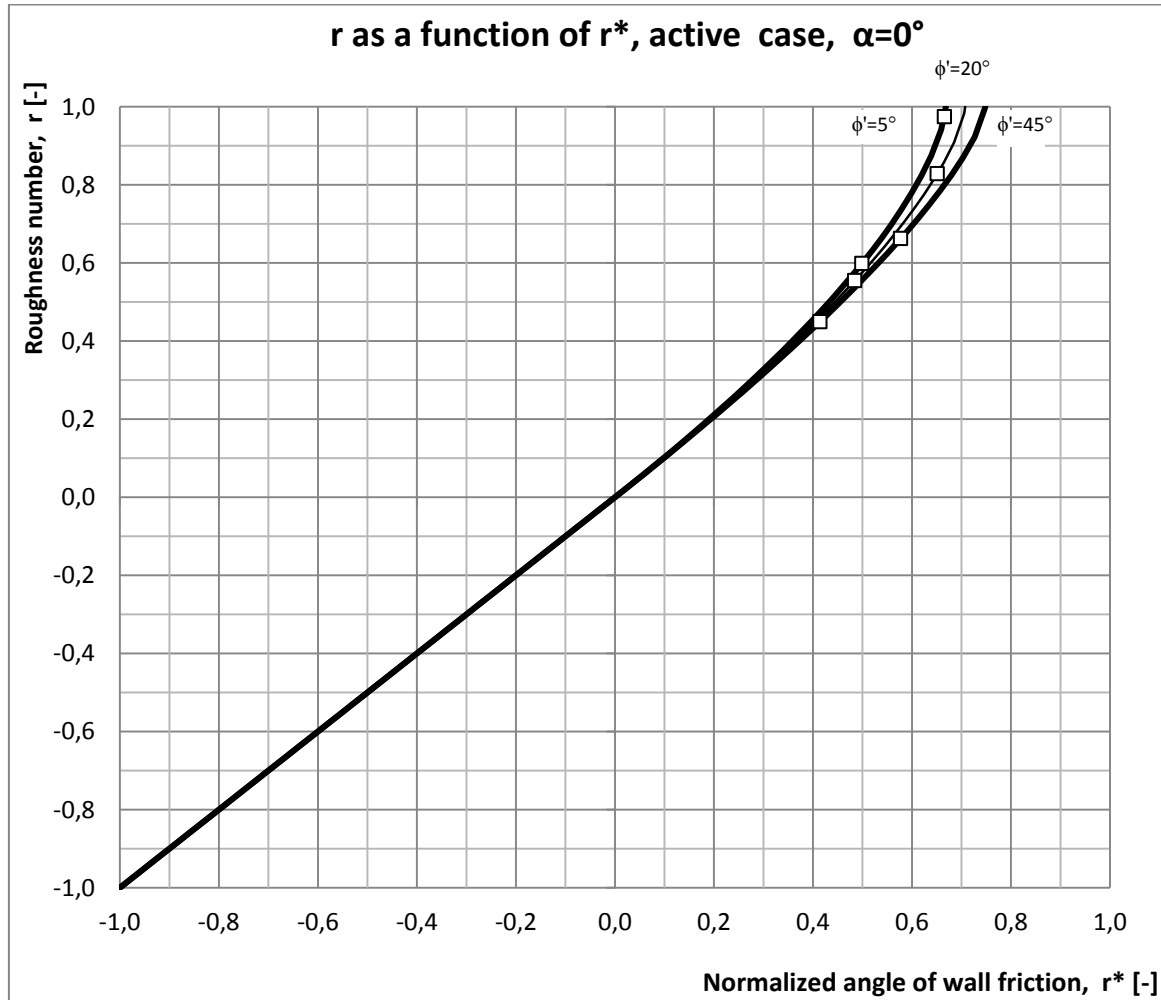
Figure 3.1: Relationship of r* and r, active case.

If the methods would return identical results on the entire range, the lines in Figure 3.1 would lie completely diagonally from $(-1, -1)$ to $(1,1)$. For lower values of the friction angle, the relationship shows linearity as both methods deliver the same results in that range. This can be explained by the fact that the stressfield method also assumes a linear shear surface in the case of negative roughness. The main result from Figure 3.1 is that for higher positive values of roughness the methods do not produce the same values. This is of importance because it is at this range that the recommended values of r^* lie.

Plotting the active earth pressure coefficient against the roughness number, r^*, for Coulomb's method and doing the same for the earth pressure method using the roughness number, r, their relationship can be observed for various friction angles. This has been done in Figure 3.2.
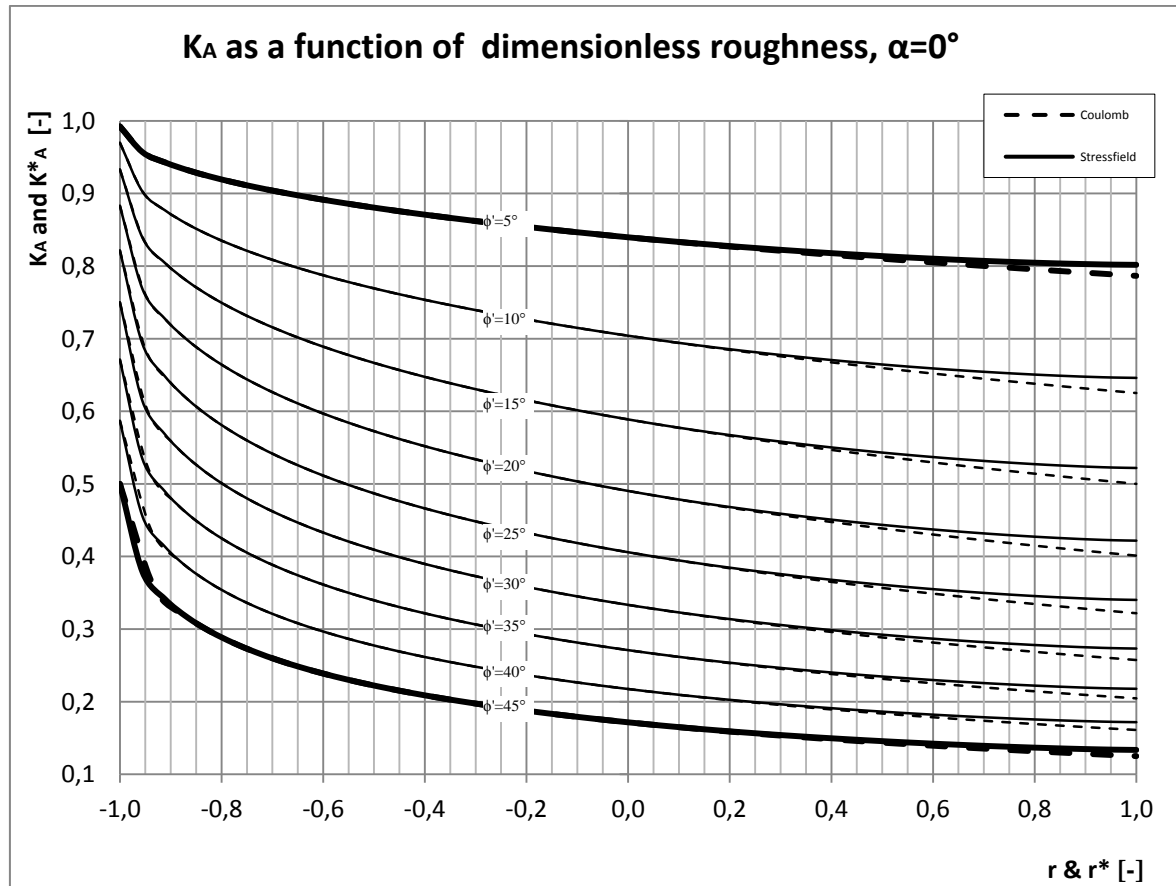
Figure 3.2: Active earth pressure coefficient as a function of r and r*.

Examining Figure 3.2 reveals that for high values of roughness Coulomb's method will produce lower values for the active earth pressure coefficient in the case of positive roughness. This difference is numerically greatest for friction angles around $\phi' = 15°$. When looking at the difference as a percentage of the earth pressure coefficient at full positive roughness the difference is greatest for $\phi' = 45°$ or around 6,5%. For negative values of roughness the methods deliver almost the same results, as was shown in Figure 3.1. The difference between the methods in the positive roughness range can be explained by the fact that Coulomb's method assumes a planar failure surface while the stressfield method assumes a combination of two planes connected by a curve in the shape of the logarithmic spiral; see Appendix E.

Although the values for the active earth pressure coefficient vary between the two methods, their difference is so small that it is safe to say that they produce almost identical results. Both methods are approved by HB016 to calculate earth pressures while designing retaining structures.

Using the same method of analysis between the two methods in the case of passive pressures reveals a different story. The relationship between r and r^* in the case of passive pressure and horizontal terrain can be seen in Figure 3.3.
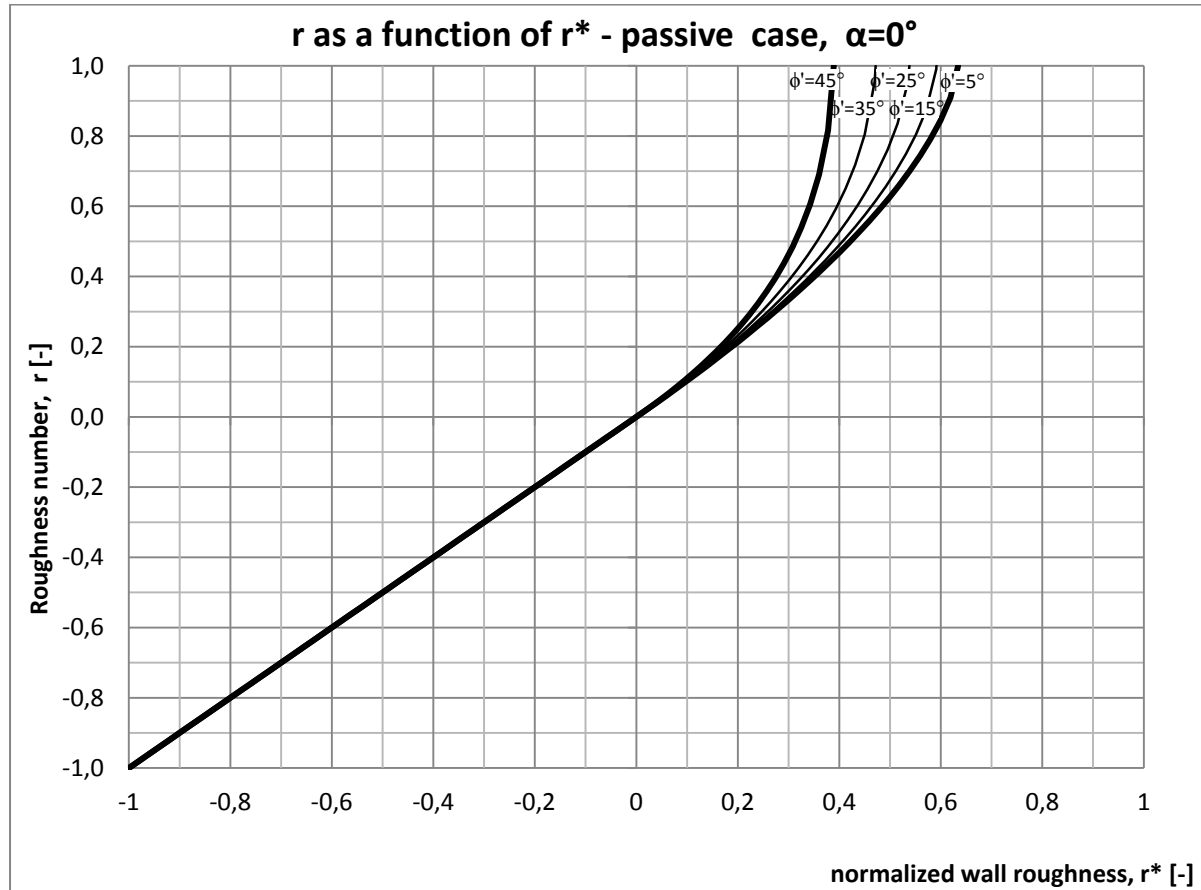
Figure 3.3: Relationship of r* and r, passive case.

In Figure 3.3 it is clear that r is used at its entire range but r^* is not. This means that for a certain roughness range the methods deliver different results. The rate of the divergence is interesting as the two methods fit almost perfectly together in the negative roughness range. On the positive side the roughness number, r, is fully utilized for all friction angles at about 40-60% of Coulombs roughness number, r^*. In the active case the two methods started to show non-linearity at roughness around $r = r^* = 0,4$.

The linearity of the negative roughness side can again be explained by the fact that both methods assume planar failure surfaces in that case. Plotting the passive earth pressure coefficient against r^* for Coulomb method and doing the same for the earth pressure method using the roughness number, r, their relationship can be observed for various friction angles. This has been done in Figure 3.4.
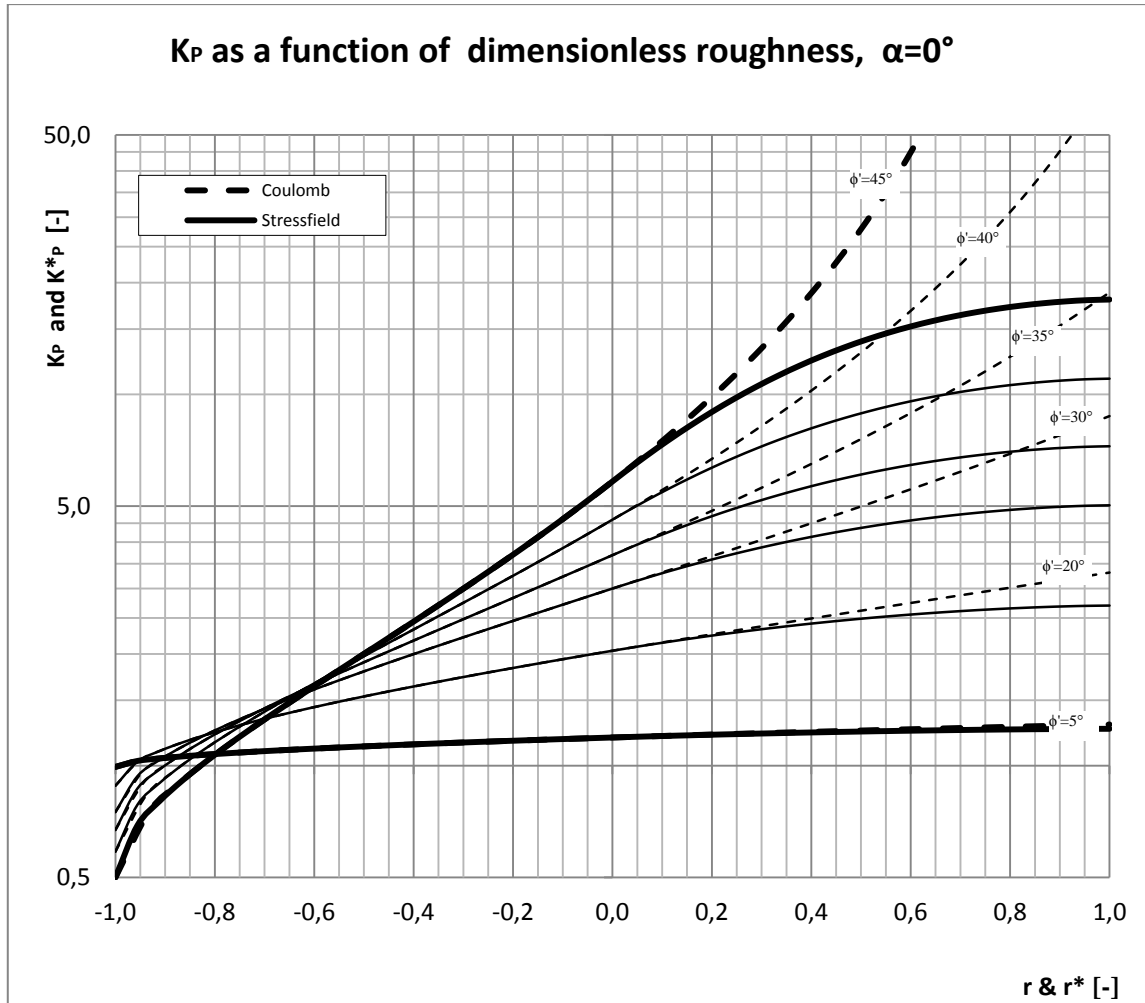
Figure 3.4: Passive earth pressure coefficient as a function of r and r*.

In Figure 3.4 it is clear that in the case of positive values of roughness, Coulomb's method starts to deviate from the stressfield method when r^* reaches a value between around $r^* = 0,1$ and $r^* = 0,25$ depending on the friction angle. The difference between the methods jumps orders for larger friction angles and therefore it is clear that Coulomb's method grossly overestimates passive pressures for those cases. The reason for this behavior is that to counter the increase in the inclination of the wall force, δ, the angle of the failure plane, β, is decreased. This results in a larger failure wedge and a larger frictional surface. When β approaches the inclination angle of the terrain α, small changes in the angle δ have large effects on the geometry and consequently the passive earth pressure as well. As the stressfield method is defined as a combination of a curved failure surface and a planar one, it is not as sensitive to change in roughness. Similar to the case of active pressures the methods show almost the same results in the case of negative roughness.

When the terrain behind the structure is inclined at an angle to the horizontal, HB016 proposes that other earth pressure coefficients, $K_{\beta A}$ or $K_{\beta P}$, be used. They are derived by using planar failure surfaces and should therefore differ from K_A and K_P.

The same analysis as was done in Figure 3.2 was done for the active case incrementing the terrain inclination by a single degree $\alpha = 1°$. The results can be seen in Figure 3.5.
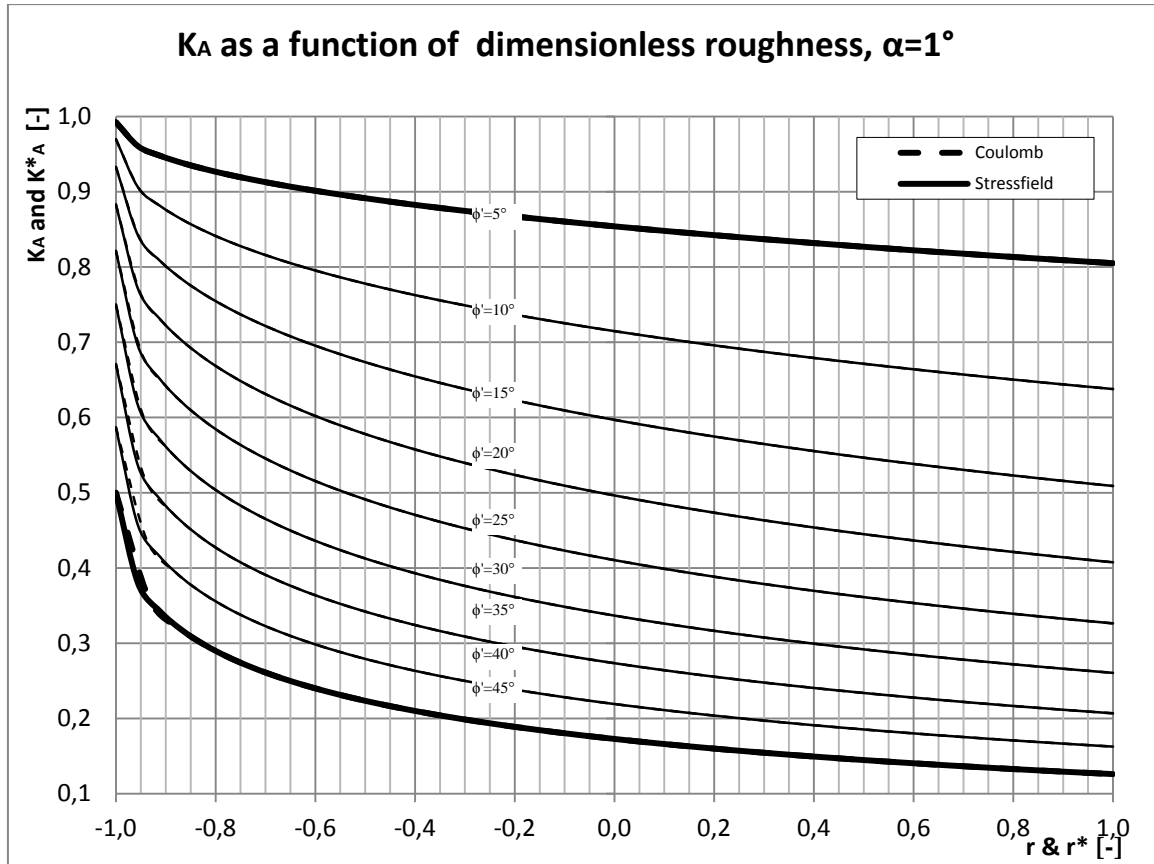
Figure 3.5: Active earth pressure coefficient as a function of r and r*, α=1°.

As was expected the effect of the logarithmic spiral has vanished and the stressfield method shows results that are almost identical to the ones derived using Coulomb's method. Besides this small change all trends that can be seen in Figure 3.2 are present here as well. As the terrain is sloped further the curves are pushed up the graph.

When doing the same analysis for the passive, it should be noted that $K_{\beta P}$ in HB016 is defined only for terrain sloping at a downward angle behind the structure. Selecting a case but using a negative slope angle of just $\alpha = -1°$ reveals a large difference from Figure 3.4, as can be seen in Figure 3.6.
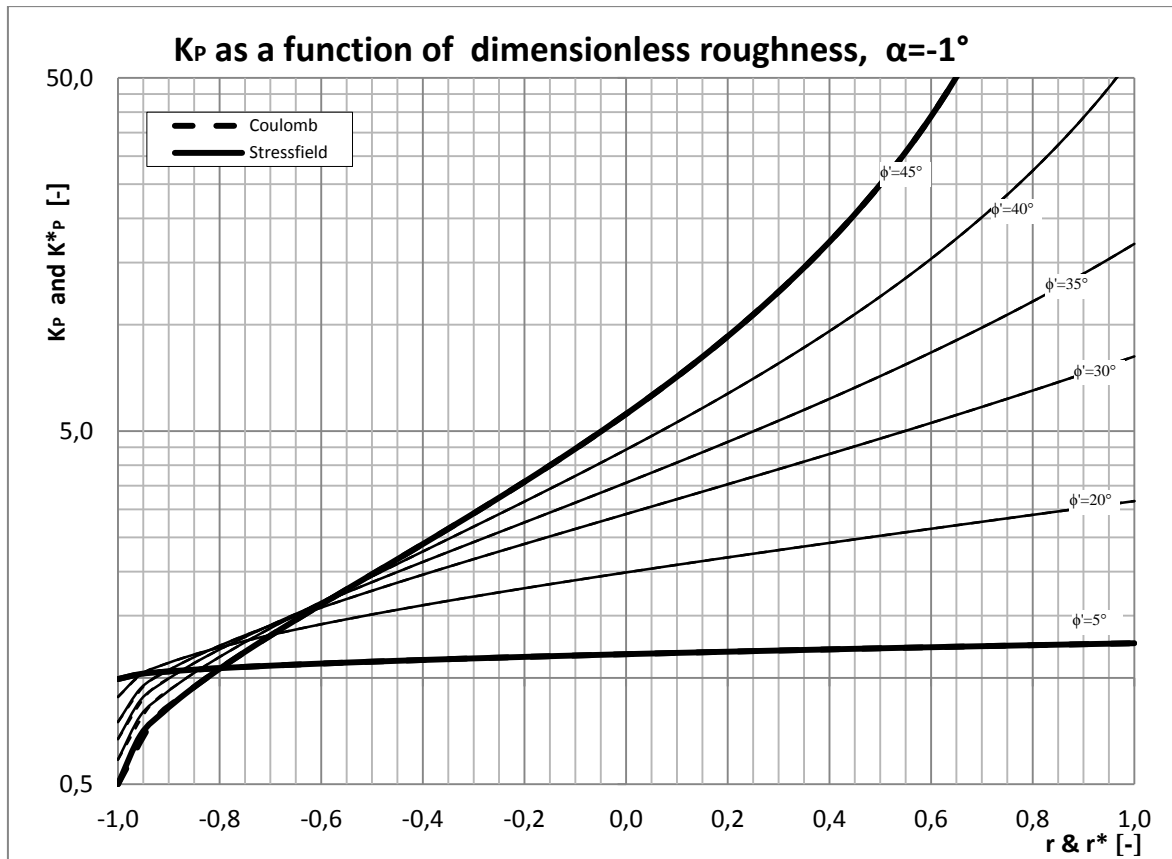
Figure 3.6: The passive earth pressure coefficient as a function of roughness, α=1°.

It is clear that the stressfield method now follows Coulomb's method closely and shows the same exponential trend for higher values of roughness and friction angles. If one were to follow the theory closely while calculating passive forces a single degree of terrain inclination for roughness value of $r = 0,8$ and $\phi' = 35°$ would result in around 65% increase in passive pressure from the horizontal case. It is unlikely that this difference would can be explained by anything else than inherit errors in the calculation methods.

In the case of negative roughness values the two methods show the same reducing trend and provide almost the same values. As negative roughness will not be used in calculations this will not be investigated further.

It is interesting to see how closely the methods fit together for the active case and a horizontal terrain and seem do diverge greatly in the passive case. It is also interesting to note the jump in values when going from a horizontal terrain in the passive case of the stressfield method to any other terrain inclination. Assuming horizontal terrain for small terrain inclination angles will probably deliver results closer to the real ones in the case of passive earth pressures.

This point is however not always an issue in practical applications because designers often overlook the passive force when designing retaining structures. This is done to be on the safe side of failure as there is always the chance that at some time, the earth mass in front of a retaining wall could be dug away. HB016 states that when designing structures connected to the Norwegian road system the passive force must not be taken into account. The reason being that the optimal placement of trenches for infrastructural facilities often

36

lies along roads making it more likely that the mass in front of the structure be dug away at some point.

3.2 Active earth pressures on walls leaning into the backfill

The inclination angle of the back of the wall, θ, in the classical presentation of Coulomb's earth pressures is defined as positive when the wall is sloped away from the backfill, this is shown in Figure 2.12 and Figure 2.13. It is proposed that the equations for active pressures also hold true for negative values of θ (State of California Department of Transportation, 1990).

HB016 provides a correction factor for the earth pressure coefficient for the case of an inclined wall. It can be calculated using equation (33). Inspecting the equation it is clear that this correction is only a function of the friction angle and the inclination of the wall and does not account for roughness. It is stated in HB016 that the method gives acceptable results for roughness in the interval $-0,5 \leq r \leq 0,7$.

Looking at the derivation of the active case of equation (22) given in Appendix E it is not difficult to derive that by adding the wall inclination angle to the rotation of the stressfield, we create an earth pressure coefficient that depends on the friction angle, wall inclination angle as well as the roughness. The new opening angle of the Prandtl zone will then be $(\omega - \theta)$ and because θ is defined as negative into the backfill this will result in a larger opening angle. Adding a the angle θ to the opening angle of the Prandtl zone will also rotate the direction of the resulting normal- and shear stress by the same angle. The resulting horizontal force will therefore be a function of the two.

Calculating earth pressures against structures that lean into the backfill is important as most dry stone walls are constructed in this manner. Selecting a roughness interval to conduct this analysis is tricky as dry stone walls cannot be thought of as a single entity that rotates as a whole about the footing with the earth mass, but rather an extremely flexible structure that can move and adjust to the backfill. HB016 proposes that the roughness for dry stone walls could be estimated as $r = 0,3$. The maximum value of roughness for K_δ calculations is proposed by HB016 to be $r = 0,7$.

The three variants of the earth pressure coefficients will be tested for friction angles varying from $\phi' = 0°$ to $\phi' = 40°$. The calculations will be performed for roughness values of $r = 0$, $r = 0,3$ and $r = 0,7$. The roughness angle for Coulombs method is adjusted in each case according to equation (57) and the link provided by Figure 3.1 to produce the same initial coefficient as the other two calculation methods. The result from all three methods and zero roughness can be seen in Figure 3.7.

It should be noted that the wall inclination angle, θ, in the following figures is the same as the wall inclination angle δ in Figure 2.11 but with the opposite sign. Equation (33) is not defined for negative values of δ. The correction coefficient K_δ is named as was done in HB016 and the wall inclination angle δ should not be confused with the wall force angle δ. It is unfortunate that the two have the same symbol but they will not appear in the same equation in this thesis.
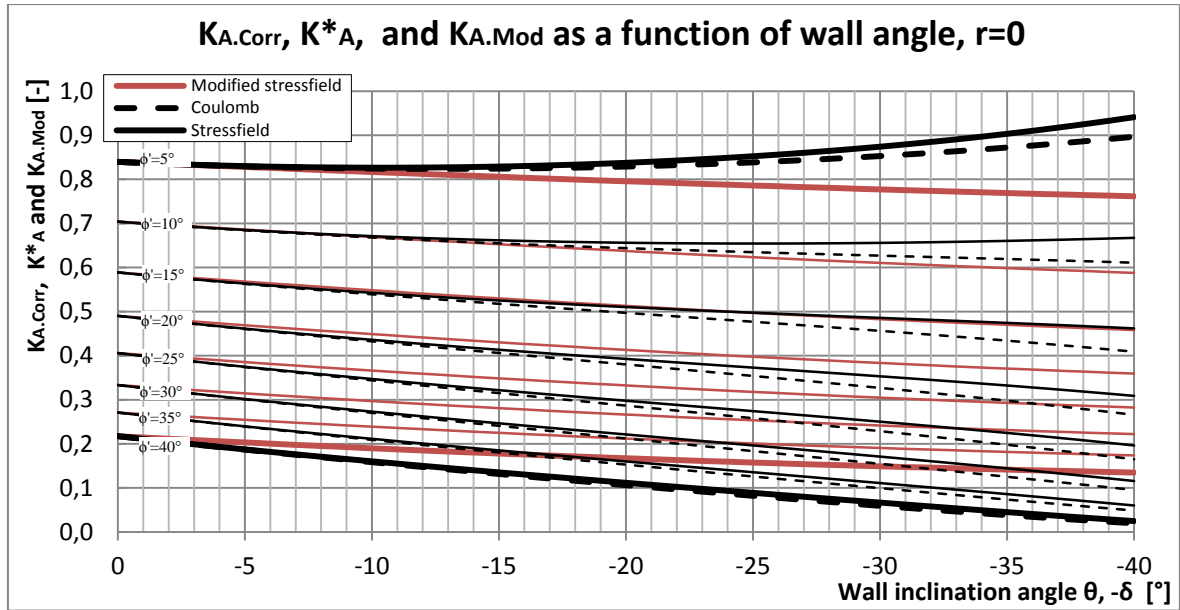
Figure 3.7: Comparison of K_A for inclined wall from three different methods. r=0.

Examining Figure 3.7 it is clear that the methods all start at the same coefficients and as the inclination of the wall face increases they all decrease at different rates. Exceptions from this are the cases with $\phi' \leq 10°$ where Coulomb's method and the stressfield method start to increase for wall inclination angles greater than ca. $\theta = -10°$. Coulomb's method and the stressfield method seem to produce a similar trend and as the friction angle increases their difference gets smaller. The modified stressfield method shows a steady decrease in the earth pressure coefficient as the wall inclination increases. The rate of decrease seems to be independent of the friction angle. This means that for friction angles lower than $\phi' \approx 15°$ the modified stressfield method gives lower values for the earth pressure coefficient but higher for friction angles above $\phi' \approx 15°$.
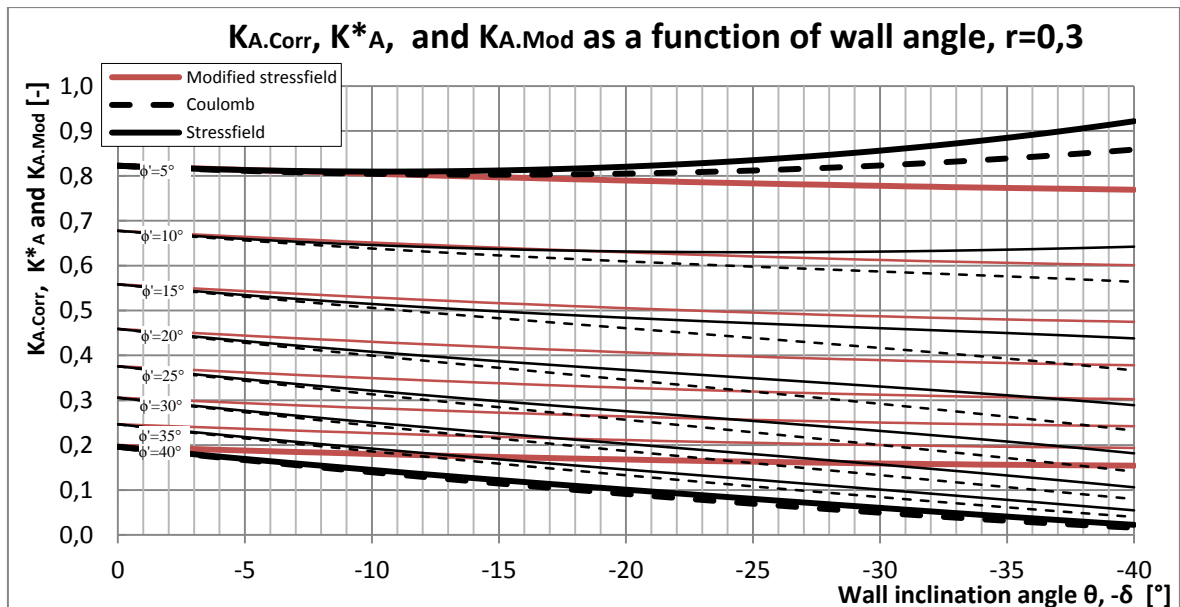
Figure 3.8: Comparison of K_A for inclined wall from three different methods. r=0,3.

Increasing the roughness to $r = 0,3$, and Coulomb's angle of wall friction to the equivalent angle, pushes all the curves a little bit down the scale. This can be seen in Figure 3.8.

Increased roughness has the effect on the modified stressfield method that as the wall inclination angle is increased the decay of the earth pressure coefficient slows down. The modified stressfield method still produces higher earth pressure coefficients for larger wall inclination angles and friction angles greater than $\phi' = 20°$.

Increasing the roughness to the maximum value of $r = 0,7$ allowed in the stressfield method and increasing Coulomb's angle of wall friction to the equivalent angle, reveals much the same trend. This has been done in Figure 3.9.
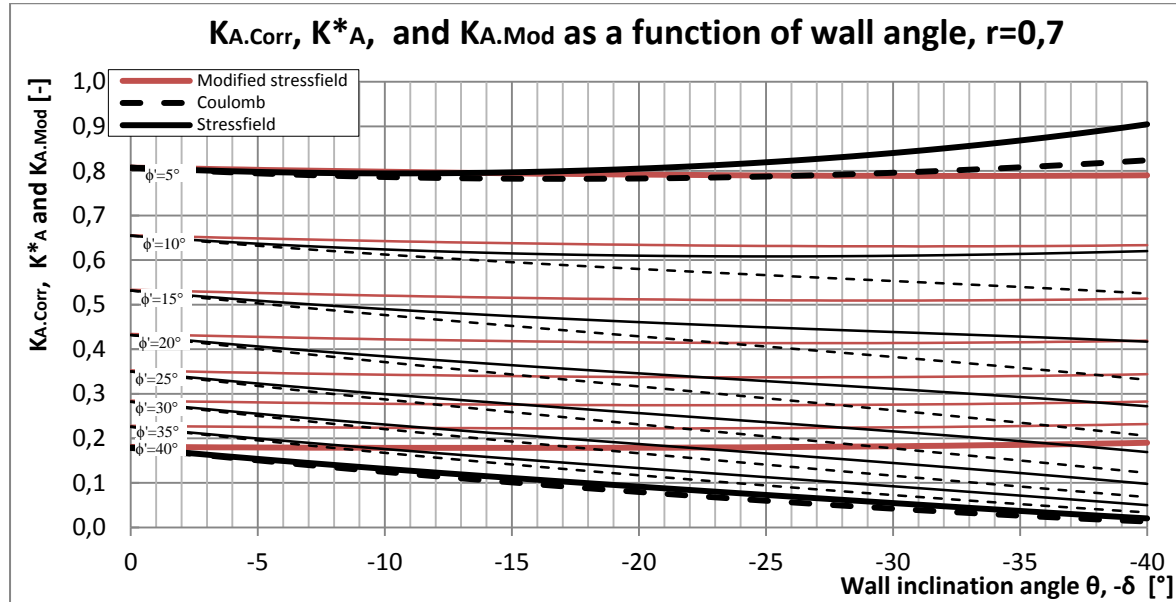
Figure 3.9: Comparison of K_A for inclined wall from three different methods. r=0,7.

As can be seen in Figure 3.9 the modified stressfield method gives decaying values of the earth pressure coefficient for small friction angles as the wall inclination angle is increased. For higher friction angles the earth pressure coefficient rises with the wall inclination angle. This behavior can be explained by the fact that the shear stresses acting between the wall and the soil have greater influence on the lateral earth pressure.

Comparison of Figure 3.7, Figure 3.8 and Figure 3.9 reveals that Coulomb's method and the stressfield method proposed by HB016 produce very similar results for all friction angles for the calculated values of roughness. The modified stressfield method produces similar results as the other two for small inclinations of the wall, but this does not apply for the whole range of δ. With increasing roughness, all three curves are pushed down the scale.

Dry stone walls are not held together by anything other than frictional forces and blocks that become unstable are free to fall independent of the whole wall. Therefore they are often designed so that they can move with the earth mass without resulting in failure of the entire structure. This is accomplished by leaning the structure into the backfill.

A normal value of wall inclination of dry stone walls in Norway is $s = 3:1$. This means that for every 3 meters of elevation difference it tilts 1 meter into the backfill. This is the equivalent of a wall inclination angle of around $\theta = 18,5°$. At this angle the methods all produce their own values although Coulomb's method and the stressfield method can be

assumed to be in a similar range for all friction angles and roughness numbers in the case of a horizontal backfill.

Retaining structures are often constructed out of pure necessity to make space for new structures or installations. Therefore the terrain behind them is often sloped; and more often than not at a considerable angle. Comparing the three methods for sloped backfill is therefore of interest. This is done for the case of $r = 0,7$.

As the roughness is increased the curves in Figure 3.9 are pushed up the scale. This starts gradually but as the backfill inclination angle nears a specific friction angle the process speeds up for the corresponding curve. As an example a backfill slope of $\alpha = 34°$ was chosen and is shown in Figure 3.10. By definition the slope is not stable at higher angles than the friction angles so all curves representing lower friction angles than $\phi' = 34°$ have vanished.
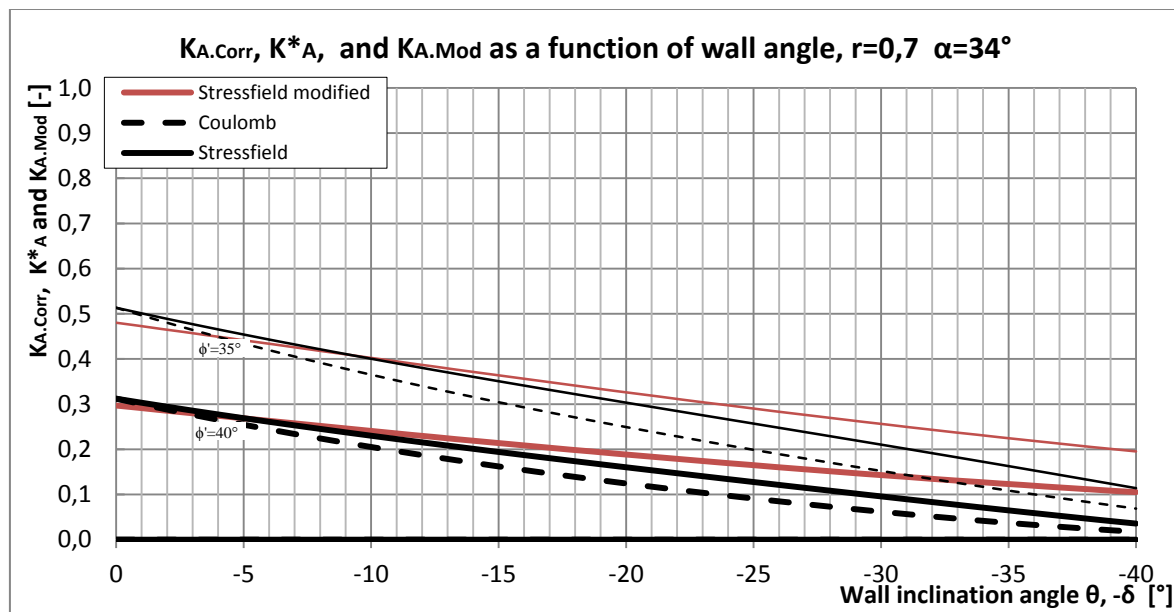
Figure 3.10: Comparison of K_A for inclined wall. r=0,7, α=34°.

Rankine proposed the idea that a stressfield under an inclined terrain will also be inclined by that same angle, the active earth pressure coefficient for his solution is given in equation (31). Substituting this earth pressure coefficient for N^+ in equation (22), remembering to use negative values for the friction angle, will develop the modified stressfield method for sloping backfill. Adding the wall inclination angle to the opening angle of the Prandtl zone reveals the relationship shown in Figure 3.10.

Figure 3.10 shows that all three methods show increased earth pressure coefficients for vertical walls that decay as the wall inclination angle leans towards the slope angle. Coulomb's method shows a faster decay for small wall inclination angles but the decay slows down as the angle is increased. As a result the largest difference between Coulomb's method and the stressfield method lies somewhere between $\theta = 20°$ to $\theta = 30°$, this is near the standard inclination of dry stone walls in Norway. The modified stressfield method shows les decay in earth pressure coefficient than the other two as the wall inclination angle is increased.

Figure 3.7 to Figure 3.10 show a correlation between all calculation methods. Although the methods do not produce identical results the results lie in a similar range in most cases. The modified stressfield method starts with the same values as the other two in the case of a horizontal backfill but shows much slower decay as the wall inclination angle is increased. In the case of an inclined backfill the modified stressfield method starts at a lower value of the coefficient than the other two but shows faster decay than in the other two cases. The way that the effect of inclined backfill was implemented has not been derived theoretically so there might be room for improvements to follow the theory more closely.

3.3 Comparison of lateral earth pressures methods to method recommended by Eurocode 7

The Eurocodes are a set of design standards published by the organization Comité Européen de Normalisation (CEN) the officially recognized standard body by the Europen Union, EU. The standards aim to provide a consistent set of design rules that combined with national annexes create a common design field for engineers throughout Europe. Among the member countries of CEN are Norway and Iceland (Wikipedia, 2011).

The Eurocode standard for geotechnical design is Eurocode 7 (EC7). It is published in two parts

1. Eurocode 7 part 1: Geotechnical design – General rules
2. Eurocode 7 part 2: Geotechnical design - Ground investigation and testing

The first part was approved by CEN in 2004 and was published as a standard along with the national annex in Norway in 2004 under the name NS-EN 1997-1:2004+NA:2008. The second part was approved by CEN in 2006 and was published as a standard along with the national annex in Norway under the name NS-EN 1997-2:2007+NA:2008.

As of March 2010 Eurocode 7, NS-EN:1997-1 and NS-EN:1997-2 along with national annexes, replace the NS-34XX standard series as the national standard for geotechnical design in Norway (Eurocode, 2008).

Appendix C in NS-EN 1997-1 provides a chapter on how earth pressures against vertical walls can be calculated. The national annex states that appendix C should be considered as an informative chapter. Therefore it should be used as a guideline when calculating earth pressures against vertical walls designed in Norway.

The lateral earth pressure coefficient is given in figures and they are divided into four categories both for the active and passive case. The case of the horizontal backfill for various roughness angle ratios comes first followed by three figures for specific roughness ratios and varying backfill ratios.

Chapter C2 in appendix C provides procedures to evaluate both the passive and active earth pressure coefficient. According to EC7 the earth pressure coefficients can be evaluated as

$$K_{P/A} = \frac{1 \pm sin(\phi') \cdot sin(2m_w \pm \phi')}{1 \mp sin(\phi') \cdot sin(2m_t \pm \phi')} e^{\pm 2 \cdot (m_t + \beta - m_w - \theta) tan(\phi')} \qquad (60)$$

where

$$m_t = \frac{1}{2} \cdot \left(arccos \left(\frac{-sin(\beta)}{\pm sin(\phi')} \right) \mp \phi' - \beta \right) \qquad (61)$$

and

$$m_w = \frac{1}{2} \cdot \left(arccos \left(\frac{sin(\delta)}{sin(\phi')} \right) \mp \phi' \mp \beta \right) \qquad (62)$$

When there is a double sign in equations (60) to (62) the top sign refers to the passive case and the bottom sign for the active. The exact theory behind there equations is unknown to me but by examining equation (60) it seems to have a contribution from a both a Rankine- and a Prandtl zone. In the following chapter the earth pressure coefficients given in figures in EC7 will be used as a base for comparison to methods already derived.

3.3.1 Active pressures according to Eurocode 7

All four earth pressure coefficient figures from EC7 have been combined into one for the active case and can be seen in Figure 3.11.
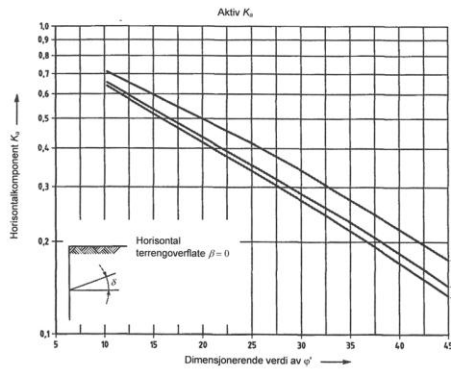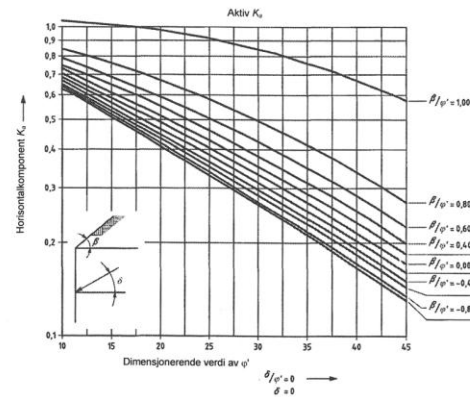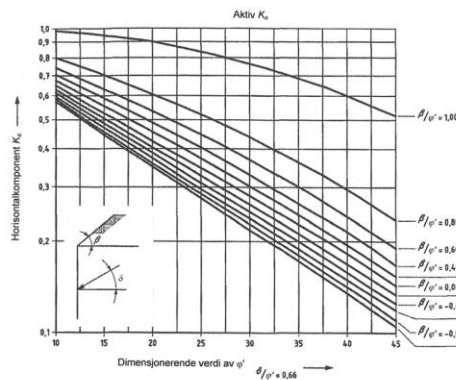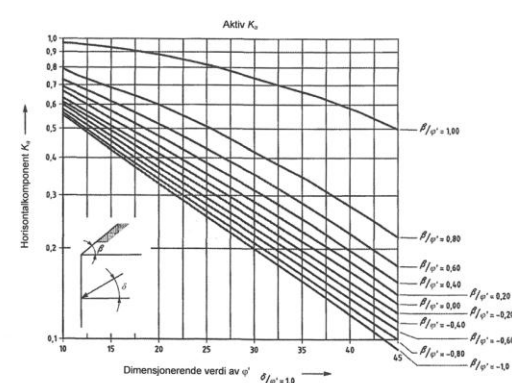
Figure 3.11: Active earth pressure coefficient, K_A, as it appears in Eurocode 7.

The explanatory figures in Figure 3.11 show that the earth pressure force is tilted at an angle δ to the horizontal. This is the same presentation as can be seen in Coulomb's method shown in Figure 2.12 and Figure 2.13.

The case of horizontal backfill

Comparing the values provided with Eurocode 7 to Coulomb's method is a straight forward task as the wall roughness is defined in the same way in both of them. In Figure 3.12 Coulomb's method has been superimposed on Figure C.1.1 in Eurocode 7.
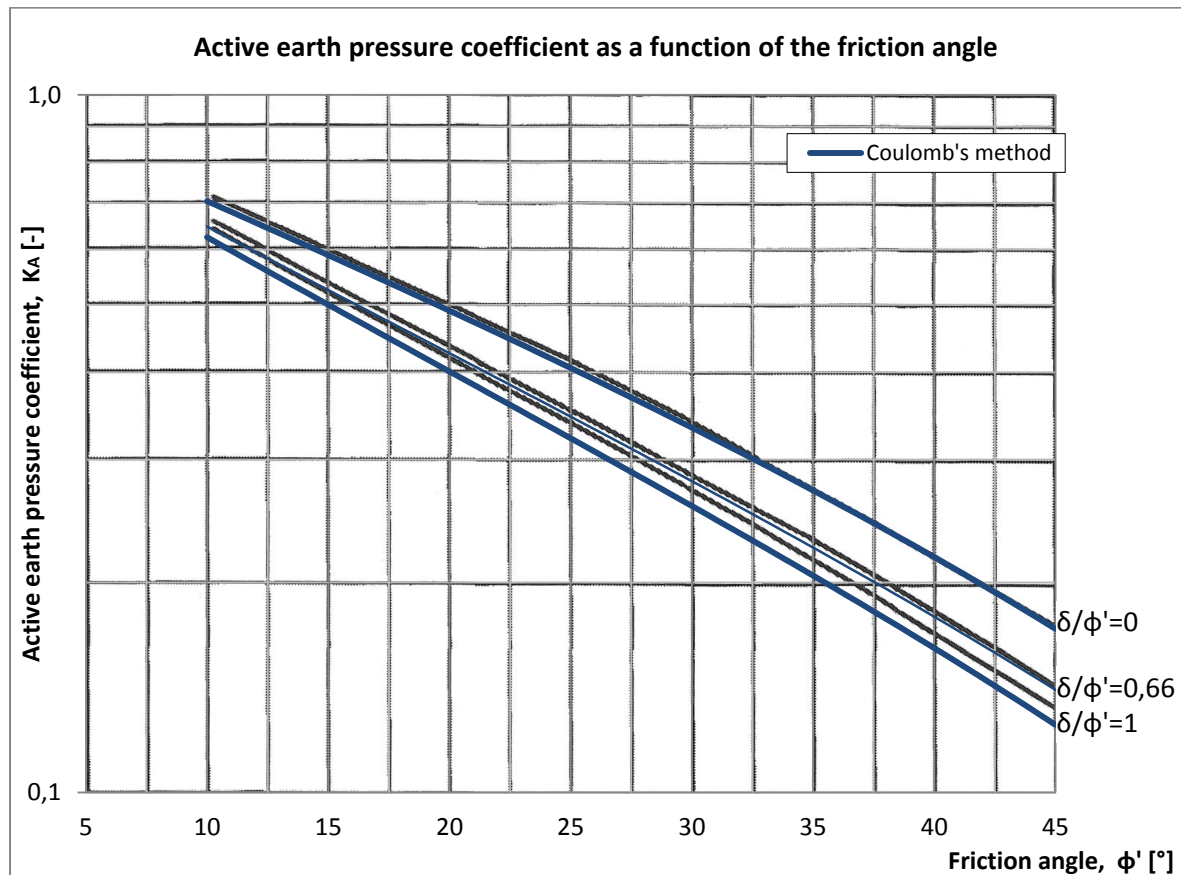
Figure 3.12: K_A from EC7 and Coulomb's method superimposed, $\beta = 0$.

It is clear that Coulomb's method follows the values given by EC7 closely by providing similar results. For the roughness angle ratios $\delta/\phi' = 0$ and $\delta/\phi' = 0,66$ Coulomb's method produces almost the same values as EC7. As the friction angle decreases the relationship Coulomb's method delivers slightly lower values than EC7. For full roughness Coulombs method produces lower values than EC7 over the entire range. It is clear that for higher angles of wall friction Coulomb's method gives lower values for the earth pressures than those proposed by EC7. As these pressures are the driving force in structure design using the values in EC7 will require a structure that can withstand larger forces thus erring on the safe side.

As the formulas provided by EC7 have a factor representing the logarithmic spiral it is interesting to see what happens when the stressfield method is used for comparison instead of Coulomb's method.
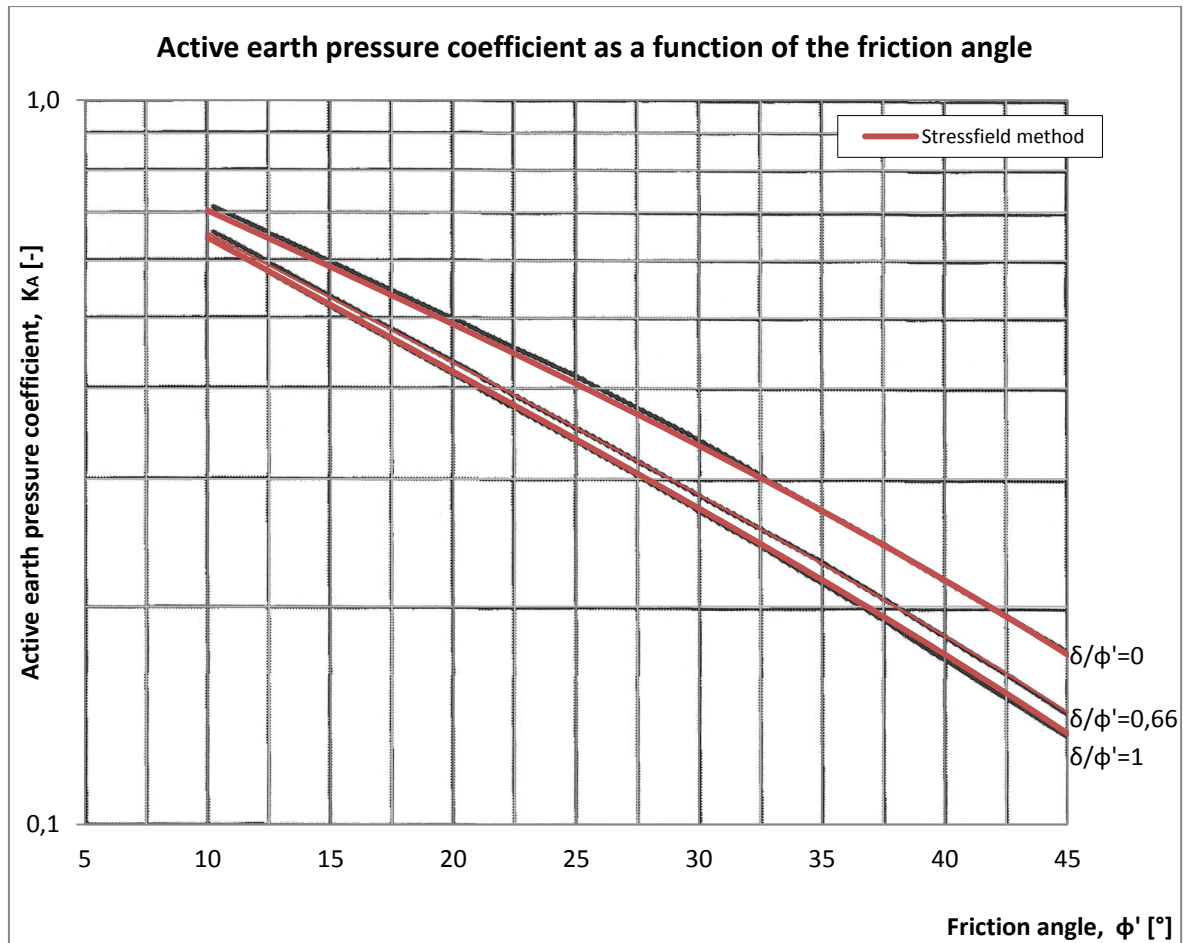
Figure 3.13: K_A according to EC7 with the stressfield method superimposed, $\beta = 0$.

Figure 3.13 shows a much closer relationship between the stressfield method and the values provided by EC7 than Coulomb's method produced. The roughness used in the calculations was calculated for each friction angle using equation (57).

The difference between the calculated values and the given values is so small that it is safe to assume that the stressfield method produces almost the same values as those presented in figure C1.1 in EC7.

The difference between the calculated values in Figure 3.12 and Figure 3.13 can be explained by the fact that Coulomb's method assumes a planar failure surface, as this is not the most critical shear surface it adds extra stiffness against failure resulting in lower values of the earth pressure coefficient.

The case of inclined backfill

For the case of an inclined backfill the stressfield method, like Coulomb's method, assumes a planar failure surface. It delivers almost exactly the same results as Coulomb's method for this case as can be seen in Figure 3.5. It is therefore interesting to see if the values calculated these methods agree with the values of K_A presented in EC7. In Figure 3.14 the stressfield method has been superimposed on figure C1.2. in EC7, the figures assume a zero roughness angle.

44
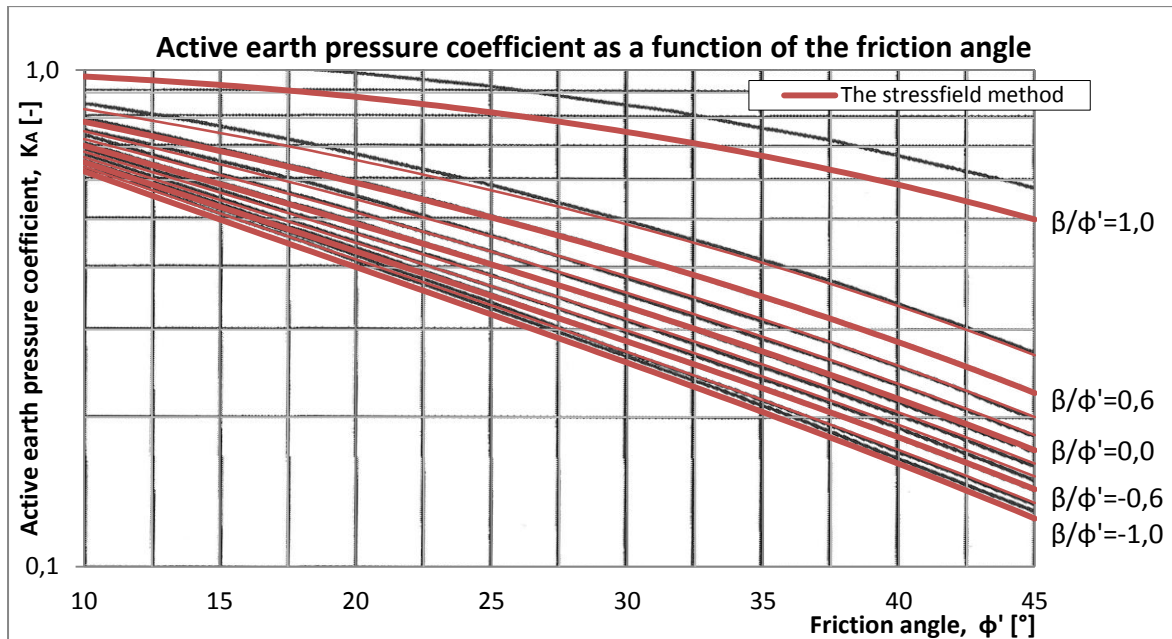
Figure 3.14: K_A from EC7 and superimposed stressfield method, $\beta \neq 0$, $\delta/\phi' = 0,0$.

Figure 3.14 shows a strong correlation between the stressfield method and the values given by EC7 for the case of zero roughness angles. When the terrain inclination angle nears the friction angle some a noticeable difference appears between the values given by EC7 and the calculated ones. This is evident both for positive and negative angles of terrain inclination. There seems to be a slightly better fit between the calculated values and the given ones for higher values of friction angles. For smaller friction angles EC7 estimates a bit larger values for the earth pressure coefficient than are calculated with the stressfield method.
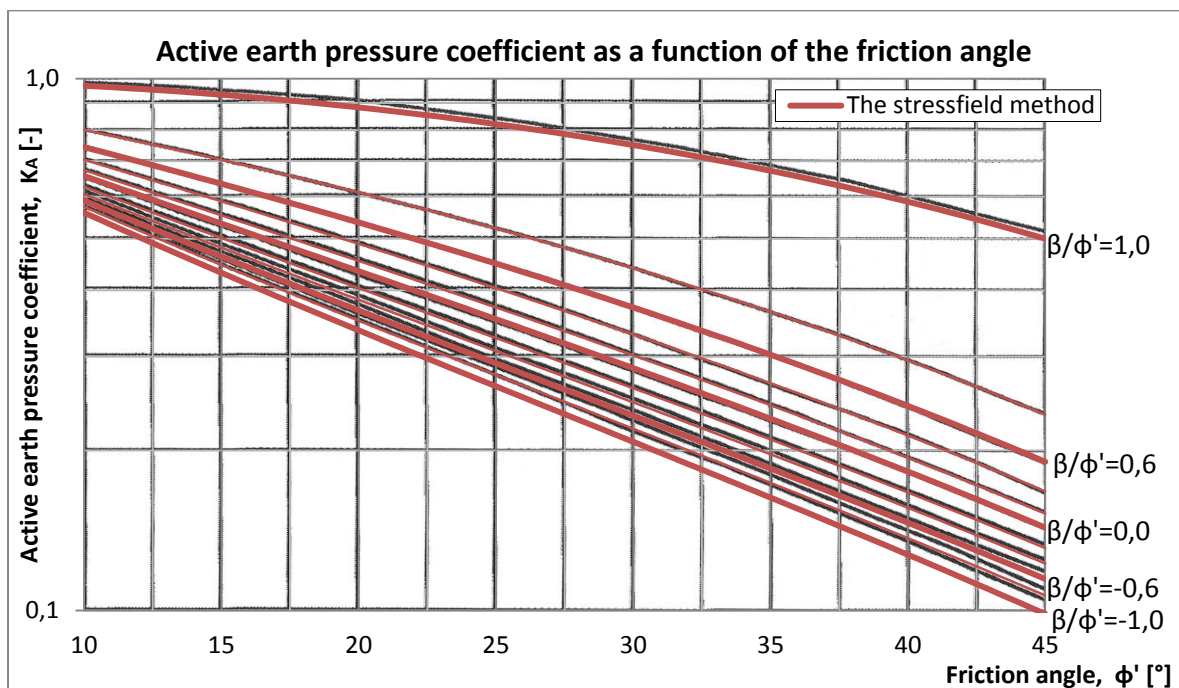
Figure 3.15: K_A from EC7 and superimposed stressfield method $\beta \neq 0$, $\delta/\phi' = 0,66$.

Figure 3.15 shows the stressfield method superimposed on the values given by figure C.1.3. in EC7. A very strong correlation is evident between the calculated values and the ones given by EC7 for most of the range β/ϕ'. However as the terrain inclination angle nears the friction angle in either the positive or negative direction EC7 provides slightly higher values for the earth pressure coefficient.
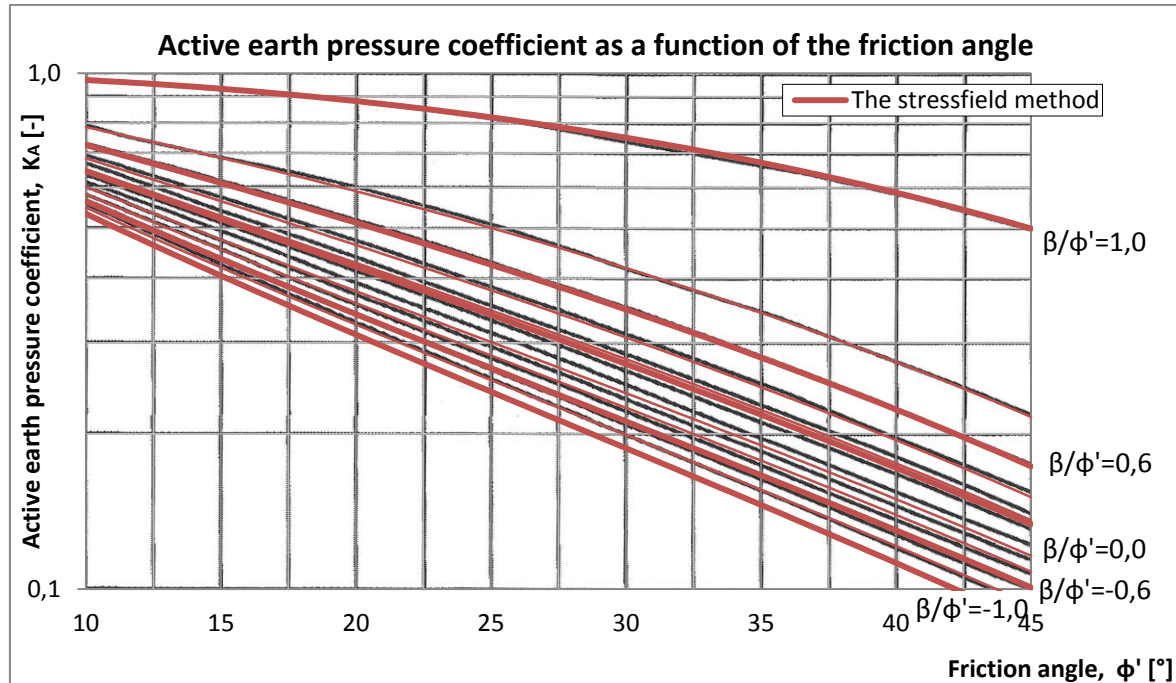
Figure 3.16: K_A from EC7 and superimposed stressfield method, $\beta \neq 0$, $\delta/\phi' = 1,0$.

Figure 3.16 shows the stressfield method superimposed in figure C1.4. from EC7. It shows the active earth pressure coefficient as a function of the friction angle and the inclination angle of the backfill when the roughness between soil and structure is fully mobilized. The stressfield method shows a reasonable fit to the values proposed by EC7 for positive inclination angles of the backfill. As the backfill is sloped at a negative angle the fit between given and calculated values gets worse.

Although it cannot be assumed that the stressfield method as presented in HB016 delivers exactly the same results as those given by EC7, the difference between the two can in most cases be overlooked. The greatest difference found with my calculations is for the case of zero wall roughness angle and a backfill inclination equal to the friction angle. The difference in this case is estimated around $10 - 15\%$. It can therefore be assumed that the stressfield method produces similar values for the active earth pressure coefficients as the ones proposed by EC7; it should be noted that the difference between the methods always erred in such a way that EC7 gave higher values for the earth pressure coefficient than the stressfield method.

3.3.2 Passive pressures according to Eurocode 7

All four earth pressure coefficient figures from EC7 have been combined into one for the passive case and can be seen together in Figure 3.17
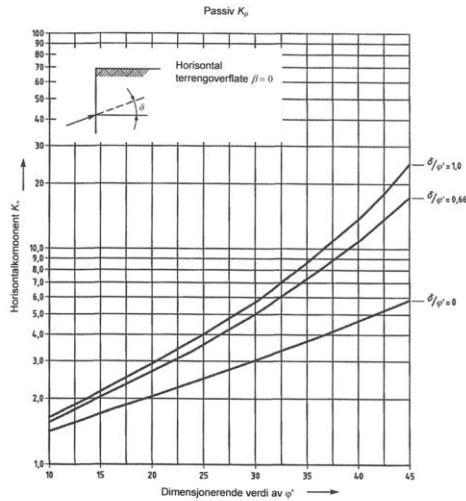
Figur C.2.1 – Koeffisientene K_p for passivt jordtrykk: med horisontal terrengoverflate ($\beta = 0$
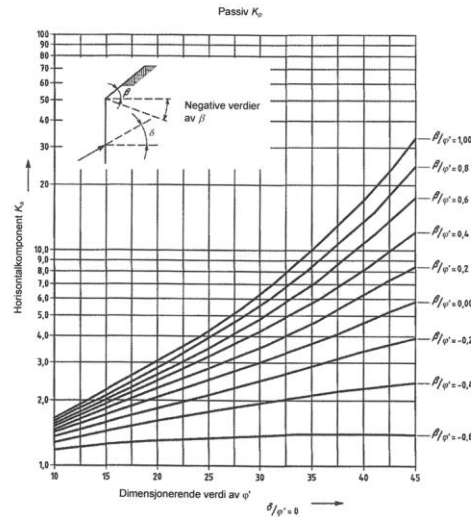
Figur C.2.2 – Koeffisientene K_p for passivt jordtrykk: med hellende terrengoverflate ($\delta/\varphi' = 0$ og $\delta = 0$).
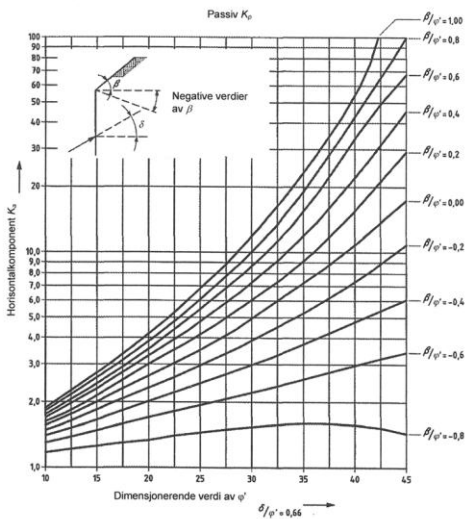
Figur C.2.3 – Koeffisientene K_p for passivt jordtrykk: med hellende terrengoverflate ($\delta/\varphi' = 0,66$)   C.2.4 – Koeffisientene K_p for passivt jordtrykk: med hellende terrengoverflate ($\delta/\varphi' = 1$)
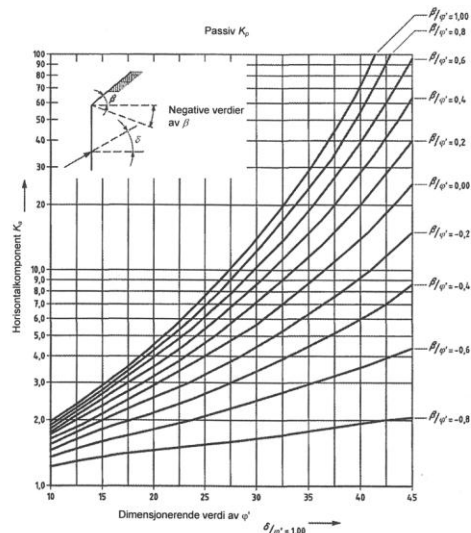
Figure 3.17: Passive earth pressure coefficient, K_P, as it appears in Eurocode 7.

As can be seen in Figure 3.17, the passive earth pressure coefficient seems to always converge to a value for in all the figures provided by EC7. This holds true for all inclination angles of the backfill and all values of roughness. This differs from the results seen for both Coulomb's method and the stressfield method that can be seen in Figure 3.6 as the passive pressure seems to grow exponentially for high roughness and friction angles. The stressfield method defined in HB016 is also not defined for backfills that are inclined upwards at an angle in the case of passive pressures. By definition it should therefore not be applied in those cases.

It has been shown that the stressfield method delivers almost exactly the same values as Coulomb's method in the case of inclined backfill; it is therefore interesting to compare them to the values proposed by EC7.

The case of horizontal backfill

In Figure 3.18 the stressfield method has been superimposed on the values given by EC7 for the case of passive earth pressures.
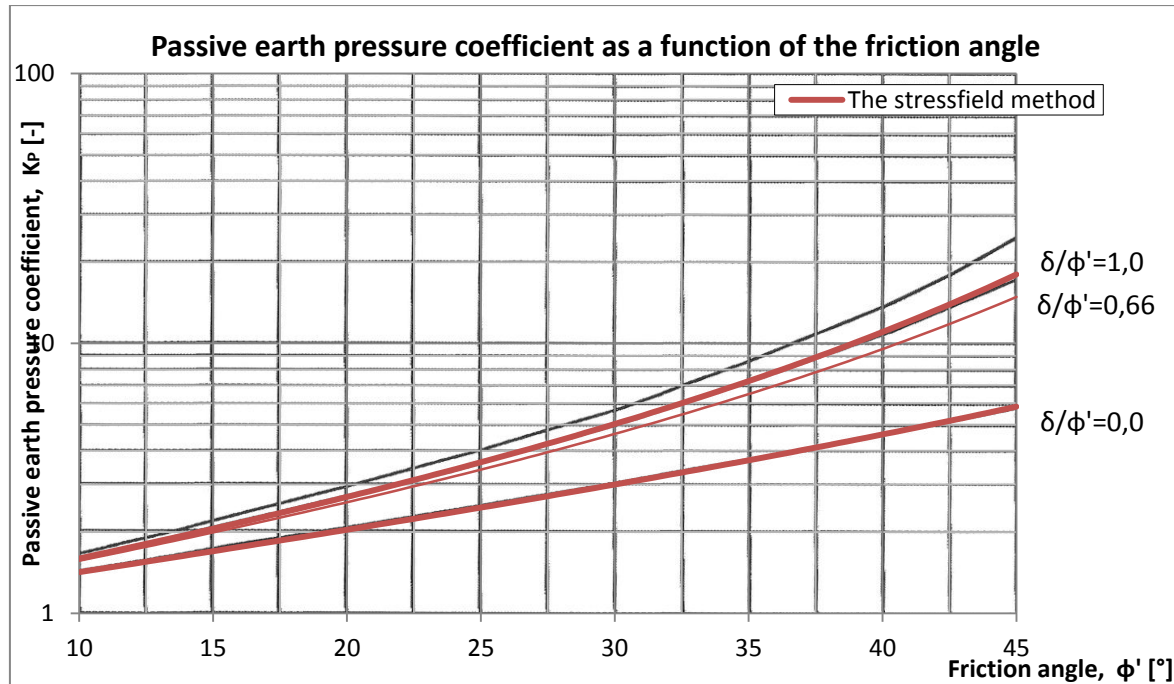
Figure 3.18: K_P according to EC7 with the stressfield method superimposed, $\beta = 0$.

The given values and the calculated ones are in total agreement in the case of no roughness but as the roughness is increased the difference between the two increases. This result is a bit surprising because of the good fit produced between the two in the active case with a horizontal backfill; see Figure 3.13.

When designing a structure that retains a mass of earth the passive force is usually a resisting force. As EC7 gives higher values of K_P than the stressfield method it here errs on the side of failure if the stressfield method can be assumed to produce accurate results.

The case of inclined backfill

As can be seen in Figure 3.6 the passive earth pressures grow exponentially according to both Coulomb's method and the stressfield method for the case of inclined backfill. Both methods assume a planar failure surface in this case and as EC7 assumes a curved one a difference as the one seen in Figure 3.4 can be expected. In Figure 3.19 the stressfield method has been superimposed onto the values given in figure C.2.2 in EC7
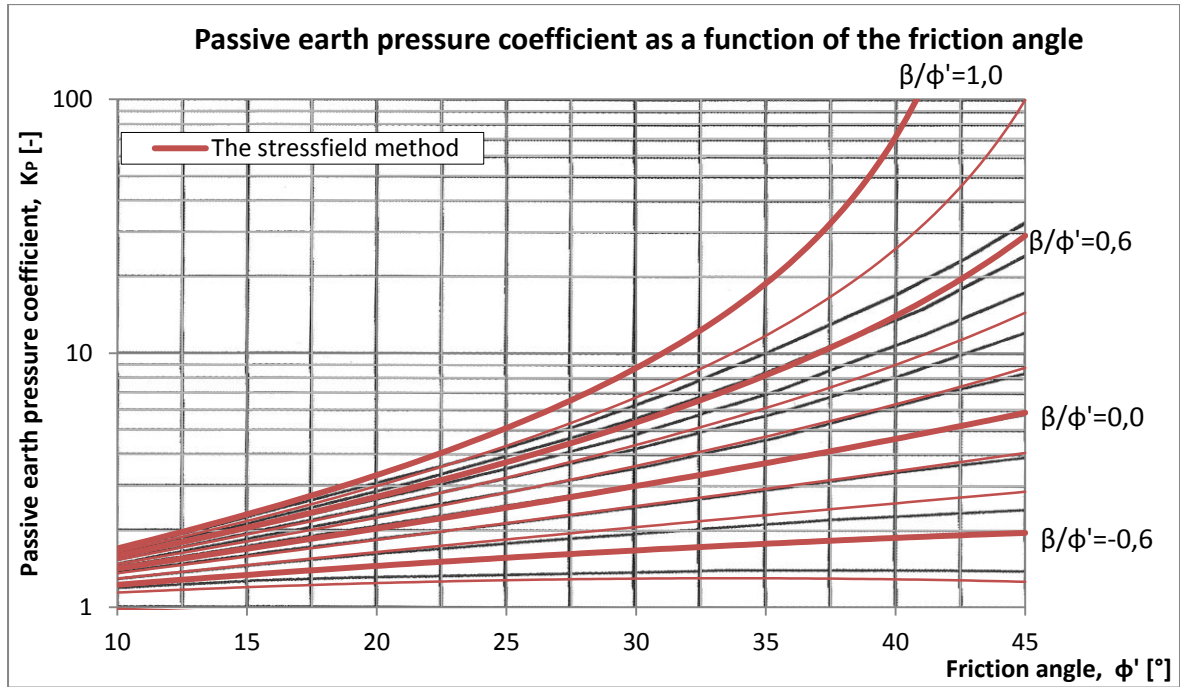
Figure 3.19: K_P from EC7 with stressfield method superimposed, $\beta \neq 0$, $\delta/\phi' = 0,0$.

It is clear from Figure 3.19 that the stressfield method and Coulomb's method do not produce similar values as the ones proposed by EC7 in the case of sloped terrain with no roughness. The fit seems to be better for small friction angles and small inclinations of the backfill. As the inclination of the backfill nears the friction angle the difference between the proposed values and the calculated ones becomes larger; this difference gets very large for large friction angles.

With increased roughness between the structure and backfill the trend seen in Figure 3.19 only increases and more of the curves show this exponential behavior. It can therefore be assumed that neither the stressfield method nor Coulomb's method can be expected to deliver results similar to those proposed by EC7 in the case of passive pressures from an inclined backfill.

It is interesting to see if the modified stressfield method from chapter 3.2 will produce better results. Making the same assumption as was done in the case of inclined terrain it is possible to use the modified stressfield method. As the Prandtl zone grows towards the backfill the passive pressures grow with increased inclination of the backfill. Adding the backfill angle to the opening angle of the Prandtl zone we end up with an equation transferring the stress from an inclined Rankine zone to a normal stress acting on a vertical wall. In this case there is no contribution from the shear stress to the earth pressure coefficient as the wall is assumed to be vertical. In this test the factor N is used as presented in equation (22) as trials with N as described with equation (31) did not produce comparable results.

The new opening angle of the Prandtl zone in equation (22) will therefore be $(\omega + \beta)$, when β is defined as positive for terrain sloping in an upwards direction. As EC7 assumes both positive and negative angles of β, the modified stressfield method will use a planar shear surface when the backfill is inclined at a downward angle, just as the method

49

proposed in HB016.   This version of the modified stressfield method has been superimposed on figure C.2.2. from EC7 in Figure 3.20.
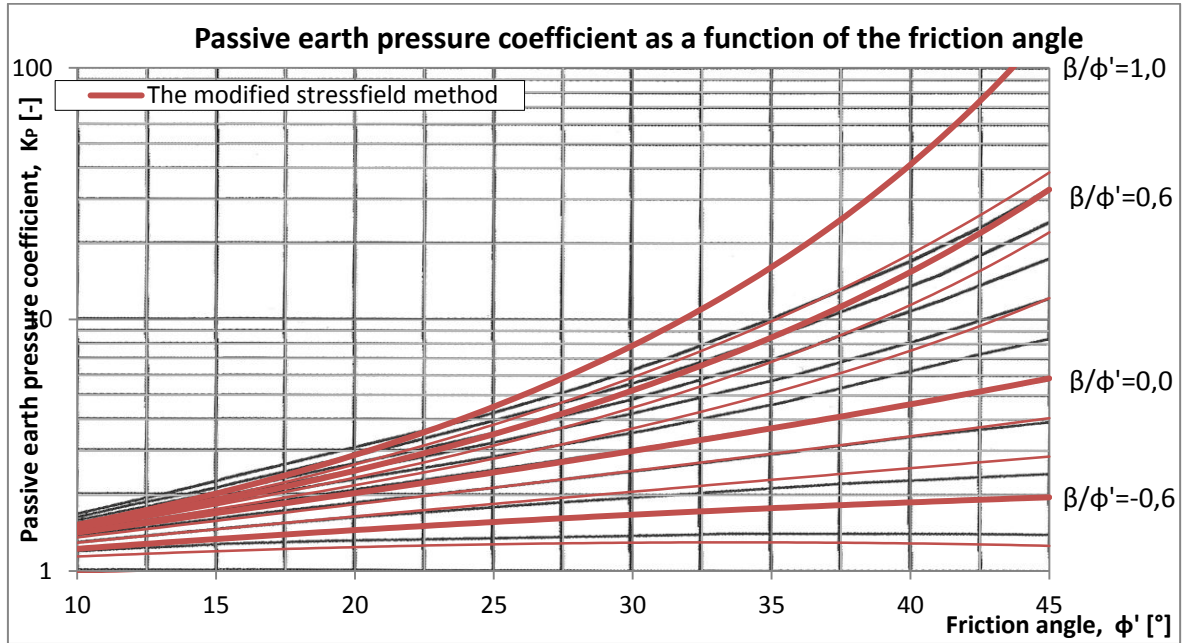
Figure 3.20: K_P from EC7 and the modified stressfield method, $\beta \neq 0$, $\delta/\phi' = 0,0$.

Figure 3.20 shows that the modified stressfield method produces similar trends as are proposed by EC7. It converges to a value for all inclination angles of the backfill, thus solving the problem with the exponential divergence seen in Figure 3.19 but at the same time the fit gets worse for smaller friction angles. The method cannot be assumed to produce the same values as are proposed by EC7. With the exception of the curve where the angle of the backfill is equal to the friction angle the modified stressfield method can be assumed to deliver results of a similar order as the ones given by EC7. The fit between the modified stressfield method and the values given by EC7 improves as the roughness is increased.
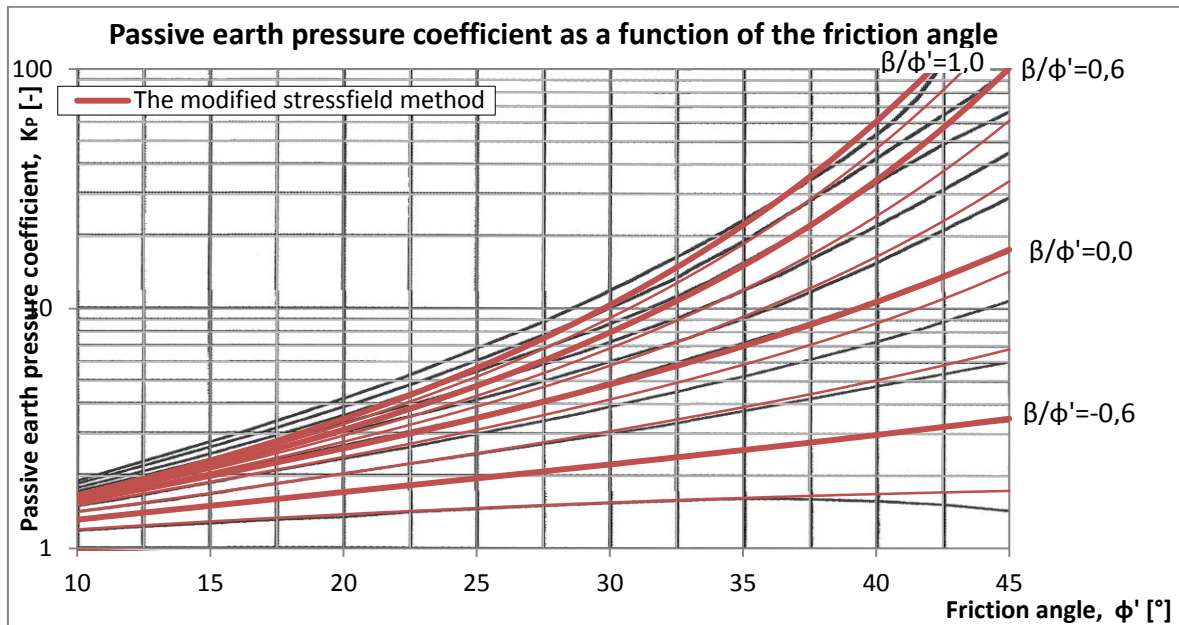

Figure 3.21: K_P from EC7 and the modified stressfield method, $\beta \neq 0$, $\delta/\phi' = 0,66$.

Figure 3.21 shows the modified stressfield method superimposed on figure C.2.3 from EC7. The modified stressfield method produces values more similar to those given by EC7 for higher values of roughness. The modified stressfield method produces lower values of K_P than are proposed by EC7 in the case of low friction angles and positive inclination angles of the backfill. As the friction angle rises the method shows faster growth than the proposed values, this results in higher values of earth pressure coefficient for friction angles larger than $\phi' = 35°$.
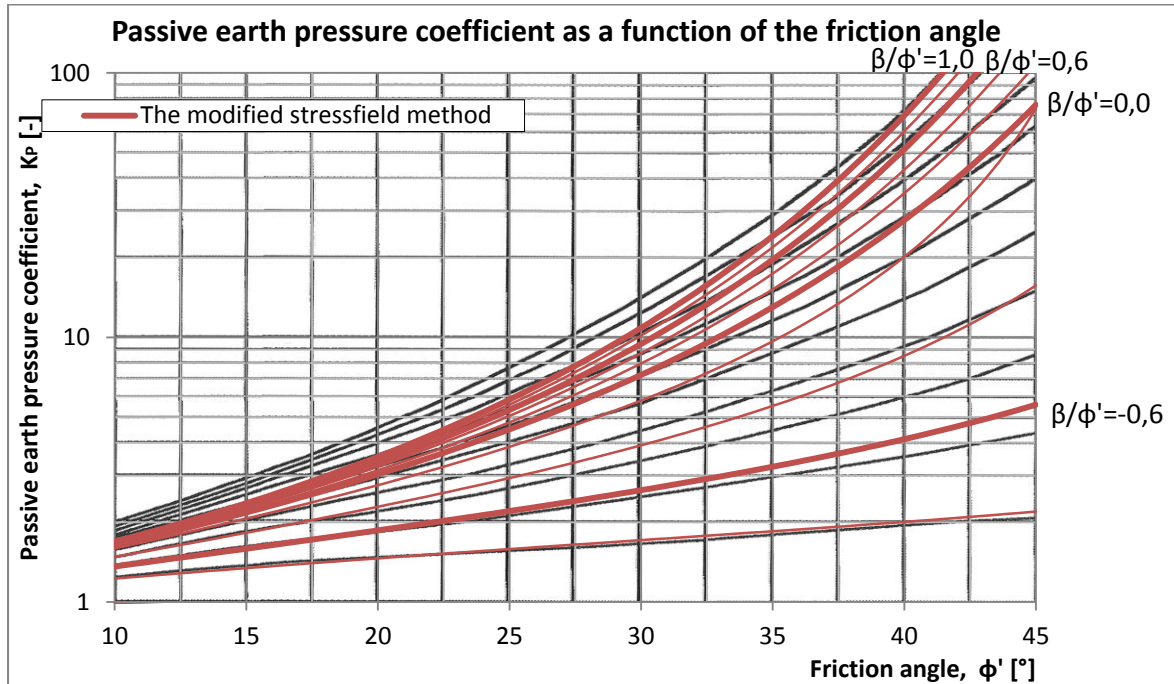
Figure 3.22: K_P from EC7 and the modified stressfield method, $\beta \neq 0$, $\delta/\phi' = 1,0$.

Figure 3.22 shows the modified stressfield method superimposed on figure C.2.4 from EC7. The roughness angle is in this case equal to the soils friction angle, corresponding to a roughness number of $r = 1,0$. It is clear from Figure 3.22 that a good fit is achieved for the negative terrain inclination angle equal to the friction angle. As the terrain inclination angle rises this fit gets worse and it gets difficult to compare the two.

It is clear that the passive earth pressure coefficients proposed by EC7 are calculated with a method other than the ones derived in this paper. For the case of an inclined backfill the method proposed by HB016 delivered results of a different order than the ones given by EC7. The modified stressfield method produced results closer to the ones proposed by EC7, the method fits best to the proposed values for the mid-range of wall roughness angles.

It is important to be aware of the limitations of the methods used to calculate the passive earth pressures. Because passive pressures are often overlooked when designing retaining walls this point is perhaps not as important as it would otherwise be.

The main result from comparing the methods derived to the values given by EC7 is there seems to be good correlation between the given values of active pressures and the calculated ones. Using the stressfield method to calculate active earth pressures should satisfy the requirements of EC7.

4 Design methods proposed by Håndbok 016

The Norwegian Road Administration (*n. Statens vegvesen*), publishes various handbooks to help designers, contractors and quality inspectors to uphold the standard requirements on each project they are involved in. These handbooks are divided into two groups: *standards* and *guidelines*. Handbooks classified as standards provide rules and requirements in each field that shall be fulfilled in order to get the NRA's approval of the project. Handbooks classified as guidelines however contain guidelines, textbooks and road traffic data.

Handbook 016 falls in the latter category and is a guidebook intended as a design aid to contribute to good and safe geotechnical design in projects that fall under the jurisdiction of the NRA. Chapter 9 is dedicated to applying the theory of earth pressures and bearing capacity to the design of retaining structures and bridge abutments. Retaining structures are then divided into retaining walls and dry stone walls.

Retaining structures come in many sizes and shapes but they all have the common purpose of creating a difference in elevation. This elevation difference may then be for practical or esthetic purposes. The main types of retaining walls are gravity walls, cantilever walls, anchored wall and sheet-pile walls. The subject of this chapter will be methods proposed to design cantilevered retaining walls.

4.1 Requirements

Frost heave

The soil mass on which the structure is founded should not be subject to frost heave. If the in situ soil has frost heaving properties it should be exchanged for a material that does not. This also applies to the masses immediately behind the structure and should be done to the depth of the frost line. This problem can also be solved be means of frost isolation (Statens vegvesen, 2010)

Drainage

Groundwater should be drained from behind the structure and its base (Statens vegvesen, 2011). If the structures serviceability and stability depend upon a successful drainage system it is required that a maintenance plan be established and followed or a drainage checking system to check if maintenance is required.

Loads

Retaining structures are to be dimensioned in accordance with load combinations from the ultimate limit state. Design loads should be considered as proposed by Håndbok 185 (Statens vegvesen, 2009).

Roughness safety factors and soil mobilization

The roughness number for a particular should be selected in accordance with Table 4.1.

Table 4.1: Proposed design values for the roughness number, r, according to HB016.

Roughness, r	State	Comment
$1/\gamma_M$ f	ULS SLS	Used when structure rotates about foundation, slides outwards or masses behind the wall settle more than the structure. Shear stresses onto structure act at a downward angle.
0	-	Used when there is no relative movement between the structure and the retained masses.
$-0,5$	-	Used when the structure settles more than the retained masses. Shear stresses onto structure act at an upward angle.

Structures on rock should be dimensioned using $r = 0$. Other values are acceptable on special occasions such as when the backfill is poorly compacted.

For the ultimate limit state the material safety factor γ_M are to be selected in with respect to the failure mechanism and the consequences of failure of the proposed structure. The material factors for the design should be selected in accordance with Table 4.2

Table 4.2: Proposed design values for the material factor, γ_M, according to HB016.

Consequence class	Failure mechanism		
	ductile, dilatant failure	neutral failure	brittle, contractant failure
1 - *Less serious*	1,25 1,40*	1,30 1,40*	1,40
2 - *Serious*	1,30 1,40*	1,40	1,50
3 - *Very serious*	1,40	1,50	1,60

The split cells in Table 4.2 are a result of minimum requirements in Eurocode 7: *Geotechnical design*, when analyzing on a total stress basis.

A guideline for deciding a consequence class for a proposed project is provided in Table 4.3.

Table 4.3: Proposed scheme to select design consequence class, CC, according to HB016.

Consequence class	Description	Example
CC3	Large consequences in the form of loss of life or large economical-, social- or environmental consequences.	Spectator stands or other building where large crowds gather and the consequences of failure are great.
CC2	Medium consequences in the form of loss of life, moderate economical-, social- or environmental consequences.	Private residences and offices, public buildings where consequences of failure are moderate.
CC1	Small consequences in the form of loss of life, and small or insignificant economical-, social- or environmental consequences.	Building where people normally do not reside or stay for long periods of time.

When the expected consequence class and failure mechanism has been evaluated the roughness number for the ultimate limit state can be calculated in accordance to Table 4.1. The mobilized friction angle for the design can then be calculated with equation (7) where the capital letter F is exchanged for the value of γ_M.

For the serviceability limit state the roughness can be evaluated in accordance with Table 4.1 where f is given by Table 4.4.

Table 4.4: Proposed design values for the degree of mobilization, f, according to HB016.

Foundation	Flexible structure	Normal structure	Stiff structure
Soft	0,8	0,75	0,70
Medium stiff	0,75	0,70	0,65
Stiff / Rock	0,70	0,65	0,60

Earth pressures

The methods used in the backfill process and compaction have an effect on the resulting earth pressures. Guidelines on the backfill and compaction process are given in Håndbok 100-1 (Statens vegvesen, 1996) and Håndbok 018 (Statens vegvesen, 2011)

Earth pressures should be calculated for the ultimate limit state, *ULS*, as well as the serviceability state, *SLS*. The most critical case shall be used for the design of the concrete/reinforcements of the structure.

Where no relative movement is expected between the soil and structure, it is proposed that at rest earth pressure be used as design pressure for the retaining structure. For normally consolidated earth, no relative movement is defined as lateral movement of less than 0,5‰ of the walls height.

For structures that are founded on rock and the distance between wall and rock-face is small in comparison to the height, the earth pressures shall be calculated in accordance with chapter 5.4.1 in HB016 (Statens vegvesen, 2010).

Earth pressures from surface loading should not affect the structure to a greater depth than 5 meters. Tensile stresses in cohesive soils should be neglected as they will disappear with the first tension crack. It is assumed that the stresses increase linearly with depth from zero at terrain level in the case of tensile stresses, this assumption both adds to the resulting lateral force and pulls its arm of application towards the surface, which adds to its force lever, c_1.

These assumptions create four stress cases that can be seen in Figure 4.1.
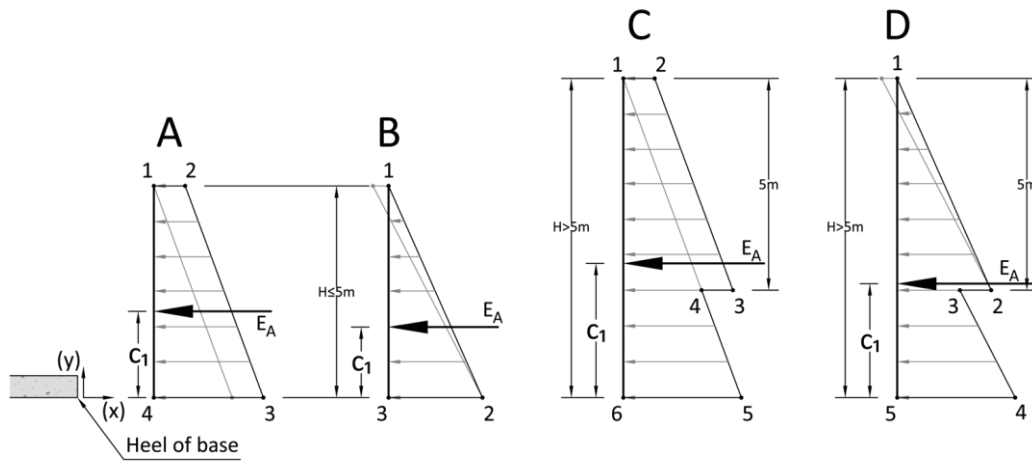
Figure 4.1: possible stress cases according as proposed by HB016.

The geometry shown in Figure 4.1 is controlled by the height of the structure, the terrain load, inclination of the terrain, unit weight of the soil, the roughness, the cohesion and the friction angle. How the stress points listed in Figure 4.1 are calculated in each case for a flat terrain behind the structure is shown in Table 4.5.

Table 4.5: Points in stress-shapes for the case of flat terrain, according to HB016.

Point number	Case A	Case B
(x_1, y_1)	$(0, H)$	$(0, H)$
(x_2, y_2)	$(K_{A.corr} \cdot (q + a) - a, H)$	$(K_{A.corr} \cdot (\gamma \cdot H + q + a) - a, 0)$
(x_3, y_3)	$(K_{A.corr} \cdot (\gamma \cdot H + q + a) - a, 0)$	$(0, 0)$
(x_4, y_4)	$(0, 0)$	
	Case C	**Case D**
(x_1, y_1)	$(0, H)$	$(0, H^*)$
(x_2, y_2)	$(K_{A.corr} \cdot (q + a) - a, H)$	$(K_{A.corr} \cdot (\gamma \cdot z + q + a) - a, H - z)$
(x_3, y_3)	$(K_{A.corr} \cdot (\gamma \cdot z + q + a) - a, H - z)$	$(K_{A.corr} \cdot (\gamma \cdot z + a) - a, H - z)$
(x_4, y_4)	$(K_{A.corr} \cdot (\gamma \cdot z + a) - a, H - z)$	$(K_{A.corr} \cdot (\gamma \cdot H + a) - a, 0)$
(x_5, y_5)	$(K_{A.corr} \cdot (\gamma \cdot H + a) - a, 0)$	$(0, 0)$
(x_6, y_6)	$(0, 0)$	

The variable z stands for the depth of application of the earth pressures originating from the terrain load. HB016 requires this value to be equal to $z = 5m$. The coordinates for the stress points, as seen in Figure 4.1, when the backfill is sloped are shown in Table 4.6.

Table 4.6: Points in stress shapes for the case of sloped terrain, according to HB016.

Point number	Case A	Case B
(x_1, y_1)	$(0, H^*)$	$(0, H^*)$
(x_2, y_2)	$\left(K_{\beta A.corr} \cdot (q + a) + \dfrac{s}{s - \omega_A} \cdot a - a, H^* \right)$	$\left(K_{\beta A.corr} \cdot (\gamma \cdot H^* + q + a) + \dfrac{s}{s - \omega_A} \cdot a - a, 0 \right)$
(x_3, y_3)	$\left(K_{\beta A.corr} \cdot (\gamma \cdot H^* + q + a) + \dfrac{s}{s - \omega_A} \cdot a - a, 0 \right)$	$(0,0)$
(x_4, y_4)	$(0,0)$	
	Case C	**Case D**
(x_1, y_1)	$(0, H^*)$	$(0, H^*)$
(x_2, y_2)	$\left(K_{\beta A.corr} \cdot (q + a) + \dfrac{s}{s - \omega_A} \cdot a - a, H^* \right)$	$\left(K_{\beta A.corr} \cdot (\gamma \cdot z + q + a) + \dfrac{s}{s - \omega_A} \cdot a - a, H^* - z \right)$
(x_3, y_3)	$\left(K_{\beta A.corr} \cdot (\gamma \cdot z + q + a) + \dfrac{s}{s - \omega_A} \cdot a - a, H^* - z \right)$	$\left(K_{\beta A.corr} \cdot (\gamma \cdot z + a) + \dfrac{s}{s - \omega_A} \cdot a - a, H^* - z \right)$
(x_4, y_4)	$\left(K_{\beta A.corr} \cdot (\gamma \cdot z + a) + \dfrac{s}{s - \omega_A} \cdot a - a, H^* - z \right)$	$\left(K_{\beta A.corr} \cdot (\gamma \cdot H^* + a) + \dfrac{s}{s - \omega_A} \cdot a - a, 0 \right)$
(x_5, y_5)	$\left(K_{\beta A.corr} \cdot (\gamma \cdot H^* + a) + \dfrac{s}{s - \omega_A} \cdot a - a, 0 \right)$	$(0,0)$
(x_6, y_6)	$(0,0)$	

The earth pressure cross section is taken to be from the heel of the footing in a vertical line to the terrain. The height of this cross section will in the case of a sloped terrain differ from the height of the structure. Therefore the variable H has been interchanged with the variable H^* in Table 4.6 representing the height of the section. The magnitude of the earth pressure force is calculated using the values from either Table 4.5 or Table 4.6 and equation (G1) given in Appendix G. The point of application, c_1, is calculated with the same values using equation (G3). Note that because the points are oriented in a clockwise direction, both equations should be used with a change in sign.

For structures connected to the road system the passive earth pressures should not be considered in the design because of the risk that the earth in front of the structure could later be dug away to make room for infrastructural facilities such as pipes and cables.

Bearing capacity

Bearing capacity is to be calculated as described in chapter 2.4. Effective stress analysis is usually applied but if cohesive materials are found within 1,5 x the foundation width the bearing capacity shall be calculated using the total stress analysis or alternatively an effective stress analysis including the effect of excess pore pressures.

The design roughness under the foundation, r_b, for structures up to the height of 5 meters should be selected in accordance with Table 4.1.

Table 4.7: Proposed foundation roughness, r_b, according to HB016.

Horizontal terrain in front of structure		Sloped terrain in front of structure	
Roughness, r_b	Material under base	Roughness, r_b	Material under base
$\leq 0{,}9$	Sand, gravel, blasted rock	$\leq 0{,}8$	Gravel and blasted rock
$\leq 0{,}8$	Clay and silt	$\leq 0{,}7$	clay, silt and sand

For higher structures it should be investigated if lower values of r_b should be used in the calculations.

Furthermore it is a requirement that when cohesive soils are used as foundation material, they should be undisturbed, drained and unfrozen to decrease the risk of the base sliding on the foundation.

Geometrical uncertainties

Any uncertainty in geometry should be taken into account in the design phase with the formula

$$a_d = a_{nom} \pm \Delta a \qquad (63)$$

where a_d is the design geometrical value, a_{nom} is the proposed/expected value and Δa is the uncertainity allowed for in the geometry. Values for Δa vary but for the base an uncertainty of about $\Delta a = 0{,}1m$ is to be expected if special measures are not taken to reduce it.

For a cantilever wall Δa should be estimated as 10% of the height above the baseplate, with the maximum value of 0,5 meters.

Geotechnical parameters

The geotechnical parameters of the backfill and foundation control the pressures acting against the structure and the bearing capacity of the foundation. To ensure a safe design it is essential to adjust each design to the local ground conditions.

In some cases previous soil investigations have been conducted in the immediate area where the proposed structure will rise and a desk study will provide a solid ground to base a design on. This is however not always the case and therefore the need for further investigations may arise. There are many methods available to determine various geotechnical parameters and they vary in extent, price and quality. It is important to evaluate how precise results are required from the investigations to ensure that an economically feasible solution is chosen.

If however no information other than a general visual description is available for ground conditions, some general parameters are given for the assumed earth types. The parameters proposed by HB016 can be seen in Table 4.8.

Table 4.8: Proposed strength parameters for assumed earth types, according to HB016.

Position		Material		Unit weight	Characteristic friction angle		Attraction
				[kN/m³]	ϕ' [°]	tan(ϕ') [-]	[kPa]
Behind and in front of retaining structure	Compacted fill masses *	**Blasted rock** **		**19**	**42**	**0,90**	**0**-10
		Gravel		19	38	0,78	0
		Sand		18	36	0,73	0
	Uncompacted natural masses	**Gravel**		**19**	**35**	**0,70**	**0**
		Sand		17	33	0,65	0
		Silt		18	31	0,60	0
		Clay and clayey silt	**Firm** ***	**20**	**26**	**0,49**	**0**
			Wet ***	19	20	0,36	0
Under footing	Compacted fill masses *	**Blasted** rock** and ****		**19**	**42**/45	**0,90**-1,00	**10**
		Gravel *****		19	38/40	0,78-0,84	10
		Sand		18	36	0,73	10
	Uncompacted natural masses	**Gravel**	Compacted	19	38	0,78	0-10
			Loose	**18**	**36**	**0,73**	**0**-5
		Sand	Compacted	18	36	0,73	0-10
			Loose	17	33	0,65	0-5
		Silt	Firm	19	33	0,65	0-10
			Wet	18	31	0,60	0-5
		Clay and clayey silt	**Firm** ***	**19**	**26**	**0,49**	**0**-20
			Wet ***	19	20	0,36	0-5

   *   *Compacted in layers on land*
   **   *Blasted and machine crushed rock. If high quality higher values can be used.*
   ***   *Clays or clayey silt, strength parameters should be obtained from undisturbed samples*
   **** *The highest values can be used for blasted rock of high quality under footing*
   ***** *The highest values can be used for gravel of high quality under footing*

Values found in Table 4.8 provide a sort of frame for the values that could be encountered in practical applications while designing retaining structures. The values highlighted with bold letters in Table 4.8 will be used as a base for the calculations in the following chapter.

4.2 Cantilever walls

A cantilever retaining wall is a relative thin wall that uses a moment to counter the lateral earth pressures. This moment can be created with a base plate buried behind the wall, a base plate that extends out in front of the wall or a combination of both variants. Figure 4.2 shows a variant of both cases in a sloped terrain and how the geometrical parameters are defined.
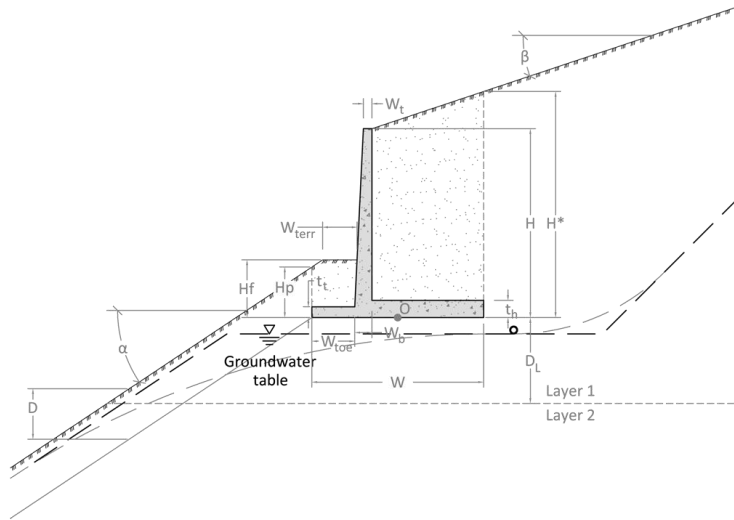
Figure 4.2: A general case of a cantilever wall showing main geometrical parameters.

In the case of a cantilever retaining wall it is the general assumption that the earth pressures act upon a plane that stretches from the heel of the footing directly up to the terrain. In the case of a sloping backfill, this will have an effect on the stress-shape coordinates put into equations (G1) and (G3). The earth mass above the heel is calculated as a part of the structure itself.
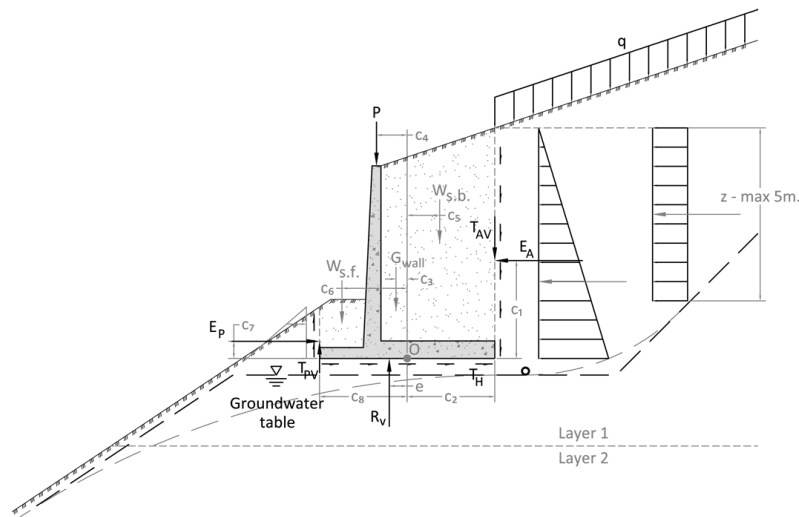
Figure 4.3: Forces acting on a general case of a cantilever retaining wall.

4.2.1 Calculation procedure

The force resultant that the structure exerts on to the foundation, R_V, can be calculated by summing up all vertical forces in Figure 4.3.

$$R_V = G_{Wall} + W_{s.f.} + W_{s.b.} + P + T_{AV}(-T_{PV}) \tag{64}$$

where G_{Wall} is the weight of the concrete structure, $W_{s.f.}$ is the weight of the soil on top of the toe, $W_{s.b.}$ is the weight of the soil on top of the heel, P is the vertical force acting on the top of the vertical wall, T_{AV} is the vertical force caused by the active shear stress and T_{PV} is the vertical force caused by the passive shear stress. The eccentricity, e, of the force resultant can be calculated by setting up a moment equilibrium about the point O. This yields the equation

$$e = \frac{E_A \cdot c_1 - T_A \cdot c_2 \pm G_{Wall} \cdot c_3 \pm P \cdot c_4 - W_{s.b.} \cdot c_5 + W_{s.f.} \cdot c_6 (-E_P \cdot c_7 - T_P \cdot c_8)}{R_V} \tag{65}$$

where E_A is the active force resultant, E_P is the passive force resultant and c_1 to c_8 are the force levers. The last terms in equations (64) and (65) come from the passive force. For structures connected to the road system this force should be neglected and these variables should be omitted.

Once the eccentricity has been calculated the effective foundation width, B_0, can be evaluated with equation (47). The force resultant is assumed to be equally distributed over the effective foundation width. This gives the foundation load as

$$\overline{q_v} = \frac{R_V}{B_0} \tag{66}$$

One of the design requirements in HB016 is that the foundations bearing capacity, calculated using equation (44) or (48), be greater than the foundation load.

$$\overline{\sigma_v} > \overline{q_v} \tag{67}$$

The roughness between foundation and the base of the structure can be derived using formula (21) as

$$r_b = \frac{F_H/B_0}{(\overline{q_v} + a - \Delta u_b) \cdot tan(\rho')} \tag{68}$$

where F_H is the horizontal force acting on the structure and Δu_b is the excess pore pressure under the footing. The requirement is that the value of r_b not exceed the values given in Table 4.7.

For practical purposes it is important to ensure that the foundation roughness requirements are met. This is because the iterative process presented by equations (46) becomes unstable for high values of roughness combined with high friction angles.

4.2.2 Assumptions and constraints

Calculating whether a retaining wall as seen in Figure 4.2 will be stable requires a great number of input parameters both in the geometry of the structure and terrain as well as in geotechnical parameters. In order to investigate trends when parameters are varied, a few variables will be fixed while others are varied.

Geotechnical parameters

The foundation and backfill are assumed to be comprised of two materials. They will be varied between types highlighted with bold letters in Table 4.8.

The material factor of safety for the calculations is set to $\gamma_M = 1{,}4$, as it can be taken as a mean value from Table 4.2. The safety factor for the load and the effect of gravity will be set equal to $\gamma_q = \gamma_G = 1{,}0$.

Geometry of the wall and terrain

The geometry of the wall will have a few fixed points. The base plate will have the same thickness behind and in front of the vertical wall. Because the height of the wall will vary greatly it will be fixed to a large value of $t_t = t_h = 0{,}7m$. Although the vertical wall will vary in height, its thickness at its bottom and at its crown will be kept constant. The values used will be $w_b = 0{,}5m$ and $w_t = 0{,}3m$.
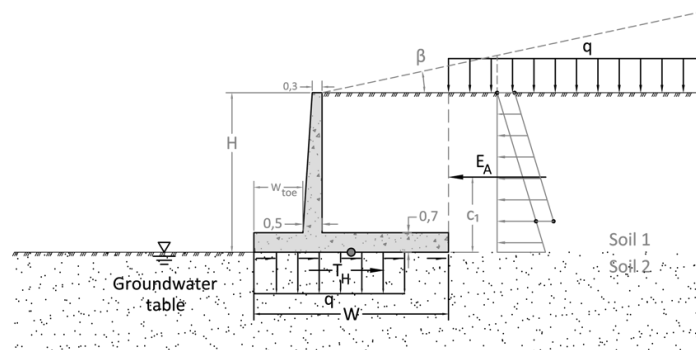
Figure 4.4: Shows the simplified geometry used in hand calculations.

When designing a cantilever wall its eventual height is often one of the few variables that are fixed throughout the design process. In order to achieve a stable structure other geometrical variables will have to be varied. The stability depends on many variables but the one with the greatest influence is the width of the base.

4.2.3 Calculated cases

The base plate widths of cantilevered walls resulting in the same foundation load as the bearing capacity is calculated for wall heights ranging from $H = 3m$ to $H = 12{,}5m$. This is done for each combination of soil types in foundation and backfill highlighted with bold letters in Table 4.8, both for a horizontal and an inclined backfill. The optimal position of the vertical wall is then calculated for each case and the minimum base plate witdth as well. The total number of cantilever walls designed in this study with hand calculation methods is around 360. The safety factor of each case when the surface load has been removed is calculated again with my own implementation of the Phi/c reduction method,

this sums up to around 720 design variants. Some cases did not yield an answer and others yielded answers of little practical importance as can be seen for selected cases in Table 0.2 and Table 0.3 in Appendix H.

4.2.4 Critical base width for L-shaped cantilever wall

Assuming a toe width equal to $w_{toe} = 0m$, a horizontal backfill with a terrain load of $q = 20kPa$ the width of the footing that gave the same foundation load as the bearing capacity was calculated. Each case has been solved so that the vertical load is equal to the bearing capacity. This results in a limit design that only has the material factor of safety, $\gamma_M = 1.4$, that acts against failure. A selection from the results from these calculations can be seen in Table 4.9.

Table 4.9: Wall heights and widths resulting in $\gamma_M = 1,4$ for varying soil types.

Case	H [m]	W [m]	W_{toe} [m]	E_A [kN]	r_b [-]	R_V [kN]	e [m]	B_0 [m]	q_v [kPa]	Foundation material	Backfill material
1	3	1,4	0,0	36,3	0,523	100,2	-0,31	0,75	133,3	Bl. Rock	Bl. rock
2	5	2,3	0,0	84,1	0,465	266,9	-0,43	1,45	183,6	Bl. Rock	Bl. rock
3	7	3,2	0,0	140,9	0,418	502,6	-0,55	2,10	239,3	Bl. rock	Bl. rock
4	10	4,6	0,0	261,6	0,393	1004,6	-0,70	3,17	316,6	Bl. rock	Bl. rock
5	3	2,3	0,0	66,8	0,594	159,6	-0,37	1,55	103,1	Bl. rock	Clay or cl. silt
6	5	4,2	0,0	156,0	0,487	465,7	-0,45	3,26	142,7	Bl. rock	Clay or cl. silt
7	7	6,2	0,0	262,9	0,408	949,4	-0,52	5,16	184,0	Bl. rock	Clay or cl. silt
8	10	9,8	0,0	490,2	0,348	2104,6	-0,57	8,65	243,2	Bl. rock	Clay or cl. silt
9	3	1,7	0,0	47,5	0,558	121,9	-0,34	1,04	116,6	Bl. rock	Gravel
10	5	3,0	0,0	110,2	0,480	335,6	-0,45	2,11	159,3	Bl. rock	Gravel
11	7	4,3	0,0	184,6	0,422	649,1	-0,55	3,16	205,4	Bl. rock	Gravel
12	10	6,3	0,0	342,8	0,383	1341,3	-0,66	4,96	270,2	Bl. rock	Gravel
13	3	2,7	0,0	36,3	0,572	181,9	-0,11	2,50	72,6	Clay or cl. silt	Bl. rock
14	5	4,1	0,0	84,1	0,548	440,6	-0,18	3,71	118,8	Clay or cl. silt	Bl. rock
15	7	5,2	0,0	140,9	0,521	776,6	-0,27	4,66	166,6	Clay or cl. silt	Bl. rock
16	10	7,0	0,0	261,6	0,508	1479,3	-0,37	6,27	235,9	Clay or cl. silt	Bl. rock
17	3	6,9	0,0	66,8	0,428	448,1	-0,04	6,80	65,9	Clay or cl. silt	Clay or cl. silt
18	5	10,6	0,0	156,0	0,396	1130,4	-0,07	10,49	107,7	Clay or cl. silt	Clay or cl. silt
19	7	14,0	0,0	262,9	0,365	2067,4	-0,11	13,81	149,7	Clay or cl. silt	Clay or cl. silt
20	10	19,3	0,0	490,2	0,348	4039,6	-0,15	19,04	212,2	Clay or cl. silt	Clay or cl. silt
21	3	4,0	0,0	47,5	0,530	257,4	-0,09	3,79	67,9	Clay or cl. silt	Gravel
22	5	6,0	0,0	110,2	0,502	629,9	-0,15	5,70	110,5	Clay or cl. silt	Gravel
23	7	7,7	0,0	184,6	0,472	1122,0	-0,22	7,29	153,8	Clay or cl. silt	Gravel
24	10	10,5	0,0	342,8	0,457	2152,5	-0,30	9,89	217,5	Clay or cl. silt	Gravel
25	3	2,3	0,0	36,3	0,455	153,4	-0,16	1,94	79,0	Gravel	Bl. rock
26	5	3,4	0,0	84,1	0,432	375,1	-0,25	2,91	128,8	Gravel	Bl. rock
27	7	4,4	0,0	140,9	0,405	669,7	-0,36	3,72	180,2	Gravel	Bl. rock
28	10	6,0	0,0	261,6	0,393	1281,5	-0,48	5,04	254,3	Gravel	Bl. rock
29	3	6,4	0,0	66,8	0,309	417,3	-0,06	6,28	66,4	Gravel	Clay or cl. silt

Case	H [m]	W [m]	W_{toe} [m]	E_A [kN]	r_b [-]	R_V [kN]	e [m]	B_0 [m]	q_v [kPa]	Foundation material	Backfill material
30	5	10,0	0,0	156,0	0,282	1065,8	-0,09	9,83	108,4	Gravel	Clay or cl. silt
31	7	13,4	0,0	262,9	0,257	1973,8	-0,13	13,12	150,4	Gravel	Clay or cl. silt
32	10	18,6	0,0	490,2	0,243	3882,0	-0,17	18,22	213,0	Gravel	Clay or cl. silt
33	3	3,4	0,0	47,5	0,408	224,3	-0,12	3,18	70,6	Gravel	Gravel
34	5	5,2	0,0	110,2	0,383	554,6	-0,19	4,84	114,6	Gravel	Gravel
35	**7**	**6,8**	**0,0**	**184,6**	**0,356**	**1000,3**	**-0,28**	**6,29**	**159,0**	**Gravel**	**Gravel**
36	10	9,3	0,0	342,8	0,342	1929,5	-0,37	8,60	224,3	Gravel	Gravel

The results in Table 4.9 show that the base width is largest when founded on soils with lower friction angles and it gets larger as the height of the structure is increased. This is as is to be expected as the bearing capacity is linked to the friction angle through all the bearing capacity factors N_q, N_γ and N_u, although the last one is not used in this case. Cases involving backfill masses with lower friction angles require larger base widths. This is as is to be expected as Figure 2.8 shows that the active earth pressure coefficient is higher for soils with lower friction angles resulting in larger overturning moments.

Plotting the width of the structure as a function of its height gives a clearer picture of what is going on, this is shown for each foundation type in Figure 4.5 to Figure 4.7 with a smaller height interval than was given in Table 4.9.
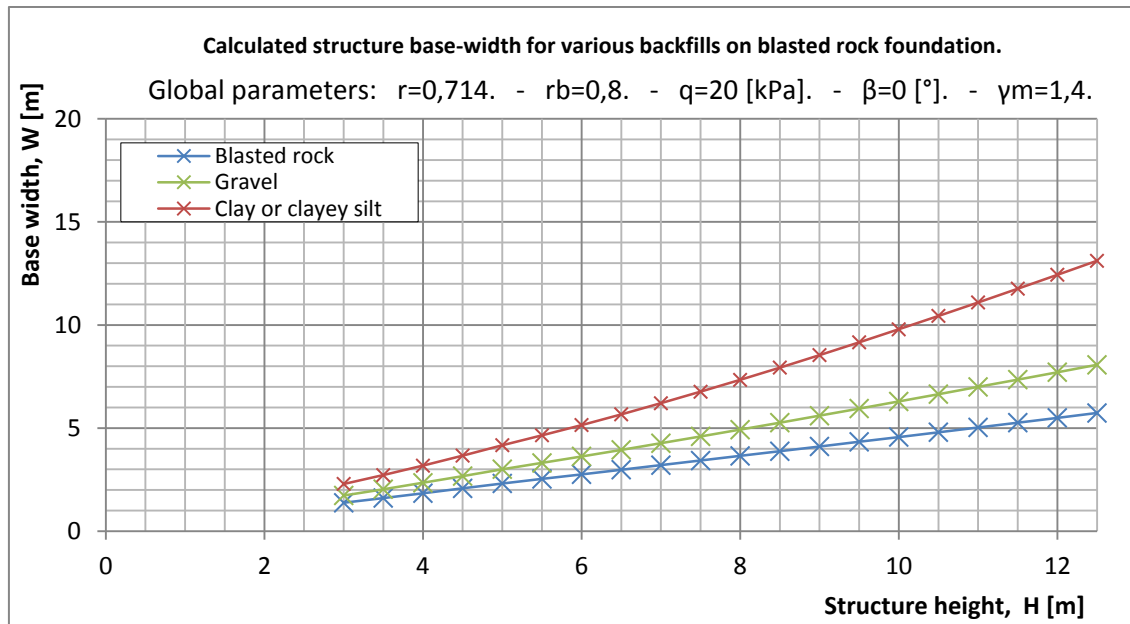

Figure 4.5: Base widths for varying backfill soils on blasted rock foundation.
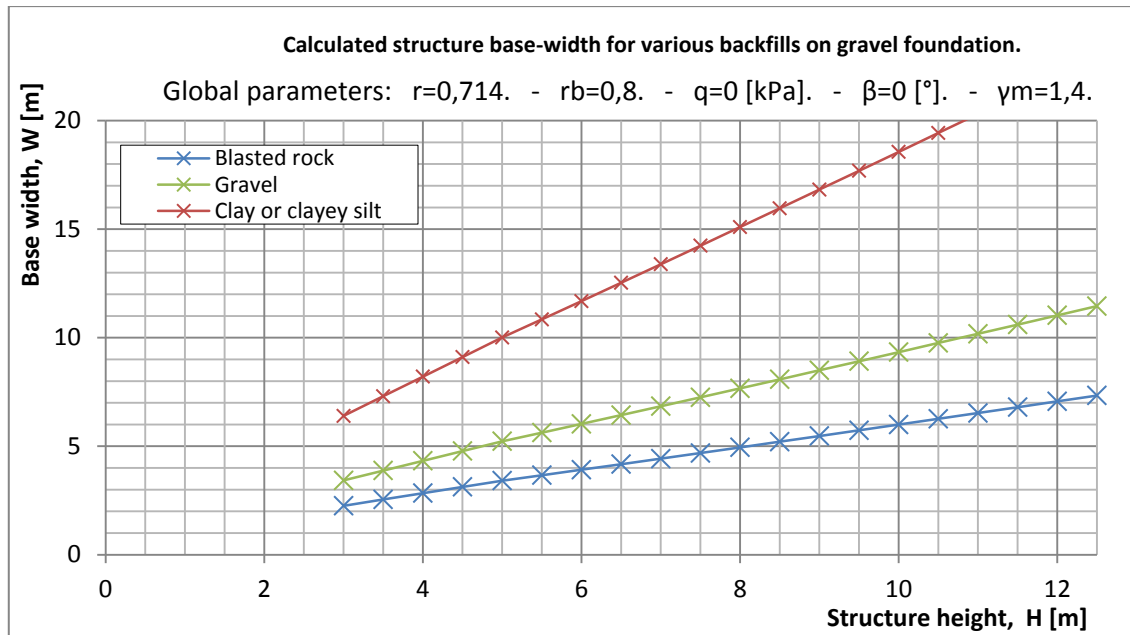
Figure 4.6: Base widths for varying backfill soils on gravel foundation.
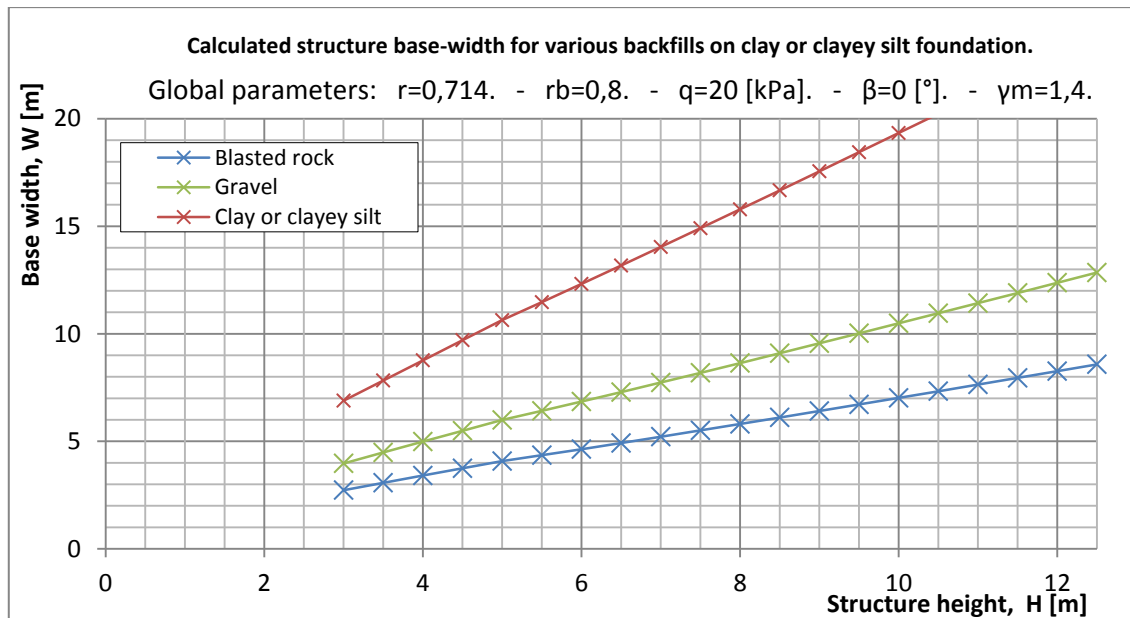

Figure 4.7: Base widths for varying backfill soils on clay or clayey silt foundation.

From figures Figure 4.5 to Figure 4.7 it is clear that with stronger materials both in the foundation and behind the structure the base width necessary to retain the backfill is reduced. What is noticeable is how slowly the curve representing clay or clayey silt rises in Figure 4.5 in comparison to the other two. As the blasted rock material used in the foundation is the only material with a non-zero attraction it raises the question if the attraction has such a large effect on the base width. The calculations have been done again for this case with the assumption of zero attraction; this can be seen in Figure 4.8.
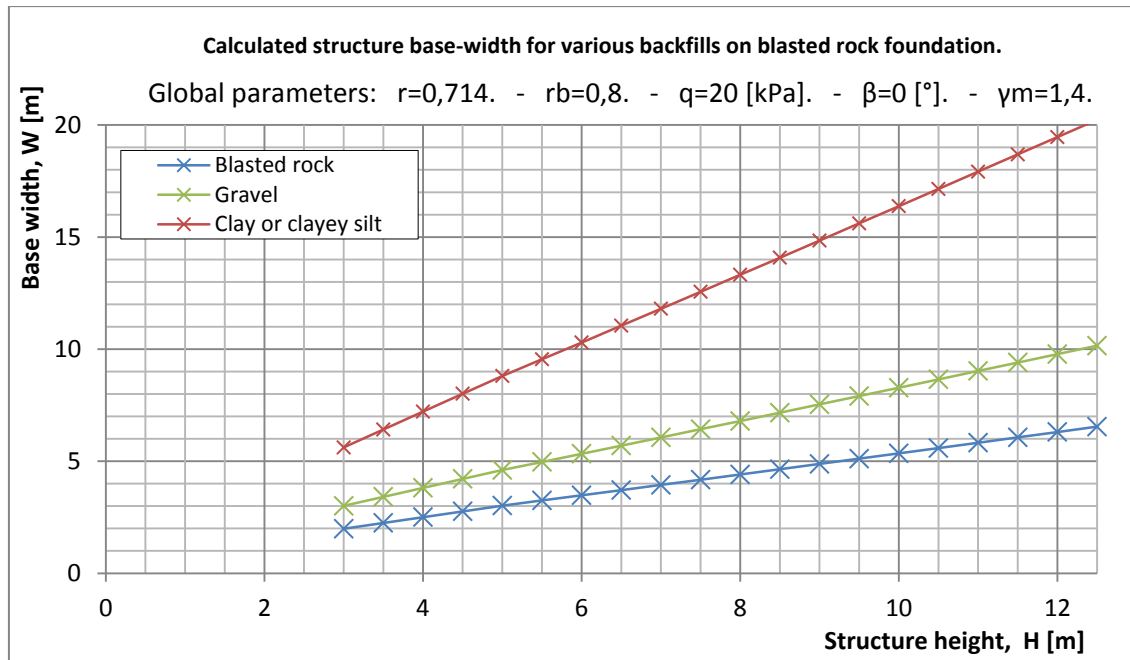
64

Figure 4.8: Base width for varying backfill soils on blasted rock foundation, a=0.

Comparing Figure 4.8 to Figure 4.5 reveals that the attraction in the foundation material has substantial impact on the required foundation with. It can be seen in Figure 4.8 that the curve representing the backfill mass with the lowest friction angle is most affected by this change.

4.2.5 Effect of varying the toe width of cantilever walls

All the examples calculated in the previous chapter are for cantilever retaining walls with zero toe width, or in other words "L"-shaped cantilever walls. By examining Figure 4.4 it is clear that when the toe width is increased while keeping the total width constant the earth mass that rests on top of the heel is decreased. This results in a decrease in total vertical force as well as a change in the internal moment balance, affecting the effective footing width as well.

In order to study the effect of various toe widths the case of a $H = 7m$, $W = 6,8m$ wall founded on gravel and retaining a gravel mass has been chosen. This case is highlighted with bold letters in Table 4.9. The base width is kept constant while the width of the toe is varied and for each case the resulting vertical pressure is subtracted from the bearing capacity. These calculations are shown in Figure 4.9.
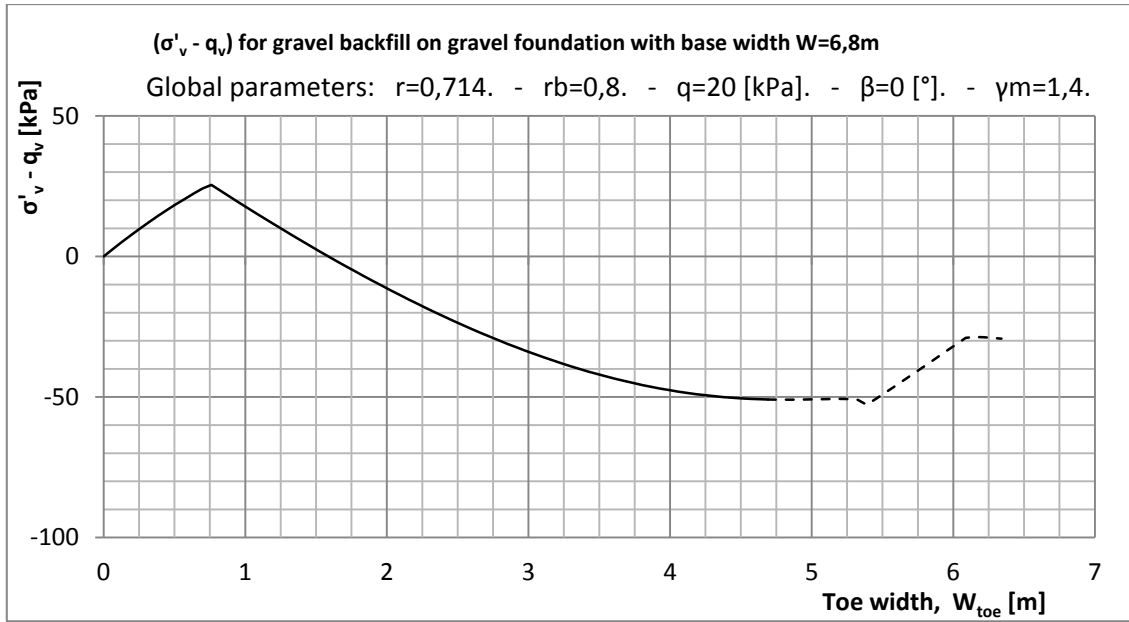
Figure 4.9: Shows the remaining bearing capacity as a function of base toe width.

Figure 4.9 shows that a clear peak in remaining bearing capacity is reached in this case when the base toe width is equal to $W_{toe} \approx 0{,}75m$. Designing a structure that utilizes the optimal toe width to maximize bearing capacity is important because it allows the designer to reduce the width of the structures base thereby reducing the volume of concrete used in the structure.

The dashed part of the curve represents a region where the maximum allowed base roughness of $r_b = 0{,}8$ is reached. The reason for this is that as the width of the toe is increased, less mass rests on top of the heel lowering the vertical load on the foundation while keeping the horizontal load constant. The resisting shear strength is linearly connected to the normal stress so when resisting shear strength drops it leads to a decrease in the divider in equation (68). This results in an increase in r_b.

The bearing capacity equation (44) dependent on the bearing capacity factor, N_γ. It can be seen in Figure 2.15 that for a constant friction angle, the bearing capacity factor N_γ reduces as the foundation roughness increases, resulting in lower bearing capacity. As the foundation roughness has a theoretical maximum value of $r_b = 1$ the bearing capacity reaches its minimum value there as well. Increasing the toe width further will therefore lower the vertical load resulting in an increase in the remaining bearing capacity. This behavior is mathematically understandable but at this point failure in the soil mass under the base is already reached and therefore this peak in bearing capacity is not important. It is useful to know why this the remaining bearing capacity increases but it is outside the scope of theoretical interest.

To further study the effect of varying the toe width it is possible to calculate the mobilization of the friction angles that result in a critical design for each toe width. The mobilization is done as is explained with equation (8) and equation (7) can then be used to calculate the factor of safety F.

To implement this method to the hand calculations the original mobilized friction angle ρ' is noted and then set equal to $\rho' = 0$, resulting in zero mobilization of the friction angle

and failure in the model. The mobilized friction angle of the backfill mass is then incrementally increased until the point of stability is reached. This mobilization marks the point of a model factor of safety of $F^* = f^* = 1$. Dividing the tangent of this fully mobilized friction angle with the tangent of the original one gives an overall model factor of safety. It should be noted that this process of reducing material strength is done by assuming that all materials have the same degree of mobilization and then increasing the all them all by the same mobilization increment. It should be noted that the increment in mobilization Δf does not necessarily mean equal increments in friction angles between the model materials. The results from these calculations, for varying toe widths, can be seen in Figure 4.10.

F* for gravel backfill on gravel foundation with base width W=6,8m

Global parameters: r=0,714. - rb=0,8. - q=20 [kPa]. - β=0 [°]. - γm=1,4.
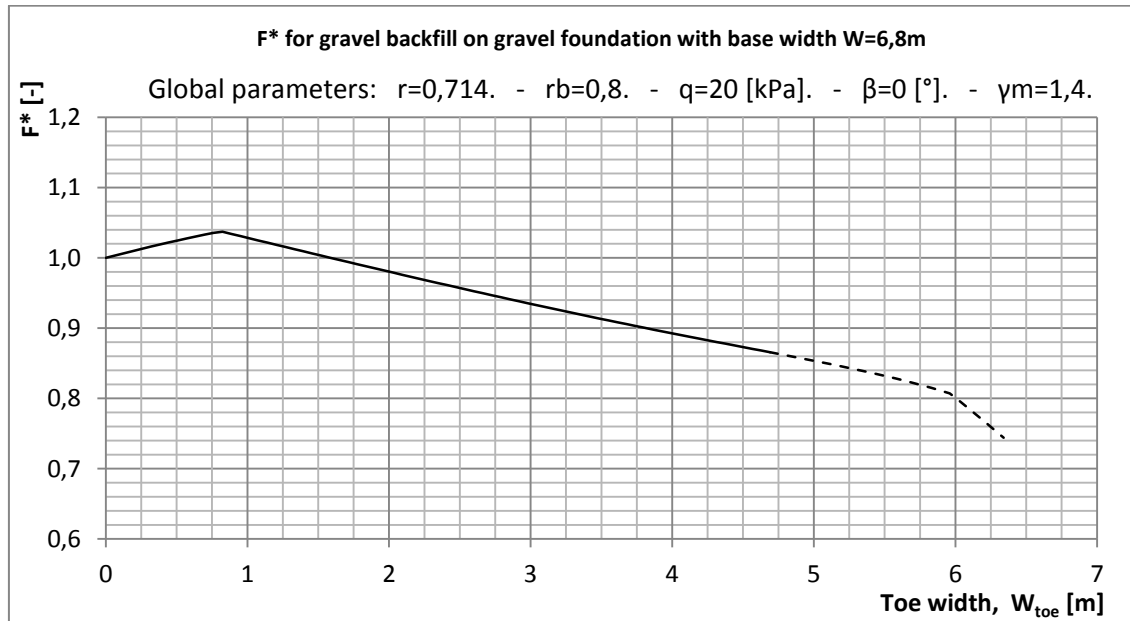
Figure 4.10: Shows the factor of safety as a function of base toe width.

The safety factor plotted in Figure 4.10 is the added safety factor when the material safety factor is also applied. It in other words shows how much extra safety is added to the design. The figure shows that when the remaining bearing capacity is at its highest value, so is the overall factor of safety and it peaks at around 4% and it happens at a toe width of around $w_{toe} \approx 0,8m$. This method of hand calculating a factor of safety is my own product and has the advantage that is shows clearly when the foundation roughness is fully utilized. The main disadvantage with this method is that requires a significantly larger number of calculations. Most of the cases calculated in this chapter are design problems that result in a vertical load equal to the bearing capacity, therefore most of result in an added model factor of safety of $F^* = 1,0$. This means that no added factor of safety if found in the final designs and thus this method does not help with the design of the structures. It does however produce information on effects of variations from the optimized designs. The finite element program PLAXIS implements a similar function to evaluate the model factor of safety called "Phi-C reduction method". In principle it is defined in the same way but PLAXIS uses actual stresses to calculate the factor of safety, which my method does not.

Comparing the two is nevertheless interesting and will be done by calculating the factor of safety, F^*, of the structures designed for a terrain load of $q = 20kPa$ without the added

surface load. To provide a comparison an additional "Phi-C" reduction calculation phase is introduced in PLAXIS before the load is applied to the model.

Using the optimal toe width from Figure 4.9 and calculating the necessary width of footing again reveals that the new width needs to be $W = 6,4m$. This is a change of around $\Delta W = 0,4m$ or a decrease of about 6%. This result is valid, and the new design requires less concrete than was used before but as the optimal toe width is linked to the total base width this solution is not optimal. Plotting the remaining bearing capacity as a function of the toe width for this reduced base width is done in Figure 4.11.
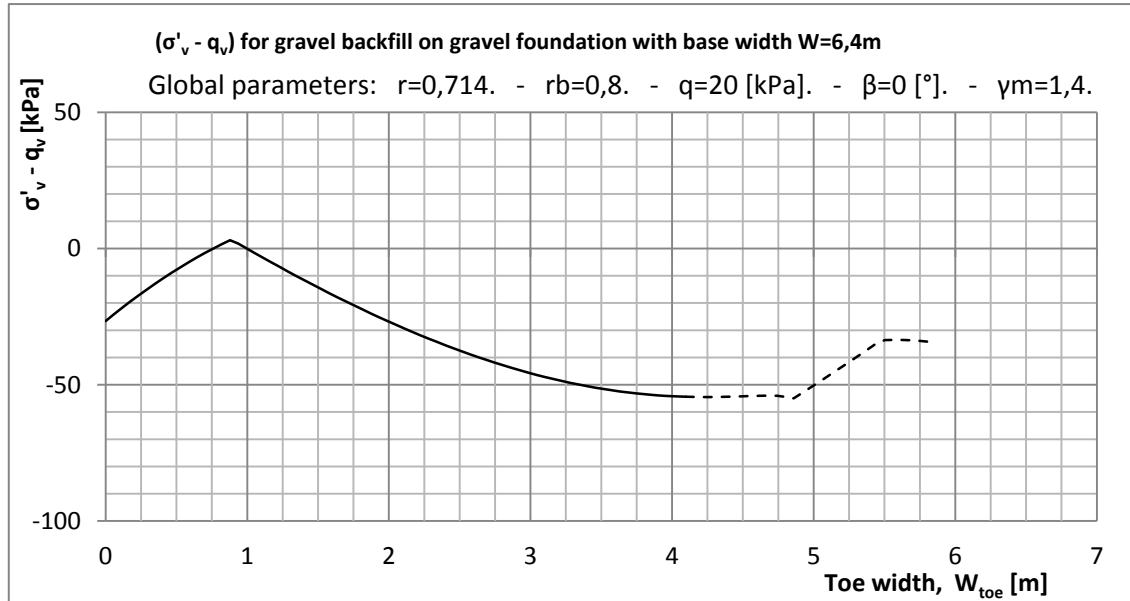
Figure 4.11: Shows the remaining bearing capacity after the first iteration.

Figure 4.11 shows that the remaining bearing capacity is zero at $W_{toe} \approx 0,75m$ but that the peak of the curve has shifted and the remaining bearing capacity is also zero at $W_{toe} \approx 1,0m$. Finding the optimal design is therefore an iterative process. Repeating the calculations several times for this case yields the optimal base width to be $W = 6,3m$ and the optimal toe width to be $W_{toe} = 0,9m$. This result is shown in Figure 4.12.
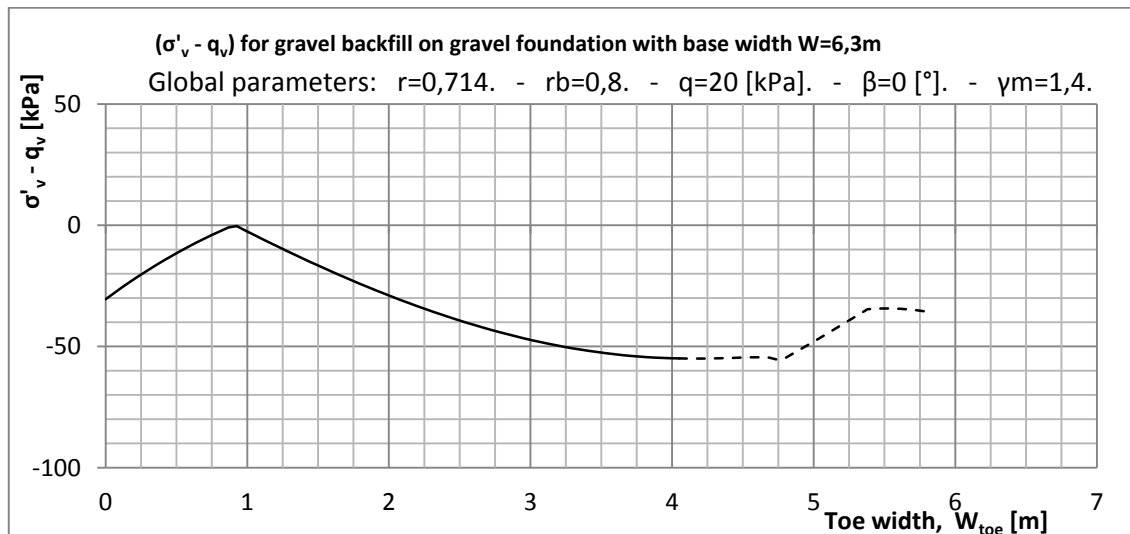
Figure 4.12: Shows the remaining bearing capacity after several iterations.

To evaluate the effect of this design change the results from the last iteration and the values given in Table 4.9 have been listed together, this has been done in Table 4.10.

Table 4.10: Wall heights and widths resulting in $\gamma_M = 1,4$ for varying soil types.

H [m]	W [m]	W_{toe} [m]	E_A [kN]	r_b [-]	R_V [kN]	e [m]	B_0 [m]	qv [kPa]	Foundation material	Backfill material
7,0	6,8	0,0	184,61	0,356	1000,3	-0,28	6,29	159,0	Gravel	Gravel
7,0	6,3	0,9	184,61	0,434	820,6	-0,01	6,26	131,1	Gravel	Gravel

It is clear that by altering the width of the toe the total base width could be reduced by around $\Delta W = 0,5m$ for this case. The vertical load is also reduced by around 20% while the effective footing is about the same size. It is interesting to see that the eccentricity of the vertical force is almost zero for the optimal design, and it makes sense that this would be the case as this maximizes the effective width of the footing. The eccentricity is plotted as a function of toe width along with the remaining bearing capacity in Figure 4.13.
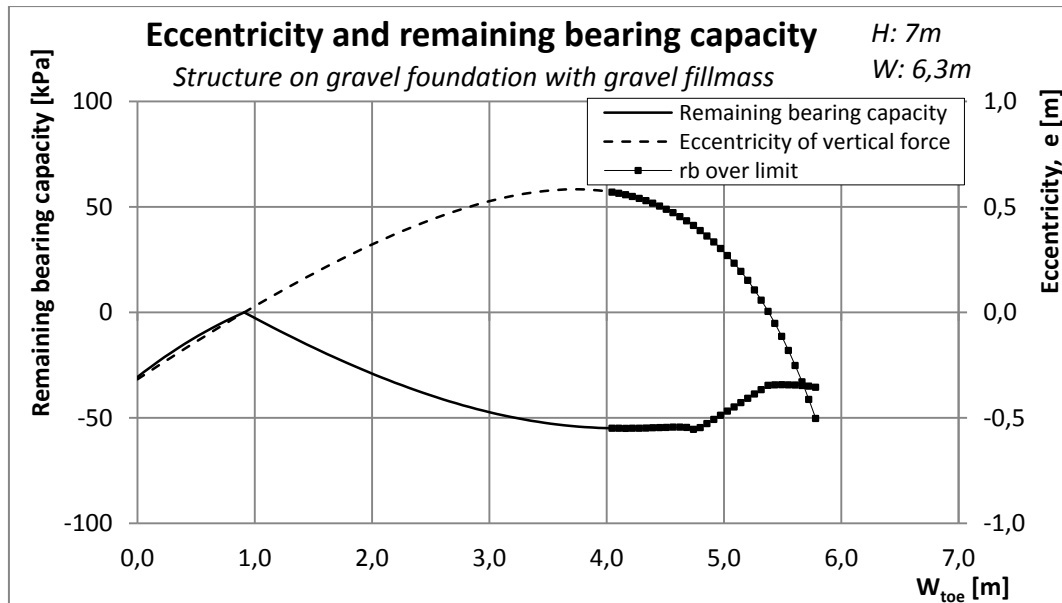
Figure 4.13: Remaining bearing capacity and eccentricity of the vertical force.

Figure 4.13 shows that the eccentricity rises from a negative value for the L shaped wall, meaning an overturning moment, to a positive value as the width of the toe is increased. The optimal toe width is $W_{toe} \approx 0,9m$ and it is at that point that the eccentricity is zero.

All the cases listed in Table 4.9 have been optimized with respect to the toe width by using this iterative process. The result of these calculations can be seen in Table 0.1 in Appendix H. It can be seen in the table that only cases involving a material with high friction angles in either backfill or foundation result in optimal toe-width cases with non-zero values of eccentricity.

Table 0.1 shows that the width of the base plate can be reduced in all cases from Table 4.9 by varying the width of the toe. The development of the eccentricity of the vertical force as a function of varying toe width varying cases of foundation materials and a gravel backfill for $H = 7m$ high structures with optimized foundation widths can be seen in

Figure 0.8 to Figure 0.10. When the backfill is of a blasted rock material the maximum remaining bearing capacity is reached when the eccentricity is near its minimum absolute value, but it never reaches zero.

To illustrate how much can be saved by optimizing the design of the toe of the structure the case of gravel foundation and a backfill of gravel for a $H = 7m$ high structure was again chosen. The optimized base width of $W = 6,3m$ is used as a reference and the toe width is incrementally increased, and for each toe width the base width that results in the same bearing capacity as foundation resulting vertical pressure. This new base width is then divided with the optimized width. The result from these calculations can be seen in Figure 4.14.
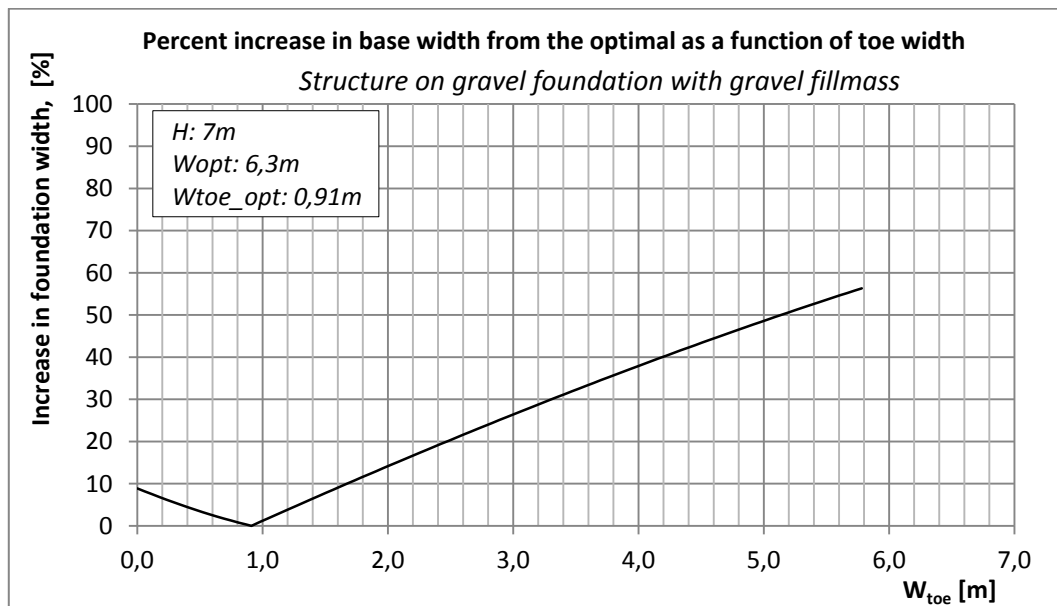
Figure 4.14: Percent increase in foundation width from the optimal.

Figure 4.14 illustrates that the width of the toe has considerable effect on the necessary width of the footing. In this case the L-shaped wall requires foundation widths that are less than 10% over the optimal width. If the toe width is increased far past the optimal width the required base width is greatly increased.

To finalize the discussion of optimal toe widths and its effect on the required base width the base widths of the cases in Table 4.9 are plotted with the optimized cases in Table 0.1 in Figure 4.15 to Figure 4.17.
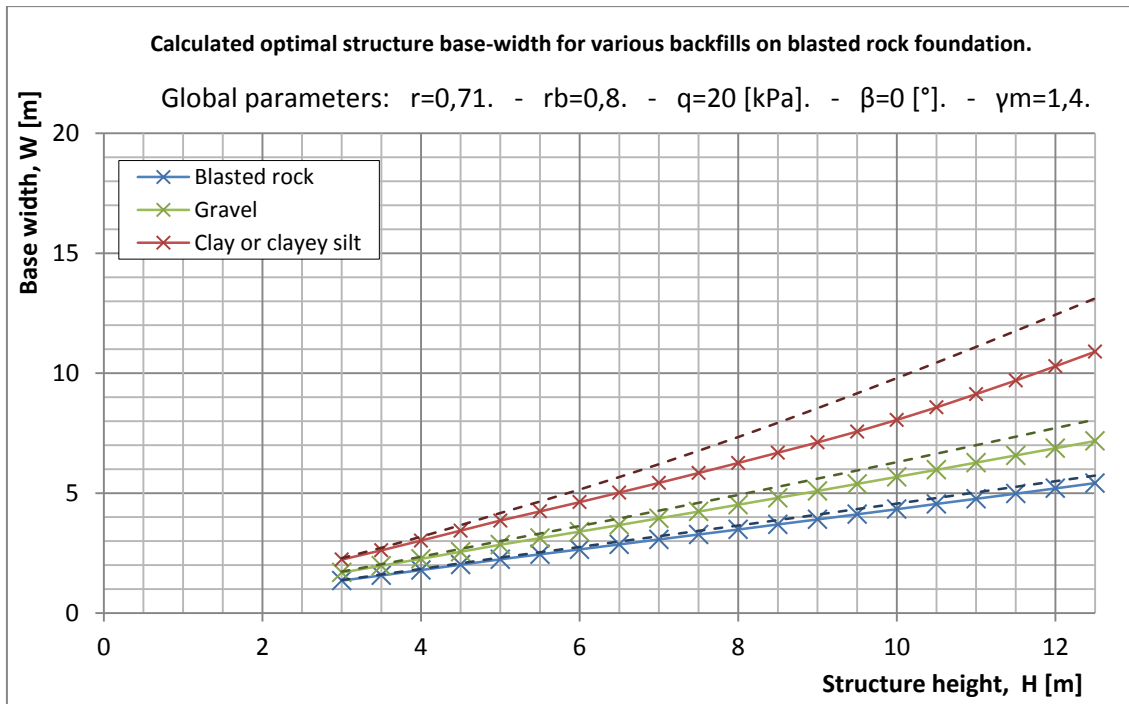
Figure 4.15: Optimized base widths for varying backfill soils, blasted rock foundation.
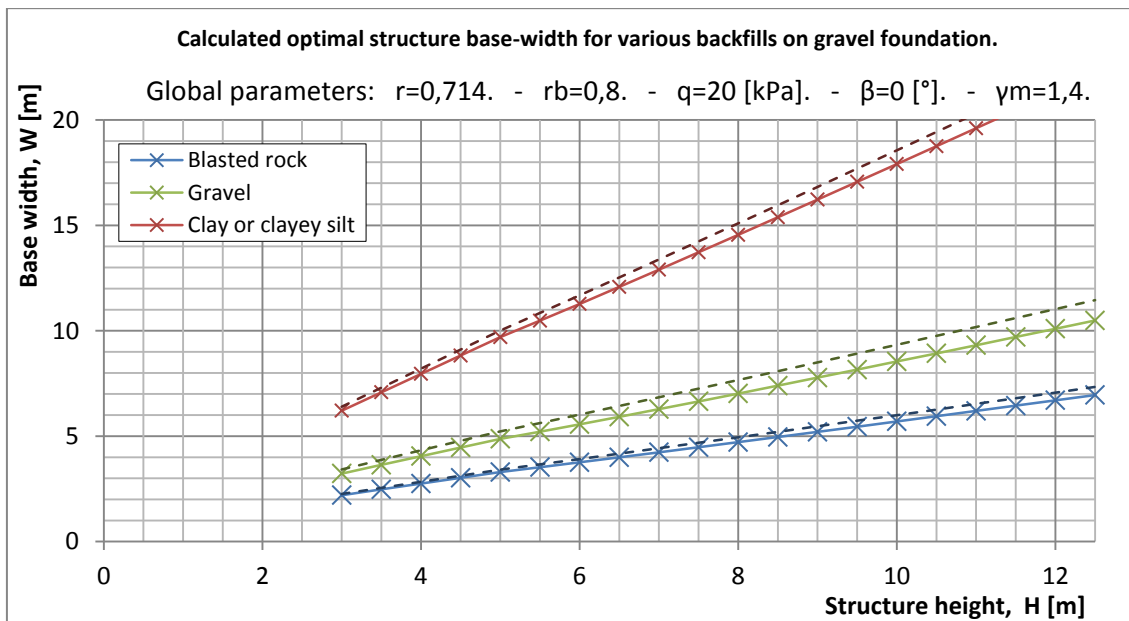
Figure 4.16: Optimized base widths for varying backfill soils, gravel foundation.
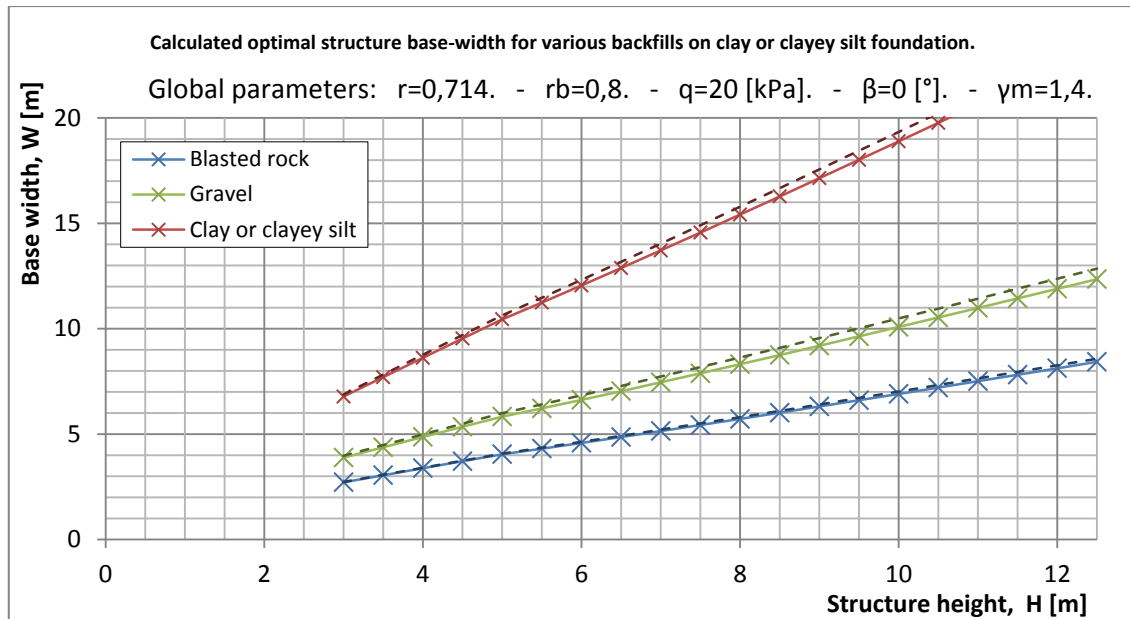
Figure 4.17:Optimized base widths for varying backfill soils, clay or clayey silt foundation.

The lines with crosses in Figure 4.15 to Figure 4.17 represent the base widths of structures with optimized toe widths; the darker-colored and dashed lines represent the base widths derived for each case with L-shaped walls. The figures show that for a backfill mass with average strength properties the required base width can be reduced in all cases. The effect of this optimization gets larger as the structures are higher. The difference is greatest in the case of a foundation of high strength. It worth noting that in the case of a blasted rock backfill the optimized toe width did not reduce the necessary base width substantially in any case.

As the blasted rock foundation material is the only material in this check that is not a frictional soil, investigating the effect of the attraction is an interesting task. In Figure 4.18 the toe width has been optimized for the case of a blasted rock foundation with zero attraction. The curves from Figure 4.8 are also plotted darker colored and dashed for comparison.
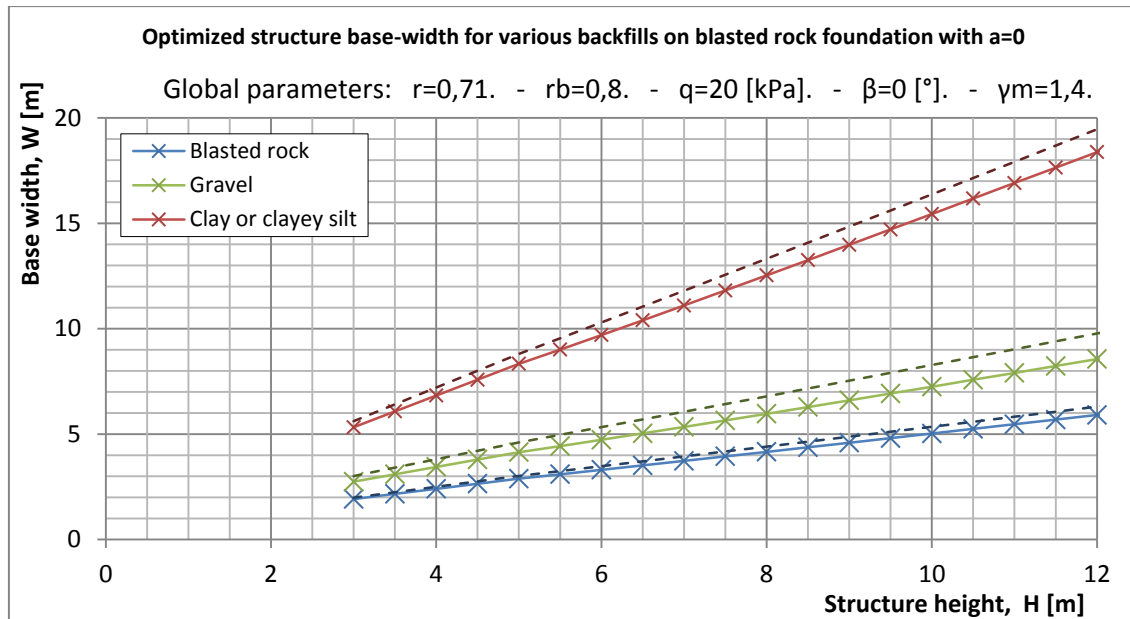
Figure 4.18: Optimized base widths for structures on blasted rock foundation, a=0.

Comparing Figure 4.18 to Figure 4.15 shows that even though the foundation soil has zero attraction it does not have a large impact on the base width that can be saved by varying the width of the toe. The change in strength properties has the biggest effect on the curves representing the case of a clay or clayey silt foundation, and it seems that less can be saved by this optimization when the foundation has zero attraction.

4.2.6 The effect of backfill inclination

One of the results from chapters 3.1 and 3.3.1 is that there seems to be consistency between methods on how to calculate active earth pressures when the backfill is inclined at an angle. The stressfield method and Coulomb's method produce almost exactly the same results and there is a clear correlation to the values proposed by EC7.

To investigate the effect of an inclined backfill on the necessary foundation width the case of a backfill inclination of $\beta = 18°$ is selected. This angle is selected as the equations proposed to calculate the active earth pressures yield values when the angle of the backfill is less or equal to the friction angle. Using a material factor of safety of $\gamma_M = 1,4$ results in a mobilized friction angle of $\rho' = 19,2°$ for clay or clayey silt materials, so all equations should yield an answer. As the figures in EC7 propose that it is the ratio between the friction angle and the terrain angle that should give correlating curves, the soils tested should give a good spread over the most of the range.

As before the necessary foundation width was calculated for the L-shaped structure and then the geometry was optimized by stepwise increasing the width of the toe and decreasing the total width of the base. The results from these calculations can be seen in Figure 4.19 to Figure 4.21.
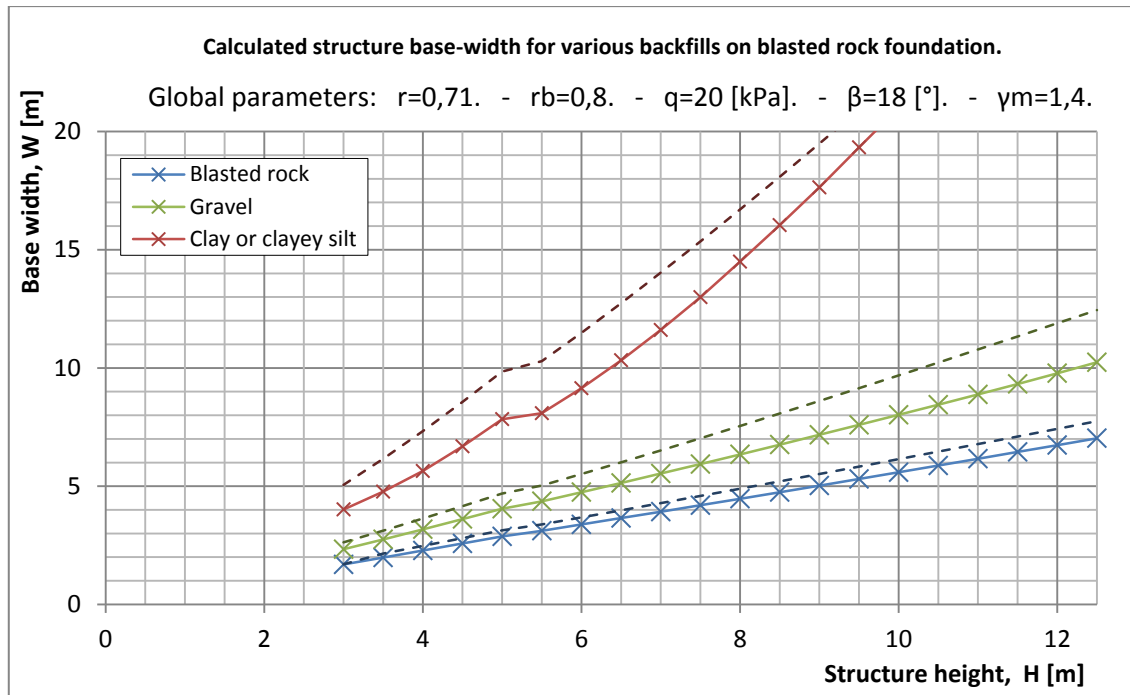
Figure 4.19: Structure base widths for a sloped backfill on blasted rock foundation

In Figure 4.19 it is evident that the depth of application of the surface load has effect on the required base width of the structure. A clear break is now visible between the calculated heights of $H = 5m$ and $H = 5,5m$ in the case of a clay or clayey silt backfill mass. This trend is not as evident in the other two curves. The numerical values for these calculations can be seen with wider intervals in Table 0.2 and Table 0.3 in Appendix H. When designing for a backfill mass of materials of weak to average strength the width of the toe has considerable effect on the required width of the base.
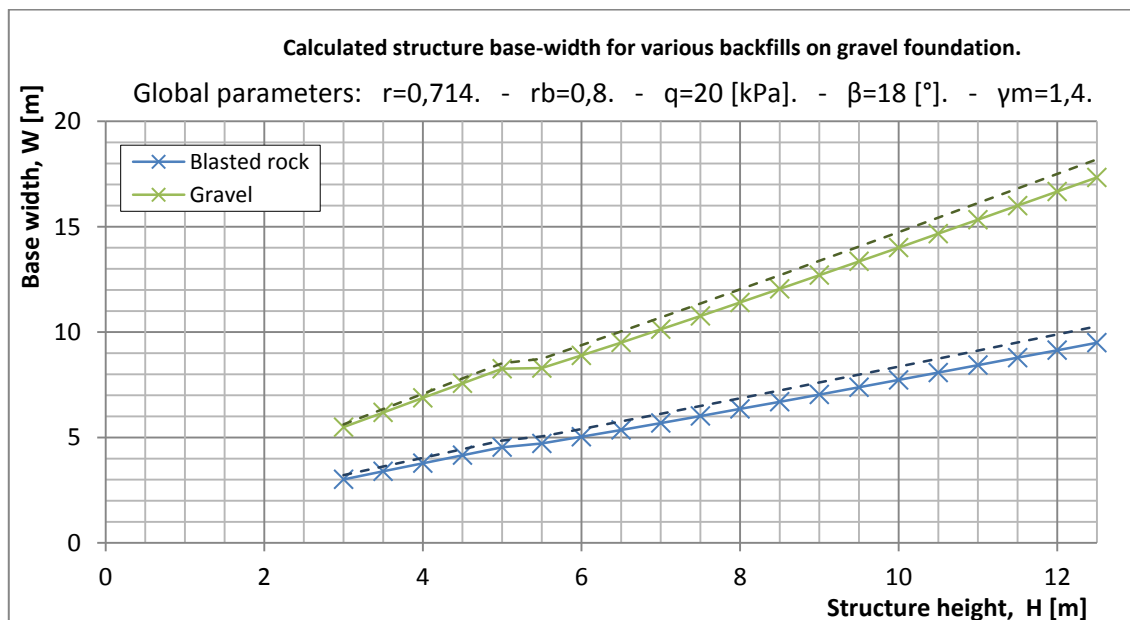
Figure 4.20: Structure base widths for a sloped backfill on gravel foundation.

Figure 4.20 shows that as the foundation strength is decreased the required foundation width is increased. In this case the curve for a gravel backfill material now shows a jump in the required base widths for structure heights less than $H \leq 5m$. The case of clay or

clayey silt backfill yielded much larger required widths of footings and is therefore not in the figure.
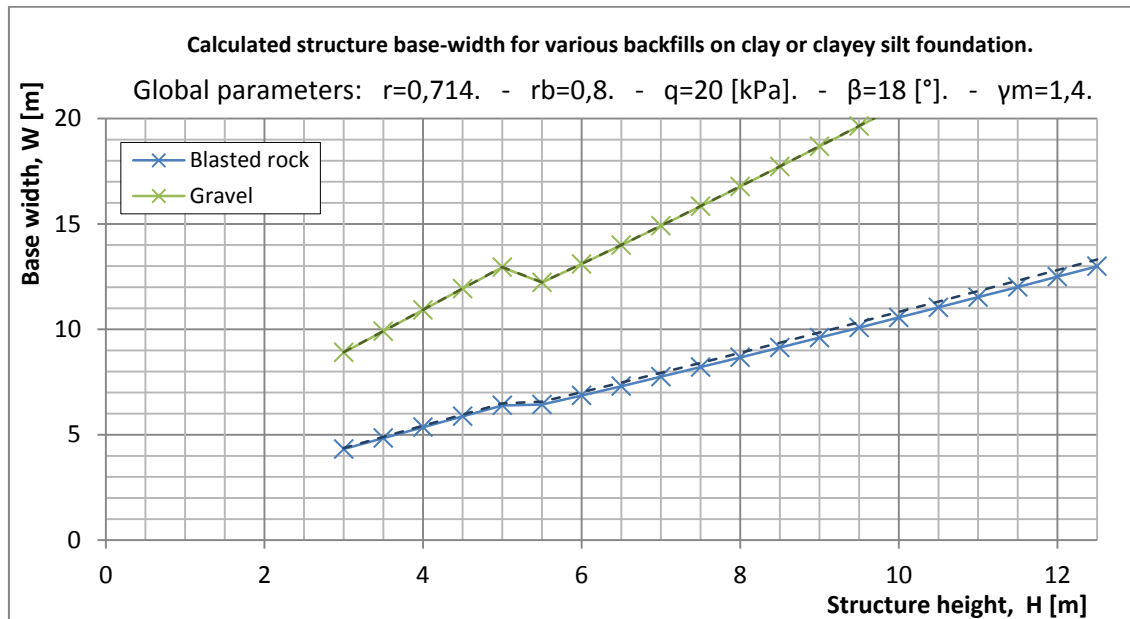
Figure 4.21: Structure base widths for a sloped backfill on clay or clayey silt foundation

As the strength of the foundation material is decreased even further the curves are pushed up the scale representing higher values of required base widths as can be seen in Figure 4.21. The case of clay or clayey silt backfill mass yielded no results in this case. The breakpoint of the application depth of the terrain load is now clearly visible in both the case of the blasted rock and gravel backfill masses. It is also evident that the effect of an optimized toe is in this case small.

5 Analysis of stability using PLAXIS

PLAXIS is a program that applies the principles of the finite element method (FEM) to soil models. The program is available in several packages and the one used in this thesis is the PLAXIS 2D version, which is designed to solve two dimensional plane-strain problems. It was first developed at the technical university of Delft in the Netherlands as a project to evaluate possible movements of the Oosterschelde-dam. Later it was launched as a commercial product and a company with the same name was created to manage its development and marketing (PLAXIS, 2011).

5.1 Finite element method in PLAXIS

The element method works by splitting the geometry up into elements that all have to apply certain mathematical rules regarding stiffness, based on the theory of elasticity. The elements provided by PLAXIS are a 6-node triangle and a 15-node triangle, where in the case of plane-strain each node has two degrees of freedom (d.o.f.). The 15-node triangle should give better results when the system nears global collapse or shows large plastic strains, but using it means solving more equations and therefore uses more calculation power.
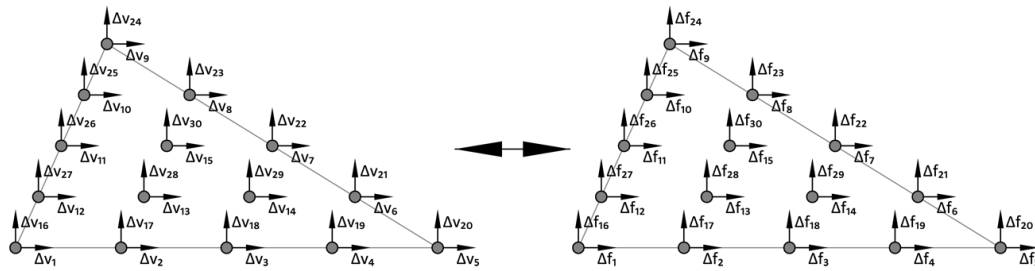
Figure 5.1: The 15-node element as used in PLAXIS with d.o.f.-s and nodal forces.

Using the theory of elasticity the program sets up a set of equations for each element as

$$\begin{bmatrix} k_{1\,1} & \dots & k_{1\,30} \\ \vdots & \ddots & \vdots \\ k_{30\,1} & \dots & k_{30\,30} \end{bmatrix} \cdot \begin{bmatrix} \Delta v_1 \\ \vdots \\ \Delta v_{30} \end{bmatrix} = \begin{bmatrix} \Delta f_1 \\ \vdots \\ \Delta f_{30} \end{bmatrix} \tag{69}$$

where the matrix on the left is called the stiffness matrix, K, Δv_i is a displacement increment of the i-th d.o.f. and Δf_i is the load increment for the i-th d.o.f. Each column of the matrix K represents the force vector required to give the corresponding degree of freedom a unit displacement while keeping the others equal to zero. The nodal displacements of each connected element are linked so that they move together. The stiffness from all elements connected to a node is added to create a global nodal stiffness matrix. The equation then becomes

$$K \cdot \Delta v = \Delta f \tag{70}$$

where the size of the matrix K, and the vectors Δv and Δf is controlled by the type and number of elements in the model. The notation in equation (70) differs for the most elementary case of the finite element method as the response of a soil model is not always linear. To cope with this behavior the program adds the load in increments and calculated

the response before adding the next load increment, this is why equation (70) has terms involving delta, Δ. The stiffness for each element is calculated numerically using the theory of virtual work.

When the system stiffness matrix has been calculated it is possible to add a load increment and calculating the displacement increment. Using the displacement increments both the resulting strain increments and the stress increments are calculated in each element. The stress calculations are done in internal integration points in each element. The stress calculation process is repeated with smaller increments if the calculations show to large unbalanced forces. The incremental displacements and stresses are then finally added to the total deformations and stresses and the process repeated for the next load increment. Detailed description on the inner workings and calculational procedures in PLAXIS can be found in the PLAXIS scientific manual (PLAXIS, 2010).

5.2 Application of PLAXIS to evaluate method proposed by HB016

The method recommended by HB016 to evaluate the stability of retaining structures is derived by using the classical theory of both earth pressures and bearing capacity. These methods were derived by modeling idealized problems and as such provide good results for those problems. To apply the equations directly on retaining structures involves some simplifications. To check if these simplifications provide accurate results some selected cases from the previous chapter will be modeled and analyzed using PLAXIS.

The size of the element mesh in the model has an effect on the results; the theory behind FEM is that with finer meshing the results should converge to the correct ones if the model is properly set up. The downside to this is that the method errors on the unsafe side predicting more stiffness against failure than is theoretically present. All calculations in this thesis are done using a standard mesh setting called "Fine", for at least one case in each soil-combination the mesh size is refined by two size-steps to check if the size of the mesh has a large effect on the results. An averaged sized model with a "fine" mesh size has around 450 elements while a locally refined mesh has around 1000-2000 elements with most of them located around the failure surface. The large gap in the number of elements for the refined case depends entirely of the input geometry of the problem and the automated mesh generator in PLAXIS.

To simulate the cases calculated in the previous chapter the derived limit state design, representing a factor of safety $F_s = \gamma_M = 1,4$, will be modeled. This ac done in 6 steps

1. Build model
2. Apply initial stresses
3. Reset displacements
4. Reduce strength of materials until failure occurs
5. Start from step 3 and add the terrain load to the model
6. Reduce strength of materials until failure occurs

The model is built as with the same base-geometrical restrictions as are introduced in chapter 4.2.2 and the calculated base- and toe widths are listed in Table 0.1 in Appendix H.

5.2.1 Material models

The behavior of materials in the calculations is described with two material models. A perfectly elastic model is chosen to describe the behavior of the structure and the Mohr-Coulomb model is used to describe the behavior of the soil.

The elastic model used to describe the structure clusters does not allow for any plastic behavior. The stiffness is set very high so that only very small deformations are observed compared to those found in the soil clusters. As the goal of this study is to study the material factors of safety that lead to failure in the soil mass based on a specific geometry this approach is considered elegant as it allows for a specific geometry of the structure.

The Mohr-Coulomb model used to describe the behavior of the soil is a linearly elastic – perfectly plastic model. The basic idea behind this type of model is that when the material is in the elastic range all deformations are reversible but once the yield surface is reached the stiffness against extra stress is zero and all extra stress goes into plastic strains that are not reversible. An illustration of this can be seen in Figure 5.2 b). The yield surface is fixed so that it is only defined by input parameters and independent of the stress path leading to failure. An illustrative figure of the MC yield surface in a principal stress space without cohesion can be seen in Figure 5.2 a). The illustration presented in Figure 5.2 a) and b) are borrowed from the PLAXIS material model manual (PLAXIS, 2010).
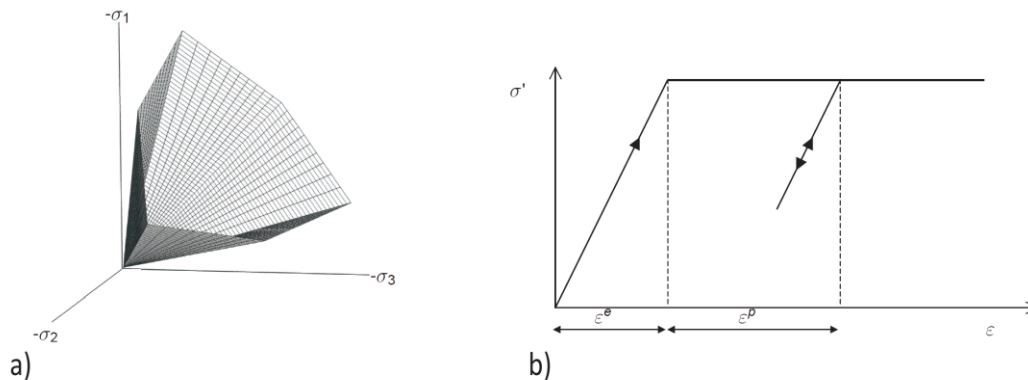
Figure 5.2: shows a) the MC yield surface in 3D b) an illustrative stress-strain curve.

To address the issue of tensile stresses the default setting for the MC material model in PLAXIS is used. By default any tensile stresses in the model result in a tensile cutoff. Another value of the cutoff stress can be chosen but this was not done in this analysis.

For the elastic material only the elastic parameters are used, E and v, along with the unit weight. For the MC material model additional parameters are inserted to describe the plastic behavior. They are the well-known MC parameters; the friction angle, ϕ', and the cohesion, c, as well as the dilatancy angle. The linearity of the MC material model produces obvious simplifications and in many applications it has been shown to produce inaccurate results. As an example it has been shown with laboratory tests that in some soil types the stiffness is dependent of the effective stress level. This behavior is not accounted for in the MC material model. For a simple ultimate strength simulation it has been shown

that a MC model where the strength parameters have been derived for the stress interval encountered in the calculations gives reasonable results (Nordal, 2009). The parameters used in the hand calculations are the same ones as are used in the MC model; this provides a solid ground to base a comparison of the methods. The input parameters used for each soil cluster type can be seen in Table 5.1.

Table 5.1: Material strength and stiffness parameters used in PLAXIS calculations.

Description	Model material name		Strength parameters				Stiffness parameters	
		Unit weight	Friction angle		Attraction a	Cohesion c	E	ν
		[kN/m³]	ϕ' [°]	$\tan(\phi')$ [-]	[kPa]	[kPa]	[kPa]	[-]
Backfill soils	B-Blasted rock	19	42	0,90	0	0	$2 \cdot 10^4$	0,25
	B-Gravel	19	35	0,70	0	0	$2 \cdot 10^4$	0,25
	B-Clay_clayey silt	20	26	0,49	0	0	$5 \cdot 10^3$	0,30
Foundation soils	F-Blasted rock	19	42	0,90	10	9	$2 \cdot 10^4$	0,25
	F-Loose gravel	18	36	0,73	0	0	$2 \cdot 10^4$	0,25
	F-Clay_clayey silt	19	26	0,49	0	0	$5 \cdot 10^3$	0,30
Structure	S-Concrete	24	-	-	-	-	$2 \cdot 10^7$	0,25

The strength of the soil is reduced in calculations steps 4 and 6 so the initial strength parameters of each soil type are inserted into the program with the material factor of safety $\gamma_M = 1$. The stiffness parameters used are selected generally for each soil type; they do influence the factor of safety but to a much less extent than the strength parameters. The dilatancy angle is set to $\psi = 0°$ in all calculations, this is has been found to be conservative (Nordal, 2009).

5.2.2 The *"Phi/c reduction"* method in PLAXIS

After initial stresses have been calculated and displacements reset in calculation phases 2 and 3 the material strength is reduced until failure. This is done in two phases; with and without the surface load.

The initial value of the material strength is registered and when failure has occurred in the soil mass the material factor of safety is calculated as is shown with equation (7) in the case of a drained material and as is shown with equation (4) in the undrained case. It is left to the user to decide when failure has fully developed by requiring that a point be selected in the soil mass. The displacement of this point can then be plotted against the calculated material factor of safety of each calculation step. When each calculation step produces large point displacements a plateau forms and the material factor of safety can be estimated. This has been done for the case of a sand backfill on a gravel foundation in Figure 5.4. The estimated average values are displayed on the right side of the figure. This kind of analysis is carried out on all PLAXIS models and the resulting safety factor-curves can be seen for each case in Appendix J.

5.2.3 Modeling and documenting failures in soil masses

As the material strength is reduced until failure occurs in the model it is important that the model be set up in such a way that the boundaries do not affect the development of the failure mechanism. This is done by using a large model, allowing for failure in the soil mass on both sides of the structure. In the case of a horizontal backfill the model size is $H \cdot W = 35m \cdot 50m$. The bottom front corner of all structures is placed at the point $(x_1, y_1) = (10,10)$. The rest of the geometry is then defined as previously described. In the cases involving an inclined backfill the simulated failure mechanisms stretched further into the backfill than in the horizontal cases; as a result the model size has been increased in these cases.

Once the model is built and materials have been assigned the initial stress state is modeled by incrementally building up the effect of gravity. PLAXIS offers a choice between this method and a simple K_0 method. In some of the cases the terrain will be sloped at an angle so the gravity method is better suited to simulate real in situ stresses. For the sake of consistency this method is used on all cases.

The model is activated using a staged construction step. This means that the whole structure and backfill is put into place simultaneously, but with no internal stresses other than hydrostatic water pressures in the foundation.

Adding the effect of gravity adds stresses to the model. The material model reacts to added stress with volume change. In reality the structure would be built to the specifications in a constant gravity field so the displacements from gravity loading are set to zero after the phase is complete.

Reducing the strength of the materials will then both reduce the bearing capacity of the foundation and add to the earth pressures from the backfill. As the stress state in the model is calculated it is possible to calculate the strength mobilization that leads to failure as well as illustrate how the most critical shear surface will develop.

Table 0.1 lists 36 geometrical cases that will be modeled, Figure 5.3 shows the geometry in as it is set up for case 1 in PLAXIS along with the "Fine" element mesh used in the calculations.
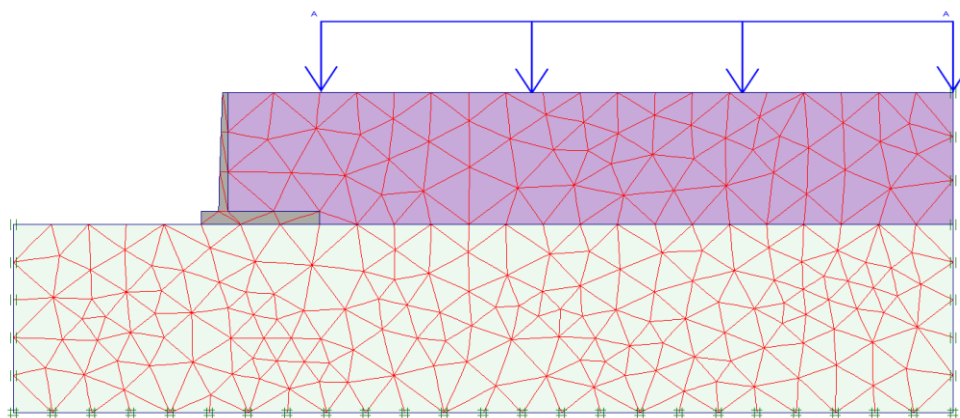
Figure 5.3: Shows the PLAXIS model of case 35; gravel backfill and foundation.

Figure 5.3 shows the setup used in the calculations of case 35. The backfill mass is modeled with the material "*B-Gravel*", the foundation is "*F-Loose gravel*" and the structure is of the elastic material "*S-Concrete*"; as defined in Table 5.1. The terrain load is set to the value of $q = 20kPa$. The boundary conditions in the model are that the bottom boundary is constrained in both the horizontal and vertical direction but the vertical boundaries are only constrained in the horizontal direction.

The bearing capacity equation, equation (48), uses effective parameters for the weight of the soil. The equation provides no factor to implement partially submerged foundation so there is a choice to calculate the foundation as submerged to terrain elevation or to omit the effect of water from the equation. In northern countries the groundwater is usually relatively close to the terrain, therefore the foundation is assumed to be fully saturated in all hand calculations and all PLAXIS models.

To measure if failure is reached in the model an internal point is picked in the expected failure wedge near terrain level behind the structure. The strength reduction is run until the model factor of safety forms a plateau when plotted against the point displacement. This is shown for the case 35 with and without the surface load in Figure 5.4.
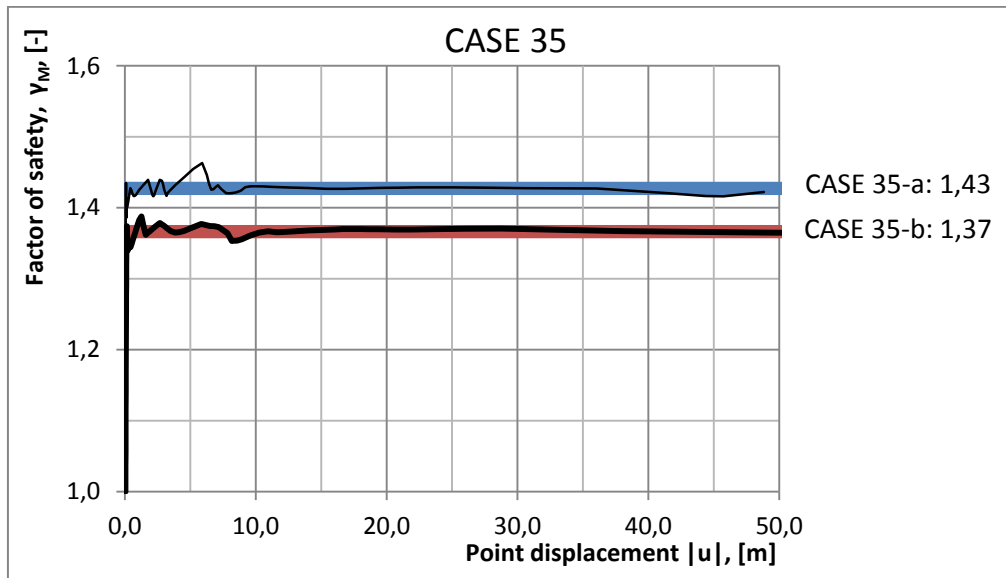
Figure 5.4: Shows the factor of safety plotted against the point displacement.

Figure 5.4 shows that the factor of safety reaches a state of equilibrium just above $\gamma_M = 1,4$ for the case without the surface and just below $\gamma_M = 1,4$ when the surface load is included. As a result of this strength reduction large point displacements are observed in the failure mass. The numerical value of the displacements is after failure only a function of how many calculation steps are run and therefore not of importance in this case.

After the strength of the model has been reduced until failure occurs in the soil body the failure mechanism can be inspected in several ways. Plotting the displacement is one way of inspecting failure as it shows how the body has moved as the soil collapsed. This is done in Figure 5.5 for case 35-b (with surface load), both with a deformed mesh and a shaded plot of the total incremental displacements.
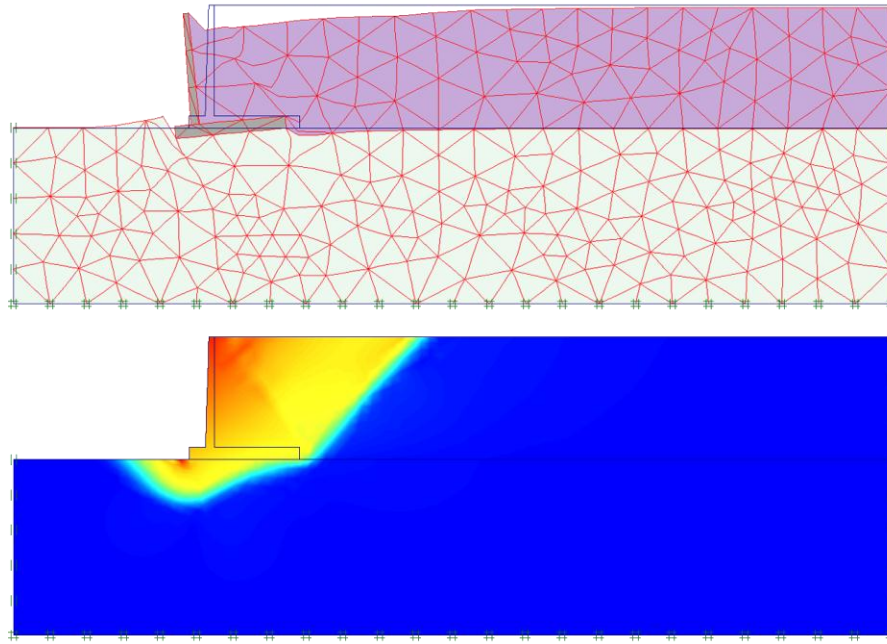
Figure 5.5: Shows the deformed mesh and total incremental displacements of case 35.

It is clear from Figure 5.5 that the shaded plot of the total incremental displacements provides a better visual description of the failure mode but it can only be assumed to provide a visualization of the boundary of the failure mechanism, the internal failures within the failure wedge are not portrayed.

Finer mesh size improves our chances of viewing the failure surfaces but fines mesh also means longer calculation times. Figure 5.6 shows the deformed mesh of case 35-b where the mesh has been locally refined two steps above the maximum provided general setting of "very fine" in PLAXIS.
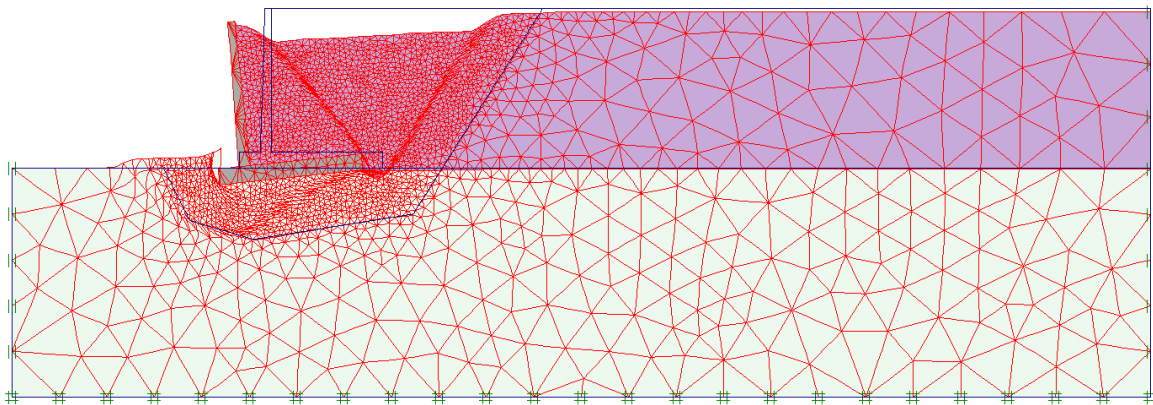
Figure 5.6: Shows the deformed mesh of case 35(refined) after failure in soil mass.

The calculation time to produce the deformed mesh seen in Figure 5.6 was well over an hour while the calculation time of the case shown in Figure 5.5 took 21 seconds. A finer mesh will decrease the discretization error of in the problem but if the goal is only to better visualize the failure mechanism it is not a very effective solution.

As failure has occurred in the model the stiffness against extra loading is zero and all added stress is transferred into strains in the planes of failure. By plotting the strain

82

increments calculated from the last loading step it is possible to better visualize where in the soil mass failure takes place. This is called an incremental strain plot and is shown for the case above in Figure 5.7.
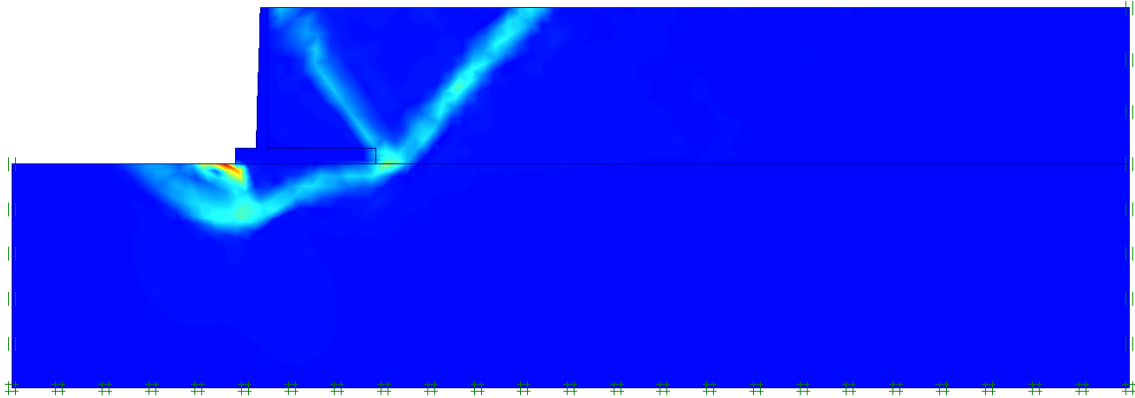
Figure 5.7: Shows the incremental strains of case 35 after failure in soil mass.

Figure 5.7 shows where the movement occurs in the model as a result of the last load step. The numerical value of the strain increments is not important as this is done after failure has occurred and large strains follow each load increment.

Inspecting Figure 5.7 it is evident that some of the assumptions made in the hand calculations are not accurate. As an example the soil above the heel of the structure does not behave as a part of the structure itself. Two distinct failure planes develop behind the structure forming a wedge that slides down as the structure moves out. The planes intersect at the base of the heel; no curved failure surface is observed in the active failure zone.

Large strains are formed at the base of the toe as it is there that the structure both sinks into the foundation and the foundation slides up and out from under it.

PLAXIS evaluates stresses in the elements with numerical integration of internal stress points and the 15-noded element used in these calculations has 12 of them. A plastic point plot shows what stress points have reached the MC-failure curve. This plot is shown for the case above in Figure 5.8.
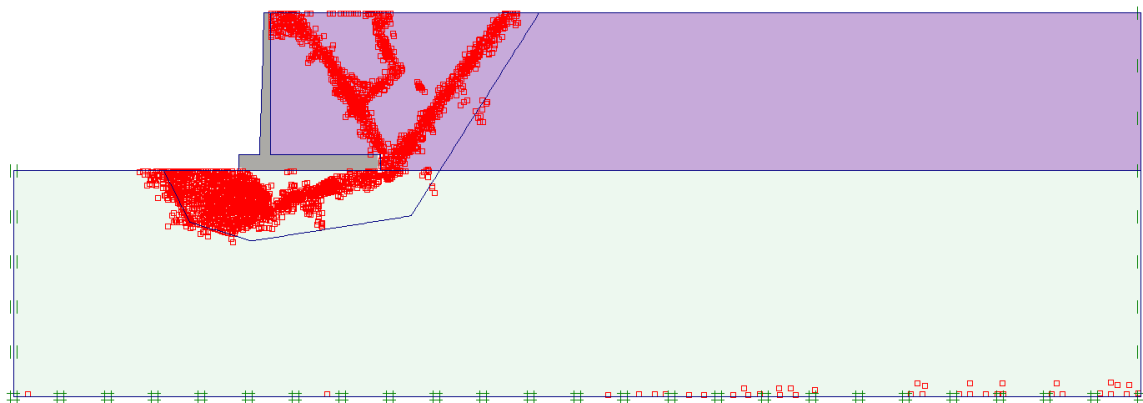
Figure 5.8: Shows the plastic points of case 35(with mesh refinement) after failure.

Figure 5.8 shows the same failure outline that is shown in Figure 5.7. The main result that can be read from the figure is that the plastic points connected to the failure are well contained to in the model and most of them fall within the refined mesh grid. It can be seen that a secondary failure mechanism has started to form from the boundary of the surface load but it does not show up on Figure 5.7. Although this plot does not show the boundary of the failure mechanism as clearly as the incremental strain plot it is extremely useful as it shows very clearly if the boundaries of the model are linked to the failure mechanism and thereby influence the result. This model seems to be set up in an adequate way.

Most of the cases designed with hand calculations for the case of a horizontal backfill were also designed for the case of an inclined backfill of $\beta = 18°$. A few cases did not yield a result and others resulted in base plates that where ten times the structures height, those cases are omitted in the PLAXIS analysis. The geometry differs from the cases of horizontal backfills but the calculation methods used are exactly the same. The incremental strains for case *35-β* with an inclined backfill after failure has occurred can be seen in Figure 5.9.
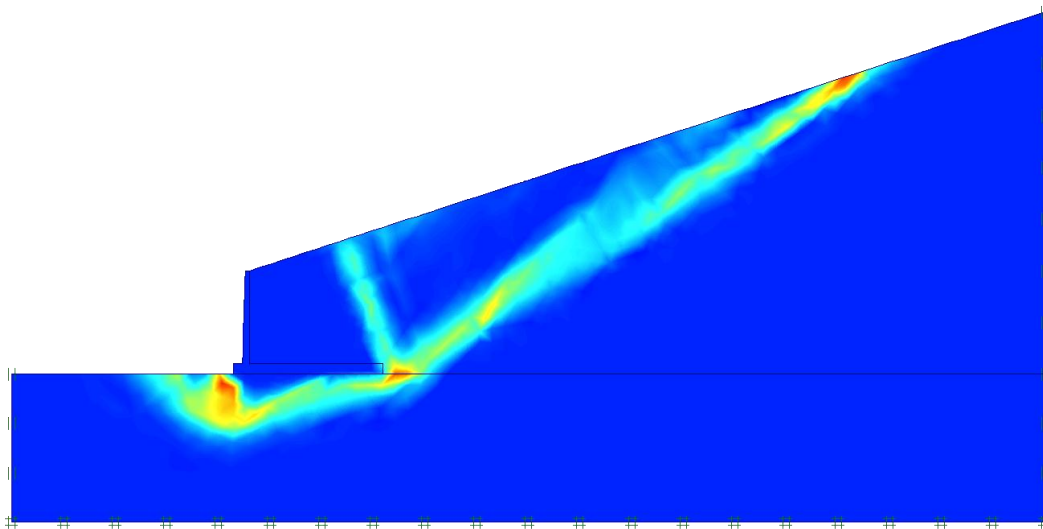
Figure 5.9: Shows the incremental strains of case 35β after failure in soil mass.

The failure surface in the active stressfield has the form of a plane, just as in the case of a horizontal backfill. The main difference in the failure mechanism is that the inclinations of the failure planes are different to those seen in Figure 5.7.

The failure surfaces in the foundation have a similar form as was seen in Figure 5.7. Both are consistent with the form that the theory assumes for failure involving a shear stress on the surface; a rotated cut-Rankine zone under the foundation with a planar failure surface, Prandtl zone with a curved shear surface and another Rankine zone with a failure plane to the surface.

5.3 Results from PLAXIS simulations

Each case in Table 0.1 and most of the cases in Table 0.3 were simulated using PLAXIS; a total of 64 cases with different wall geometries. The failure modes of each simulated case can be seen in Appendix I and the development of the material factor of safety leading to the failure can be seen for each case in Appendix J. If models with refined mesh are counted seperately then results from 86 PLAXIS models are presented in this paper; additional 12 models were built for various checks but are not presented here, bringing the total number of separate PLAXIS models to 98.

Using the methods presented in HB016 each case in Table 0.1 is designed so that the model has a material factor of safety (MFS) equal to $\gamma_M = 1,4$. Then the surface load was removed from those designs and the factor of safety calculated again using my own version of the *"Phi/c reduction"* method. This was done for the height interval of $\Delta H = 0,5m$ from $H = 3m$ to $H = 12,5m$.

With this approach it is possible to compare the safety factors derived with hand calculations to those derived by PLAXIS simulations. The results are divided into subchapters by foundation material varying from the strongest to the weakest. For each case of foundation material the backfill material is varied from the strongest to the weakest.

5.3.1 Blasted rock foundation – horizontal terrain

The results from hand calculations and PLAXIS simulations for the case of a blasted rock foundation can be seen in Figure 5.10 to Figure 5.12.
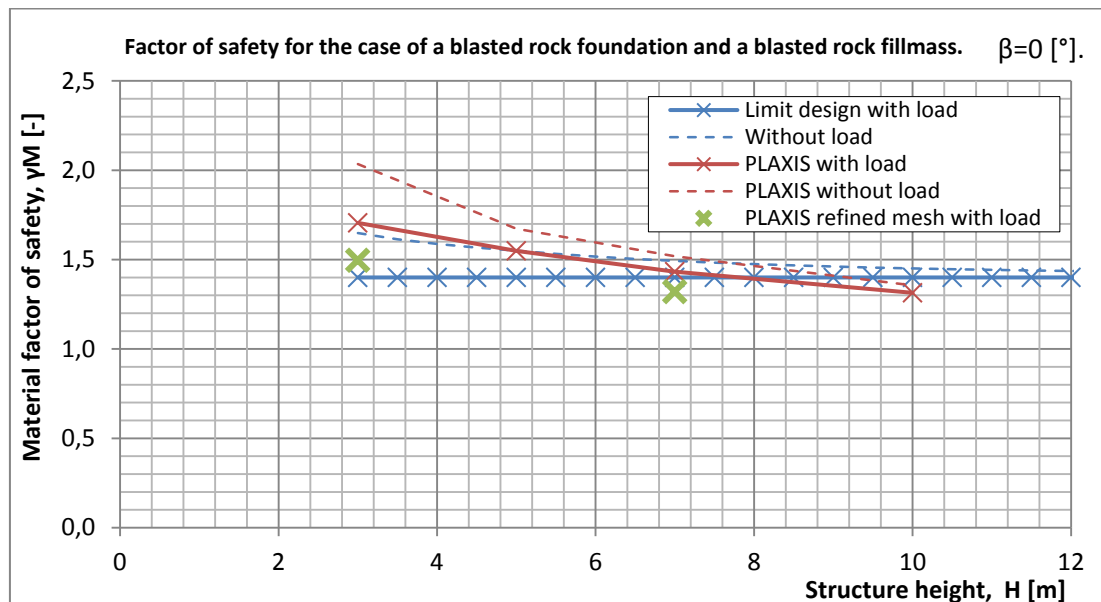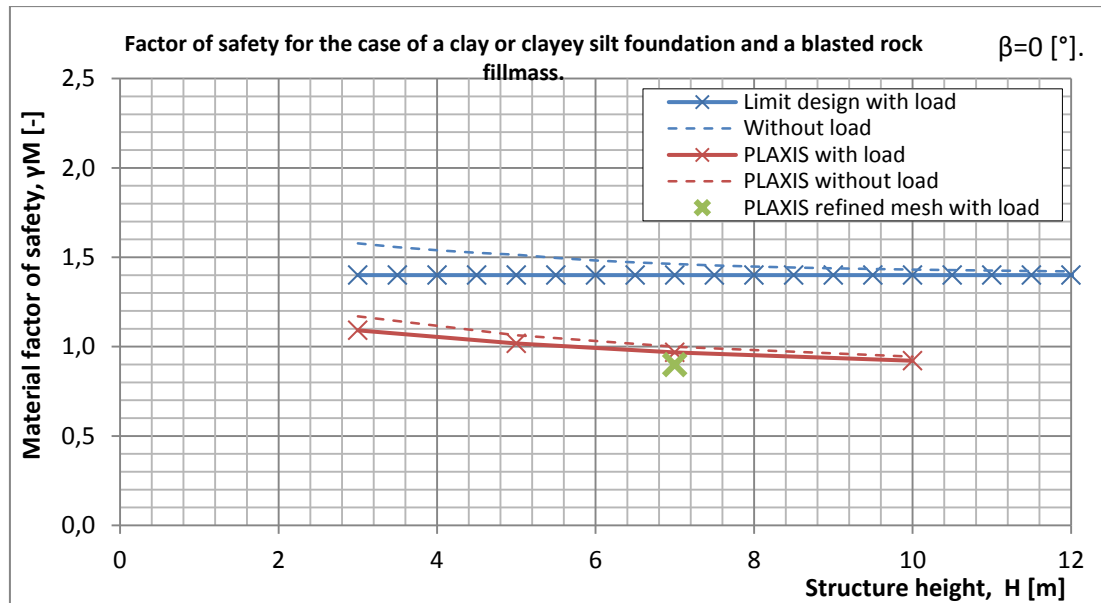

*Figure 5.10: Cases with blasted rock foundation and blasted rock backfill.*
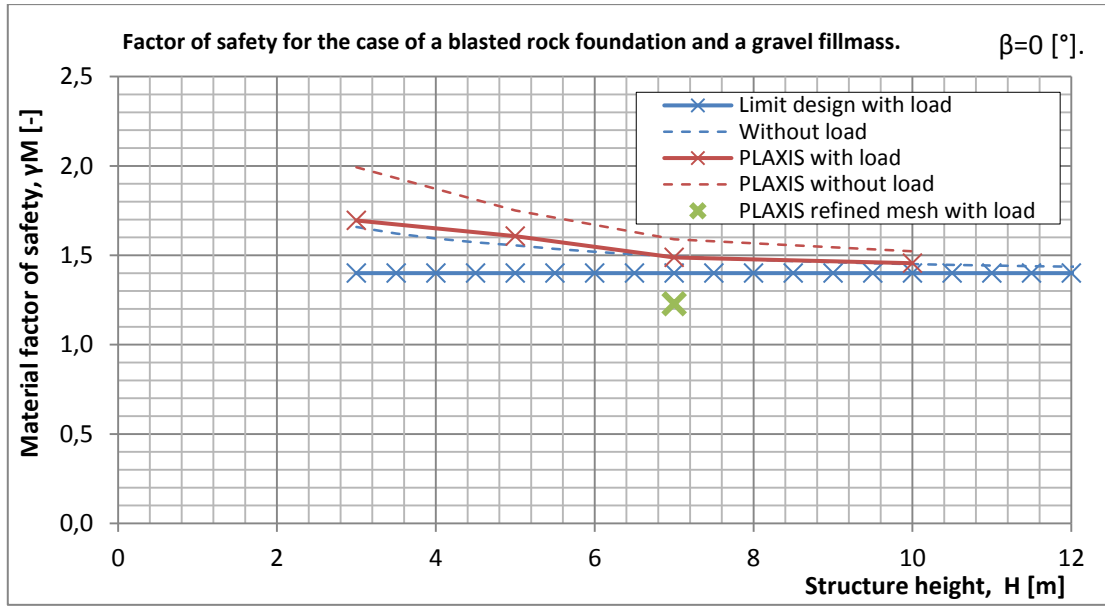
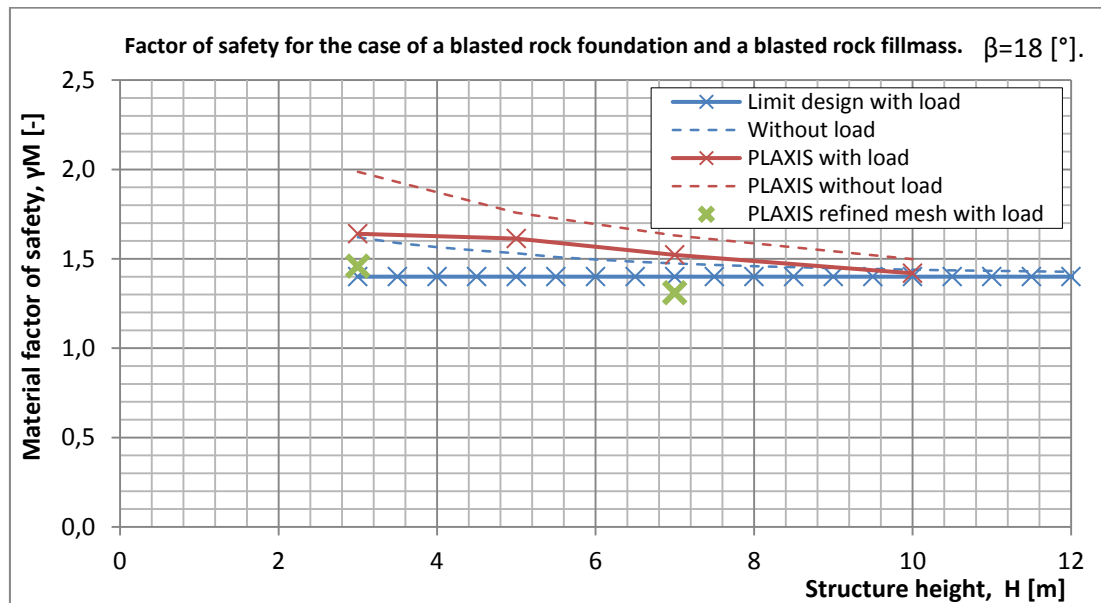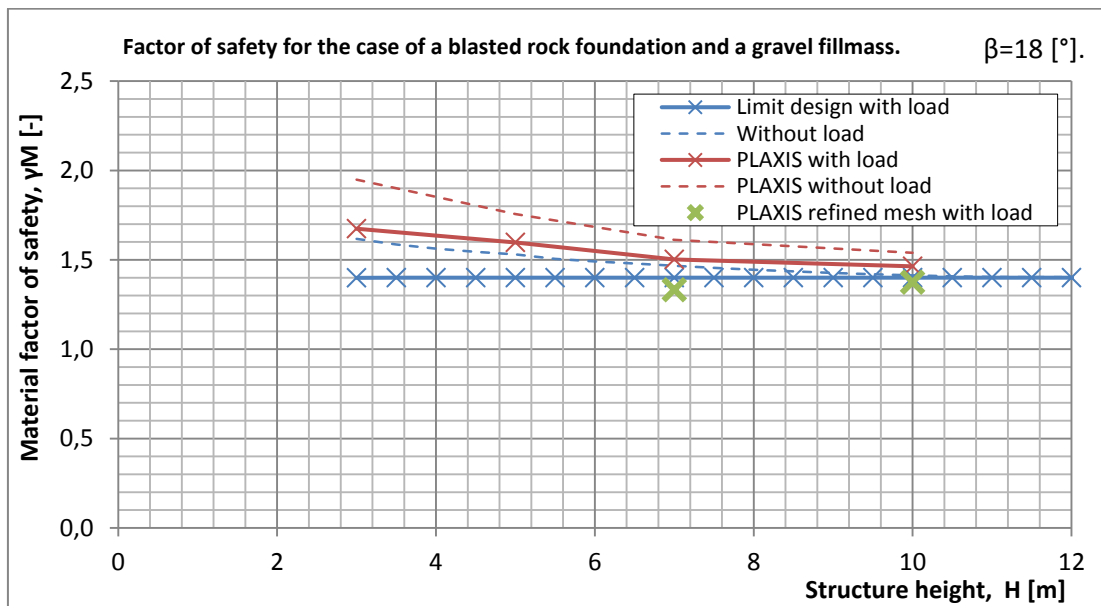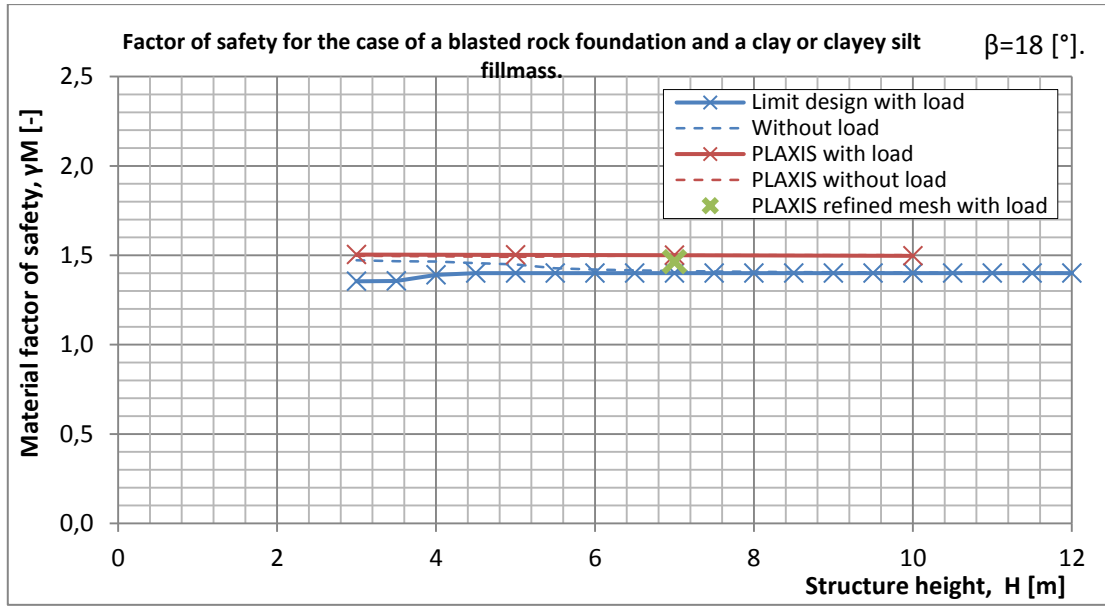*Figure 5.11: Cases with blasted rock foundation and gravel backfill.*
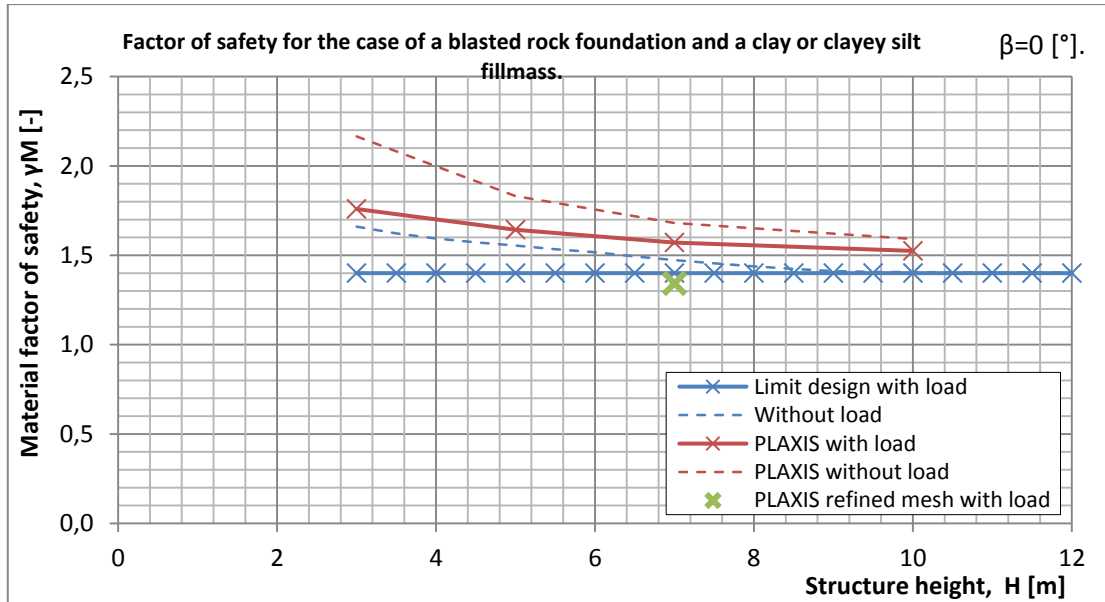
Figure 5.12: Cases with blasted rock foundation and clay or clayey silt foundation.

The red curves in Figure 5.10 to Figure 5.12 show the results from the PLAXIS analysis while the blue curves show the hand calculated values. Generally the blue curve with markings will have a constant MFS of $\gamma_M = 1,4$ as it is the limit design with this material factor of safety according to HB016. In a few cases where the terrain is inclined at an angle the roughness criteria caused the design to have a slightly lower MFS.

The green marks show the results from PLAXIS simulations where the number of elements has been significantly increased around the expected failure surface. The difference between the results derived with coarser mesh and refined mesh is around 5-20% depending on the case and the refined mesh always produced lower factors of safety. Further refinements produced slightly less but similar results. Due to exponential growth in calculation time this was only tested on very few cases.

I assume that the red curve provides an accurate description of the changes in factor of safety between cases and for the sake of comparison I assume that the green points represent accurate values although they have been found to be slightly high. The combined assumption is then that if the red curve is shifted so that it passes through the green point, we get an accurate description of what would happen if all cases were calculated using a very fine mesh.

Bearing this in mind it can be interpreted from Figure 5.10 to Figure 5.12 that the factor of safety of the designs is generally slightly lower according to the PLAXIS simulations than it is according to HB016. Variation of the backfill material does in this case not seem to have a large influence on the result. The red curves clearly indicate that the factor of safety in the HB016 designs decreases as the structures are higher. It can therefore be stated that the factors of safety according to HB016 are in agreement with the ones calculated with PLAXIS simulations for lower structures in the case of a blasted rock material in the foundation.

The difference between values from the simulations with and without the surface load is in some agreement with the difference found with my method. They both show large difference for low structures that decreases as the structures get higher. This is due to the fact that the surface load, q, is proportionally much larger for smaller structures and therefore influences the active pressure field to a much greater extent.

5.3.2 Gravel foundation − horizontal terrain

The results from hand calculations and PLAXIS simulations for the case of a gravel foundation can be seen in Figure 5.13 to Figure 5.15.
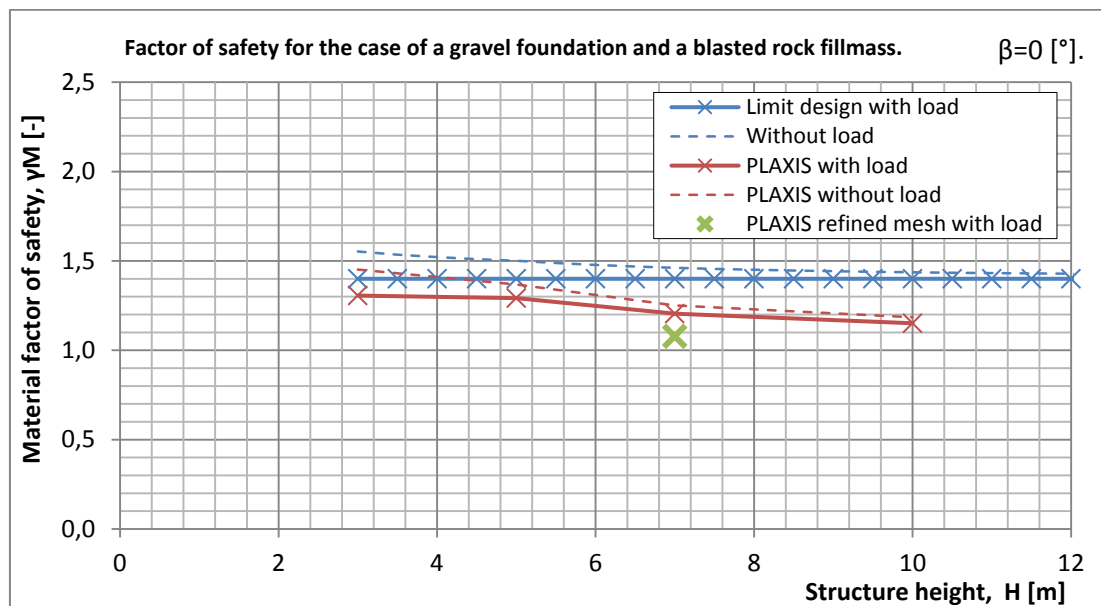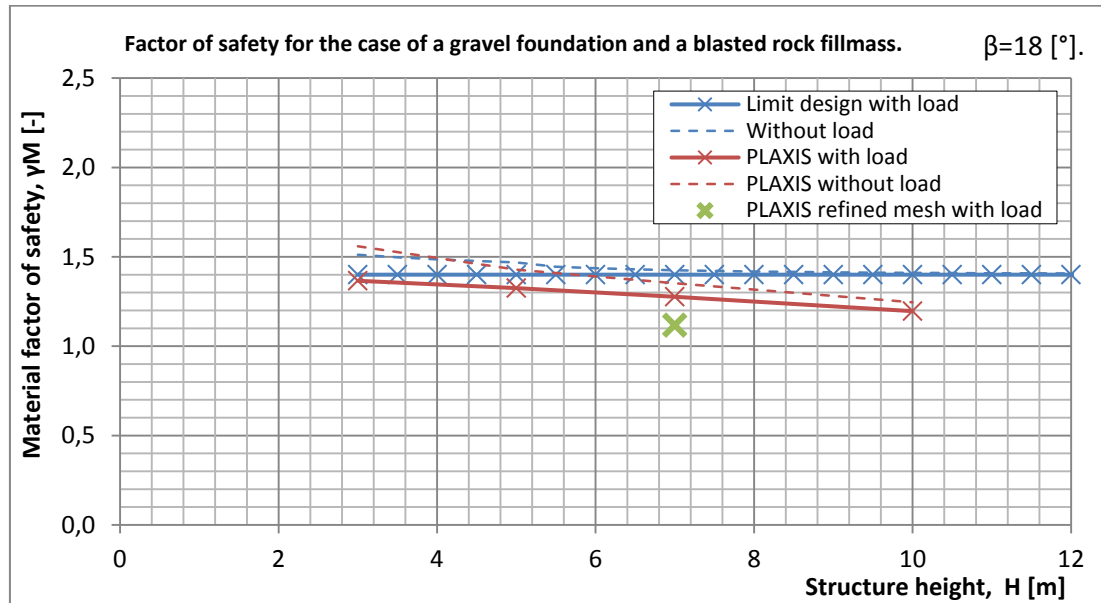

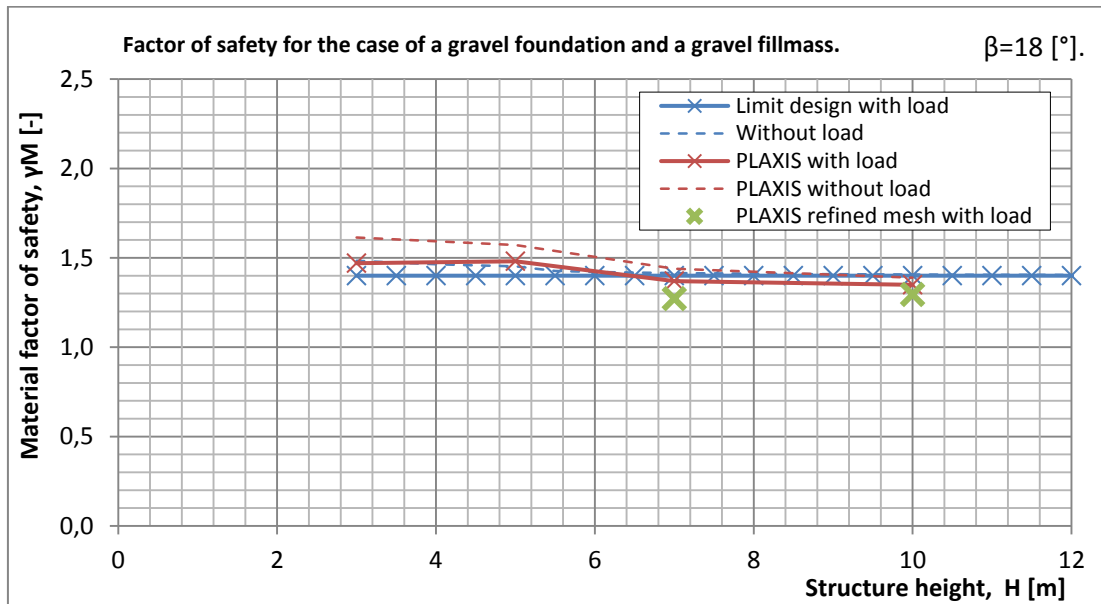*Figure 5.13: Cases with gravel foundation and blasted rock backfill.*
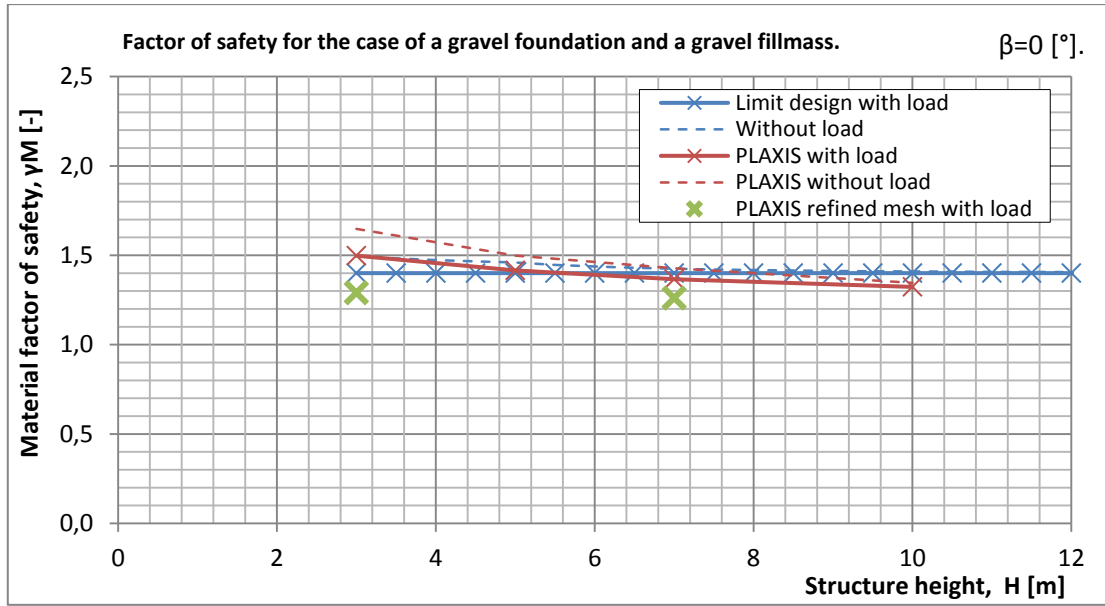
Figure 5.14: Cases with gravel foundation and gravel backfill.
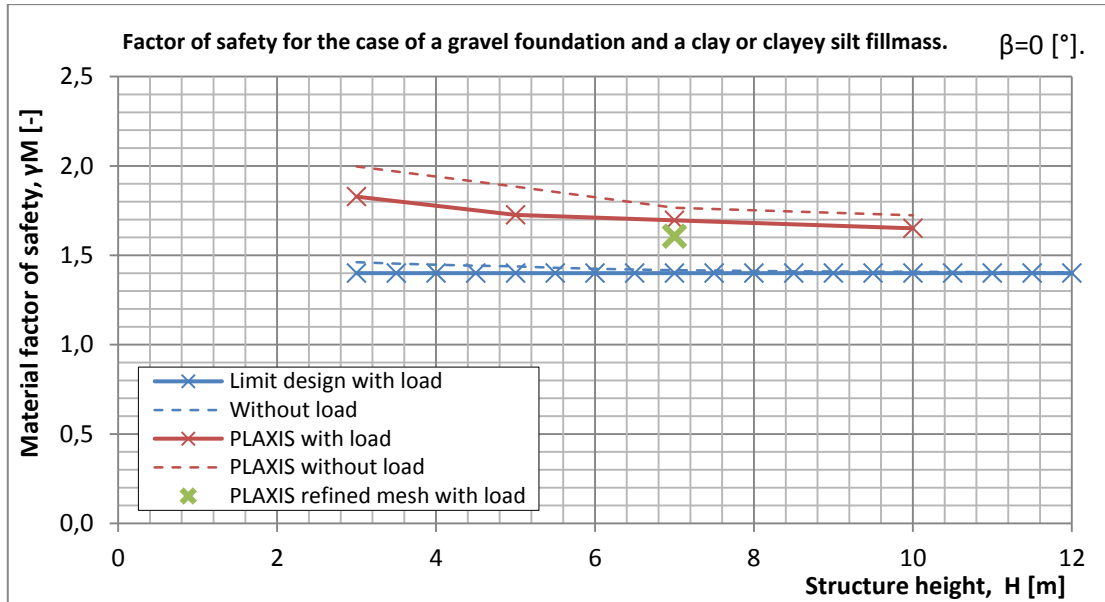
Figure 5.15: Cases with gravel foundation and clay or clayey silt backfill.

Interpreting the results shown in Figure 5.13 to Figure 5.15 with the same assumptions as before reveals that in the case of a gravel foundation material HB016 grossly overestimates the MFS of the designs for the case of a blasted rock backfill material. If the red curve with markings is shifted to the green point it is clear that a $H = 10m$ high structure has a factor of safety of around $\gamma_M = 1,0$; in other words on the verge of failure. It would seem that in this case the method presented in HB016 does not require a wide enough foundation in this case.

As the strength of the backfill is decreased the red curves are shifted up the scale. Two refinement models were calculated in the case of a gravel backfill. It can be seen in Figure 5.14 that they mark a slightly less inclined curve than was calculated using a coarser mesh and are slightly lower than the limit design line. The results can be considered to agree with design proposed by HB016 in this case.

It can be interpreted from Figure 5.15 that according to the PLAXIS simulations HB016 proposes a design that overshoots the desired MFS in the case of a clay or clayey silt backfill material.

5.3.3 Clay or clayey silt foundation – horizontal terrain

The results from hand calculations and PLAXIS simulations for the case of a clay or clayey silt foundation can be seen in Figure 5.16 to Figure 5.18.
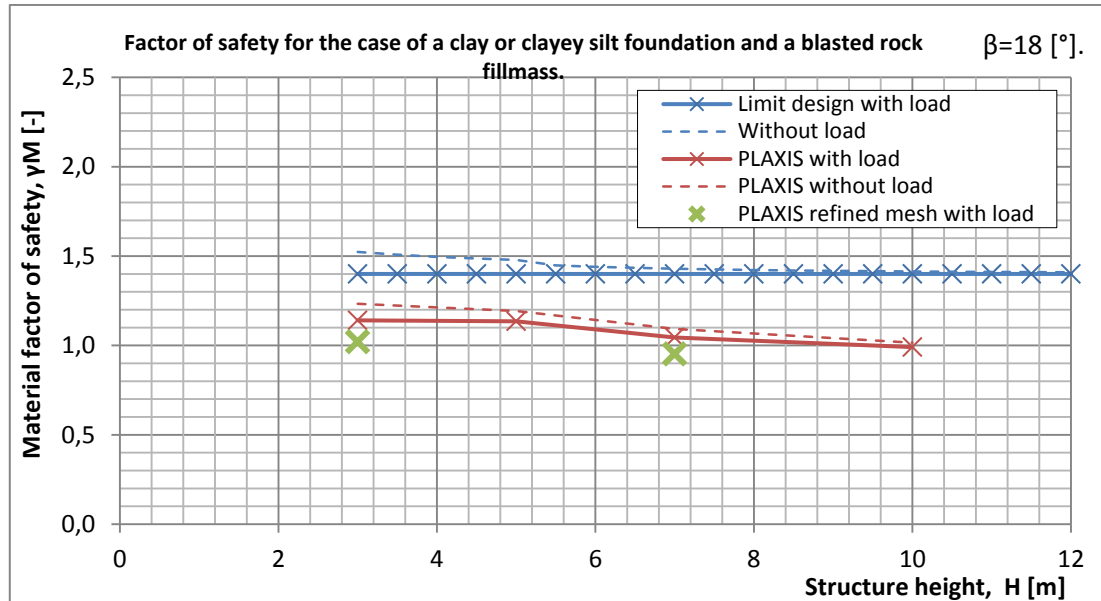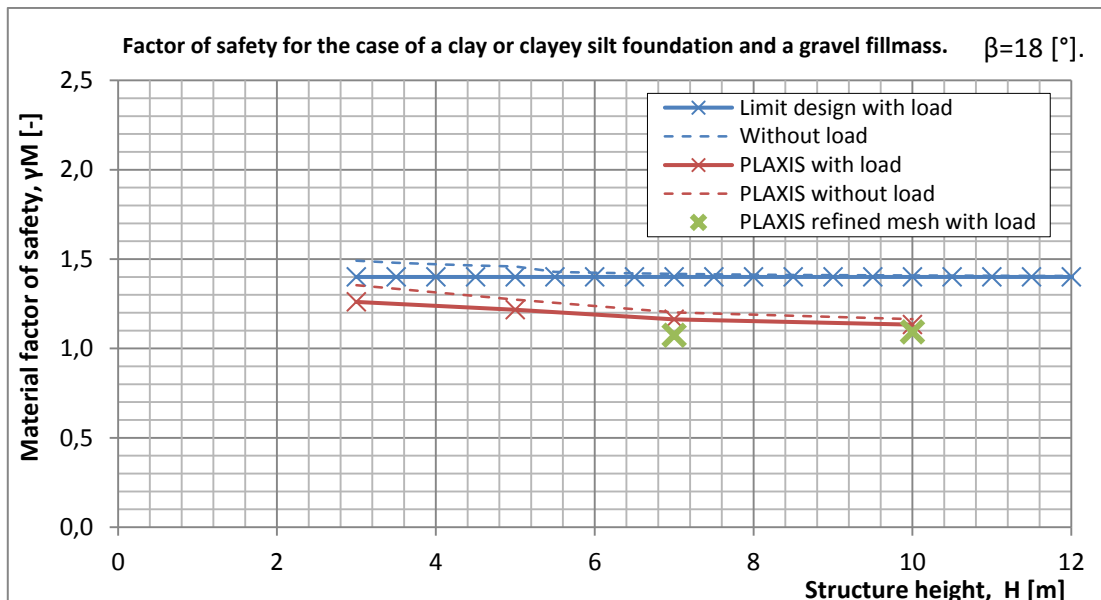

Figure 5.16: Cases with clay or clayey silt foundation and blasted rock backfill.
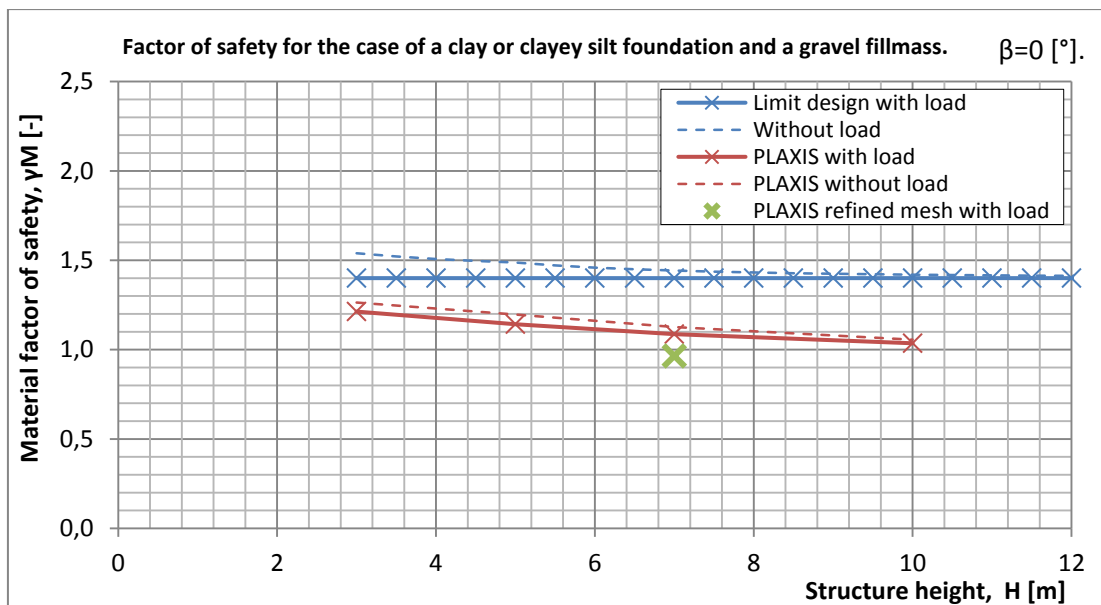
Figure 5.17: Cases with clay or clayey silt foundation and gravel backfill.
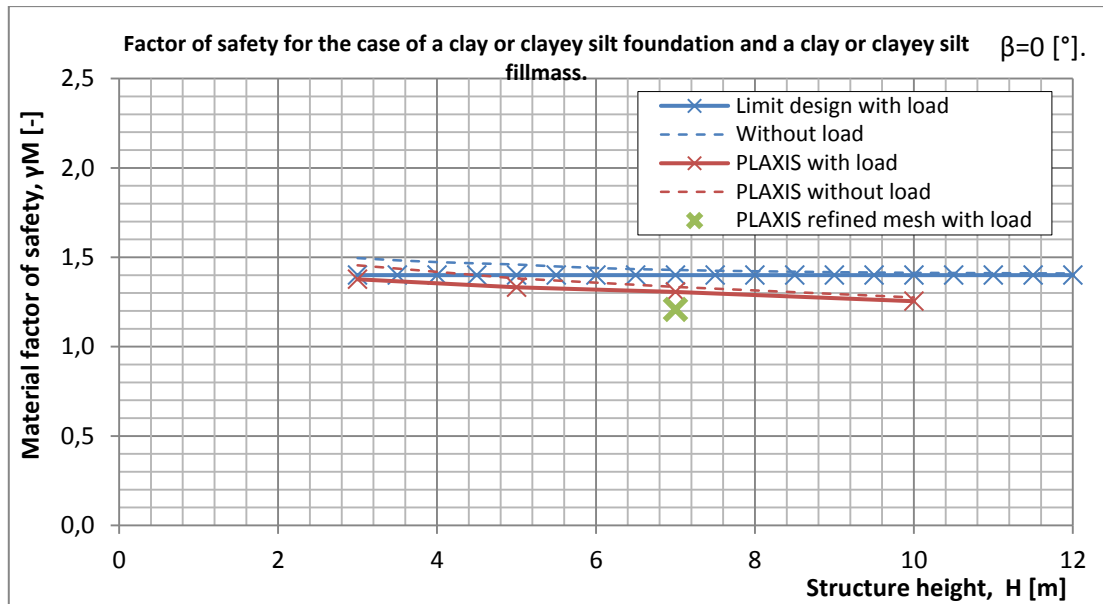
Figure 5.18: Cases with clay or clayey silt foundation and clay or clayey silt backfill.

It is easy to deduct from Figure 5.16 and Figure 5.17 that according to the PLAXIS simulations the design proposed by HB016 grossly overestimates the MFS. The cases calculated with refined mesh both collapsed under initial loading resulting in a material factor of safety below $\gamma_M = 1,0$. The inclination of the red curves indicate that for lower structures the factor of safety increases but can be assumed to be in the critical range for in the entire range.

In the case of a clay or clayey silt backfill material the simulated material factor of safety is greater than in the other two cases. It is clear from Figure 5.18 that the MFS is still a bit lower than the one derived with methods in HB016.

5.3.4 Blasted rock foundation – inclined terrain

The results from hand calculations and PLAXIS simulations for the case of a blasted rock foundation can be seen in Figure 5.19 to Figure 5.21.

Figure 5.19: Cases with blasted rock foundation and blasted rock backfill.

Figure 5.20: Cases with blasted rock foundation and gravel backfill.

Figure 5.21: Cases with blasted rock foundation and clay or clayey silt backfill.

Interpreting Figure 5.19 and Figure 3.18 with the same assumptions as before reveals that the results from PLAXIS simulations are similar to the ones derived with the methods in HB016; in both cases the results from simulations with mesh refinements lie close to the MFS of $\gamma_M = 1,4$. The inclination of the marked red curve in Figure 5.19 indicates a decrease in material factor of safety for higher walls.

The results in Figure 5.21 differ from all other results in this study as the strength reduction resulted in slope failure and not a failure of retaining capabilities of the structure. This can be seen in Figure 0.63 to Figure 0.66 in Appendix I. This result can be verified in a very simple way in this case as

$$\gamma_M = \frac{tan(26)}{tan(18)} = 1,5$$

This is in good agreement with the results from the PLAXIS simulation.

Another interesting part of Figure 5.21 is that for the first three heights the factor of safety according to HB016 is not equal to $\gamma_M = 1,4$. This is because that in these cases the foundation roughness exceeded the maximum allowed value of $r_b = 0,8$. The method I used to design the width of the footing only depends on finding the root of the remaining bearing capacity as is shown in Figure 4.9, Figure 4.11 and Figure 4.12.

This maximum value of r_b is low for a blasted rock foundation according to Table 4.7 but was used in all calculations. The roughness was found to be critical in one other case in the study. This was in the case of a $H = 3m$ high wall on blasted rock with a gravel backfill innclined 18° as is shown in Figure 5.20. The calculated roughness in that case is is $r_b = 0,801$. This can be seen in Table 0.3 in Appendix H.

5.3.5 Gravel foundation – inclined terrain

The results from hand calculations and PLAXIS simulations for the case of a gravel foundation can be seen in Figure 5.22 and Figure 5.23.

Figure 5.22: Cases with gravel foundation and blasted rock backfill.

Figure 5.23: Cases with gravel foundation and gravel backfill.

Figure 5.22 shows that in the case of a gravel foundation and a blasted rock backfill the PLAXIS simulations revealed considerably lower MFS than is calculated using the methods proposed by HB016. If we accept the trend shown with a coarser mesh and extend it from the green mark we could end up with a design that will fail under initial conditions for structures with heights of around $H = 10m$.

Figure 5.23 shows a much better fit between the MFS derived with the methods in HB016 and the values from the PLAXIS simulations. As the red curves shows an increase in the

MFS as the structure height is decreased a better fit is expected for lower structures if the mesh size were reduced there as well.

The case of a clay or clayey silt backfill yielded extremely large limit design foundation widths and was not modeled in PLAXIS.

5.3.6 Clay or clayey silt foundation – inclined terrain

The results from hand calculations and PLAXIS simulations for the case of a clay or clayey silt foundation can be seen in Figure 5.24 to Figure 5.25.

Figure 5.24: Cases with clay or clayey silt foundation and blasted rock backfill.

Figure 5.25: Cases with clay or clayey silt foundation and gravel backfill.

Figure 5.24 and Figure 5.25 clearly show that the PLAXIS simulations revealed much lower MFS than were calculated using the methods in HB016.

The case of a blasted rock backfill shown in Figure 5.24 yielded failure under initial loading for the case of a H=7m high wall and a MFS of $\gamma_M = 1,02$ for the case of a $H = 3m$ high wall. This should be considered critical as a finer mesh size would lower this number slightly resulting in failure under initial loading.

In the case of a gravel backfill yielded somewhat higher MFS but they are so close to the factor $\gamma_M = 1,0$ that they could be considered critical.

5.3.7 Summary of PLAXIS simulation results

Horizontal backfill

For the case of a blasted rock foundation material all the tested structure designs produced a similar MFS in PLAXIS simulations as were derived with methods proposed by HB016. The backfill material does not appear to have a large influence on this result.

For the case of gravel foundation material variations in backfill materials has a large effect on the MSF for each design when calculated with PLAXIS. Stronger backfill materials produce a lower MFS than weaker materials. The case of a gravel backfill material seemed to create the best fit to the values derived with methods proposed by HB016. For a blasted rock backfill material the simulated MFS was lower than the methods in HB016 suggested and could even be considered critical for high structures.

For the case of a clay or clayey silt foundation material both the case of blasted rock- and gravel backfill materials produced MFS indicating failure under initial conditions. The case of clay or clayey silt backfill material proved to have a MFS higher than the other two cases but still lower than the ones calculated with methods proposed by HB016. It should be mentioned that the foundation widths required to produce those MFS are around two times the structures height.

Inclined backfill

For the case of a blasted rock foundation material PLAXIS simulations of the tested designs yielded similar MFS as were derived with methods proposed by HB016. This result holds true for all tested backfill materials.

For the case of a gravel foundation material the PLAXIS simulations of the designs resulted in MFS lower than the ones calculated with methods proposed by HB016. The MFS increased as the strength of the backfill mass decreased. The cases with a clay or clayey silt backfill materials resulted in excessive base widths and were therefore not simulated in PLAXIS

For the case of a clay or clayey silt foundation material variations in the backfill material had some effect on the MFS simulated in PLAXIS. The case of a blasted rock backfill material resulted in a critical MFS for a $H = 3m$ high structure and failure under initial conditions for a $H = 7m$ high structure. The case of a gravel fillmass yielded slightly higher MFS but could still be considered critical. The cases with a clay or clayey silt fillmass material gave no solution with hand calculation methods and therefore there was no basis for a comparison with PLAXIS. It should be mentioned that for the case of a gravel backfill on a clay or clayey silt foundation the required base widths ranged from 2 to 3 times the structures height for the tested height interval.

6 Conclusions

6.1 Study of earth pressures

In the study of earth pressures both Coulomb's method and the stressfield method were found to deliver similar values of active earth pressure coefficients. There is a slight difference between the two as the stressfield method assumes a curved failure surface while Coulomb's method assumes a failure plane. In the case of an inclined backfill both methods assume failure planes for all values of wall friction and produce almost identical results. The case of passive earth pressures revealed that for higher values of roughness Coulomb's method produces much higher pressure coefficients than the stressfield method. This behavior is a result of the fact that an increase in the angle of wall friction forces the failure plane to tilt closer to the horizontal; as the angle of the shear plane nears the inclination angle of the backfill small variations in the tilt angle have large effect on the length of the failure plane. For inclined backfill both methods assume a planar failure surface and show deliver almost identical results.

When compared to the values provided in Eurocode 7 both methods were found to provide very similar results in the case of active earth pressures although the stressfield method was a better fit in the case of a horizontal backfill. As the difference between the values provided in Eurocode 7 and the ones calculated with the classical earth pressure theories is found to be small I assume that both methods can be used to calculate the active pressures to the standards requirements. The same cannot be said for the case of passive earth pressures where the calculated values cannot be assumed to give the same results as the ones given in Eurocode 7. I tried to develop a simple modification of the stressfield method to incorporate the effect of curved failure surfaces in the case of inclined backfills. The modification solved the problem of exponential growth in passive pressures for high roughness but did not provide a good fit to the values provided by Eurocode 7. The chapter is in the Norwegian annex marked as informative and therefore designers can still use the conventional methods to calculate earth pressures.

6.2 Structure design with hand calculation methods

Using the methods prescribed in HB016 I designed the optimal base- and toe widths of cantilevered retaining walls with varying foundation and backfill materials for a number of height intervals. Some base geometrical features were kept constant in all of them in order to have a better chance to evaluate the effect of change in other parameters. All cases are calculated without passive pressures to avoid errors originating in the inconsistencies found between calculational methods mentioned above. In this analysis the base widths of 180 structures have been optimized with respect to the toe width with an iterative process for the case of a horizontal backfill and a terrain load representing heavy traffic without an additional safety factor. This process is repeated for all cases when the backfill is inclined at an angle of 18°, although not all those cases yielded results.

The results from the hand calculations are the limit designs that are supposed to have a material factor of safety of $\gamma_M = 1,4$ according to the methods proposed by HB016 as well as calculated material factor of safety for each case where the surface load has been removed.

The cases for a blasted rock foundation were calculated again with the cohesion set to zero. It is shown that the cohesion has a noticeable influence on the required base widths but the difference was greatest for a backfill material with substantially lower strength than that used in the foundation.

The influence of the depth of application of the surface load is not clearly visible in any case for a horizontal backfill mass. The surface load is set to a value that is supposed to represent heavy traffic so I was expecting to see a breakpoint in the design curves around that height.

The effect of the terrain load is clearly visible in the case of inclined backfill. This effect is exaggerated when either the backfill material or the foundation material have friction angles close to the inclination angle of the slope. When the material factor of safety of $\gamma_M = 1,4$ has been added to the clay or clayey silt material the mobilized friction angle is around $\rho = 19°$. The small difference between the mobilized friction angle in the backfill material and the inclination of the backfill explains why so large foundation widths were required in the case of a gravel foundation and why no solution was found in the case of a clay or clayey silt foundation.

Optimizing the toe width revealed that for many of the hand calculated cases the eccentricity of the vertical force is around zero and only cases involving a blasted rock material in either foundation or backfill produced designs with nonzero eccentricity. The eccentricity was plotted against the toe width for some of the cases where the optimal toe width did not coincide with zero eccentricity. It was found that the minimum absolute value of the eccentricity was very close to the optimal toe size. This makes sense as the effective footing is largest for small values of eccentricity.

For each final design the surface load was removed and the resulting addition in material factor of safety of the model was calculated using a simplified version of the Phi-C reduction method.

6.3 Evaluation of proposed designs using PLAXIS

A selection of the designs derived with hand calculation methods were modeled in PLAXIS. The strength parameters for each soil type were put in without any added safety factors and stiffness parameters were selected generally for each soil type. The strength of the materials in the model was reduced until failure occurred in the soil mass both with and without the surface load applied.

The results from the comparison between numerical and handcalculation methods are in some cases alarming. It seems that the handcalculation methods underestimate earth pressures from strong backfill materials; according to PLAXIS simulations some of the tested designs involving strong backfill materials are on the verge of failure under initial

conditions. The comparison also shows that according to PLAXIS simulations the handcalculation methods overestimate the strength of weak foundation materials and many of the tested designs failed under initial conditions. Failure of large structures founded on weak materials is perhaps not a very important point as it is standard practice to exchange weak materials for stronger ones in the foundation.

I chose to design the test models with only a material factor of safety against failure; in real life other safety factors will have to be taken into account that would probably improve over all factor of safety of the construction.

For the cases with a blasted rock foundation material the material factors of safety calculated with PLAXIS are in agreement with those derived with hand calculation methods. This holds true for both a horizontal backfill as well as a backfill that is inclined by $\beta = 18°$. The backfill material does not seem to have much influence on this result although for the case of clay or clayey silt backfill material with an inclined backfill did result in a slope failure and not a failure of the retaining capabilities of the structure.

For the cases with a gravel foundation material the material factors of safety calculated with PLAXIS were greatly influenced by the backfill material. Assuming that the trend shown for a coarser element mesh holds true for finer meshes it is estimated that some of the proposed designs with a blasted rock backfill material will fail under initial conditions indicating a material factor of safety of less than $\gamma_M = 1,0$. This is true for both the case of a horizontal backfill as well as a backfill inclined by $\beta = 18°$. When the fillmass is modelled as a gravel material the PLAXIS simulations resulted in material factors of safety slightly lower but close to those evaluated with hand calculation methods. This is true for both the case of a horizontal backfill as well as a backfill that is inclined by $\beta = 18°$. Fillmass with a clay or clayey silt material had a material factor of safety higher than the ones proposed by the methods in HB016 for the cases with a horizontal backfill, the cases with an inclined backfill yielded large base plate widths and as a result were not modeled in PLAXIS.

The cases with clay or clayey silt backfill material the material factors of safety calculated with PLAXIS were lower than the ones derived with hand calculation methods in all cases. When the backfill was modeled with a blasted rock material some of the designs failed under initial conditions in both the case of a horizontal and an inclined backfill. Assuming that the trend shown with a coarser mesh also applies for finer mesh the PLAXIS simulations revealed that none of the designs produced with methods in HB016 meet the material factor of safety requirements of HB016. The cases with a gravel backfill material produced slightly higher material factors of safety than the cases with blasted rock backfill material when modeled in PLAXIS. In the case of a horizontal backfill many of the designs still fail under initial conditions but the cases with an inclined backfill had a bit higher material factors of safety according to PLAXIS simulations. For the case of clay or clayey silt backfill material and a horizontal backfill PLAXIS simulations yielded much higher material factors of safety than was found for stronger backfill materials.

As there are large discrepancies between material factors of safety derived with hand calculation methods and the ones simulated in PLAXIS a direct comparison of the effect of omitting the surface load from the designs cannot be carried out. Comparing the difference between the material factor of safety curves with and without loads from PLAXIS simulations and hand calculation methods shows that the hand calculation method gives an

increase in the factor of safety close to that simulated with PLAXIS. Because of the large difference in material factors of safety between hand calculation methods and PLAXIS simulations for the limit designs this result, although extremely pleasing, is of little practical importance.

6.4 Geometry of simulated failure surfaces

The most noticeable result from the PLAXIS simulations is that the failure surfaces in the backfill are in all cases almost planar; this can be seen more clearly in the results obtained with a finer mesh size. As the method to calculate earth pressures for the case of a horizontal backfill proposed by HB016 assumes a roughness that depends on the material factor of safety it follows that the failure surface should in all cases have a curved section. The assumption that all the soil on top of the heel acts as a part of the structure and that a vertical failure plane will develop from the heel of the base to the surface does not appear to be accurate according to the PLAXIS simulations. What is found with finite element simulations is that a planar shear surface develops into the mass that rests on top of the heel. This shear plane reaches the back of the vertical wall and then travels along it to the surface or if the base plate is long enough travels along one plane to the surface. It is clear that modeling the earth mass resting on top of the heel as a part of the structure does not provide an accurate description of the failure modes that were found with numerical simulations.

It is possible that by taking into account the probable geometry of the failure wedge when calculating earth pressures a better model can be created to design cantilevered structures. An idea for a study on this could be to measure the angles of shear surfaces from simulated failures with the finite element method for different types of backfill materials. If a connection between the inclinations of the shear surfaces into the mass above the base and the friction angle and inclination of the backfill can be established it can be used as an equivalent wall inclination angle input parameter in Coulomb's equation.

Using the same logic as for equation (34) it is possible to derive a relationship between the frictional force and the driving force in the force diagram of Figure 2.12. Knowing the equivalent-wall inclination angle, the angle of the failure plane and the friction angle of the backfill it should be possible to calculate the angle of roughness from simulated cases. If the roughness angle is known it is possible to calculate the shear stress acting along the plane of the equivalent back wall.

It is possible that such a study would change both the size and orientation of the active earth pressures used to design the geometry of cantilevered retaining walls and perhaps contribute to a better relationship between the design material factors of safety and the ones derived with numerical methods.

References

Bourke Paul Calculating The Area And Centroid Of A Polygon [Online] // Paul Bourke. - July 1988. - 02 12, 2011. - http://www.paulbourke.net/geometry/polyarea/.

Das Braja M. Principles of Geotechnical Engineering [Book]. - Pacific Grove, CA. : Brooks/Cole, 2002.

Døssland Torgeir Bereevne for sålefundament i skråterreng [Report]. - Trondheim : NTH, 1980.

Døssland Torgeir Skjerflategeometri og vertikal jordreaksjon ved ulike teoretiske løysingar for bereevnefaktoren $N\gamma$ [Report]. - Trondheim : NTH, 1980.

Erlingsson Sigurður Reference material for the subject "Jarðtækni og grundun 1" // Jarðtækni og grundun 1. Lecture notes. - Reykjavík : [s.n.], 2006.

Eurocode EN 1992-1-1:2004 [Book]. - Brussels : CEN, 2004.

Eurocode NS-EN 1997-1:2004+NA:2008 [Book]. - Lysaker : Norsk Standard, 2008. - Vol. I.

Grande Lars Olav Samvirke mellom pel og jord [Book]. - Trondheim : Norges Tekniske Høgskole Universitetet I Trondheim, 1976.

Janbu Nilmar [et al.] Reference material for the subject "Theoretical Soil Mechanics" // Theoretical Soil Mechanics. - Trondheim : NTNU, August 2006.

Janbu Nilmar, Grabde Lars Olav and Eggereide Kåre Effective Stress Stability Analysis For Gravity Structures [Book]. - Trondheim, Norway : NTH, 1976.

Nordal Steinar Finite Elements In Geotechnical Engineering // Lecture notes: TBA 4115 Finite Elements In Geotechnical Engineering. - Trondheim : NTNU, 2009.

PLAXIS Plaxis - Plaxis company history [Online] // Plaxis. - Plaxis, April 2011. - April 24, 2011. - http://www.plaxis.nl/page/4863///History/.

PLAXIS PLAXIS 2D 2010 - Material model manual [PDF document]. - Delft : PLAXIS ; PLAXIS, 2010.

PLAXIS PLAXIS 2D 2010 - Reference manual [PDF document]. - Delft : PLAXIS, 2010.

PLAXIS PLAXIS 2D 2010 - Scientific manual [PDF document]. - Delft : PLAXIS, 2010.

Sandven Rolf Geotechnics, Material Properties // TBA4110 - Geotechnics, Material Properties - Equipment, proceidures and parameter interpretation. - Trondheim : NTNU, 2000.

State of California Department of Transportation Division of Structure Construction
Trenching And Shoring Manual Revision 12 [Book]. - Sacramento : State of California
Department of Transportation - Division of Structure Construction, 1990.

Statens vegvesen Håbdbok 100 [Book]. - Oslo : Statens vegvese - Bruavdelingen, 1985.

Statens vegvesen Håndbok 016: Geoteknikk i vegbygging [Book]. - Oslo : Statens
Vegvesen, Vegdirektoratet - Trafikksikkerhet, miljø- og teknilogiavdelingen, 2010.

Statens vegvesen Håndbok 018: Vegbygging [Book]. - Oslo : Statens Vegvesen,
Vegdirektoratet - Trafikksikkerhet, miljø- og teknilogiavdelingen, 2011.

Statens vegvesen Håndbok 100: Bruhåndbok-1 [Book]. - Oslo : Statens vegvesen -
Bruavdelingen, 1996.

Statens vegvesen Håndbok 185: Bruprosjektering (normal) [Book]. - Oslo : Statens
vegvesen - Teknologiavdelingen, Bruseksjonen, 2009.

Ugural Ansel C. and Fenster Saul K. Advanced Strength And Applied Elasticity, fourth
edition [Book]. - New Jersey : Prentice Hall Professional Technical Reference, 2003.

Wikipedia European Committee for Standardization [Online] // Wikipedia. - Wikimedia
Foundation,   Inc,   February   11,   2011. -   April   21,   2011. -
http://en.wikipedia.org/wiki/European_Committee_for_Standardization.

Appendix A: Stress on an arbitrary plane

Using a soil element with a shear plane with stresses acting on it, as is shown in Figure 0.1, it is possible to set up equations of equilibrium.
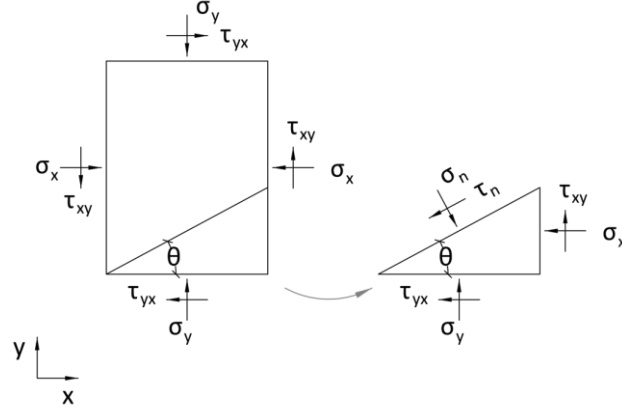
Figure 0.1: A soil element and a free body diagram.

If we define the long edge in the free body diagram as having a unit length we can easily set up a force diagram for this situation in the direction of the normal stress and normal shear stress as:

$$\sigma_n \cdot 1 = \sigma_y \cos(\theta)\cos(\theta) + \tau_{yx}\cos(\theta)\sin(\theta) + \sigma_x \sin(\theta)\sin(\theta) + \tau_{xy}\sin(\theta)\cos(\theta) \quad \text{(A1)}$$

and

$$\tau_n \cdot 1 = \sigma_y \cos(\theta)\sin(\theta) - \tau_{yx}\cos(\theta)\cos(\theta) + \sigma_x \sin(\theta)\cos(\theta) + \tau_{xy}\sin(\theta)\sin(\theta) \quad \text{(A2)}$$

By noting that $\tau_{yx} = \tau_{xy}$, (Ugural, et al., 2003), these equations reduce to:

$$\sigma_n = \sigma_x \sin^2(\theta) + \sigma_y \cos^2(\theta) + 2\tau_{xy}\sin(\theta)\cos(\theta) \qquad \text{(A3)}$$

$$\tau_n = \sigma_y \cos(\theta)\sin(\theta) - \sigma_x \cos(\theta)\sin(\theta) + \tau_{xy}(\sin^2(\theta) - \cos^2(\theta)) \qquad \text{(A4)}$$

These equations can be further simplified by the introduction of double angles as:

$$\sigma_n = \frac{\sigma_y + \sigma_x}{2} + \frac{\sigma_y - \sigma_x}{2}\cos(2\theta) + \tau_{xy}sin(2\theta) \qquad \text{(A5)}$$

$$\tau_n = \frac{\sigma_y - \sigma_x}{2}sin(2\theta) - \tau_{xy}cos(2\theta) \qquad \text{(A6)}$$

Principal planes

We can calculate the extreme values of σ_n as the inclination of the plane, θ, increases by differentiating with respect to θ and setting it equal to zero, this yields the equation

$$tan(2\theta) = tan(\pi + 2\theta) = \frac{\tau_{xy}}{\frac{1}{2}(\sigma_y - \sigma_x)} = \frac{-\tau_{xy}}{-\frac{1}{2}(\sigma_y - \sigma_x)} \tag{A7}$$

These tangents can be represented graphically as is done in Figure 0.2.
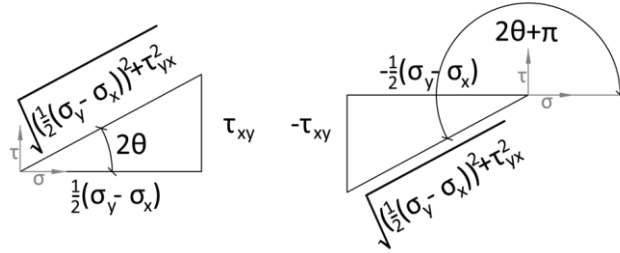
Figure 0.2: two different angles of the solution.

These two cases yield two distinct possibilities for the value of $\cos(2\theta)$ and $\sin(2\theta)$

$$cos(2\theta) = \frac{\frac{1}{2}(\sigma_y - \sigma_x)}{\sqrt{\left(\frac{1}{2}(\sigma_y - \sigma_x)\right)^2 + \tau_{xy}^2}} \quad , \quad sin(2\theta) = \frac{\tau_{xy}}{\sqrt{\left(\frac{1}{2}(\sigma_y - \sigma_x)\right)^2 + \tau_{xy}^2}} \tag{A8}$$

and

$$cos(2\theta) = -\frac{\frac{1}{2}(\sigma_y - \sigma_x)}{\sqrt{\left(\frac{1}{2}(\sigma_y - \sigma_x)\right)^2 + \tau_{xy}^2}} \quad , \quad sin(2\theta) = -\frac{\tau_{xy}}{\sqrt{\left(\frac{1}{2}(\sigma_y - \sigma_x)\right)^2 + \tau_{xy}^2}} \tag{A9}$$

These angles represent two planes that are perpendicular to each other. If we put these values into the equation (A5) we get the well-known formulas

$$\sigma_{n,1} = \frac{\sigma_y + \sigma_x}{2} + \sqrt{\left(\frac{1}{2}(\sigma_y - \sigma_x)\right)^2 + \tau_{xy}^2} \tag{A10}$$

$$\sigma_{n,2} = \frac{\sigma_y + \sigma_x}{2} - \sqrt{\left(\frac{1}{2}(\sigma_y - \sigma_x)\right)^2 + \tau_{xy}^2} \tag{A11}$$

However if we put them into equation (A6), we get zero in both cases. The two planes for which this is true are called the principal planes and the stresses that act on them are named major- and minor-principal stresses, represented by σ_1 and σ_3. As can be verified with equations (A6), (A8) and (A9), principal planes do not have shear stresses acting on them by definition.

If the coordinate system in Figure 0.1 is defined so that the edges of the element are perpendicular to the principal planes the boundary shear forces reduce to zero and equations (A10) and (A11) reduce to

$$\sigma_n = \frac{\sigma_1 + \sigma_3}{2} + \frac{\sigma_1 - \sigma_3}{2}\cos(2\theta) \qquad \text{(A12)}$$

$$\tau_n = \frac{\sigma_1 - \sigma_3}{2}\sin(2\theta) \qquad \text{(A13)}$$

We can find the maximum shear stress by using equation (A7) and setting τ_{xy} equal zero and getting that

$$tan(2\theta + n\pi) = 0 \qquad \text{(A14)}$$

This means that $2\theta = \frac{\pi}{2}$ or rather $\theta = \frac{\pi}{4}$ which then finally gives us the maximum shear stress as

$$\tau_{max} = \frac{\sigma_1 - \sigma_3}{2} \qquad \text{(A15)}$$

And it acts upon a plane inclined $\frac{\pi}{4}$ from the horizontal.

Appendix B: The MC-failure criterion and the beauty of the attraction

The Mohr coulomb failure criterion in a $\sigma - \tau$ space is defined by equation (6) and graphically presented by Figure 0.3. However in practical applications it can often be useful to present the failure envelope in other spaces. One practical reason might be that identifying the friction angle and cohesion by finding a best tangent line through a set of half circles is mathematically more challenging than calculating a best fit line through a point set.

There are many ways to define the MC failure criterion in the two dimensional space and this chapter is dedicated to four of them. The main reason for these derivation is to establish that while they all have their special properties, one property in particular is common to all of them. The first case is to derive the MC failure criterion in the $\sigma_1 - \sigma_3$ space as σ_1 and σ_1 are often the two known variables from experiments/exercises. Case 2 is the $s - t$ space, which is a bit simpler version of case 1. Case 3 is the $p' - q$ space which is a popular presentation of the MC failure envelope as it keeps the volumetric and distortional stress separate and is therefore a common way to present effective stress paths from triaxial tests (Nordal, 2009). Finally we will derive the failure criterion for the deviator/NTH plot, which is popular as its variables are directly related to the forces applied to a sample in a triaxial cell.

Case 1: the σ_1-σ_3 space
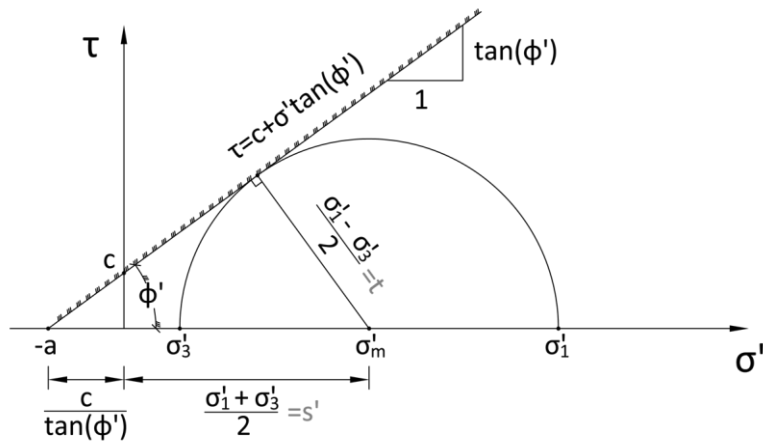
Figure 0.3: The Mohr-Coulomb failure envelope along with key variables.

Looking at the right angled triangle defined by the failure envelope, the half circles radii and the line $a - \sigma'_m$ we can define the following equation:

$$sin(\phi') = \frac{\frac{\sigma'_1 - \sigma'_3}{2}}{\frac{\sigma'_1 + \sigma'_3}{2} + \frac{c}{tan(\phi')}} \tag{B1}$$

From which we can derive

$$\sigma'_1 sin(\phi') + \sigma'_3 sin(\phi') + 2c\, cos(\phi') = \sigma'_1 - \sigma'_3 \tag{B2}$$

And trying to isolate σ_1' on the left side we get

$$\sigma_1'\big(1 - sin(\phi')\big) = 2c\,cos(\phi') + \sigma_3'\big(1 + sin(\phi')\big) \tag{B3}$$

Then finally isolating the minor principal stress by division we get the well-known formula

$$\sigma_1' = \sigma_3' \frac{1+sin(\phi')}{1-sin(\phi')} + \frac{2c\,cos(\phi')}{1-sin(\phi')} \tag{B4}$$

or if we twist it around as

$$\sigma_3' = \sigma_1' \frac{1-sin(\phi')}{1+sin(\phi')} - \frac{2c\,cos(\phi')}{1+sin(\phi')} \tag{B5}$$

This formula is often noted as

$$\sigma_3' = \sigma_1' tan(\psi') + c^* \tag{B6}$$

This is done with substitution in order to retain the form of the original MC-criterion but it should be noted that $c^* \neq c$ and $\psi' \neq \phi'$. However if we instead substitute in for c with

$$c = a \cdot tan(\phi') \tag{B7}$$

we get

$$\sigma_1' = \sigma_3' \frac{1+sin(\phi')}{1-sin(\phi')} + \frac{2a\,sin(\phi')}{1-sin(\phi')} \tag{B8}$$

Now by adding a to both sides we get

$$(\sigma_1' + a) = \sigma_3' \frac{1+sin(\phi')}{1-sin(\phi')} + \frac{2a\,sin(\phi')}{1-sin(\phi')} + a\frac{1-sin(\phi')}{1-sin(\phi')} \tag{B9}$$

and with a little algebra we get the desired result

$$(\sigma_1' + a) = (\sigma_3' + a)\frac{1+sin(\phi')}{1-sin(\phi')} \tag{B10}$$

It can be verified that the intersection of equation (B10) and the symmetry line $\sigma_1' = \sigma_3'$ is the point $\big(-a, -a\big)$.

Case 2: the $s - t$ space

Another popular form of the MC failure criterion is to define the radius and the center of Mohr circle as variables (MIT– NGI-plot).

$$s' = \frac{\sigma_1' + \sigma_3'}{2} \tag{B11}$$

$$t = \frac{\sigma_1' - \sigma_3'}{2} \tag{B12}$$

Then we can set up the same initial equation as was done in equation (B1)

$$sin(\phi') = \frac{t}{s'+a} \tag{B13}$$

which is turned to the relation

$$t = (s' + a)sin(\phi') \tag{B14}$$

If we now investigate the intersection with the t axis we get

$$s' = -a \tag{B15}$$

Case 3: p'-q space in a triaxial test

The mean stress is defined as

$$p' = \frac{1}{3}(\sigma_1 + \sigma_2 + \sigma_3) \tag{B16}$$

and because we are taking the special case of the triaxial test we have $\sigma_2 = \sigma_3$ which gives

$$p' = \frac{1}{3}(\sigma_1 + 2\sigma_3) \tag{B17}$$

The deviator stress is defined as

$$q = (\sigma_1 - \sigma_3) \tag{B18}$$

we can continue from (B14) as $q = 2t$

$$q = 2s'sin(\phi') + 2a \cdot sin(\phi') \tag{B19}$$

if we write out the principal stresses and substitute $a = c/tan(\phi')$ we get

$$q = (\sigma_1 + \sigma_3)sin(\phi') + 2c \cdot cos(\phi') \tag{B20}$$

With a little twist we get

$$q = \frac{1}{3}\left((2\sigma_1 + 4\sigma_3) + \sigma_1 - \sigma_3\right)sin(\phi') + 2c \cdot cos(\phi') \tag{B21}$$

With substitution we can turn (B20) into

$$q = \left(2p' + \frac{q}{3}\right)sin(\phi') + 2c \cdot cos(\phi') \tag{B22}$$

we scale this to get

$$3q = 6p'sin(\phi') + qsin(\phi') + 6c \cdot cos(\phi') \tag{B23}$$

factor and get

$$q\big(3 - sin(\phi')\big) = 6p'sin(\phi') + 6c \cdot cos(\phi') \tag{B24}$$

and finally we get the desired result

$$q = \frac{6p' \, sin(\phi')}{3 - sin(\phi')} + \frac{6c \cdot cos(\phi')}{3 - sin(\phi')} \tag{B25}$$

If we now investigate the intersection with the p' axis we get

$$p' = c \cdot \frac{cos(\phi')}{sin(\phi')} = -a \tag{B26}$$

Case 4: The deviator plot

For completeness sake we define

$$N^- = \frac{1 - sin(\phi')}{1 + sin(\phi')} \tag{B27}$$

and name N^- the minor principal stress ratio and define

$$N^+ = \frac{1 + sin(\phi')}{1 - sin(\phi')} \tag{B28}$$

and we name N^+ the major principal stress ratio, as it is contains the link between the principal stresses that have been shifted by the attraction. It is worth noting that $(N^+ \cdot N^-) = 1$ and $N^-_{(-\phi')} = N^+$.

Substituting equation (B28) into equation (B10) we get

$$(\sigma_1' + a) = (\sigma_3' + a) \cdot N^+ \tag{B29}$$

we subtract and divide and get

$$\frac{1}{2}\big((\sigma_1' + a) - (\sigma_3' + a)\big) = \frac{1}{2}\big((\sigma_3' + a) \cdot N^+ - (\sigma_3' + a)\big) \tag{B30}$$

Then we have derived the desired result

$$\frac{(\sigma_1' - \sigma_3')}{2} = \frac{(N^+ - 1)(\sigma_3' + a)}{2} \tag{B31}$$

If we now investigate the intersection with the σ_3' axis we get the familiar result

$$\sigma_3' = -a \tag{B32}$$

Conclusion

We have now defined the MC failure criterion using different variables and notations. Out of four commonly used presentations of the Mohr-Coulomb failure criterion, three had the intersection with the horizontal axis as the numerical value of $-a$ and the fifth has a special connection to the variable as well. It is clear that the attraction, a, is a common factor to all of them and can be used along with the friction angle, ϕ', to link the major and minor principal stresses.

Appendix C: Stresses on critical and inclined planes

We now continue on this path and advance what we know about the principal stress ratio and then examine stresses on other planes than the critical planes in a soil element that has reached its shear strength.

Stresses on the critical plane

In Figure 0.4 the Mohr-Coulomb failure criterion has been shifted by the attraction and both the shear and normal stress have been normalized by $(\sigma_3' + a)$.
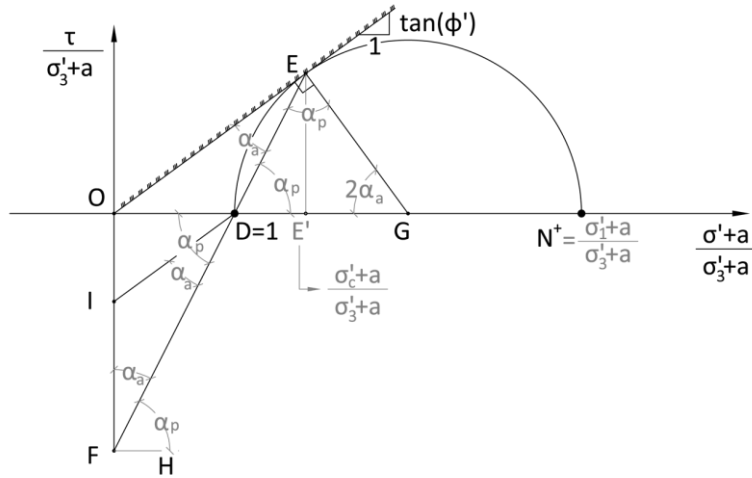
Figure 0.4: A dimensionless version of the MC failure envelope.

Because the triangle EDG has two sides equal it also has two equal angles. It is easy to establish the angle $\angle OGE$ as the triangle it forms with the scaled MC failure line is a right triangle. $\angle OGE$ it therefore equal to

$$\angle OGE = \frac{\pi}{2} - \phi' = 2 \cdot \left(\frac{\pi}{4} - \frac{\phi'}{2}\right) = 2\alpha_a \tag{C1}$$

With a little algebra we can calculate that the other two angles of EDG are equal to α_p. By noting that

$$\angle GDE = \angle HFD = \alpha_p = \frac{\pi}{4} + \frac{\phi'}{2} \tag{C2}$$

The angle α_a complements the angle α_p, and thus we know that

$$\angle OEF = \angle OFE = \alpha_a = \frac{\pi}{4} - \frac{\phi'}{2} \tag{C3}$$

Furthermore the two sides connecting to point O are equal in length and because the point D has been normalized to be equal to one we get that they are equal to $tan(\alpha_p)$.

The power of point theorem gives the relationship

$$tan(\alpha_p) \cdot tan(\alpha_p) = 1 \cdot N^+ \tag{C4}$$

which can be written out as

$$\frac{1+sin(\phi')}{1-sin(\phi')} = tan^2\left(\frac{\pi}{4} + \frac{\phi'}{2}\right) \tag{C5}$$

Let's now extrapolate another relationship for N^+. The line DI in Figure 0.4 is parallel to OE. Therefore we know from before that the angle $\angle IDF$ is equal to the angle $\angle OEF$. Therefore we can conclude that the triangle IDF is an isosceles triangle. We can calculate the distance $|OI|$ as

$$|OI| = tan(\phi') \tag{C6}$$

therefore the distances $|ID|$ and $|IF|$ are equal to

$$|ID| = |IF| = \sqrt{tan^2(\phi') + 1} \tag{C7}$$

The distance $|OF|$ can now be calculated as

$$|OD| = |IF| = tan(\phi') + \sqrt{tan^2(\phi') + 1} \tag{C8}$$

Using the same method as used in equation (C4) we can now conclude that

$$N^+ = tan^2\left(\frac{\pi}{4} + \frac{\phi'}{2}\right) = \left(tan(\phi') + \sqrt{tan^2(\phi') + 1}\right)^2 \tag{C9}$$

Let's now inspect the relationship between the actual stress acting on the critical plane and the major and minor principal stresses acting on the specimen. We note that the triangles OEG and OEE' have a common angle and a right angle and thus we have

$$\frac{|OE|}{|OG|} = \frac{|OE'|}{|OE|} \tag{C10}$$

Writing $|OE|$ and $|OG|$ in terms of N (noting equation (C4)) we get the relationship

$$|OE'| = \frac{\sigma_c' + a}{\sigma_3' + a} = \frac{2N^+}{N^+ + 1} \tag{C11}$$

Using equations (C11), (B29)

and the simple relationship between equations (B27) and (B28) it is possible to show that

$$\frac{\sigma_c' + a}{\sigma_1' + a} = \frac{2N^-}{N^- + 1} \tag{C12}$$

Now we have formulated equations linking the major and the minor principal stress to the normal stress acting on the critical plane (Janbu, et al., 2006)

Stresses on an inclined plane – passive case

We have now discussed how to calculate stresses acting on the on the most critical plane so we have the tools to calculate the stresses transferred from the soil to a structure if the connection between the two is completely rough. Let's investigate on what happens when the stress triangle hits the structure at an angle other than the most critical one. By using equation (21) we can define a reduced failure criterion that results in a cut-shear element. This is illustrated in Figure 0.5.
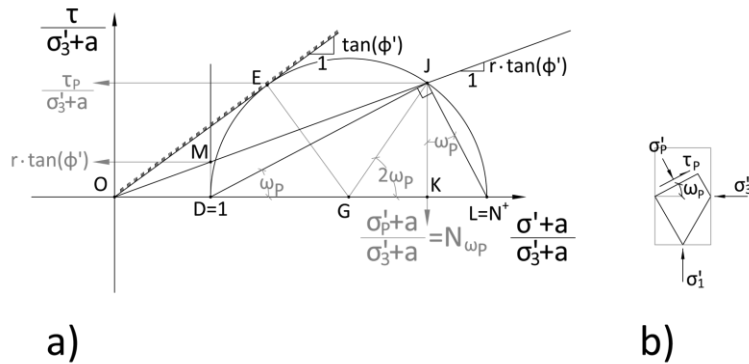
Figure 0.5: a) dimensionless MC-criterion b) the cut shear element passive pressures.

By investigating Figure 0.5 a) it is possible to derive a relationship between the magnitude of $|OK|$, he principal stress ratio N^+, and the passive cut angle ω_P. This is done by noting that

$$|DK| = cos(\omega_P) \cdot |DJ|$$ (C13)

and

$$|JK| = cos(\omega_P) \cdot |JL|$$ (C14)

By noting that the triangle DJL is right triangle, the distance $|DJ|$ can be defined as

$$|DJ| = \sqrt{|DK|^2 + |JK|^2}$$ (C15)

or as

$$|DJ| = \sqrt{cos^2(\omega_P) \cdot (|DJ|^2 + |JL|^2)}$$ (C16)

By substitution this becomes

$$|DJ| = (N^+ - 1) \cdot cos(\omega_P)$$ (C17)

The distance $|DK|$ can now be expressed as

$$|DK| = (N^+ - 1) \cdot cos^2(\omega_P)$$

We can create the desired link as

$$N_{\omega_P} = \frac{\sigma'_P + a}{\sigma'_3 + a} = 1 + (N^+ - 1) \cdot cos^2(\omega_P)$$ (C18)

By noting equation (C4) this can be developed further as

$$N_{\omega_P} = \frac{\sigma_P' + a}{\sigma_3' + a} = 1 + \frac{(N^+ - 1)}{1 + tan^2(\omega_P)} = 1 + \frac{tan^2(\alpha_p) - 1}{1 + tan^2(\omega_P)} = \frac{tan^2(\omega_P) + tan^2(\alpha_p)}{1 + tan^2(\omega_P)} \qquad (C19)$$

We now define f_ω as the mobilization of α_p using the same principle as in equation (8)

$$f_\omega = \frac{tan(\omega_P)}{tan(\alpha_P)} \qquad (C20)$$

Now by substituting equation (C20) into equation (C19) we get the desired result as

$$N_{\omega_P} = \frac{\sigma_P' + a}{\sigma_3' + a} = \frac{(f_\omega^2 + 1) \cdot N^+}{1 + f_\omega^2 \cdot N^+} \qquad (C21)$$

We can develop a relationship between the variable f_ω in equation (C20) and r further by using the fact that the triangles OJK and ODM have the same shape. Therefore the following applies

$$\frac{r \cdot tan(\phi')}{1} = \frac{(N_{\omega_P} - 1) tan(\omega_P)}{N_{\omega_P}} \qquad (C22)$$

substituting in for N_{ω_+} using equation we get

$$r \cdot tan(\phi') = \frac{\left(\frac{(f_\omega^2 + 1) \cdot N^+ - 1 - f_\omega^2 \cdot N^+}{1 + f_\omega^2 \cdot N^+}\right) \cdot tan(\omega_P)}{\frac{(f_\omega^2 + 1) \cdot N^+}{1 + f_\omega^2 \cdot N^+}} = \left(\frac{(f_\omega^2 + 1) \cdot N^+ - 1 - f_\omega^2 \cdot N^+}{(f_\omega^2 + 1) \cdot N^+}\right) \cdot tan(\omega_P) \qquad (C23)$$

which reduces to

$$r \cdot tan(\phi') = \frac{(N^+ - 1) \cdot tan(\omega_P)}{(f_\omega^2 + 1) \cdot N^+} \qquad (C24)$$

We note that the term $(N^+ - 1)$ is in fact the diameter of the half circle in Figure 0.5 and we substitute it for two times the radius of the half circle S_+

$$r \cdot tan(\phi') = \frac{2 \cdot S_+ \cdot tan(\omega_P)}{(f_\omega^2 + 1) \cdot N^+} \qquad (C25)$$

We note that by looking at the triangle OEG in Figure 0.5 a) and remembering that one term in equation (C4) represents the distance $|OE|$ that

$$tan(\phi') = \frac{S_+}{tan(\alpha_p)} \qquad (C26)$$

We substitute this in for $tan(\omega_P)$ and S_+ in equation (C25) with equations (C20) and (C26) and get

$$r \cdot tan(\phi') = \frac{2 \cdot tan(\phi') \cdot tan(\alpha_p) \cdot f_\omega \cdot tan(\alpha_p)}{(f_\omega^2 + 1) \cdot N^+} \qquad (C27)$$

Using equation (C4) this reduces to

$$r = \frac{2 \cdot f_\omega}{f_\omega^2 + 1} \tag{C28}$$

and can by use of the quadratic formula be turned into the desired result

$$f_\omega = \frac{1}{r}\left(1 - \sqrt{1 - r^2}\right) \tag{C29}$$

where r is selected as a primary parameter (Grande, 1976). The other solution from the quadratic formula is of no practical importance.

It is clear that the only factor that controls the how mobilized the stress on the stress on the rotated plane is the roughness, r. The resulting stresses on the arbitrary plane will then be

$$\sigma_P' = N_{\omega_P} \cdot (\sigma_3' + a) - a \tag{C30}$$

and

$$\tau_P = r \cdot \tan(\phi') \cdot (\sigma_P' + a) \tag{C31}$$

Stresses on an inclined plane – passive case

Deriving the equations for the active earth pressures is similar to the case of passive pressures. For those interested to try on their own, the easiest way to begin is to normalize figure Figure 0.5 a) with the major principal stress instead of the minor principal stress. The important equations will be presented here without derivations.

The plane mobilization number f_ω, only depends on the roughness so equations (C28) and (C29) apply for both cases. f_ω has another definition, see equation (C20), and it differs between the active and passive case. For the active case it becomes

$$f_\omega = \frac{\tan(\omega_A)}{\tan(\alpha_A)} \tag{C32}$$

Knowing the roughness number, r, it is possible to calculate f_ω and finally the resulting angle to the arbitrary plane ω_A. The stress ratio N_{ω_A} is expressed as

$$N_{\omega_A} = \frac{\sigma_A' + a}{\sigma_1' + a} = \frac{(f_\omega^2 + 1) \cdot N^-}{1 + f_\omega^2 \cdot N^-} \tag{C33}$$

The resulting stresses on the arbitrary plane will then be

$$\sigma_A' = N_{\omega_A} \cdot (\sigma_1' + a) - a \tag{C34}$$

And

$$\tau_A = r \cdot \tan(\phi') \cdot (\sigma_A' + a) \tag{C35}$$

Appendix D: The logarithmic spiral

As is stated in chapter 2.3.3, the shape of the curved part of a failure surface behind a retaining structure is commonly thought of as a logarithmic spiral. In Figure 0.6 a) we see the building block of the logarithmic spiral.
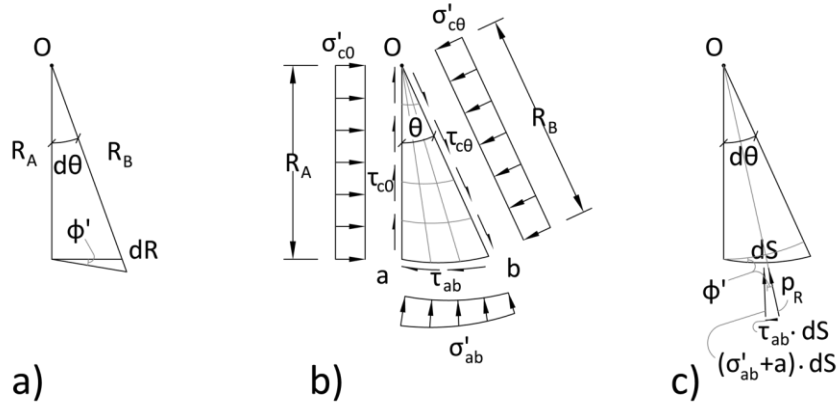
Figure 0.6: The logarithmic spiral from building block to moment diagram.

The angle $d\theta$ in Figure 0.6 a) is considered so small that the arcs can be approximated with lines and the little triangle is assumed to have a right angle. From this we can set up the following equation

$$R_A \cdot d\theta = \frac{dR}{tan(\phi')} \tag{D1}$$

By isolating the variables we are able to integrate both sides

$$\int_{\theta_A}^{\theta_B} tan(\phi')d\theta = \int_{R_A}^{R_B} \frac{dR}{R_A} \tag{D2}$$

and get

$$tan(\phi') \cdot \theta = ln\left(\frac{R_B}{R_A}\right) \tag{D3}$$

We raise both sides to the power of e and multiply with R_A to get the final result

$$R_B = R_A e^{tan(\phi') \cdot \theta} \tag{D4}$$

So the logarithmic spiral has the property that the angle from the radius to the tangent of the curve is conveniently defined as ϕ'. This becomes very convenient when we look at the forces acting on the boundary adjacent to the origin. Because we are looking at stress fields where one of the prerequisites is that every part of the soil is on the verge of failing then we also know by inspecting Figure 2.3 that the normal and shear stresses are on the MC failure line, σ_f' and τ_f. The relationship between the two is then simply

$$tan(\phi') = \frac{\tau_f}{\left(\sigma_f'+a\right)} \tag{D5}$$

The resulting force acting on the boundary of the spiral will then be oriented backwards by the angle ϕ' at the same time that the trajectory of the spiral is angled outwards by the angle ϕ'. The end result is that the boundary force, P_R in Figure 0.6 c) is directed towards the origin. If we take a moment equilibrium about the origin we can omit the shear forces and the outer boundary forces and get

$$R_a \cdot (\sigma_{c0} + a)\frac{R_a}{2} - R_b \cdot (\sigma_{c\theta} + a)\frac{R_b}{2} = 0 \qquad (D6)$$

We can deduct from this that

$$\frac{R_b^2}{R_a^2} = \frac{(\sigma_{c0} + a)}{(\sigma_{c\theta} + a)} \qquad (D7)$$

Putting together equations (D4) and (D7) we get the desired result

$$(\sigma_{c\theta} + a) \cdot e^{2\theta tan(\phi')} = (\sigma_{c0} + a) \qquad (D8)$$

A special case is when we assume undrained conditions as can be seen in Figure 2.2. Then the friction angle is zero and we end up with a unit multiplier in equations (D4) and (D7). This means that the spirals in Figure 0.6 b) reduce to circles and the stress acting on one side is the same as the stress acting on the other.

116

Appendix E: Stressfields in weightless soils

The earth pressures caused by stressfields in weightless soils has been defined for the case of completely smooth wall in Appendix B. In Appendix D a way to calculate the stress distribution through a rotation of the stressfield is provided. Let's finish this topic by examining what happens when the walls surface is neither completely smooth nor completely rough. A stressfield behind a vertical structure with a roughness number, r, between 1 and 0 can be described by using a complete Rankine zone connected to a Prandtl zone with an arbitrary opening angle and another Rankine zone that cuts the structure at an angle. This is shown schematically in Figure 2.6.

It clear that the opening angle of the logarithmic spiral shown in Figure 2.6 is the same angle as the angle of the arbitrary shear plane that cuts the structure. This means that for a given roughness and a friction angle of the soil it is possible to calculate the opening angle of the logarithmic spiral with equations (C29) and (C20) or (C32), depending on the earth pressure case. The total earth pressure from the combined fields can be calculated by tracing the stress from the planes OA to OB and finally OC.

Combined stressfields – passive case

The stressfield combined from two Rankine zones and a Prandtl zone as a result of a roughness between 0 and 1 for the passive case is shown in Figure 2.6 a). The stresses acting on plane OA_P can be calculated by means of equation (C11) as

$$\sigma'_{OA_P} + a = \frac{2N^+}{N^+ + 1} \cdot (q'_v + a) \tag{E1}$$

The stresses acting on plane OB_P can be calculated by means of equation (D8) as

$$\sigma'_{OB_P} + a = e^{2 \cdot \omega_P \cdot tan(\phi')} \cdot \left(\sigma'_{OA_P} + a \right) \tag{E2}$$

The stresses acting on plane OC_P can be calculated by means of equations (C11) and (C21) as

$$\sigma'_{OC_P} + a = \frac{(f_\omega^2 + 1) \cdot N^+}{1 + f_\omega^2 \cdot N^+} \cdot \frac{\left(\sigma'_{OB_P} + a \right)}{\frac{2N^+}{N^+ + 1}} \tag{E3}$$

By means of substitution we can now present the stress acting on the structure as a function of the surface load as

$$\sigma'_{OC_P} + a = \frac{(f_\omega^2 + 1) \cdot N^+}{1 + f_\omega^2 \cdot N^+} \cdot \frac{1}{\frac{2N^+}{N^+ + 1}} \cdot e^{2 \cdot \omega_P \cdot tan(\phi')} \cdot \frac{2N^+}{N^+ + 1} \cdot (q'_v + a) \tag{E4}$$

Which simplifies to the desired result as

$$\sigma'_{OC_P} + a = \frac{(f_\omega^2 + 1) \cdot N^+}{1 + f_\omega^2 \cdot N^+} \cdot e^{2 \cdot \omega_P \cdot tan(\phi')} \cdot (q'_v + a) \tag{E5}$$

Combined stressfields – active case

The stresses acting on plane OA_A can be calculated by means of equation (C11) as

$$\sigma'_{OA_A} + a = \frac{2N^-}{N^- + 1} \cdot (q'_v + a) \tag{E6}$$

The stresses acting on plane OB_A can be calculated by means of equation (D8) as

$$\sigma'_{OB_A} + a = \frac{\left(\sigma'_{OA_A} + a\right)}{e^{2 \cdot \omega_A \cdot tan(\phi')}} \tag{E7}$$

The stresses acting on plane OC_A can be calculated by means of equations (C11) and (C21) as

$$\sigma'_{OC_A} + a = \frac{(f_\omega^2 + 1) \cdot N^-}{1 + f_\omega^2 \cdot N^-} \cdot \frac{\left(\sigma'_{OB_A} + a\right)}{\frac{2N^-}{N^- + 1}} \tag{E8}$$

By means of substitution we can now present the stress acting on the structure as a function of the surface load as

$$\sigma'_{OC_A} + a = \frac{(f_\omega^2 + 1) \cdot N^-}{1 + f_\omega^2 \cdot N^-} \cdot \frac{1}{\frac{2N^-}{N^- + 1} \cdot e^{2 \cdot \omega_A \cdot tan(\phi')}} \cdot \frac{2N^-}{N^- + 1} \cdot (q'_v + a) \tag{E9}$$

Which simplifies to the desired result as

$$\sigma'_{OC_A} + a = \frac{(f_\omega^2 + 1) \cdot N^-}{1 + f_\omega^2 \cdot N^-} \cdot e^{-2 \cdot \omega_A \cdot tan(\phi')} \cdot (q'_v + a) \tag{E10}$$

What is interesting to see is that if we now change signs for ϕ' in the active case. Equation (E10) transforms into (E5). Equation (E5) will therefore be presented in thesis without identifying the earth pressure case.

The Stressfields shown in Figure 2.6 are valid for $r \geq 0$. Although this is not covered in this thesis, the NTNU method proposes a planar shear surface for negative values of roughness and the earth pressures in that case can be calculated using equation (23). For sloped terrain behind the wall, the parameter r in equation (23) is interchanged for the parameter t. This is an approximation and is not without limitations (Janbu, et al., 2006).

The derivations shown for both cases of pressures are done with the assumption that the soil is weightless. The general assumption is then that the equations also apply for soils with weight. When calculating earth pressures against structures the term q'_v in equations (E5) and (E10) is then substituted with σ'_v which is calculated using equation (2).

Appendix F: At rest coefficient of earth pressure

The generalized Hooke's law for an isotropic homogenous material can be presented as

$$\Delta\varepsilon_1 = \frac{1}{E}(\Delta\sigma_1' - v\Delta\sigma_2' - v\Delta\sigma_3')$$
$$\Delta\varepsilon_2 = \frac{1}{E}(-v\Delta\sigma_1' + \Delta\sigma_2' - v\Delta\sigma_3') \qquad \text{(F1)}$$
$$\Delta\varepsilon_3 = \frac{1}{E}(-v\Delta\sigma_1' - v\Delta\sigma_2' + \Delta\sigma_3')$$

Where ε stands for the strain, σ' is the principal stress and v is Poisson's ratio (Ugural, et al., 2003). Hook's law implies that if we have a change in strain in one principal direction we will create stresses in the other two principal directions and causing either strains there as well.

If look at the situation created in an oedometer we do not allow for any strains in the minor principal direction and the stress in the minor and intermediate principal direction is the same. The oedometer situation can be seen in Figure 0.7.
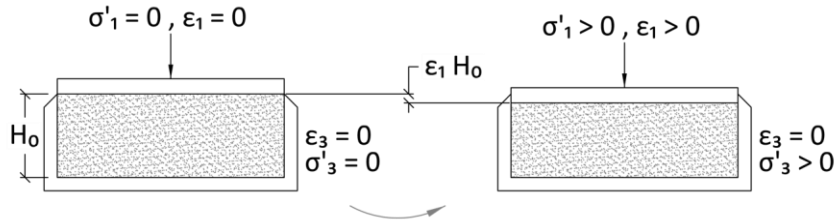
Figure 0.7: A soil sample under compression in an oedometer cell.

Using the equation for the minor principal strain in equations (F1) and putting $\sigma_2' = \sigma_3'$ and zero strain we can derive the relationship

$$\Delta\sigma_3' = \Delta\sigma_1' \cdot \frac{v}{1-v} \qquad \text{(F11)}$$

Thus creating a link between the horizontal and vertical stress by means of the theory of elasticity. The term involving Poisson's ratio can be called K_0 as referred to by equation (9) (Nordal, 2009).

Appendix G: Calculations by coordinates

The area of a non-self-intersecting polygon defined by finite number of points, (x_n, y_n), can be calculated as

$$A = \frac{1}{2} \cdot \sum_{i=0}^{N-1} [x_i \cdot y_{i+1} - x_{i+1} \cdot y_i] \tag{G1}$$

The centroid of the polygon can then be calculated as

$$x_c = \frac{1}{6A} \cdot \sum_{i=0}^{N-1} [(x_i + x_{i+1}) \cdot (x_i \cdot y_{i+1} - x_{i+1} \cdot y_i)] \tag{G2}$$

And

$$y_c = \frac{1}{6A} \cdot \sum_{i=0}^{N-1} [(x_i + x_{i+1}) \cdot (x_i \cdot y_{i+1} - x_{i+1} \cdot y_i)] \tag{G3}$$

This method assumes that the points be in order around the perimeter and to get a correct sign on the area their number should increase along a counterclockwise direction (Bourke, 1988). As I have chosen to increment the point numbers along clockwise paths around the stress shapes, see Figure 4.1, equations (G1) to (G3) is used with a change in sign.

While there are more common methods of calculating the area and center of mass of stress shapes, this one is chosen because it can easily be extended to account for more complex stress cases.

Appendix H: Results from hand calculations

Table 0.1: Shows the results from toe optimization of cases in Table 4.9.

Case	H [m]	W [m]	W_{toe} [m]	E_A [kN]	r_b [-]	R_V [kN]	e [m]	B_0 [m]	q_v [kPa]	Foundation material	Backfill material
1	3	1,4	0,3	36,3	0,599	86,4	-0,29	0,77	111,6	Bl. rock	Bl. rock
2	5	2,2	0,5	84,1	0,565	216,4	-0,36	1,51	143,2	Bl. rock	Bl. rock
3	7	3,1	0,8	140,9	0,532	389,9	-0,45	2,18	179,1	Bl. rock	Bl. rock
4	10	4,3	1,2	261,6	0,516	754,7	-0,51	3,31	228,3	Bl. rock	Bl. rock
5	3	2,2	0,5	66,8	0,695	133,3	-0,31	1,62	82,5	Bl. rock	Clay or cl. silt
6	5	3,9	1,2	156,0	0,662	332,7	-0,25	3,35	99,4	Bl. rock	Clay or cl. silt
7	7	5,4	1,9	262,9	0,636	592,2	-0,17	5,08	116,5	Bl. rock	Clay or cl. silt
8	10	8,1	2,6	490,2	0,566	1266,8	0,00	8,05	157,3	Bl. rock	Clay or cl. silt
9	3	1,7	0,4	47,5	0,649	103,0	-0,30	1,08	95,2	Bl. rock	Gravel
10	5	2,9	0,8	110,2	0,616	256,3	-0,34	2,17	117,8	Bl. rock	Gravel
11	**7**	**3,9**	**1,2**	**184,6**	**0,585**	**458,4**	**-0,37**	**3,21**	**142,6**	**Bl. rock**	**Gravel**
12	10	5,7	1,9	342,8	0,571	883,7	-0,33	5,02	176,2	Bl. rock	Gravel
13	3	2,7	0,2	36,3	0,608	171,1	-0,05	2,63	65,2	Clay or cl. silt	Bl. rock
14	5	4,0	0,4	84,1	0,598	403,5	-0,05	3,94	102,3	Clay or cl. silt	Bl. rock
15	7	5,1	0,6	140,9	0,585	690,8	-0,06	5,02	137,6	Clay or cl. silt	Bl. rock
16	10	6,9	0,9	261,6	0,580	1294,0	-0,05	6,80	190,3	Clay or cl. silt	Bl. rock
17	3	6,8	0,1	66,8	0,440	435,6	0,00	6,78	64,2	Clay or cl. silt	Clay or cl. silt
18	5	10,4	0,2	156,0	0,409	1094,5	0,00	10,45	104,8	Clay or cl. silt	Clay or cl. silt
19	7	13,7	0,3	262,9	0,380	1985,1	0,00	13,71	144,8	Clay or cl. silt	Clay or cl. silt
20	10	18,9	0,4	490,2	0,363	3880,1	0,00	18,89	205,5	Clay or cl. silt	Clay or cl. silt
21	3	3,9	0,3	47,5	0,570	239,1	0,00	3,89	61,5	Clay or cl. silt	Gravel
22	5	5,8	0,4	110,2	0,546	578,8	0,00	5,83	99,3	Clay or cl. silt	Gravel
23	**7**	**7,5**	**0,6**	**184,6**	**0,525**	**1009,9**	**0,00**	**7,46**	**135,4**	**Clay or cl. silt**	**Gravel**
24	10	10,1	0,8	342,8	0,509	1932,1	0,00	10,08	191,6	Clay or cl. silt	Gravel
25	3	2,2	0,4	36,3	0,535	130,5	-0,06	2,09	62,5	Gravel	Bl. rock
26	5	3,3	0,7	84,1	0,529	306,1	-0,07	3,16	96,9	Gravel	Bl. rock
27	7	4,2	1,0	140,9	0,517	525,7	-0,10	4,03	130,3	Gravel	Bl. rock
28	10	5,7	1,4	261,6	0,513	982,8	-0,11	5,48	179,4	Gravel	Bl. rock
29	3	6,2	0,2	66,8	0,324	397,2	0,00	6,21	64,0	Gravel	Clay or cl. silt
30	5	9,7	0,2	156,0	0,297	1012,8	0,00	9,70	104,5	Gravel	Clay or cl. silt
31	7	12,9	0,3	262,9	0,272	1861,4	0,00	12,90	144,3	Gravel	Clay or cl. silt
32	10	17,9	0,4	490,2	0,257	3670,6	0,00	17,91	205,0	Gravel	Clay or cl. silt
33	3	3,2	0,5	47,5	0,480	190,9	0,00	3,22	59,2	Gravel	Gravel
34	5	4,9	0,7	110,2	0,456	465,8	0,00	4,87	95,6	Gravel	Gravel
35	**7**	**6,3**	**0,9**	**184,6**	**0,436**	**815,1**	**0,00**	**6,28**	**129,7**	**Gravel**	**Gravel**
36	10	8,5	1,2	342,8	0,420	1571,8	0,00	8,54	184,0	Gravel	Gravel

As the eccentricity of the vertical resultant force is not always zero as can be seen in Table 0.1 it is interesting to see how the eccentricity of the force resultant for changes with varying toe width for different cases of foundation and backfill masses. This has been done for the selected cases highlighted with bold letters in Table 0.1 and can be seen fin Figure 0.8 to Figure 0.10.
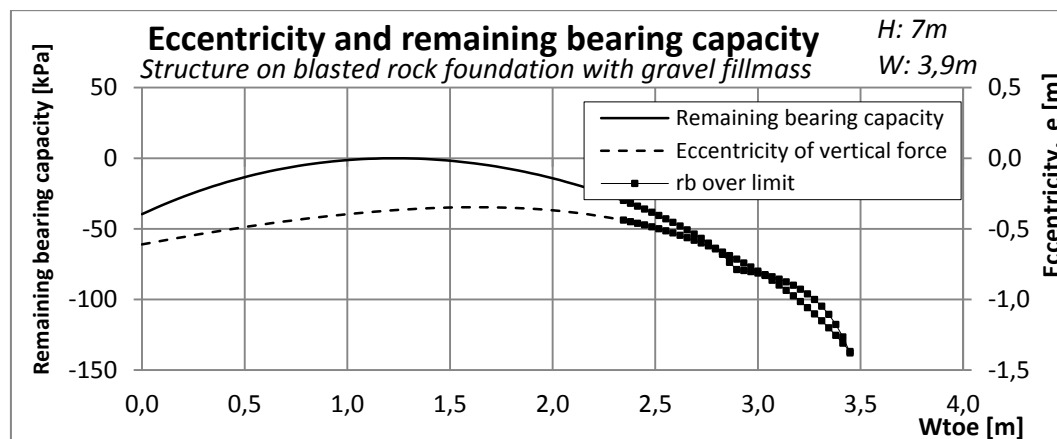
Figure 0.8: Eccentricity and remaining bearing capacity, blasted rock foundation.
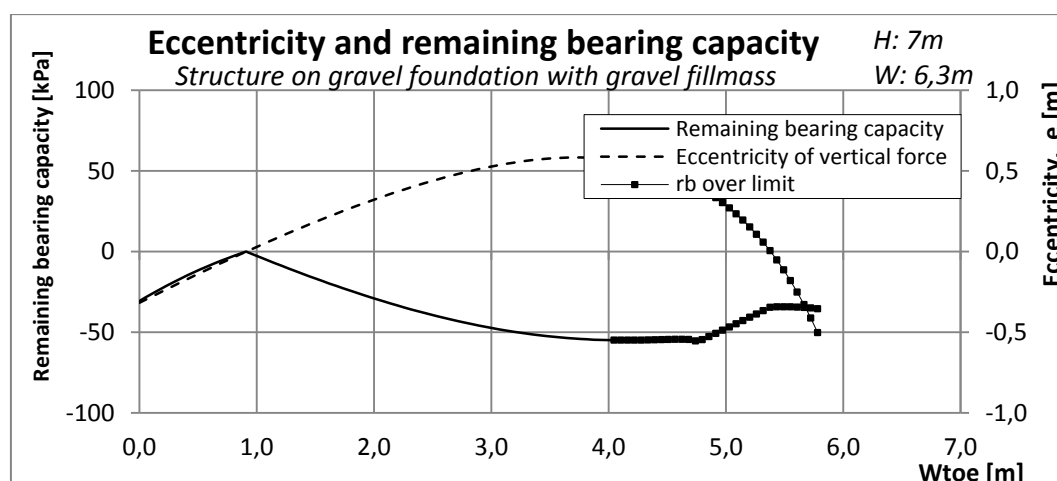
Figure 0.9: Eccentricity and remaining bearing capacity, gravel foundation.
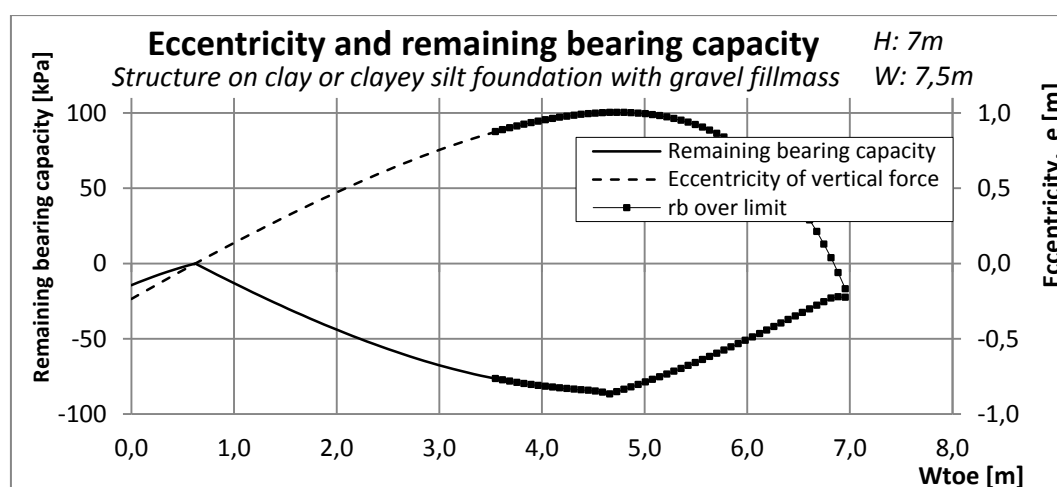
Figure 0.10: Eccentricity and remaining bearing capacity, clay/clayey-silt foundation.

The results from hand calculations of L-shaped retaining walls with varying height, foundation material and backfill material for the backfill inclination of $\beta = 18°$ and a surface load of $q = 20kPa$ can be seen in Table 0.2.

Table 0.2: Wall heights and widths with a sloping backfill resulting in $\gamma_M = 1.4$.

Case	H [m]	W [m]	W_{toe} [m]	E_A [kN]	r_b [-]	R_V [kN]	e [m]	B_0 [m]	q_v [kPa]	Foundation material	Backfill material
1β	3	1,7	0,0	56,8	0,577	141,9	-0,35	1,11	127,3	Bl. rock	Bl. rock
2β	5	3,1	0,0	139,5	0,522	393,6	-0,49	2,15	183,1	Bl. rock	Bl. rock
3β	7	4,3	0,0	234,1	0,476	735,4	-0,63	3,01	244,7	Bl. rock	Bl. rock
4β	10	6,1	0,0	450,6	0,455	1493,3	-0,80	4,54	329,1	Bl. rock	Bl. rock
5β	3	5,1	0,0	209,2	0,680	435,1	-0,36	4,32	100,8	Bl. rock	Clay or cl. silt
6β	5	9,8	0,0	581,5	0,591	1437,3	-0,33	9,17	156,8	Bl. rock	Clay or cl. silt
7β	7	14,0	0,0	1008,5	0,527	2843,8	-0,33	13,36	212,8	Bl. rock	Clay or cl. silt
8β	10	22,3	0,0	2179,7	0,496	6614,2	-0,14	22,04	300,1	Bl. rock	Clay or cl. silt
9β	3	2,6	0,0	89,5	0,625	204,3	-0,39	1,84	110,9	Bl. rock	Gravel
10β	5	4,7	0,0	225,5	0,554	596,2	-0,50	3,69	161,7	Bl. rock	Gravel
11β	7	6,5	0,0	379,8	0,497	1135,5	-0,62	5,26	215,7	Bl. rock	Gravel
12β	10	9,7	0,0	750,2	0,470	2400,6	-0,73	8,21	292,5	Bl. rock	Gravel
13β	3	4,4	0,0	81,0	0,670	347,1	-0,03	4,29	80,8	Clay or cl. silt	Bl. rock
14β	5	6,5	0,0	188,0	0,646	835,0	-0,08	6,31	132,3	Clay or cl. silt	Bl. rock
15β	7	7,9	0,0	296,9	0,613	1389,8	-0,18	7,56	183,8	Clay or cl. silt	Bl. rock
16β	10	10,8	0,0	565,3	0,605	2682,1	-0,25	10,32	259,9	Clay or cl. silt	Bl. rock
17β	3	-	-	-	-	-	-	-	-	Clay or cl. silt	Clay or cl. silt
18β	5	-	-	-	-	-	-	-	-	Clay or cl. silt	Clay or cl. silt
19β	7	-	-	-	-	-	-	-	-	Clay or cl. silt	Clay or cl. silt
20β	10	-	-	-	-	-	-	-	-	Clay or cl. silt	Clay or cl. silt
21β	3	8,9	0,0	188,1	0,655	824,0	0,31	8,29	99,4	Clay or cl. silt	Gravel
22β	5	13,0	0,0	422,4	0,637	1904,0	0,36	12,21	155,9	Clay or cl. silt	Gravel
23β	7	14,9	0,0	615,9	0,610	2896,2	0,24	14,42	200,8	Clay or cl. silt	Gravel
24β	10	20,6	0,0	1189,6	0,603	5661,8	0,34	19,92	284,2	Clay or cl. silt	Gravel
25β	3	3,2	0,0	69,5	0,539	248,6	-0,15	2,90	85,8	Gravel	Bl. rock
26β	5	4,9	0,0	163,5	0,516	610,8	-0,25	4,34	140,7	Gravel	Bl. rock
27β	7	6,1	0,0	264,7	0,484	1054,5	-0,38	5,36	196,6	Gravel	Bl. rock
28β	10	8,4	0,0	503,2	0,476	2038,9	-0,50	7,35	277,6	Gravel	Bl. rock
29β	3	**48,4**	0,0	2756,2	0,475	11187,9	5,38	37,66	297,1	Gravel	Clay or cl. silt
30β	5	**69,5**	0,0	5815,6	0,466	24042,1	7,36	54,75	439,1	Gravel	Clay or cl. silt
31β	7	**75,5**	0,0	7167,7	0,448	30823,3	7,27	60,94	505,8	Gravel	Clay or cl. silt
32β	10	**107,5**	0,0	14528,5	0,447	62604,3	10,36	86,78	721,4	Gravel	Clay or cl. silt
33β	3	5,6	0,0	132,1	0,545	467,4	-0,03	5,54	84,3	Gravel	Gravel
34β	5	8,5	0,0	309,3	0,519	1147,5	-0,07	8,36	137,2	Gravel	Gravel
35β	7	10,7	0,0	489,4	0,483	1953,5	-0,16	10,36	188,6	Gravel	Gravel
36β	10	14,7	0,0	940,3	0,475	3813,2	-0,21	14,32	266,3	Gravel	Gravel

Table 0.3: Shows the results from toe optimization of cases in Table 0.2.

Case	H [m]	W [m]	W_{toe} [m]	E_A [kN]	r_b [-]	R_V [kN]	e [m]	B_0 [m]	q_v [kPa]	Foundation material	Backfill material
1β	3	1,7	0,7	50,0	0,720	96,8	-0,28	1,12	86,1	Bl. rock	Bl. rock
2β	5	2,9	1,1	122,5	0,677	259,2	-0,33	2,21	117,2	Bl. rock	Bl. rock
3β	7	3,9	1,4	207,4	0,632	479,4	-0,41	3,10	154,6	Bl. rock	Bl. rock
4β	10	5,6	1,9	395,3	0,615	951,6	-0,44	4,72	201,8	Bl. rock	Bl. rock
5β	3	4,0	2,1	136,9	0,904	196,9	-0,08	3,86	51,0	Bl. rock	Clay or cl. silt
6β	5	7,8	1,7	433,6	0,716	863,2	-0,01	7,82	110,4	Bl. rock	Clay or cl. silt
7β	7	11,6	1,7	803,7	0,609	1935,9	-0,01	11,59	167,0	Bl. rock	Clay or cl. silt
8β	10	21,0	0,7	2019,1	0,514	5895,7	0,00	20,99	280,8	Bl. rock	Clay or cl. silt
9β	3	2,3	1,0	73,2	0,801	123,9	-0,26	1,81	68,5	Bl. rock	Gravel
10β	5	4,0	1,7	180,2	0,761	332,0	-0,22	3,61	91,9	Bl. rock	Gravel
11β	7	5,5	2,3	304,2	0,717	608,2	-0,21	5,11	119,0	Bl. rock	Gravel
12β	10	8,0	3,4	581,9	0,704	1205,8	-0,05	7,93	152,1	Bl. rock	Gravel
13β	3	4,3	0,1	79,4	0,680	335,1	0,00	4,32	77,6	Clay or cl. silt	Bl. rock
14β	5	6,4	0,3	182,5	0,664	789,2	0,00	6,39	123,5	Clay or cl. silt	Bl. rock
15β	7	7,8	0,6	283,3	0,646	1258,5	0,00	7,75	162,4	Clay or cl. silt	Bl. rock
16β	10	10,6	0,7	539,7	0,638	2429,8	0,00	10,56	230,2	Clay or cl. silt	Bl. rock
17β	3	-	-	-	-	-	-	-	-	Clay or cl. silt	Clay or cl. silt
18β	5	-	-	-	-	-	-	-	-	Clay or cl. silt	Clay or cl. silt
19β	7	-	-	-	-	-	-	-	-	Clay or cl. silt	Clay or cl. silt
20β	10	-	-	-	-	-	-	-	-	Clay or cl. silt	Clay or cl. silt
21β	3	8,9	0,0	188,1	0,655	824,0	0,31	8,29	99,4	Clay or cl. silt	Gravel
22β	5	12,9	0,0	422,4	0,637	1904,0	0,36	12,21	155,9	Clay or cl. silt	Gravel
23β	7	14,9	0,0	615,9	0,610	2896,2	0,24	14,42	200,8	Clay or cl. silt	Gravel
24β	10	20,6	0,0	1189,6	0,603	5661,8	0,34	19,92	284,2	Clay or cl. silt	Gravel
25β	3	3,0	0,7	61,3	0,618	191,1	0,00	3,01	63,5	Gravel	Bl. rock
26β	5	4,5	1,0	145,8	0,602	466,3	0,00	4,54	102,8	Gravel	Bl. rock
27β	7	5,7	1,4	234,3	0,593	760,9	0,00	5,68	133,8	Gravel	Bl. rock
28β	10	7,7	1,8	446,4	0,582	1479,0	0,00	7,73	191,4	Gravel	Bl. rock
29β	*3*	***48,4***	*0,0*	*2756,2*	*0,475*	*11187,9*	*5,38*	*37,66*	*297,1*	*Gravel*	*Clay or cl. silt*
30β	*5*	***69,5***	*0,0*	*5815,6*	*0,466*	*24042,1*	*7,36*	*54,75*	*439,1*	*Gravel*	*Clay or cl. silt*
31β	*7*	***75,5***	*0,0*	*7167,7*	*0,448*	*30823,3*	*7,27*	*60,94*	*505,8*	*Gravel*	*Clay or cl. silt*
32β	*10*	***107,5***	*0,0*	*14528,5*	*0,447*	*62604,3*	*10,36*	*86,78*	*721,4*	*Gravel*	*Clay or cl. silt*
33β	3	5,5	0,2	128,0	0,555	444,1	0,00	5,49	80,9	Gravel	Gravel
34β	5	8,3	0,3	296,7	0,535	1068,7	0,00	8,26	129,4	Gravel	Gravel
35β	7	10,1	0,6	457,1	0,511	1723,4	0,00	10,13	170,2	Gravel	Gravel
36β	10	14,0	0,8	882,5	0,501	3396,3	0,00	14,01	242,5	Gravel	Gravel

As the backfill inclination nears the internal friction angle of the clay and clayey silt material with the material safety factor of $\gamma_M = 1.4$ the variable s in equation (26) nears the value of $s = 1$. This means that t in equation (25) nears the value of $t = 0$ resulting in

a large value for the active earth pressure coefficient. The cases involving clay or clayey silts in the backfill mass reveal much larger values of the necessary foundation width than the other two backfill materials. I was unable to find a solution for the case of a structure founded on clay or clayey silt retaining a backfill of the same material.

Two cases of a $H = 3m$ high structure founded on a blasted rock material exceeded the maximum allowed foundation roughness $r_b = 0,8$, they have been marked with brackets. The case for clay or clayey silt backfill on gravel foundation revealed extremely large foundation widths, the values are presented for the sake of completeness.

Appendix I: Failure modes from numerical simulations

The numerical simulation is done as is described in chapter 5.2. A general mesh coarseness of "fine" is selected for the initial analysis; at least one case of each material combination was selected for further analysis with local mesh refinements. This refinement entails creating a material cluster around the expected failure surface and increasing the number of elements with the refinement process two times. This is done to get an idea of how the discretization affects the results. For each case two separate analyses were run; one without terrain loading and one without. These figures show results from the 5.th step, strength reduction of model with terrain load $q = 20kPa$ applied.

"Fine"-mesh size – horizontal backfill
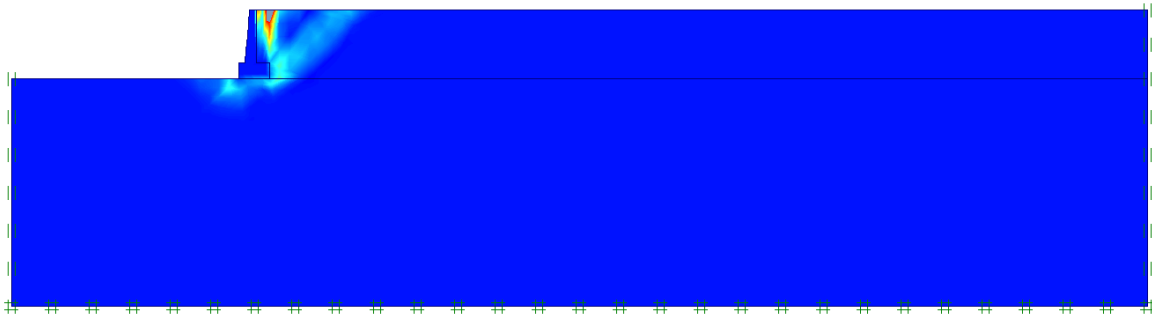
Figure 0.11: Failure mode of case 1 with terrain load.
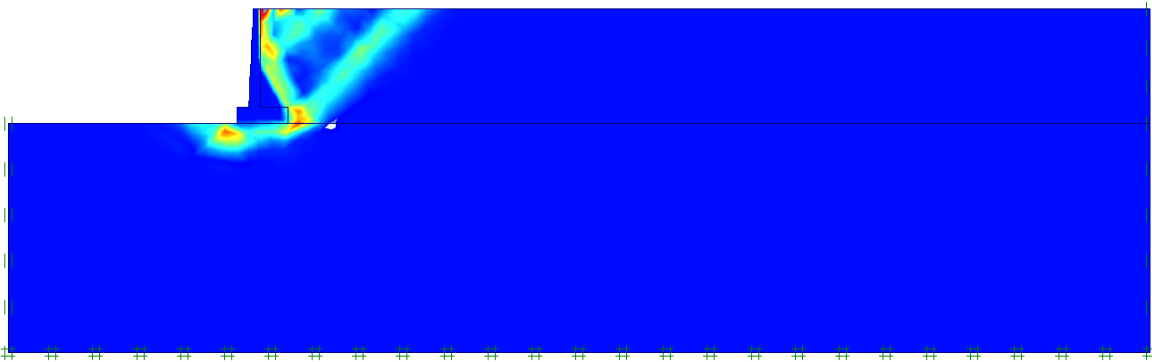
Figure 0.12: Failure mode of case 2 with terrain load.
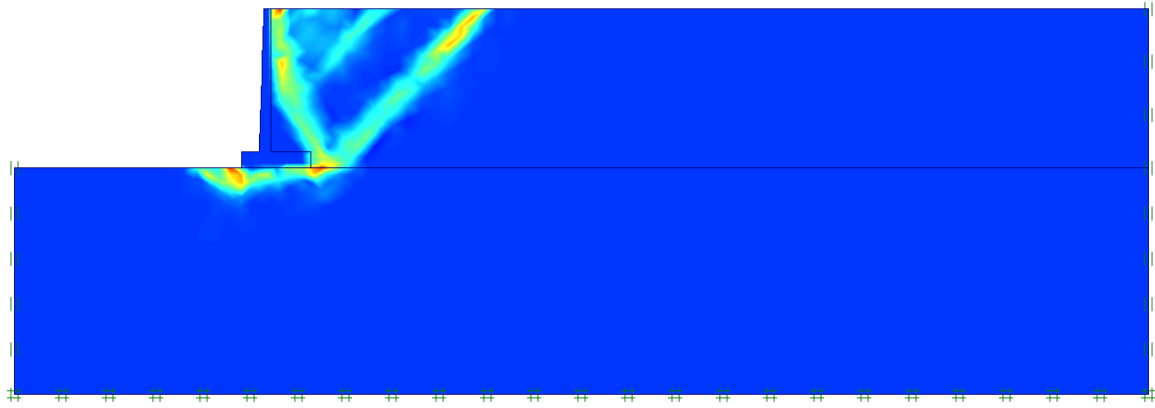
Figure 0.13: Failure mode of case 3 with terrain load.
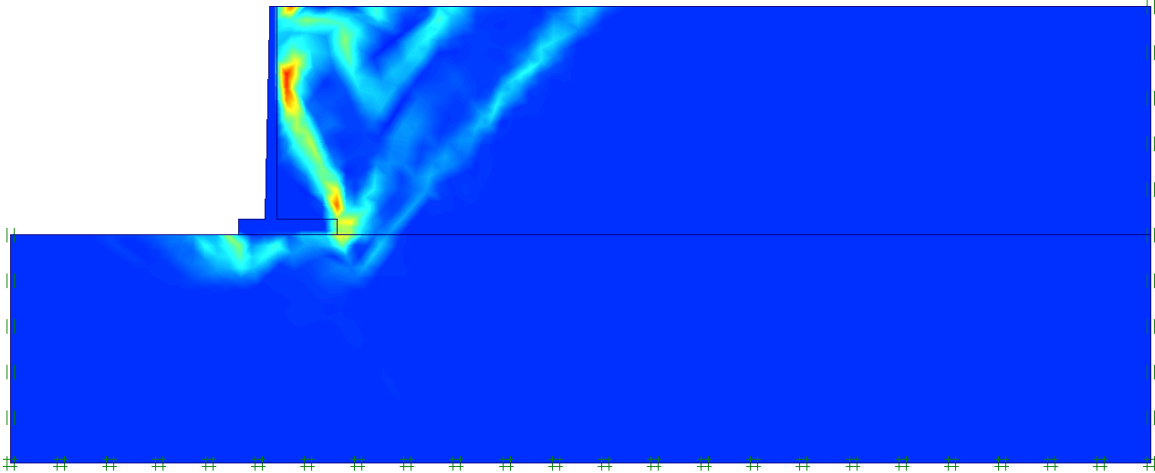
Figure 0.14: Failure mode of case 4 with terrain load.
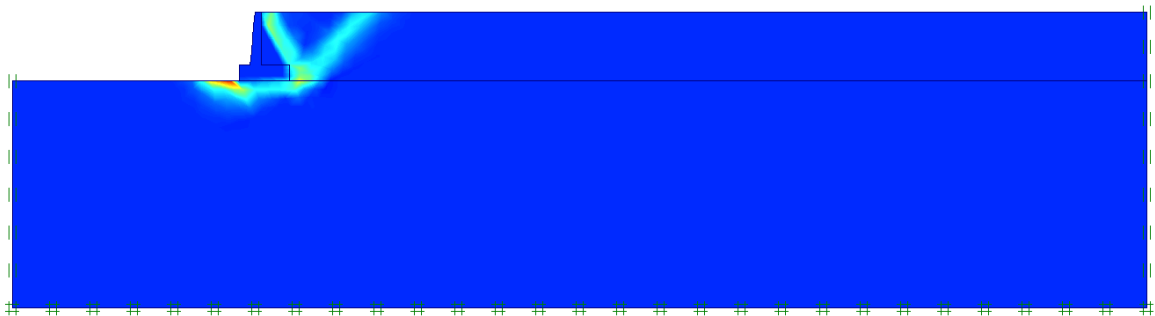
Figure 0.15: Failure mode of case 5 with terrain load.
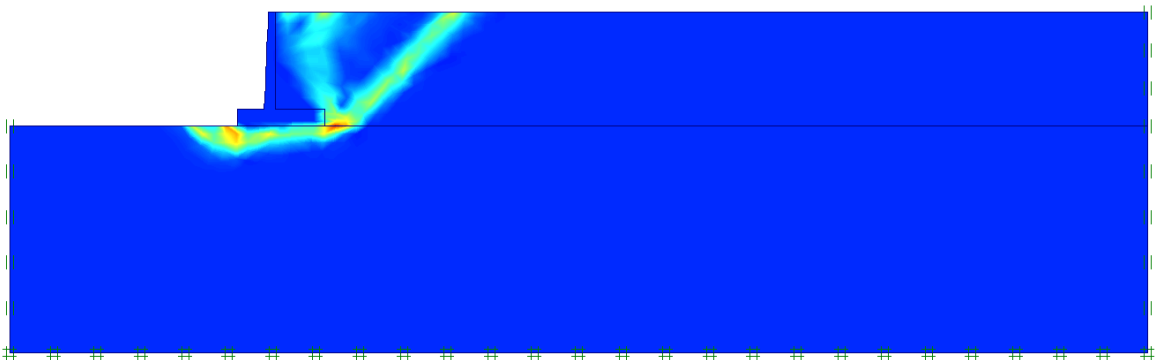
Figure 0.16: Failure mode of case 6 with terrain load.

127
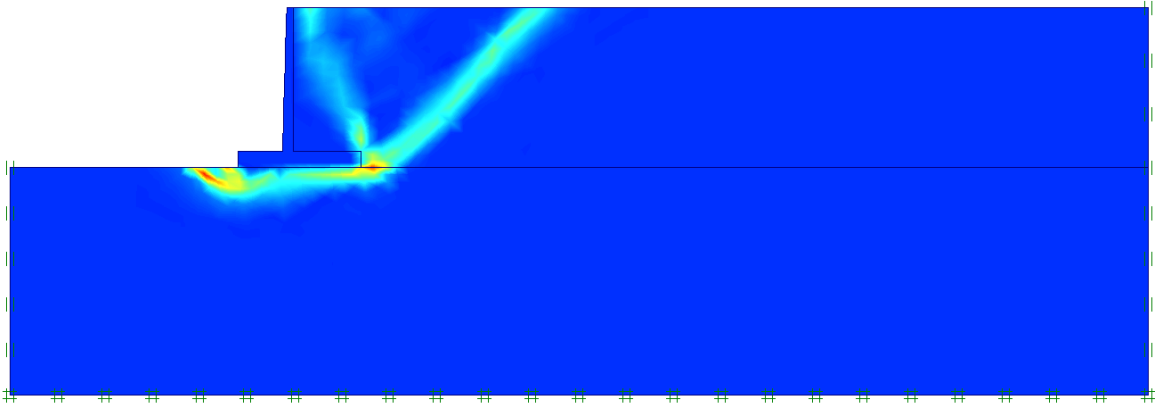
Figure 0.17: Failure mode of case 7 with terrain load.
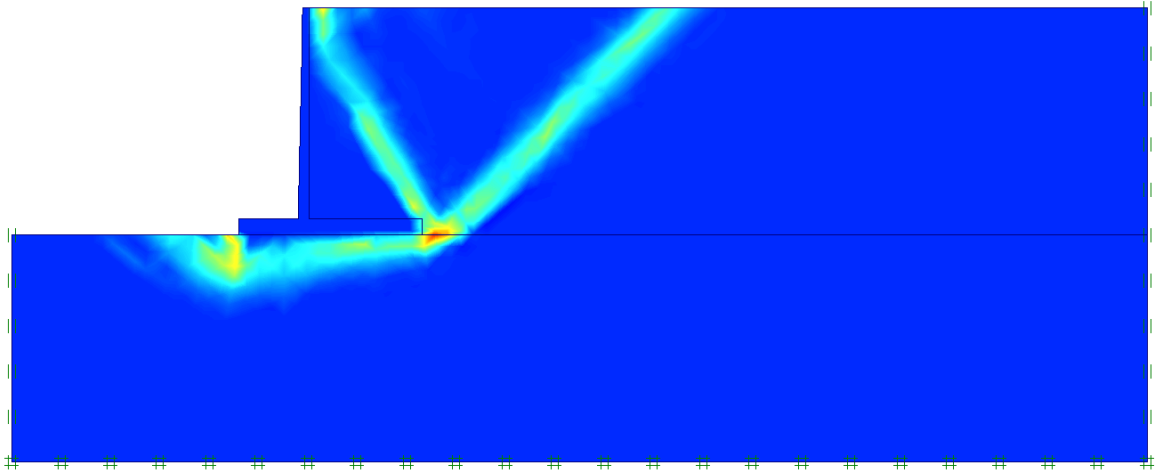
Figure 0.18: Failure mode of case 8 with terrain load.
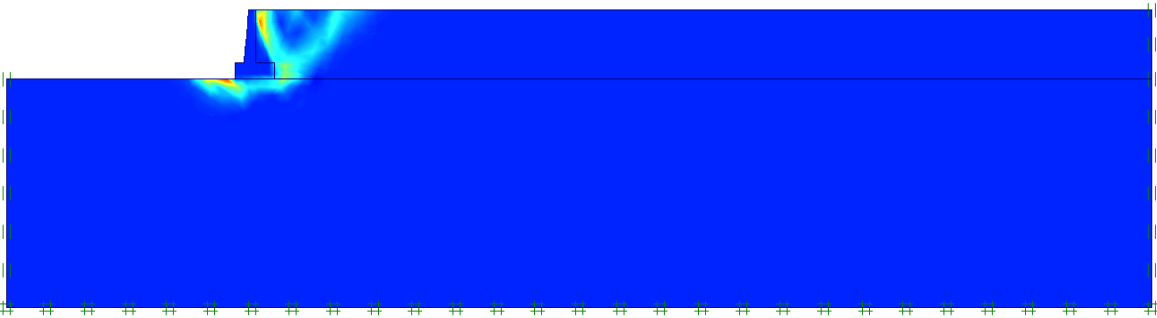
Figure 0.19: Failure mode of case 9 with terrain load.
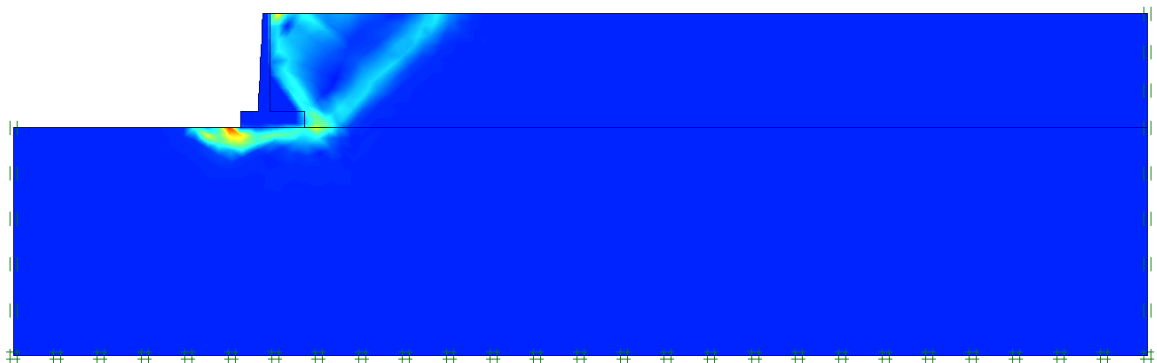
Figure 0.20: Failure mode of case 10 with terrain load.
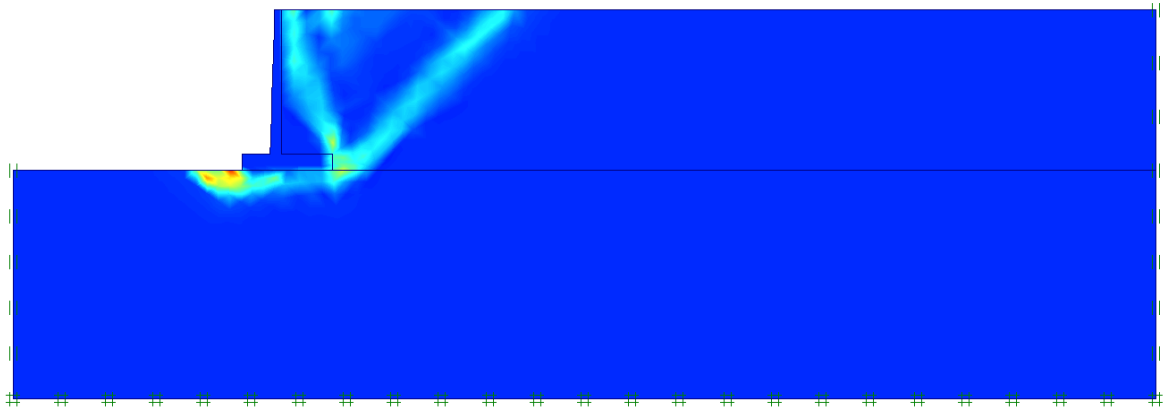
Figure 0.21: Failure mode of case 11 with terrain load.
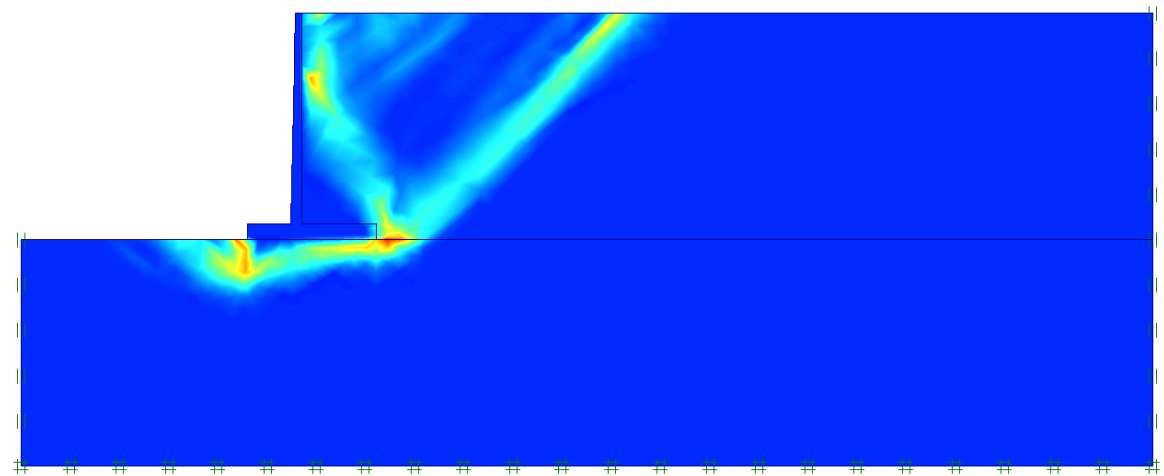
Figure 0.22: Failure mode of case 12 with terrain load.
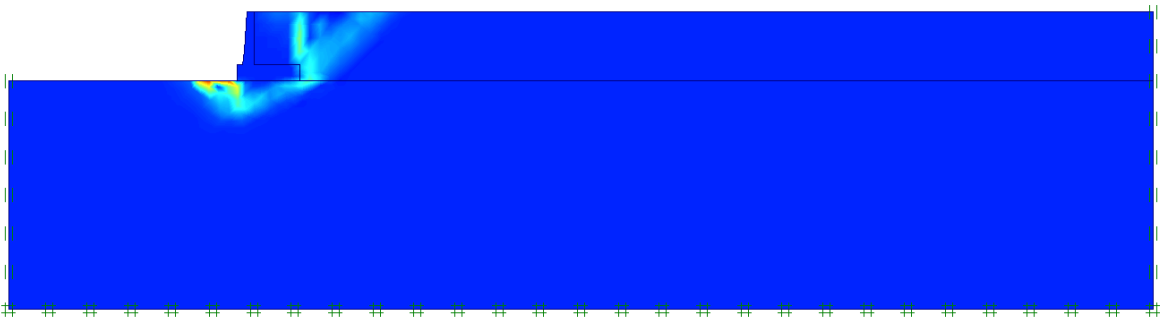
Figure 0.23: Failure mode of case 13 with terrain load.
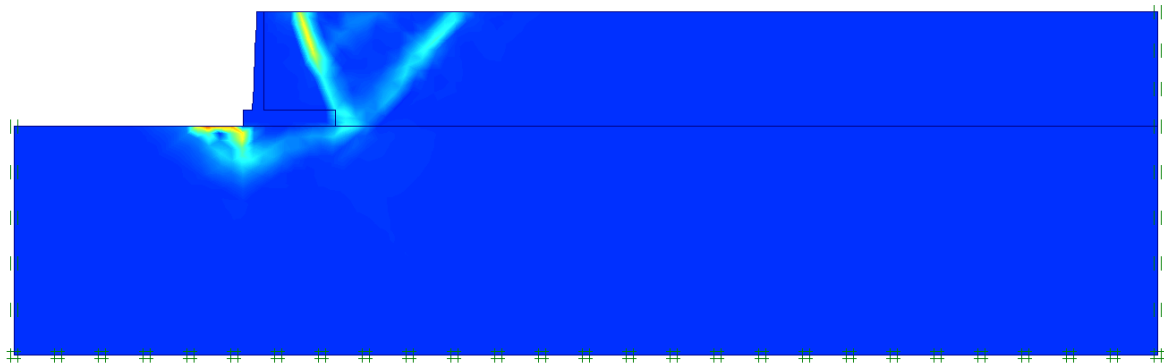
Figure 0.24: Failure mode of case 14 with terrain load.
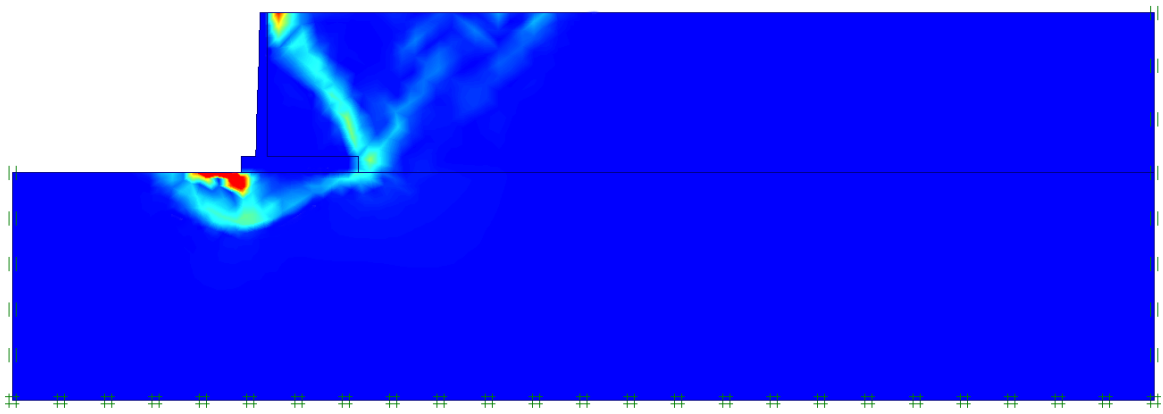
Figure 0.25: Failure mode of case 15 with terrain load.
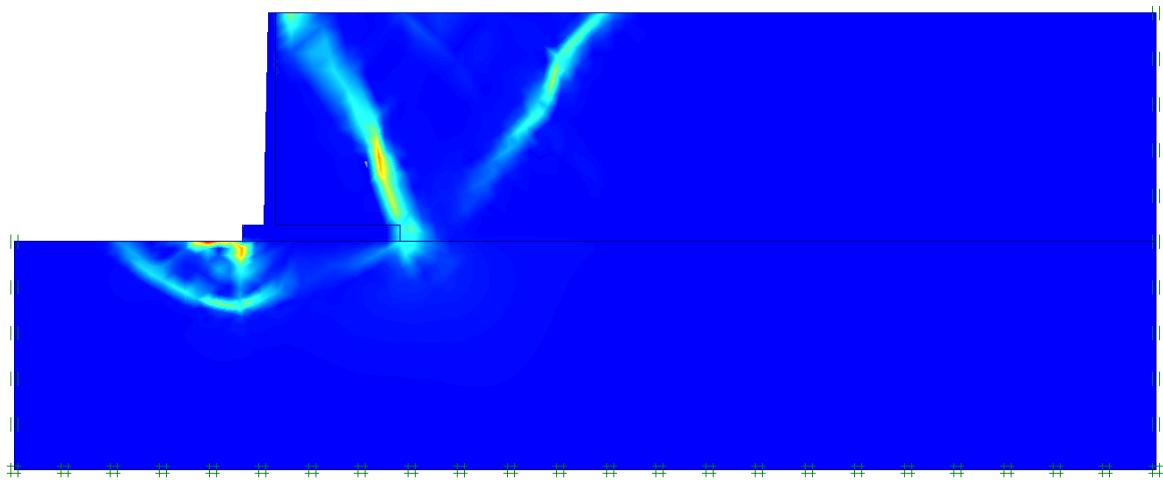
Figure 0.26: Failure mode of case 16 with terrain load.
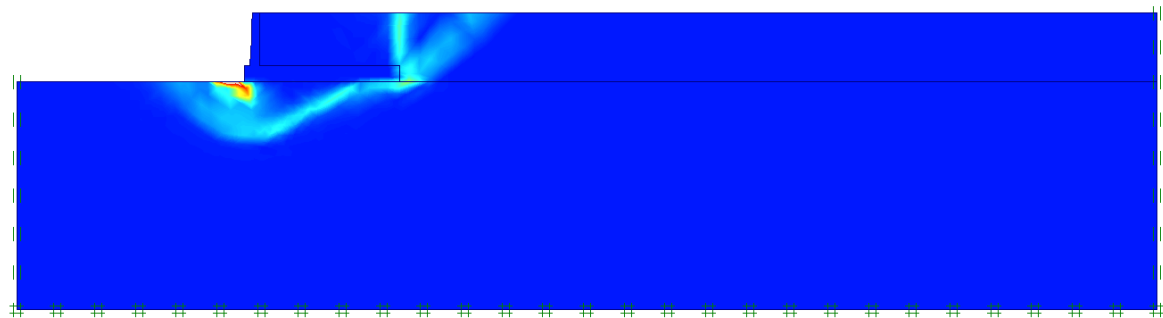
Figure 0.27: Failure mode of case 17 with terrain load.
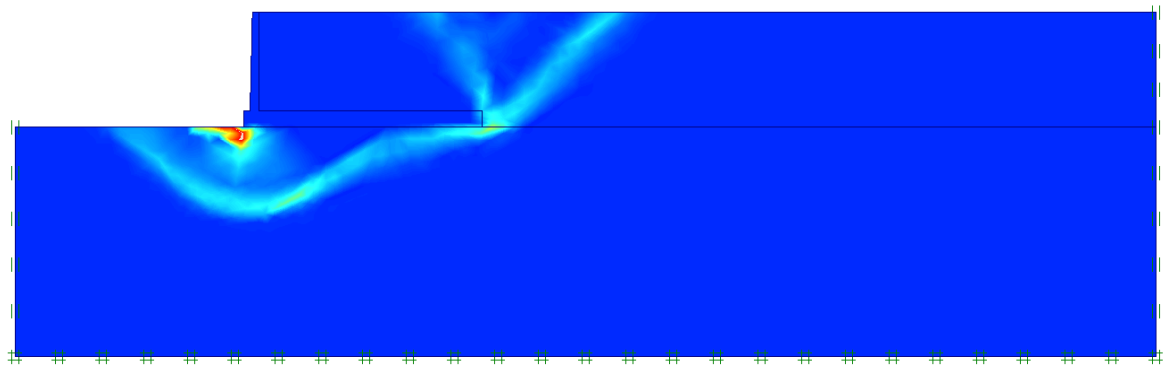
Figure 0.28: Failure mode of case 18 with terrain load.

130
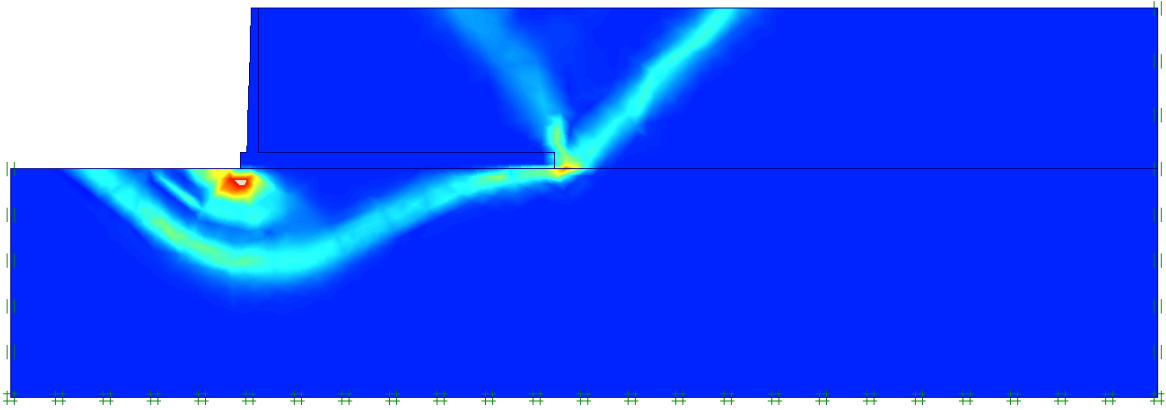
Figure 0.29: Failure mode of case 19 with terrain load.
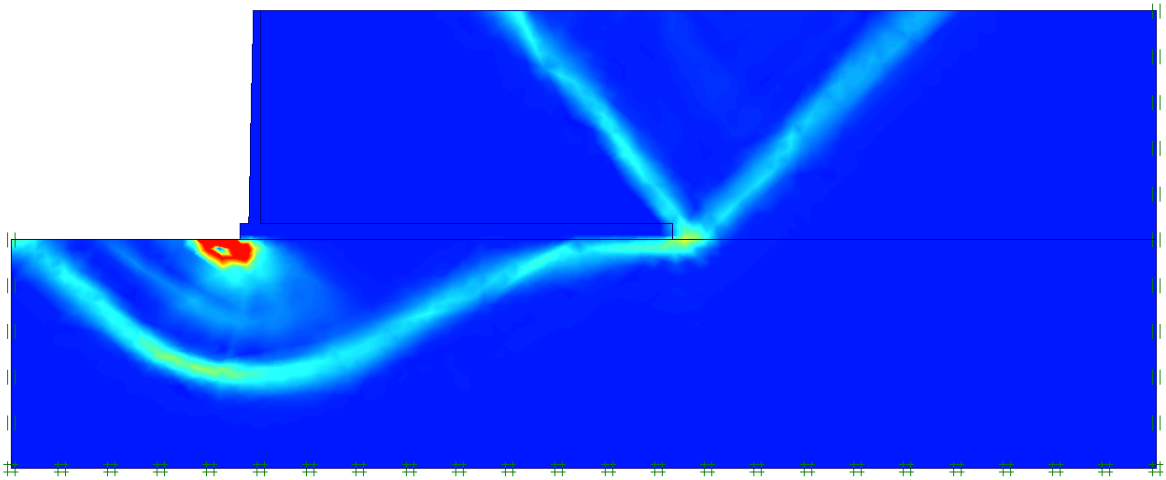
Figure 0.30: Failure mode of case 20 with terrain load.
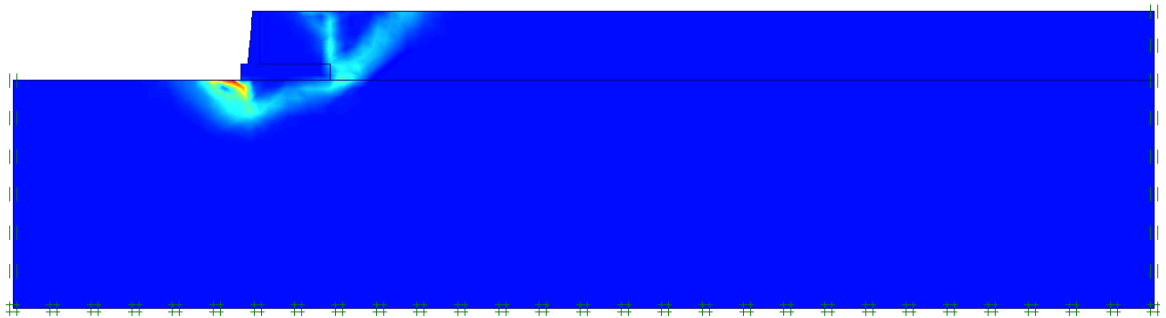
Figure 0.31: Failure mode of case 21 with terrain load.
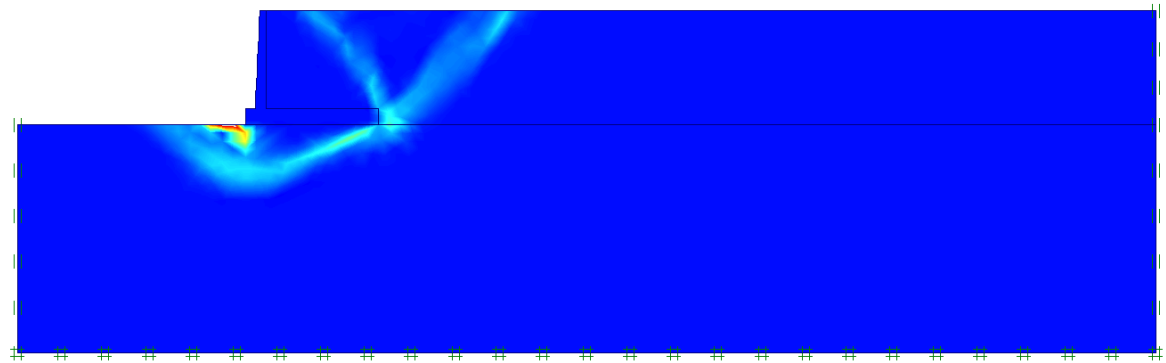
Figure 0.32: Failure mode of case 22 with terrain load.
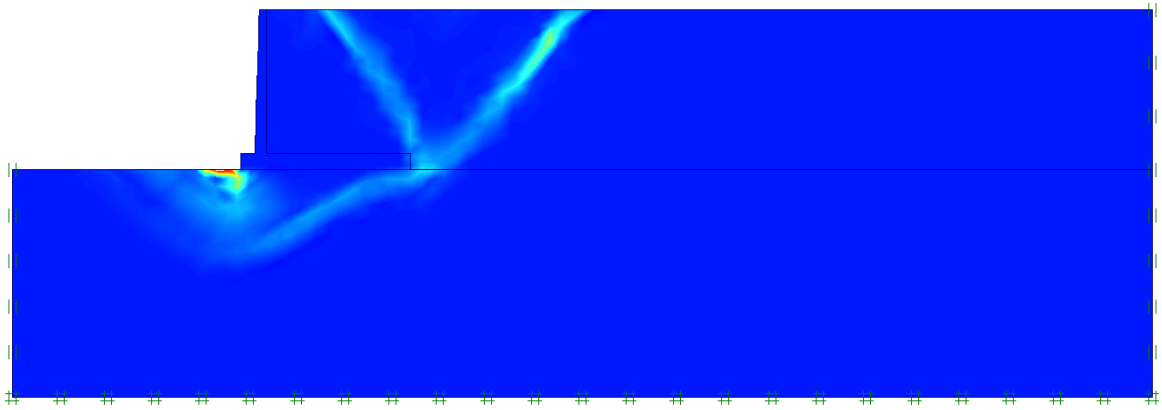
Figure 0.33: Failure mode of case 23 with terrain load.
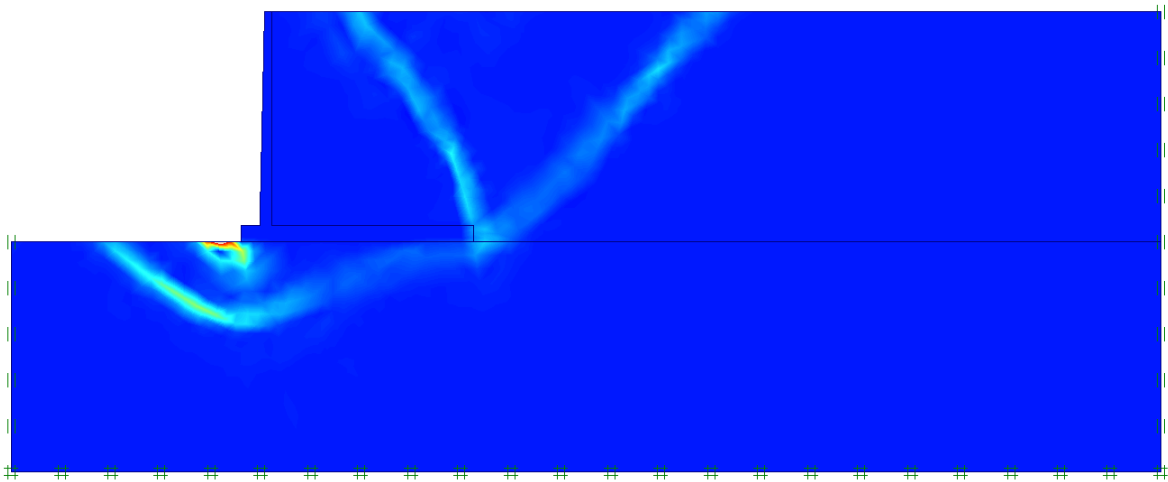
Figure 0.34: Failure mode of case 24 with terrain load.
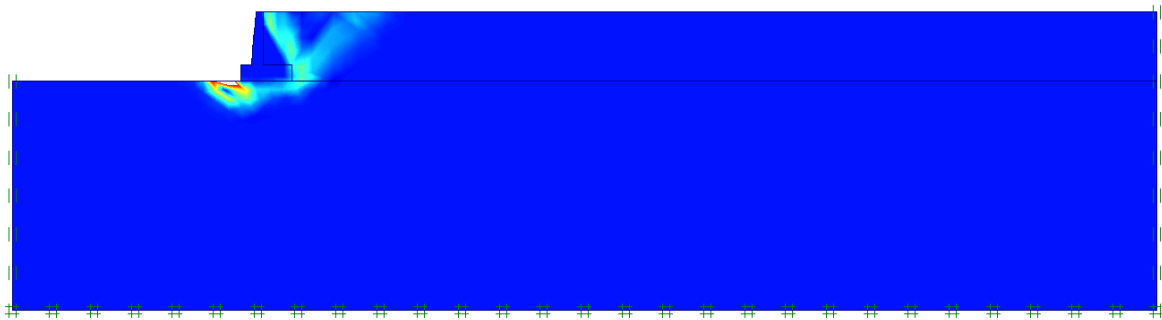
Figure 0.35: Failure mode of case 25 with terrain load.
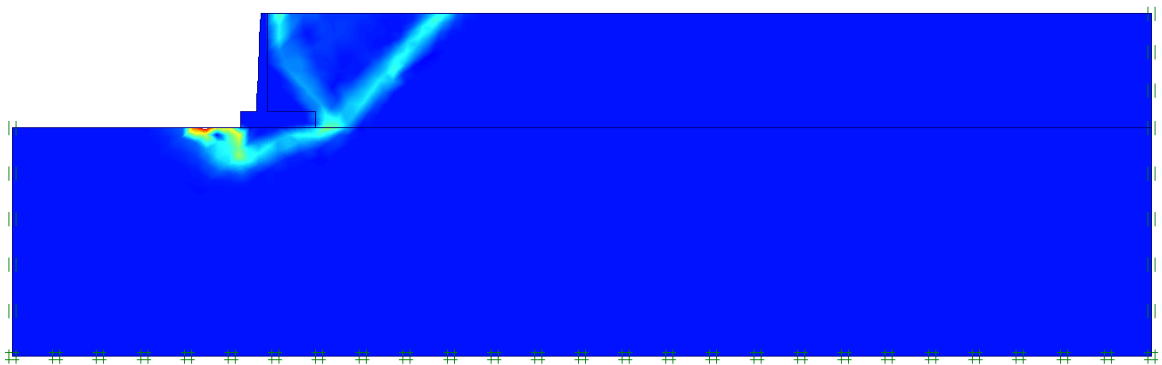
Figure 0.36: Failure mode of case 26 with terrain load.
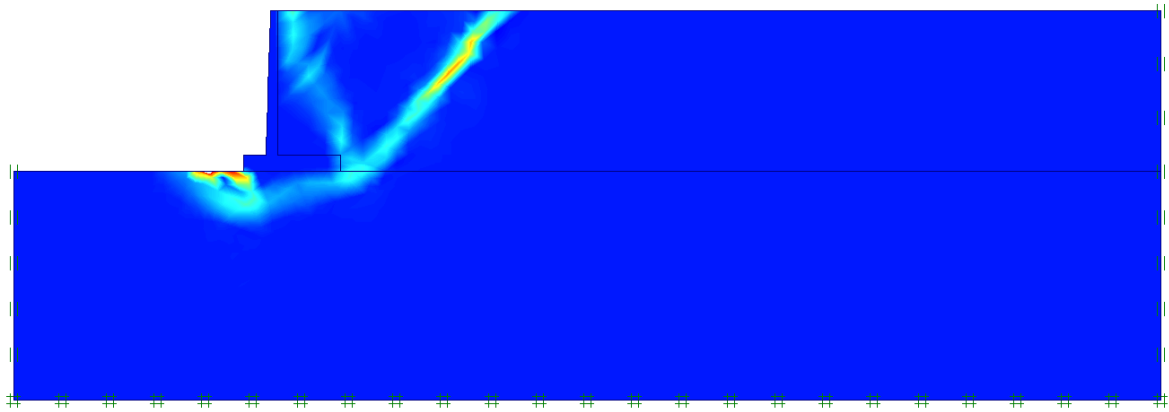
Figure 0.37: Failure mode of case 27 with terrain load.
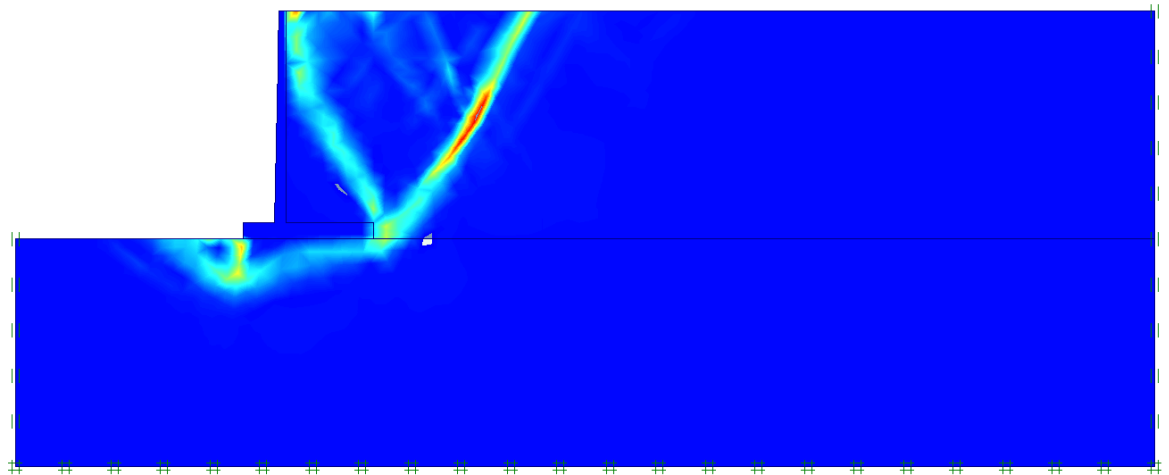
Figure 0.38: Failure mode of case 28 with terrain load.
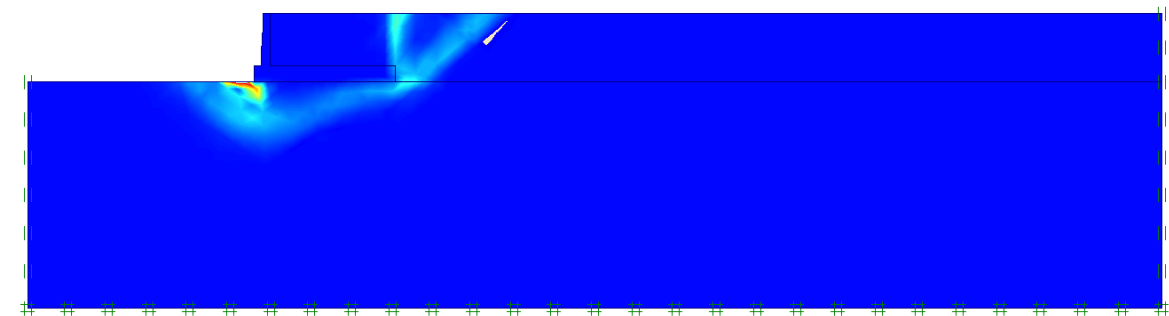
Figure 0.39: Failure mode of case 29 with terrain load.
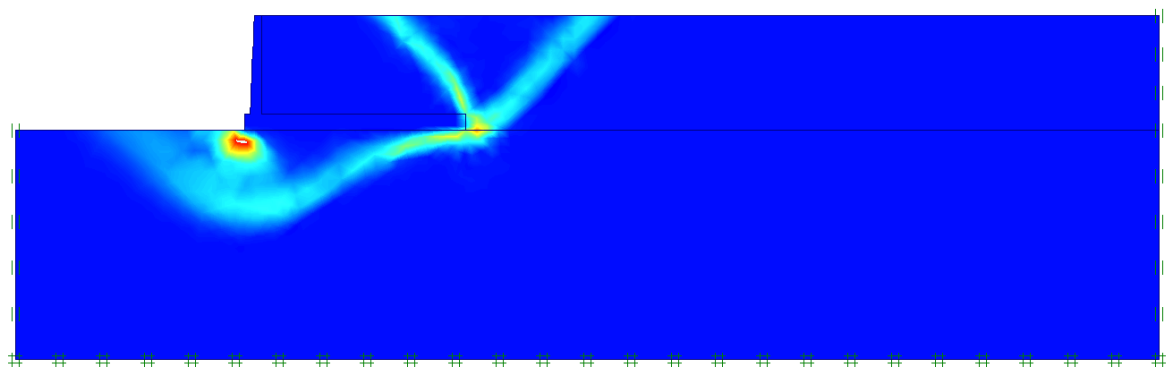
Figure 0.40: Failure mode of case 30 with terrain load.

133
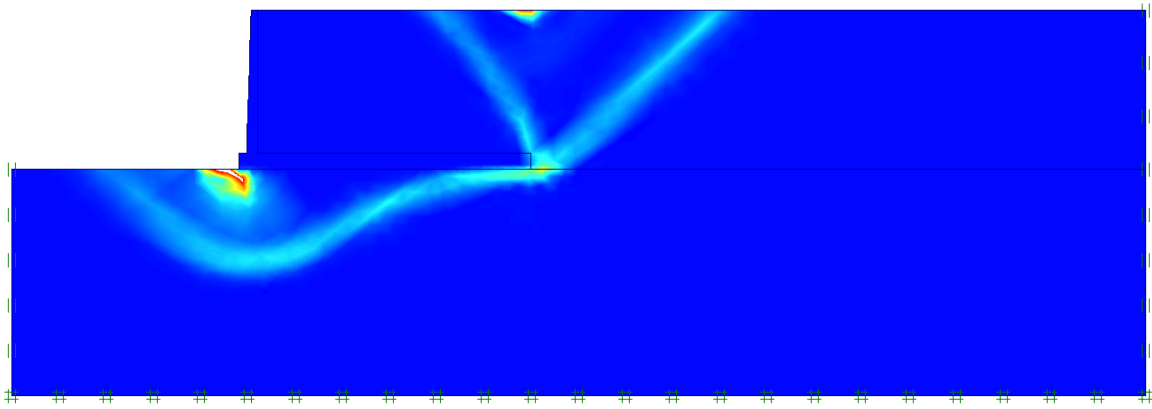
Figure 0.41: Failure mode of case 31 with terrain load.
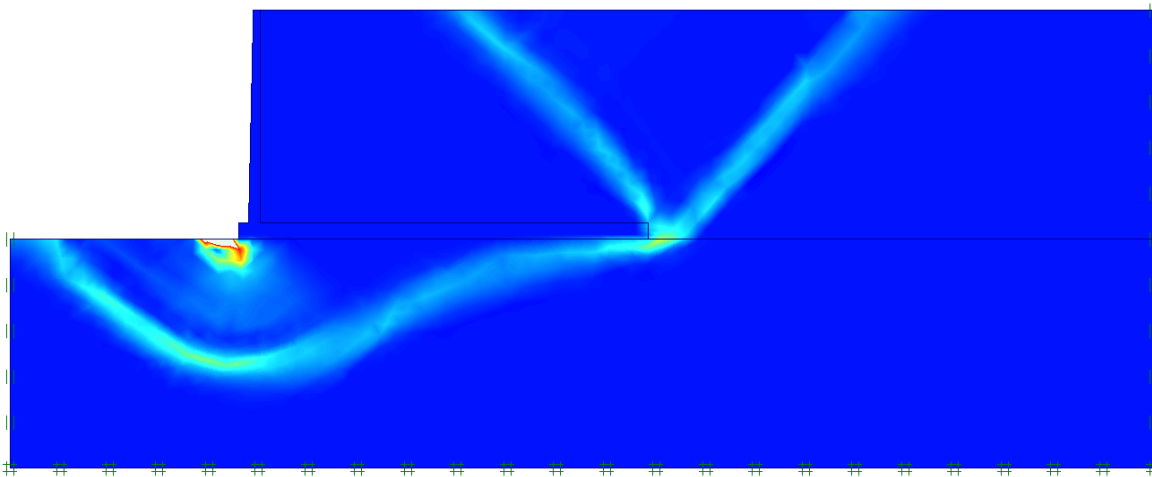
Figure 0.42: Failure mode of case 32 with terrain load.
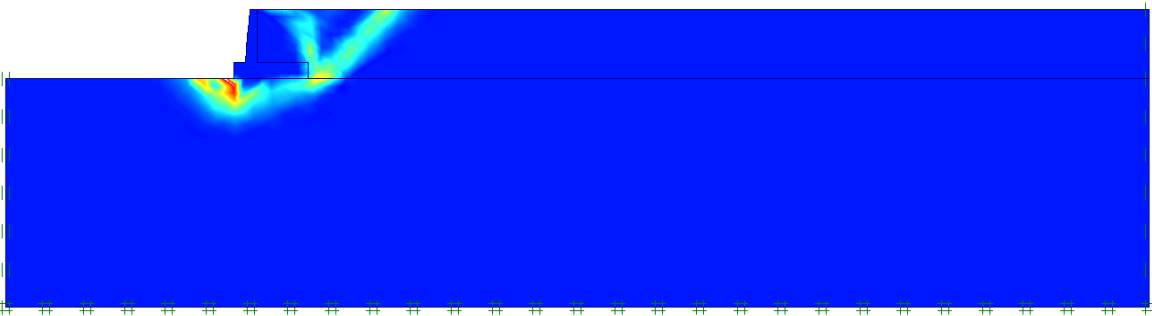
Figure 0.43: Failure mode of case 33 with terrain load.
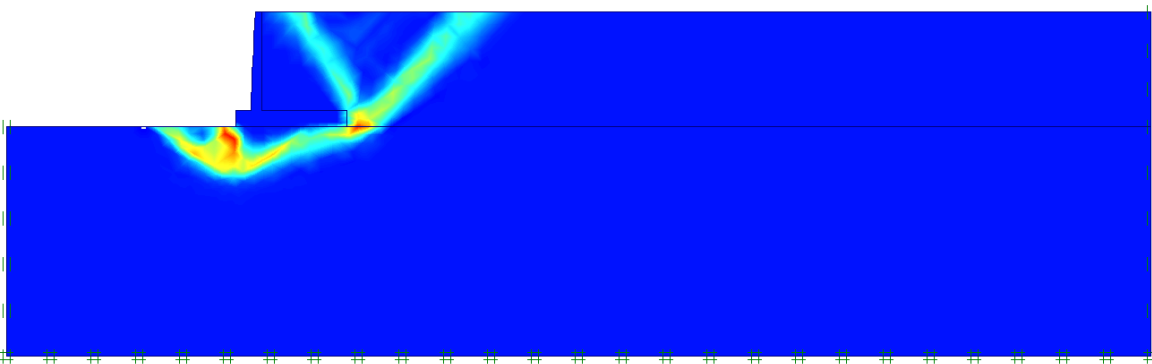
Figure 0.44: Failure mode of case 34 with terrain load.
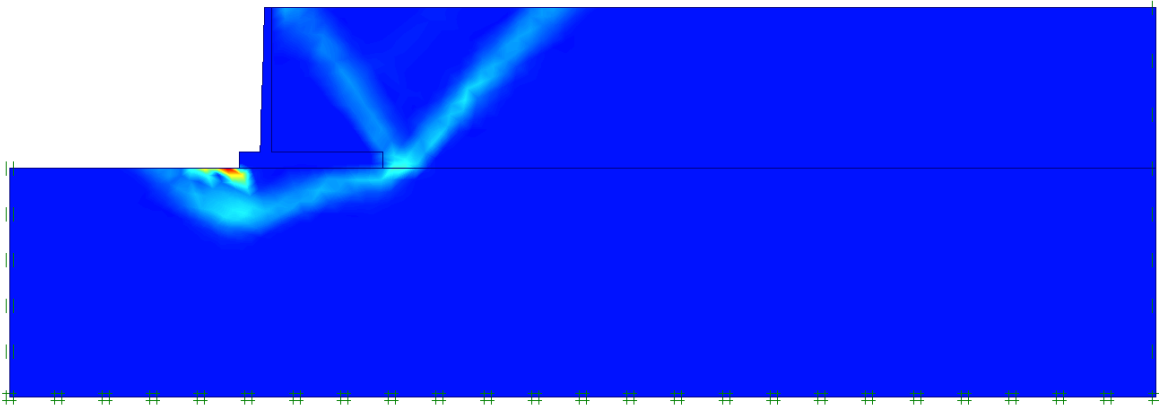
Figure 0.45: Failure mode of case 35 with terrain load.
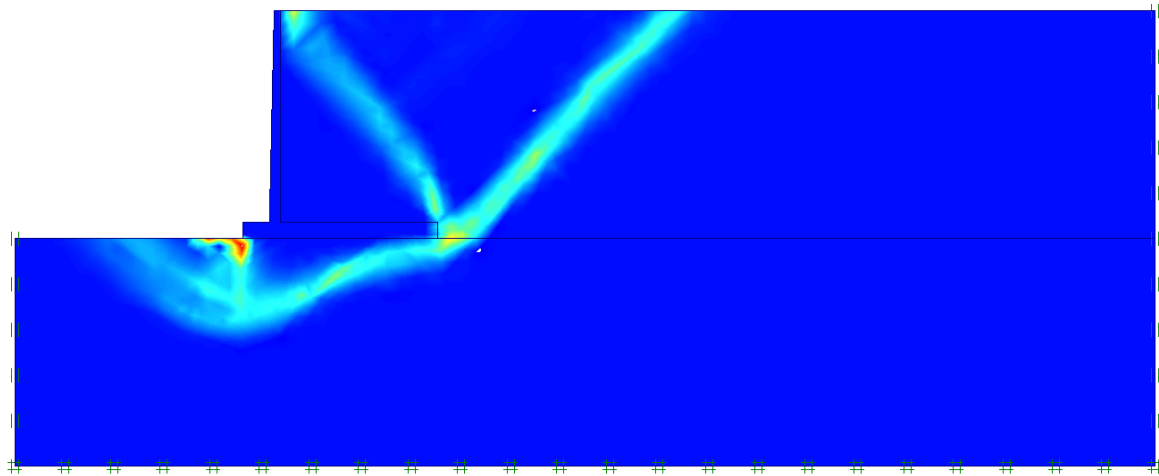
Figure 0.46: Failure mode of case 36 with terrain load.

Locally refined mesh size – horizontal backfill
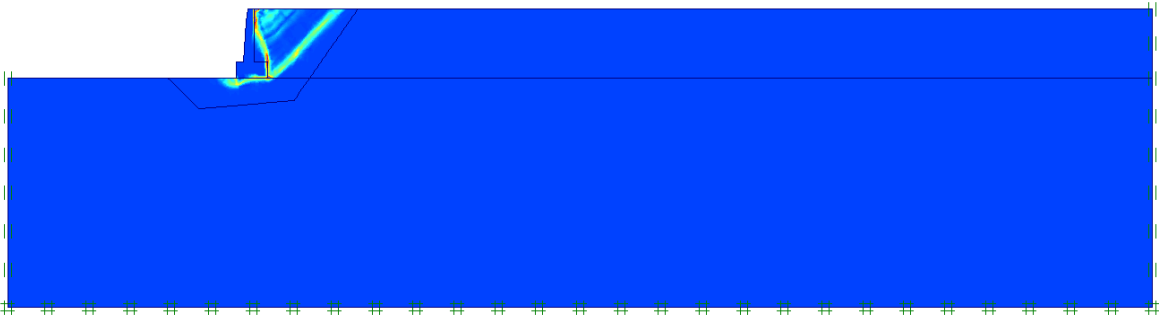
Figure 0.47: Failure mode of case 1 with locally refined mesh and terrain load.
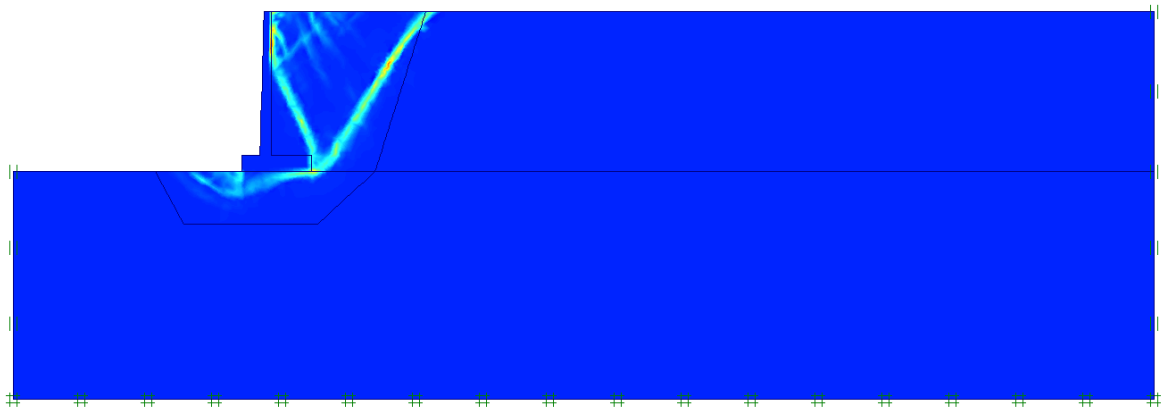
Figure 0.48: Failure mode of case 3 with locally refined mesh and terrain load.
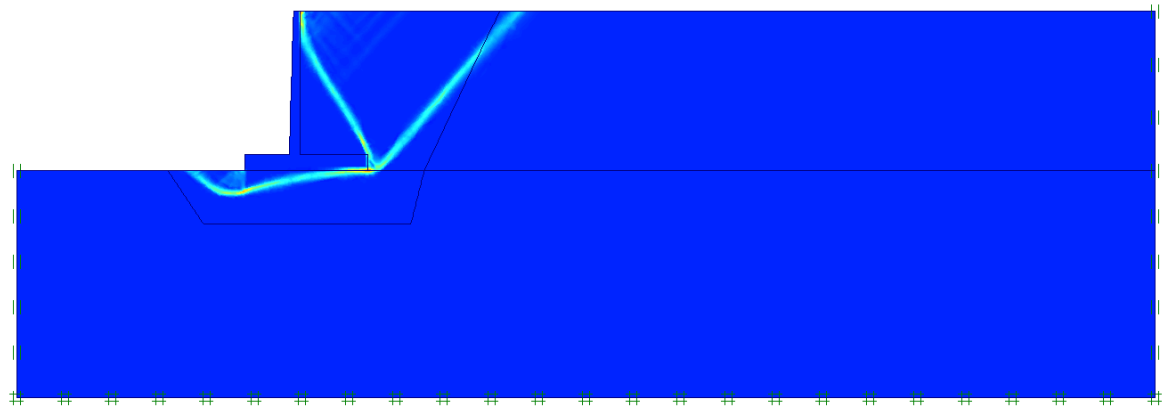
Figure 0.49: Failure mode of case 7 with locally refined mesh and terrain load.
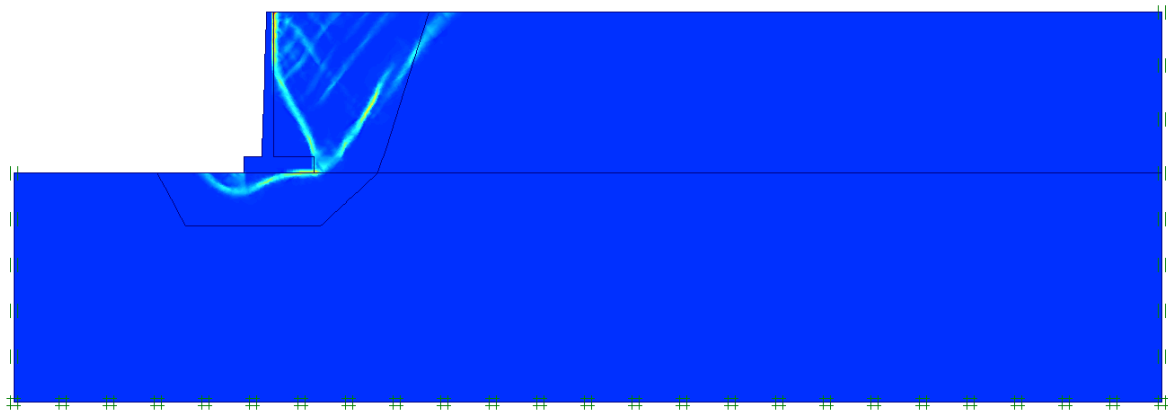
Figure 0.50: Failure mode of case 11 with locally refined mesh and terrain load.
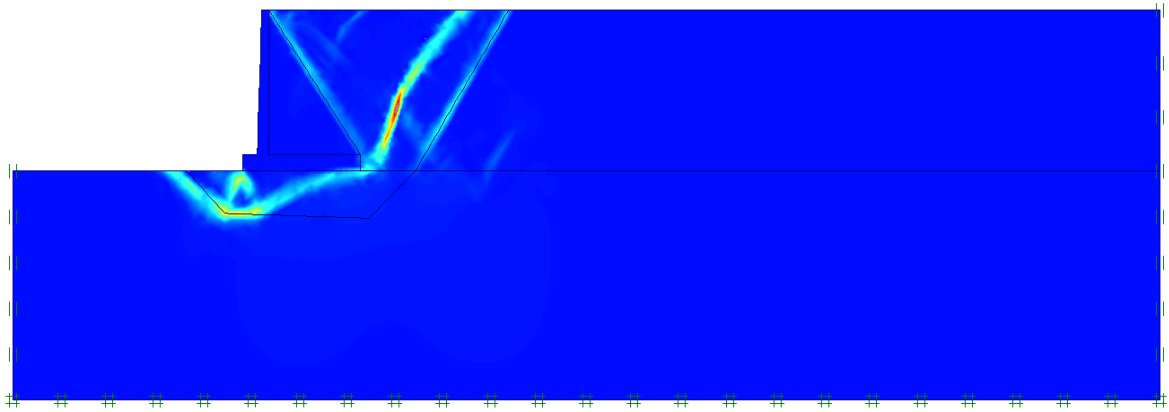
Figure 0.51: Failure mode of case 15 with locally refined mesh and terrain load.
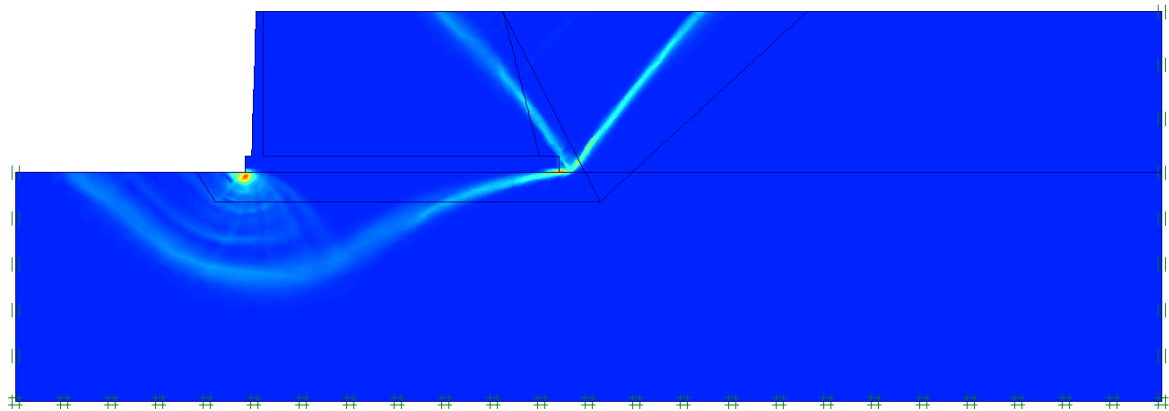
Figure 0.52: Failure mode of case 19 with locally refined mesh and terrain load.
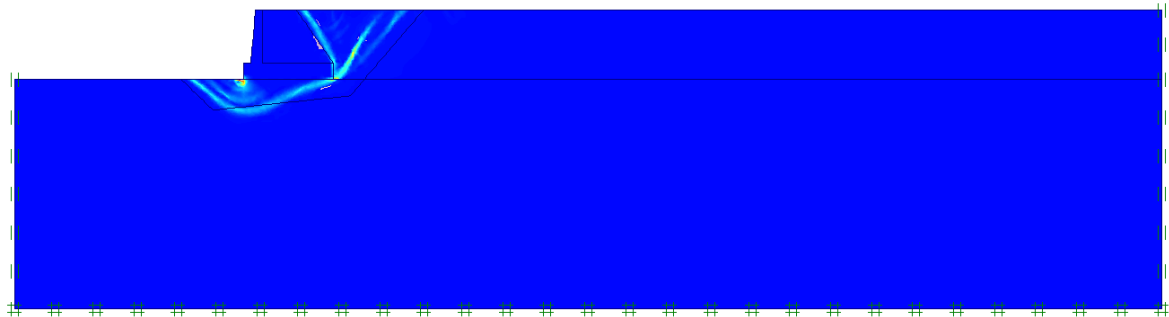
Figure 0.53: Failure mode of case 21 with locally refined mesh and terrain load.
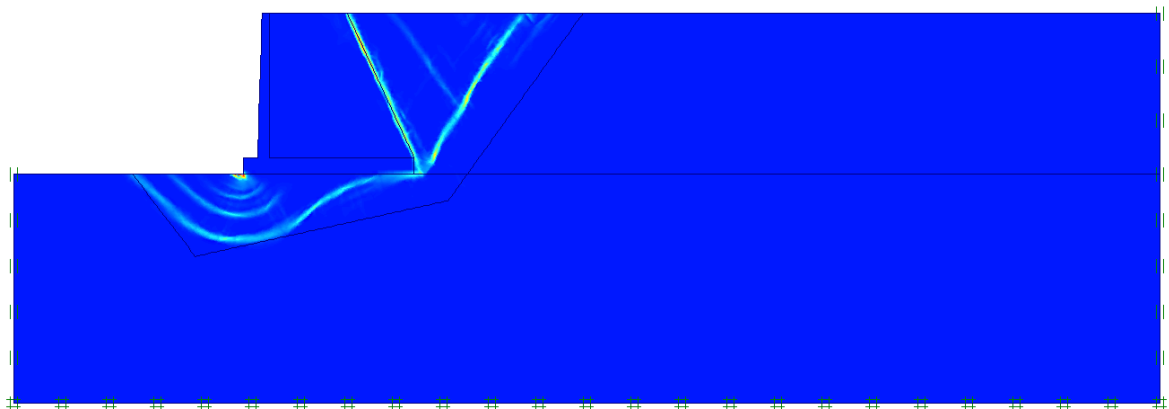
Figure 0.54: Failure mode of case 23 with locally refined mesh and terrain load.

137
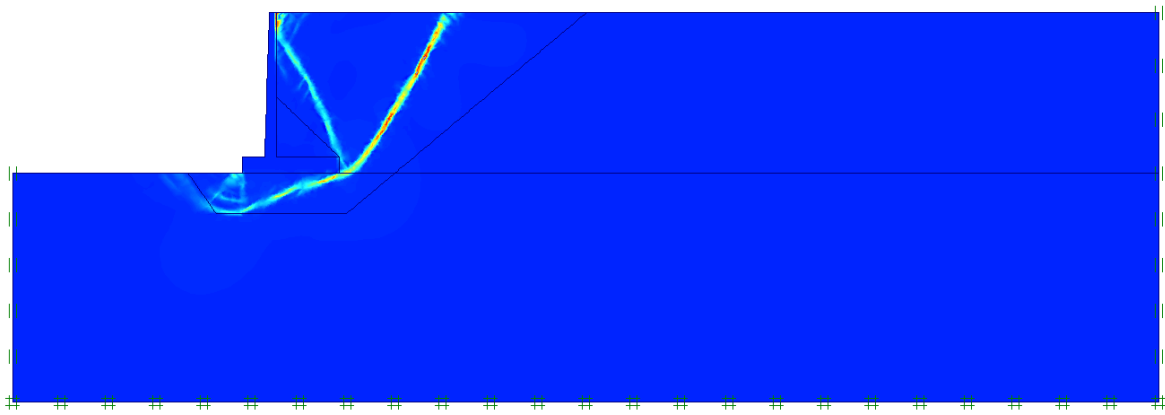
Figure 0.55: Failure mode of case 27 with locally refined mesh and terrain load.
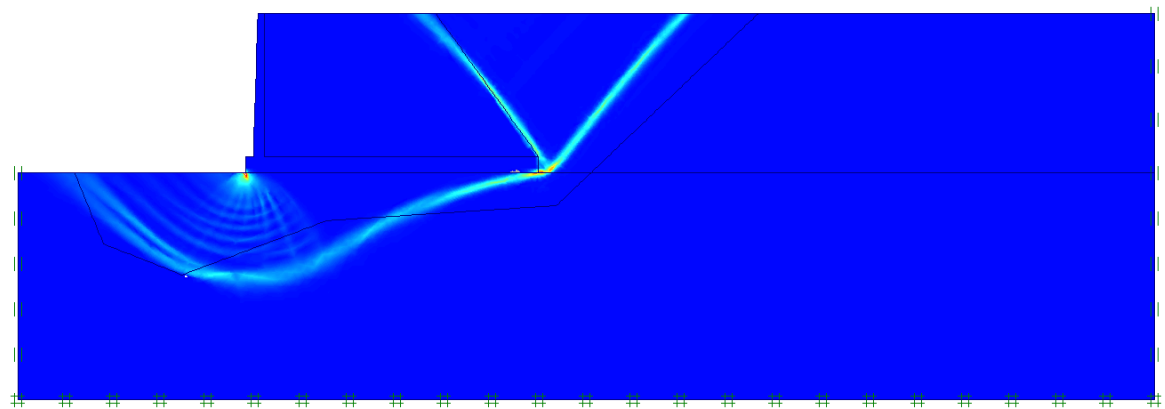
Figure 0.56: Failure mode of case 31 with locally refined mesh and terrain load.
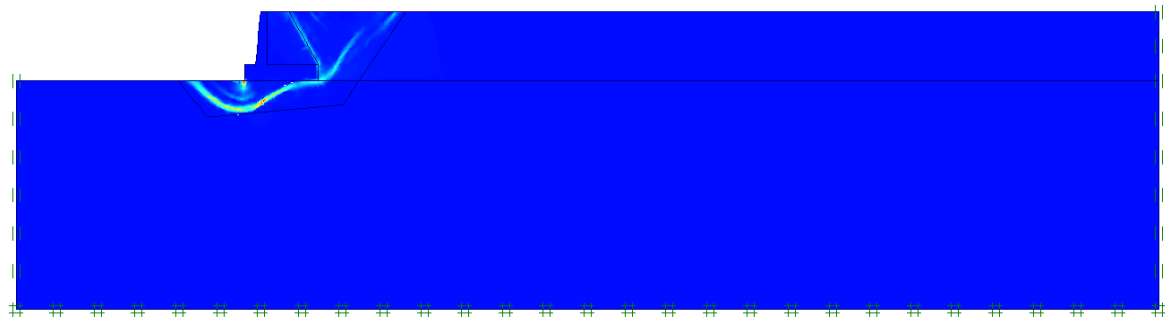
Figure 0.57: Failure mode of case 33 with locally refined mesh and terrain load.
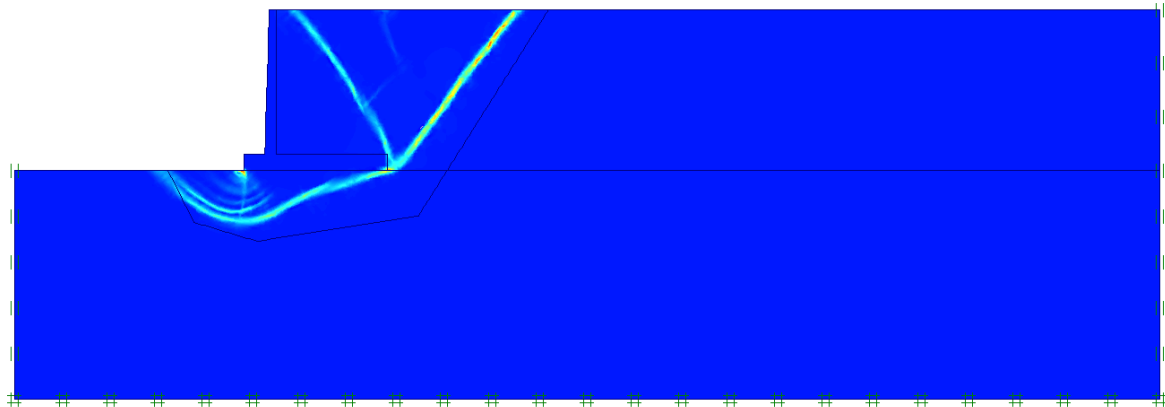
Figure 0.58: Failure mode of case 35 with locally refined mesh and terrain load.

"Fine"-mesh size – inclined backfill
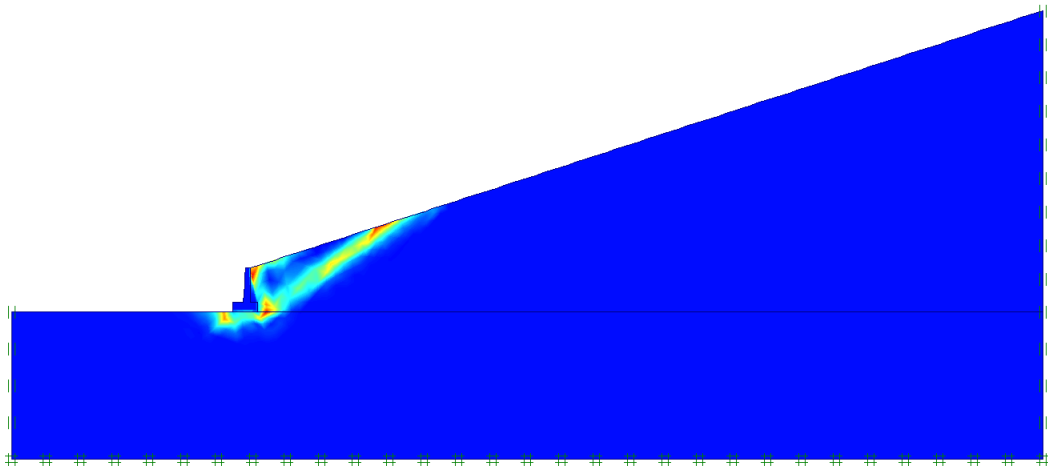
Figure 0.59: Failure mode of case 1β with terrain load.
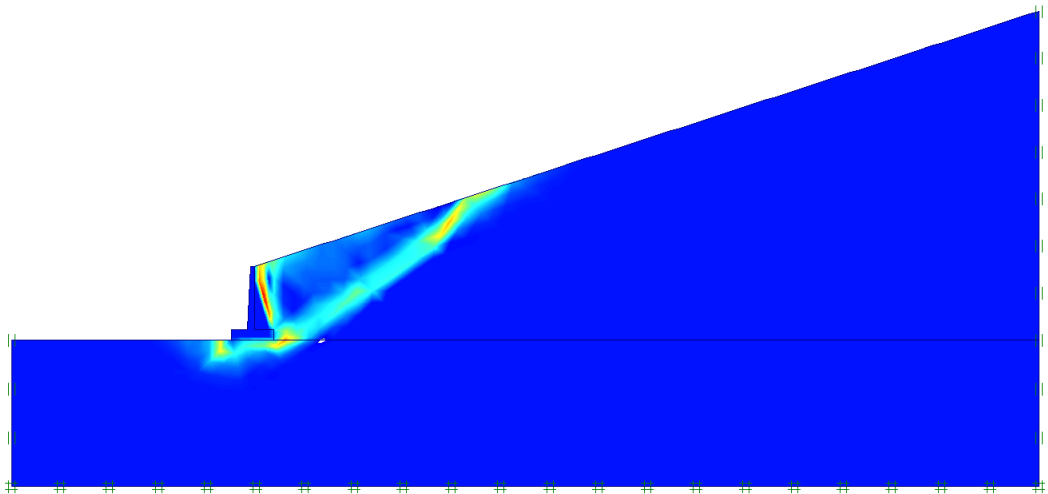
Figure 0.60: Failure mode of case 2β with terrain load.
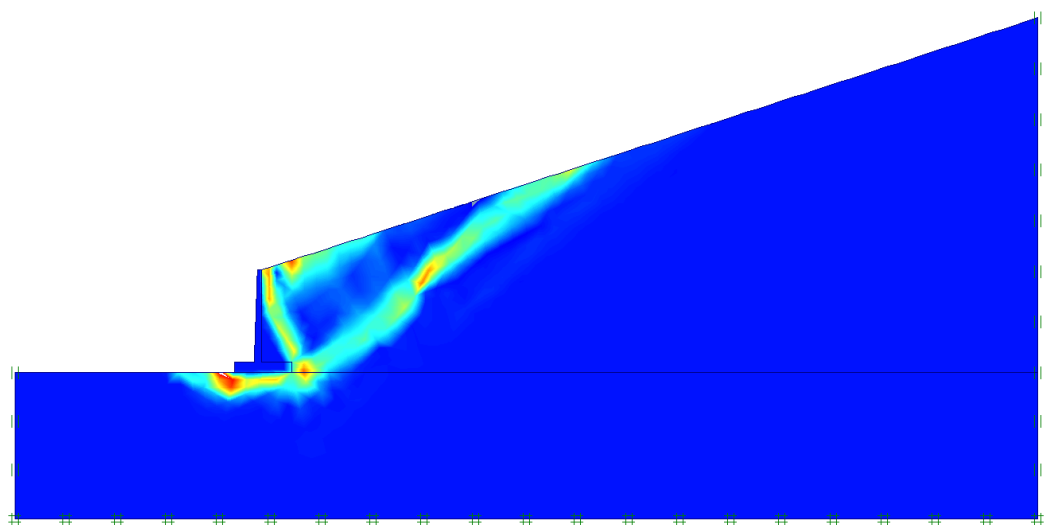
Figure 0.61: Failure mode of case 3β with terrain load.
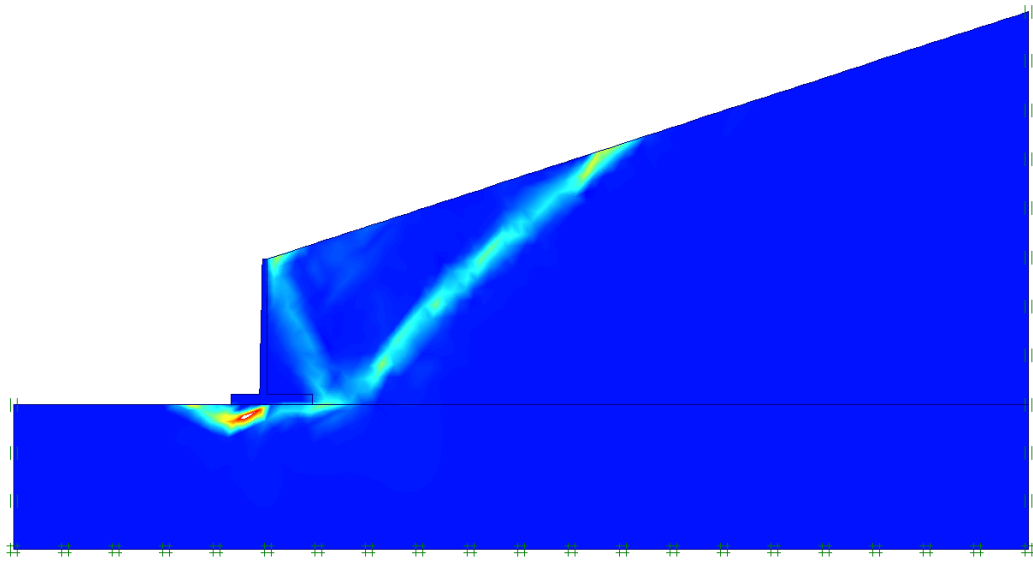
Figure 0.62: Failure mode of case 4β with terrain load.
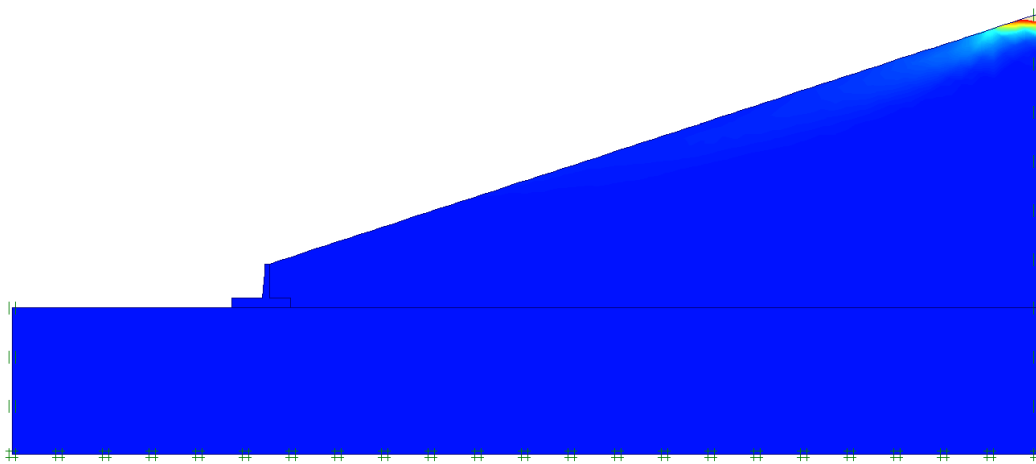
Figure 0.63: Failure mode (*) of case 5β with terrain load.
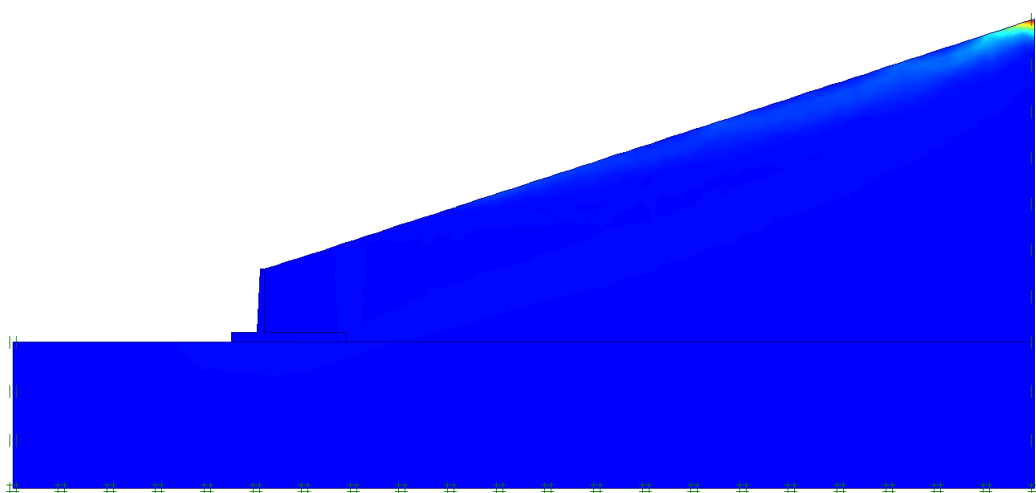
Figure 0.64: Failure mode (*) of case 6β with terrain load.
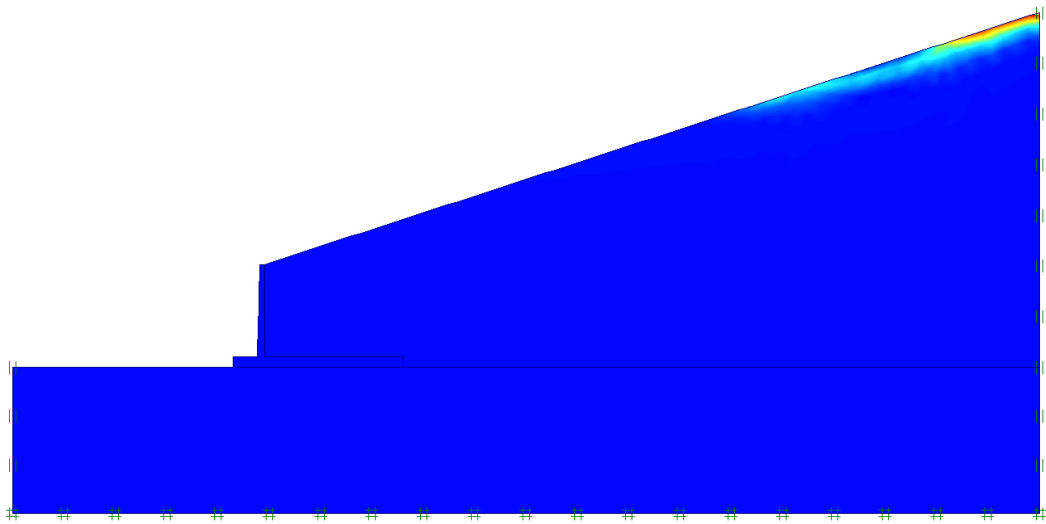
Figure 0.65: Failure mode (*) of case 7β with terrain load.
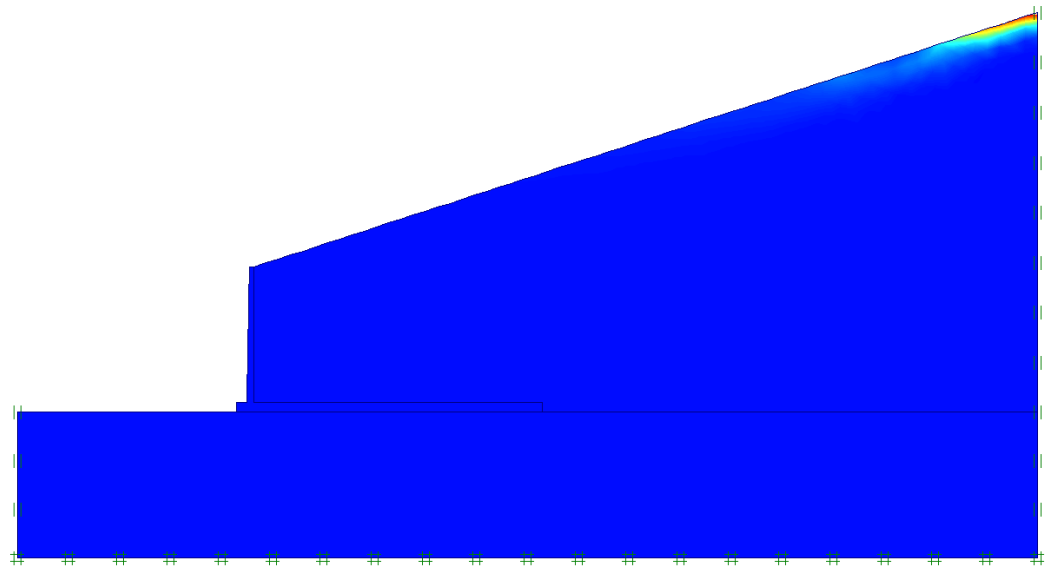
Figure 0.66: Failure mode (*) of case 8β with terrain load.
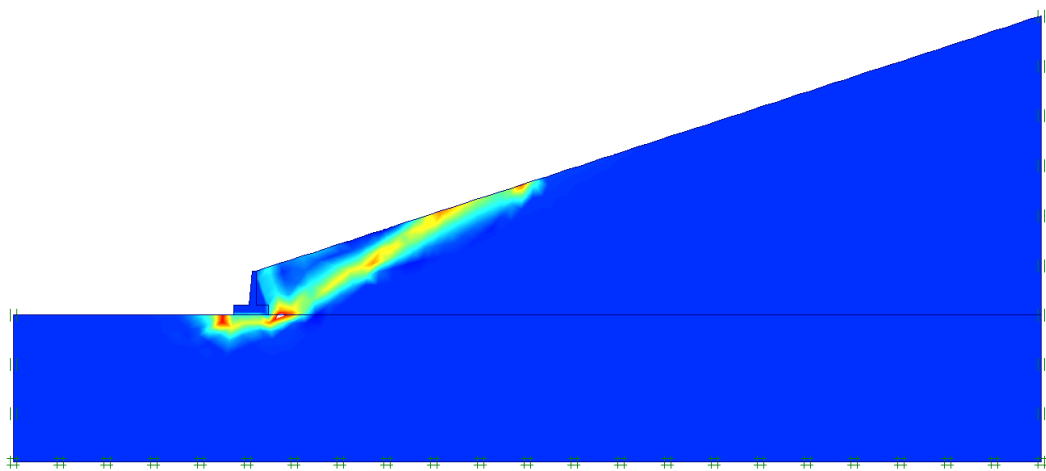
Figure 0.67: Failure mode of case 9β with terrain load.

141
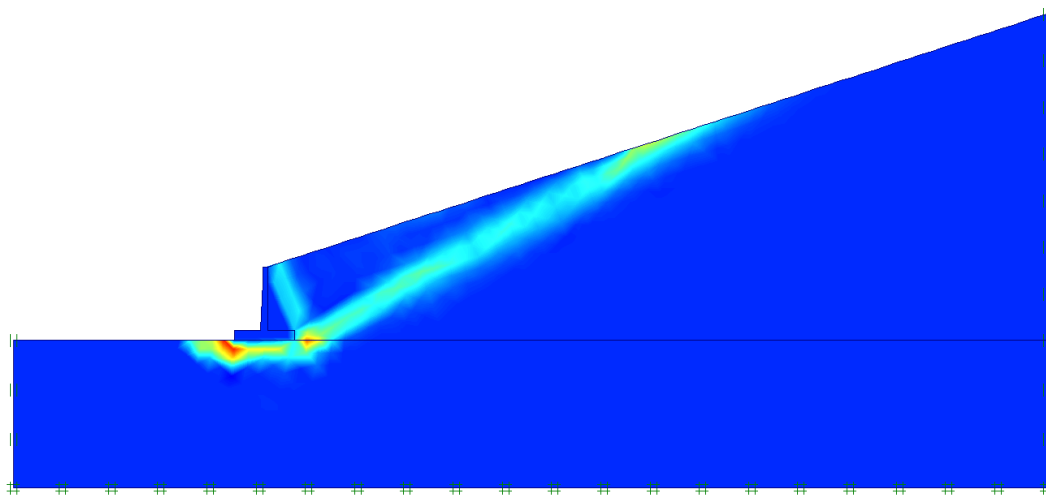
Figure 0.68: Failure mode of case 10β with terrain load.

Figure 0.69: Failure mode of case 11β with terrain load.

Figure 0.70: Failure mode of case 12β with terrain load.

Figure 0.71: Failure mode of case 13β with terrain load.

Figure 0.72: Failure mode of case 14β with terrain load.

Figure 0.73: Failure mode of case 15β with terrain load.

143

Figure 0.74: Failure mode of case 16β with terrain load.

Figure 0.75: Failure mode of case 21β with terrain load.
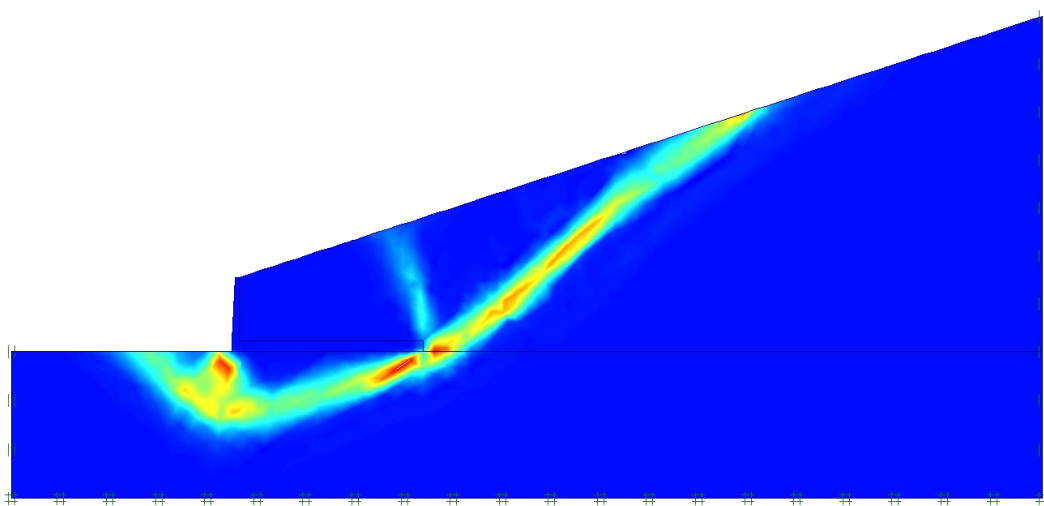
Figure 0.76: Failure mode of case 22β with terrain load.

144
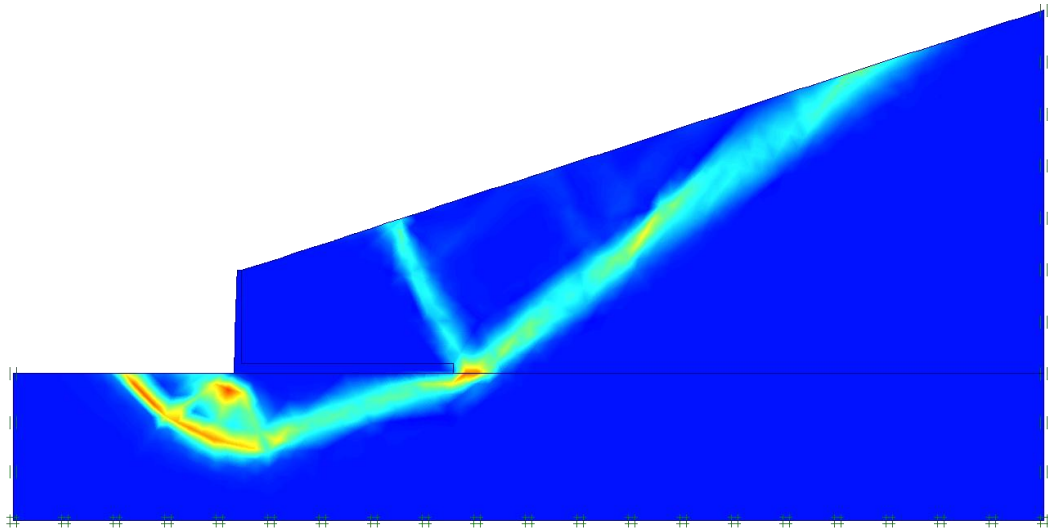
Figure 0.77: Failure mode of case 23β with terrain load.
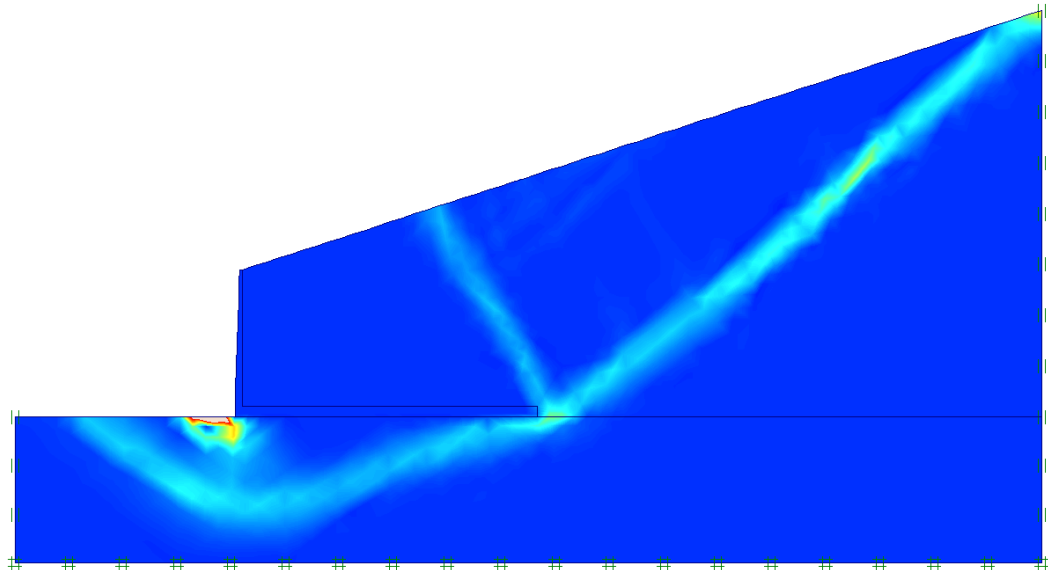
Figure 0.78: Failure mode (**) of case 24β with terrain load.
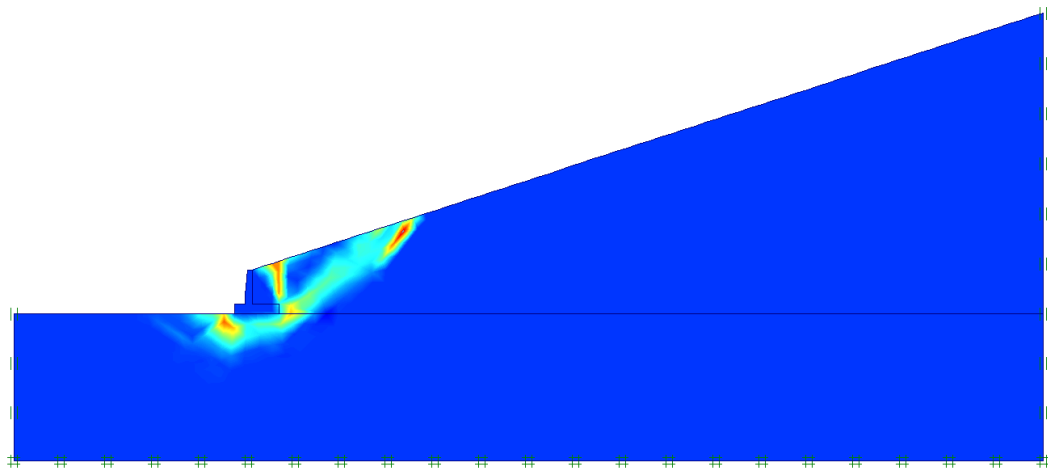
Figure 0.79: Failure mode of case 25β with terrain load.

145
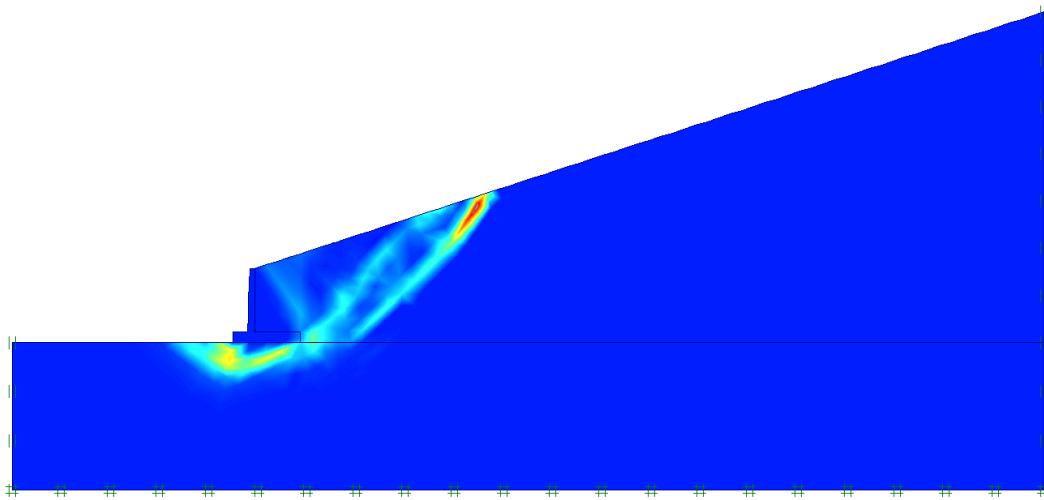
Figure 0.80: Failure mode of case 26β with terrain load.
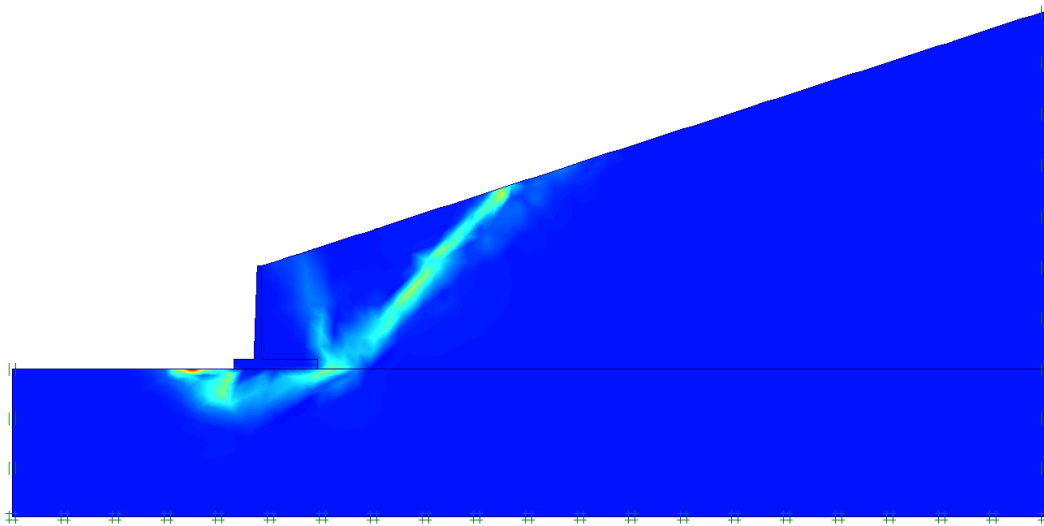
Figure 0.81: Failure mode of case 27β with terrain load.
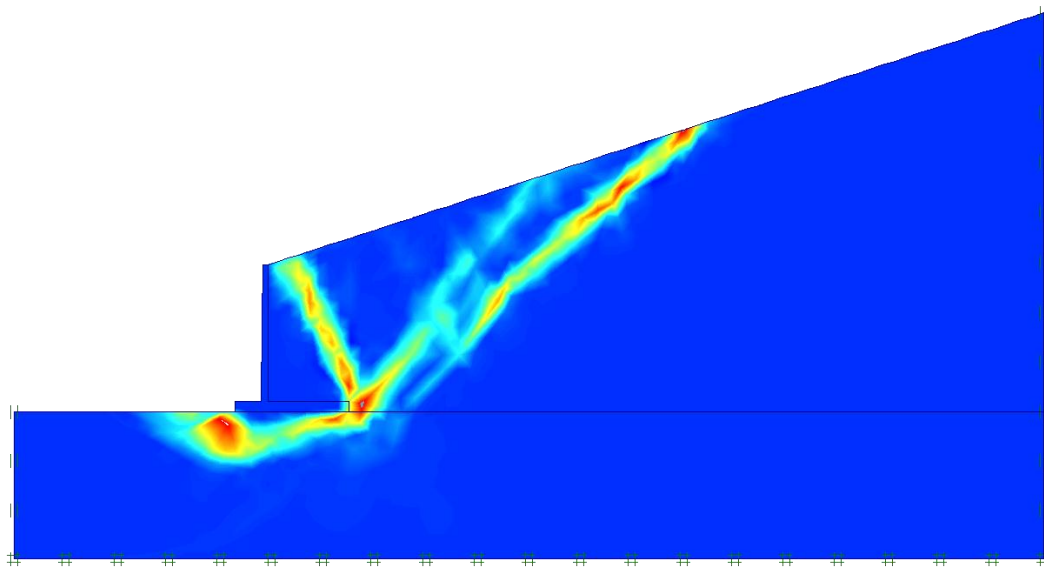
Figure 0.82: Failure mode of case 28β with terrain load.
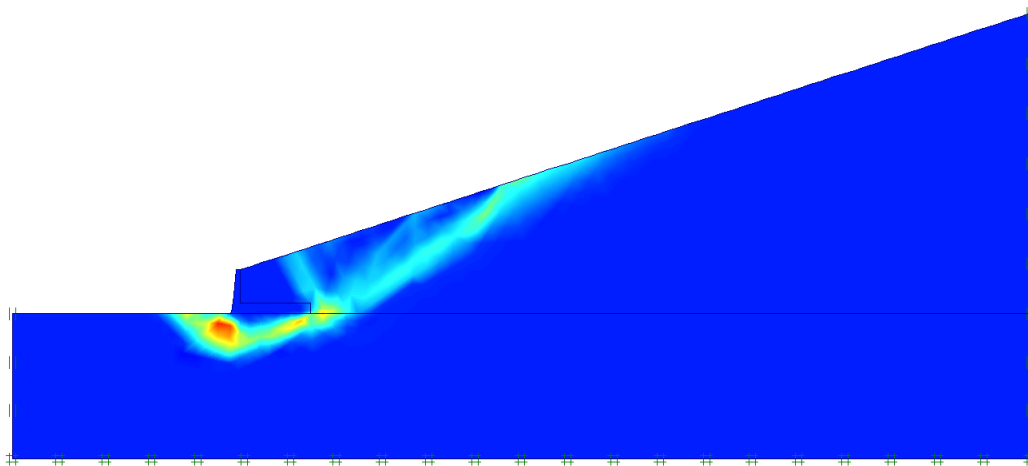
Figure 0.83: Failure mode of case 33β with terrain load.
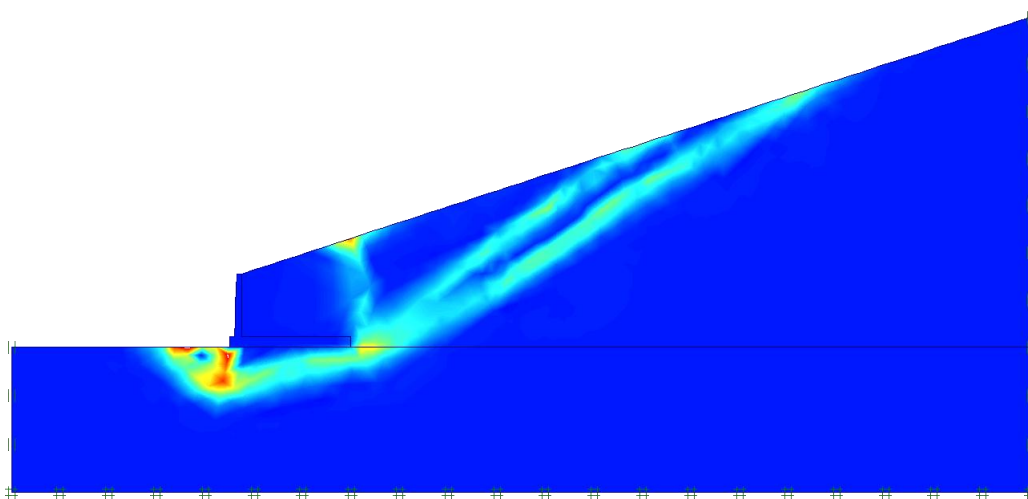
Figure 0.84: Failure mode of case 34β with terrain load.
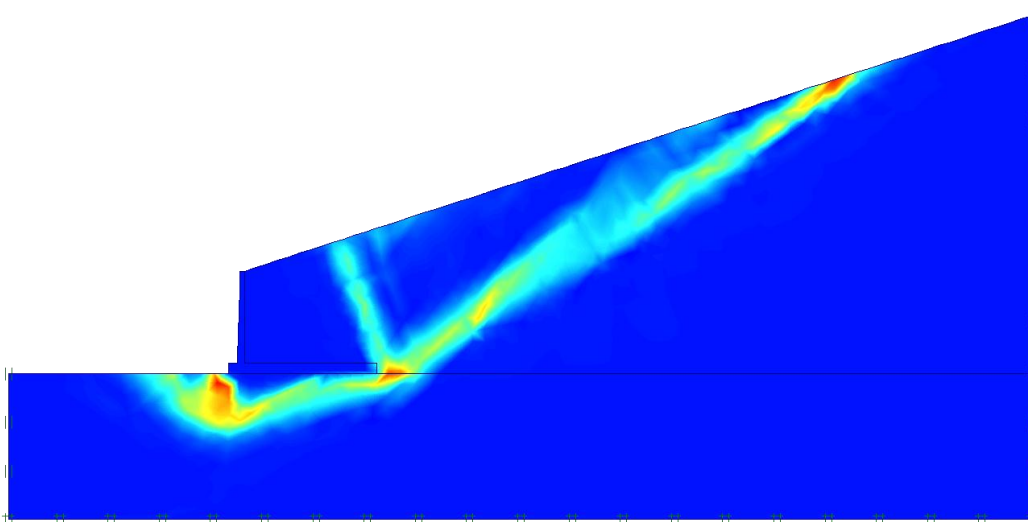
Figure 0.85: Failure mode of case 35β with terrain load.
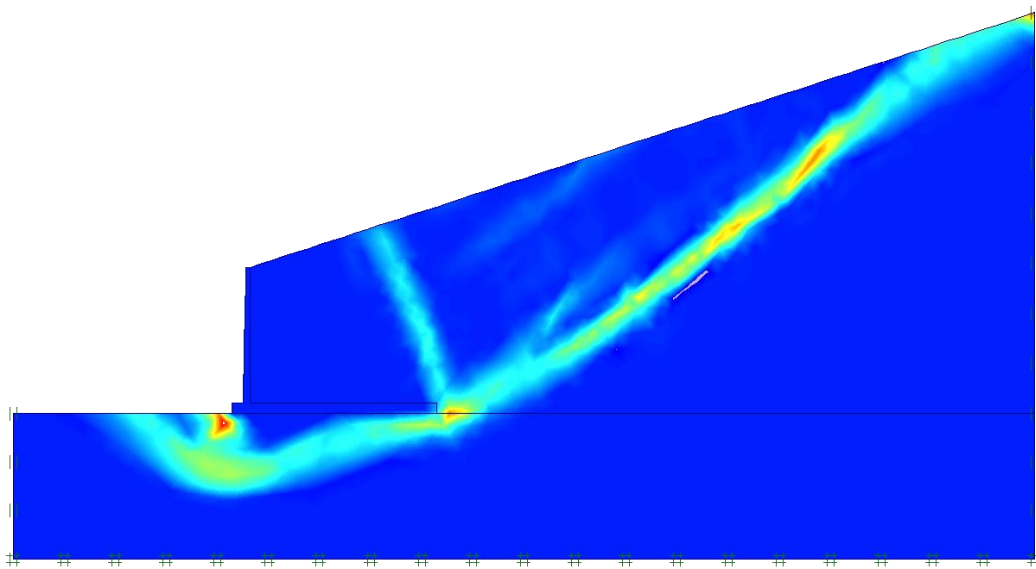
Figure 0.86: Failure mode (**) of case 36β with terrain load.

*) A slope failure; structure does not fail!

**) failure mechanism touches the boundaries of the model. A larger model is required to produce good results

Locally refined mesh size – inclined backfill
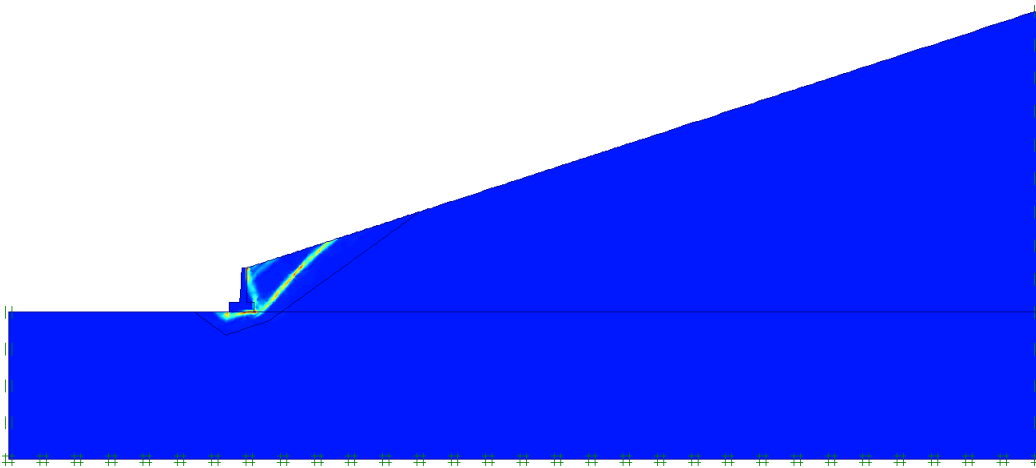
Figure 0.87: Failure mode of case 1β with a locally refined mesh and terrain load.
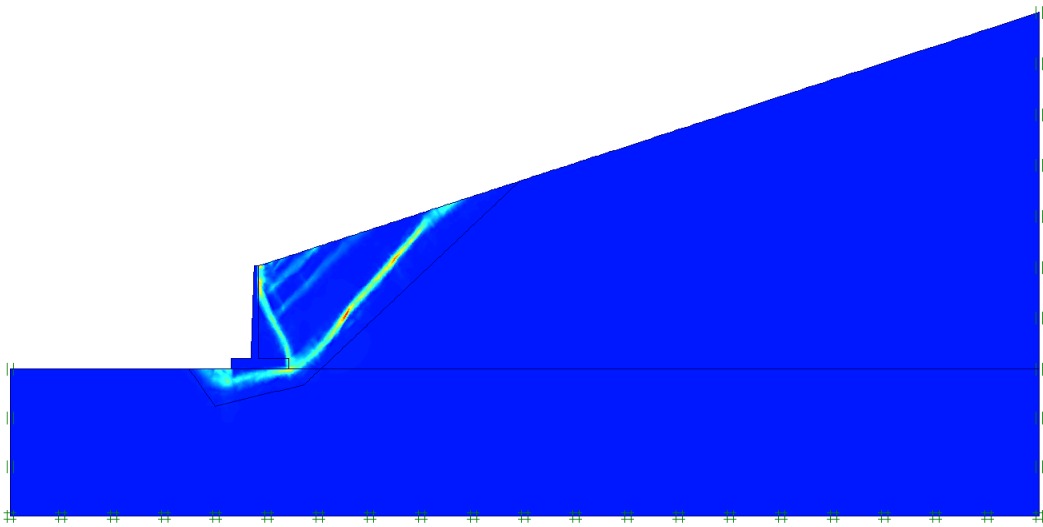
Figure 0.88: Failure mode of case 3β with a locally refined mesh and terrain load.
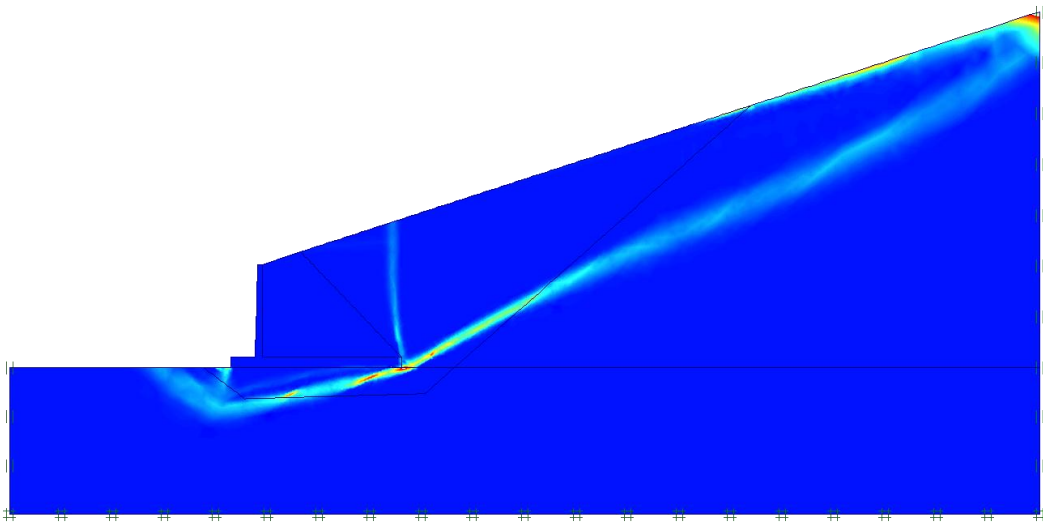
Figure 0.89: Failure mode (*) of case 7β with a locally refined mesh and terrain load.
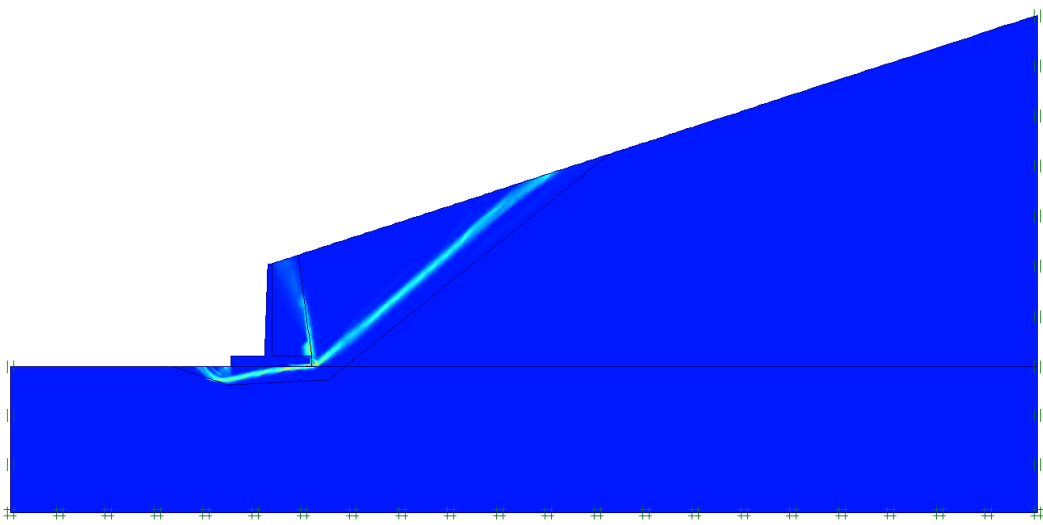
Figure 0.90: Failure mode of case 11β with a locally refined mesh and terrain load.
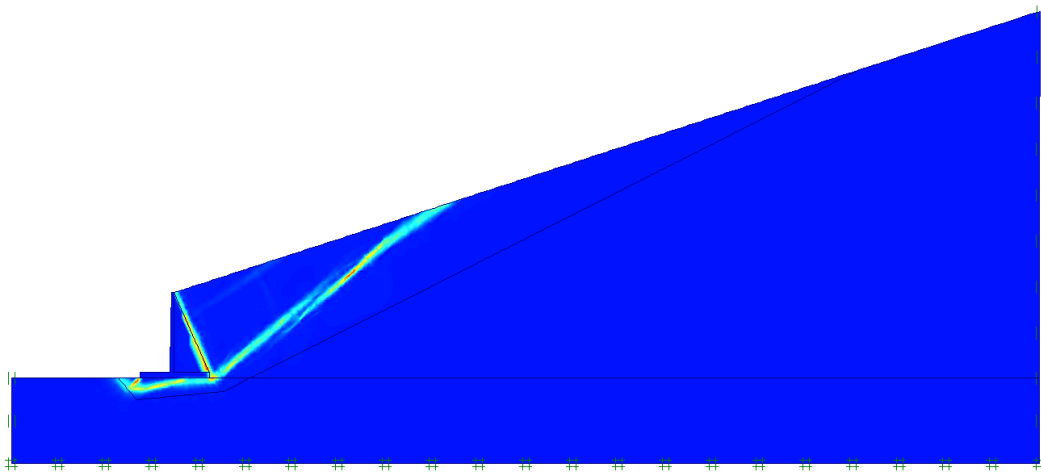
Figure 0.91: Failure mode of case 12β with a locally refined mesh and terrain load.
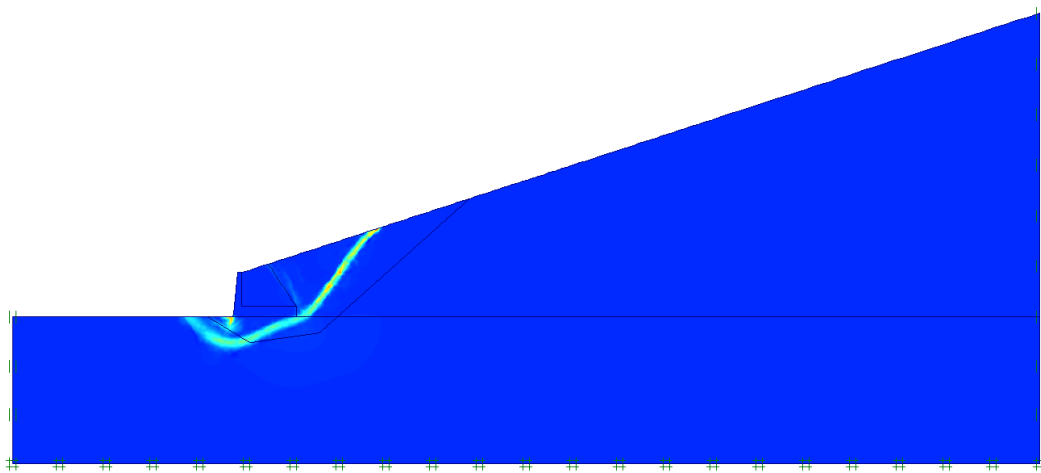
Figure 0.92: Failure mode of case 13β with a locally refined mesh and terrain load.
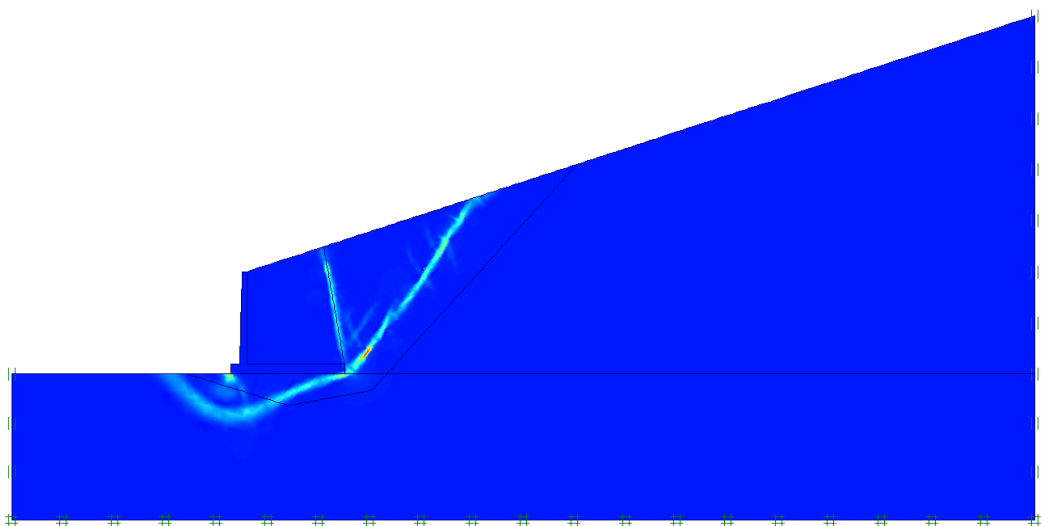
Figure 0.93: Failure mode of case 15β with a locally refined mesh and terrain load.

150
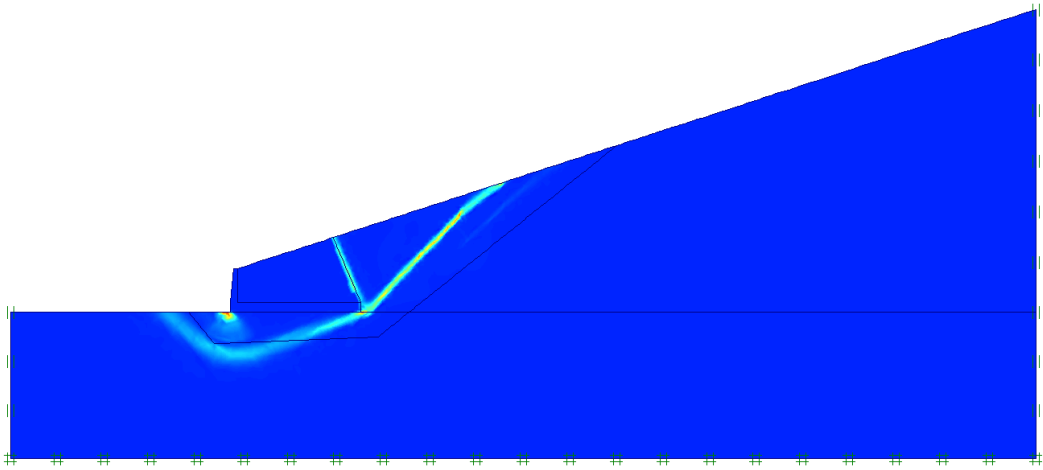
Figure 0.94: Failure mode of case 21β with a locally refined mesh and terrain load.
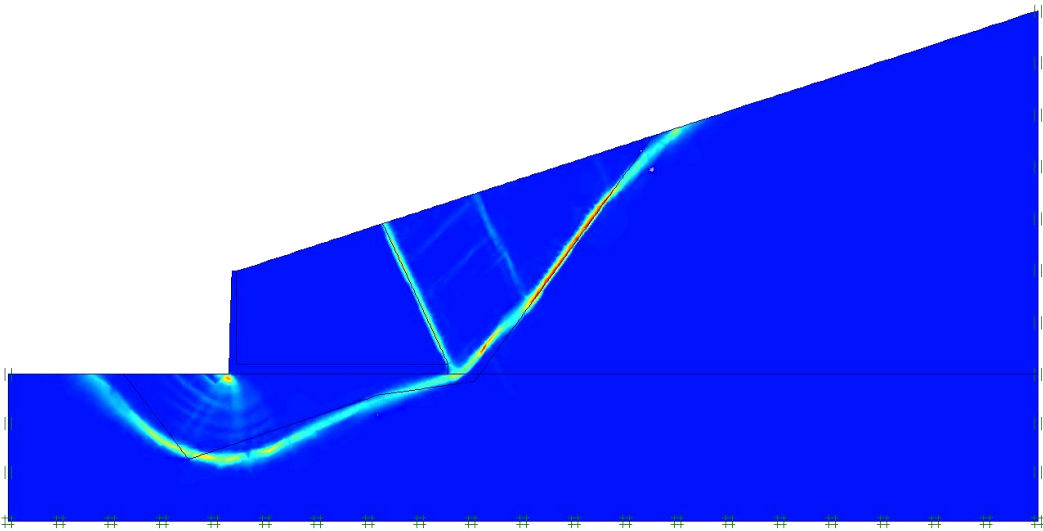
Figure 0.95: Failure mode of case 23β with a locally refined mesh and terrain load.
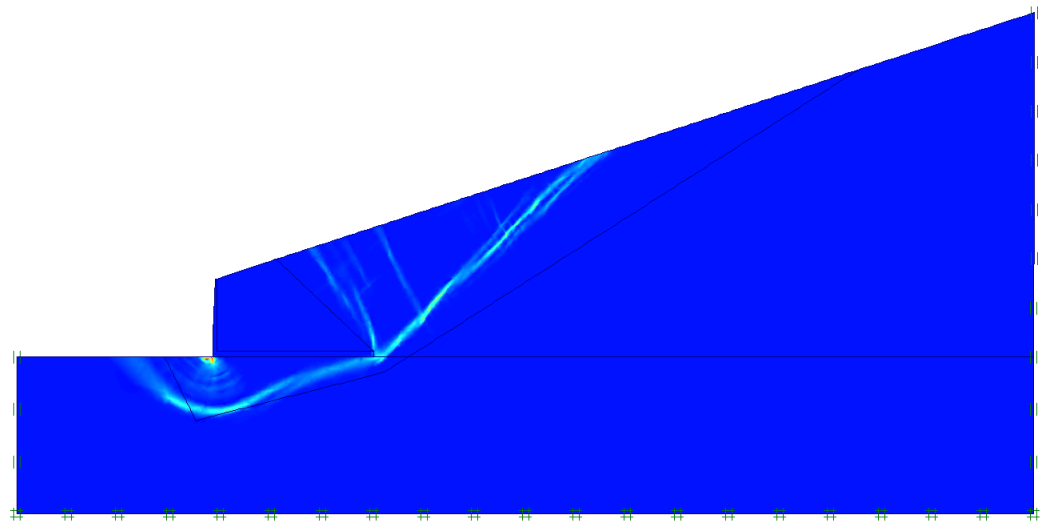
Figure 0.96: Failure mode (**) of case 24β with a locally refined mesh and terrain load.

151
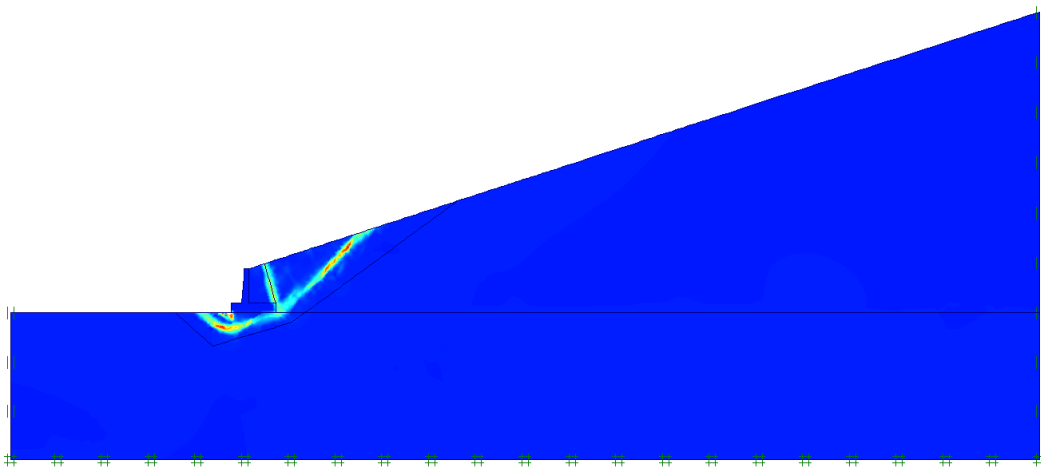
Figure 0.97: Failure mode of case 25β with a locally refined mesh and terrain load.
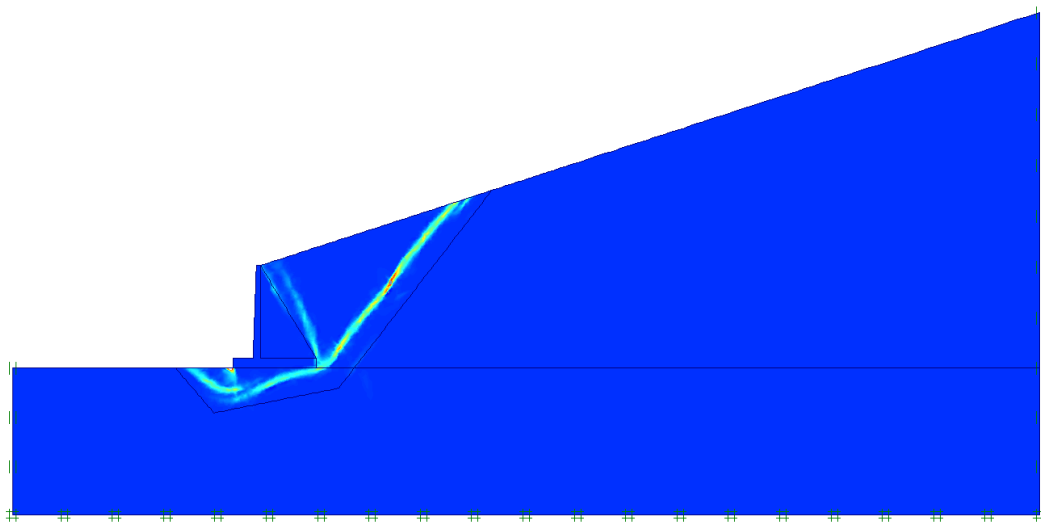
Figure 0.98: Failure mode of case 27β with a locally refined mesh and terrain load.
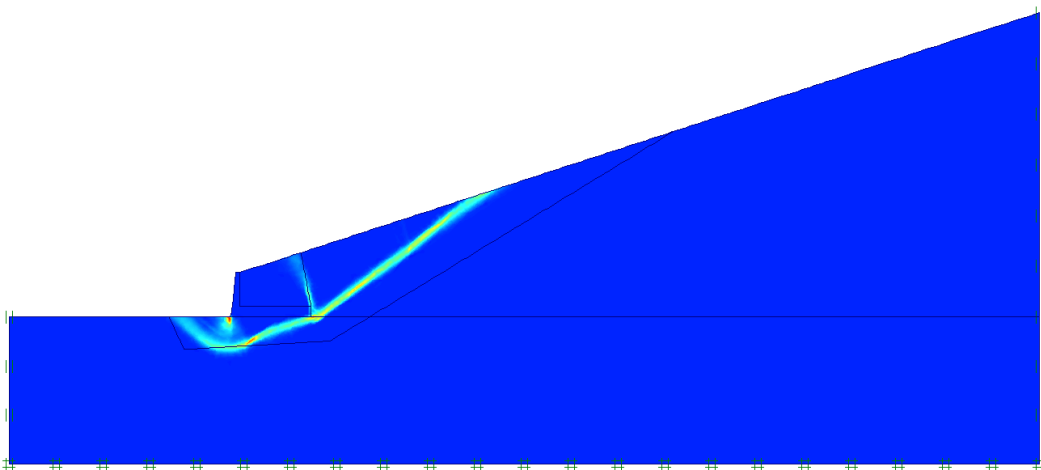
Figure 0.99: Failure mode of case 33β with a locally refined mesh and terrain load.
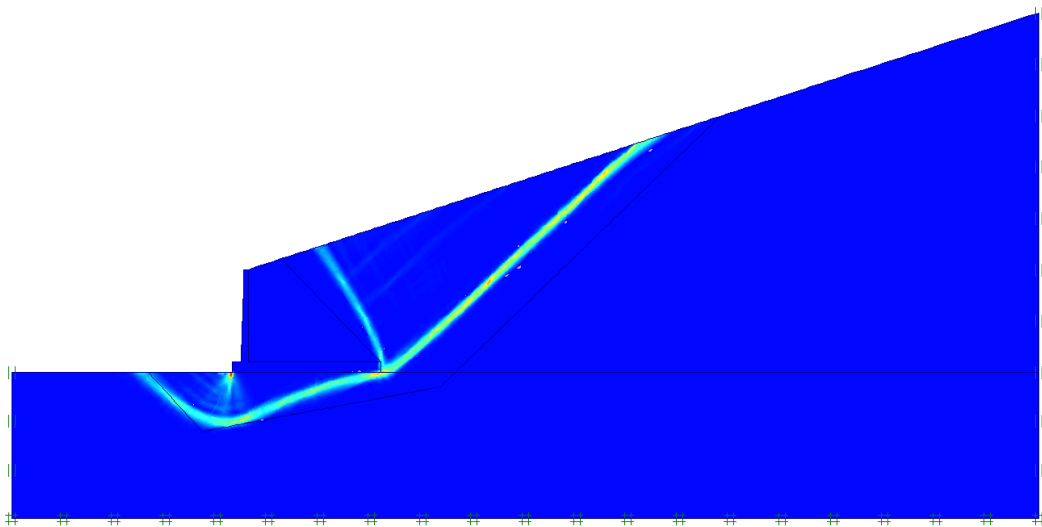
Figure 0.100: Failure mode of case 35β with a locally refined mesh and terrain load.
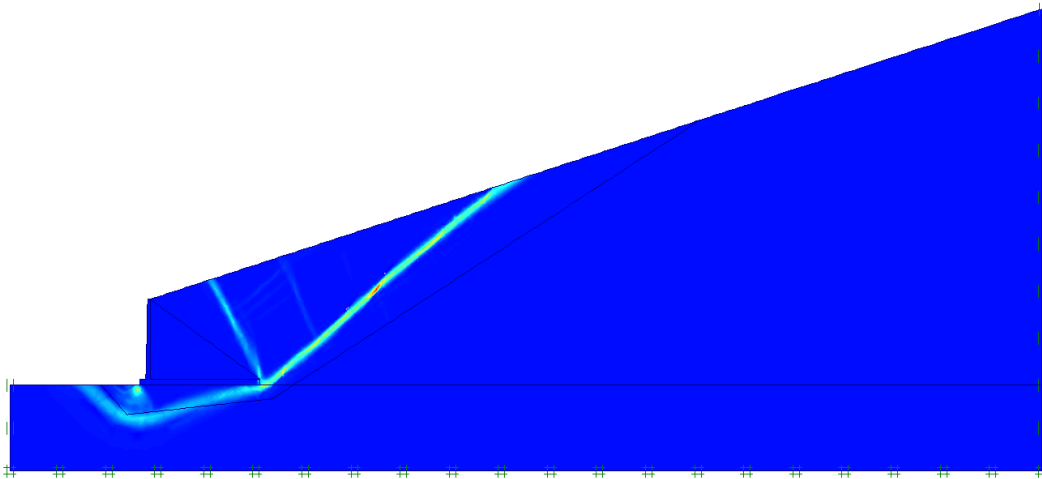
Figure 0.101: Failure mode (**) of case 36β with a locally refined mesh and terrain load.

(*) Case resulted in slope failure but a secondary failure mechanism is nearly formed

(**) Results are shown for an increased model size as the failure mechanism touched the original model boundaries

Appendix J: Development of results from numerical simulations

The development of the factor of safety leading to model failure during all PLAXIS simulations is given in this chapter. An average has been taken for the part of each curve that is assumed to have reached an equilibrium state. Some cases produced a very distinct plateau but others had more difficulties reaching a good balance, in those cases the simulation was run until I was satisfied that the results oscillated around a specific solution. The assumed average values from the simulations have been drawn in each figure as with a blue line representing case-a, failure without surface load, and a red line represents case-b, failure with surface load. The numerical value of the assumed average values is presented on the right side of each figure.

"Very fine" mesh coarseness – horizontal backfill
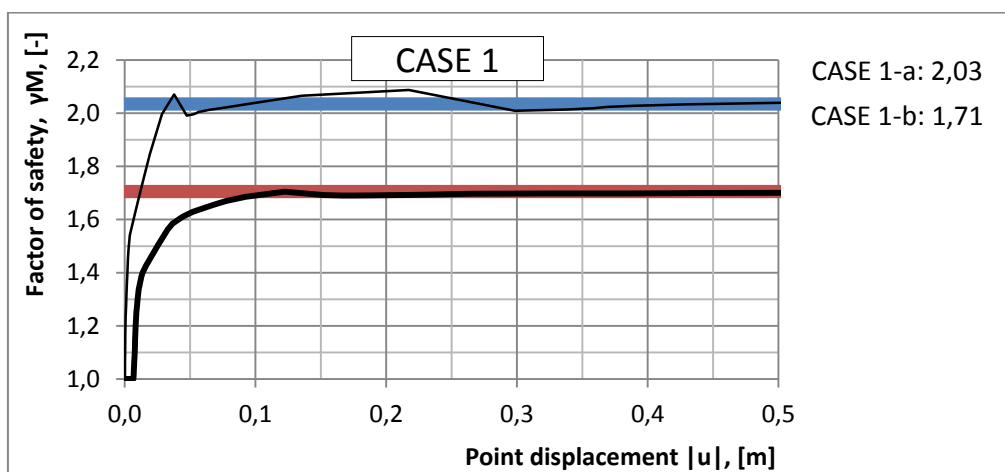
Figure 0.102: Results from PLAXIS run of case 1.
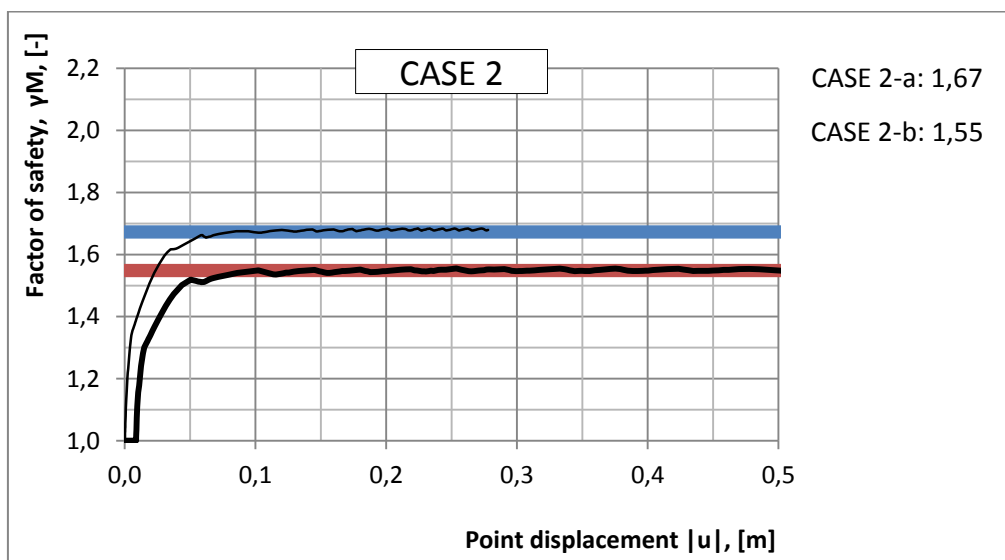
Figure 0.103: Results from PLAXIS run of case 2.
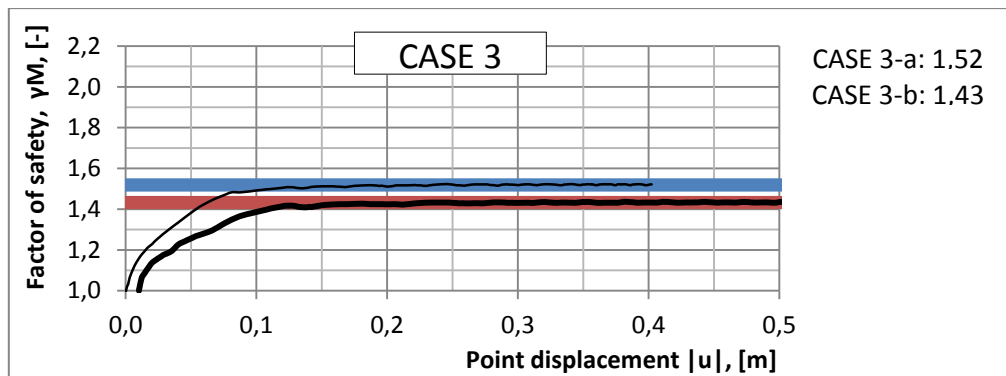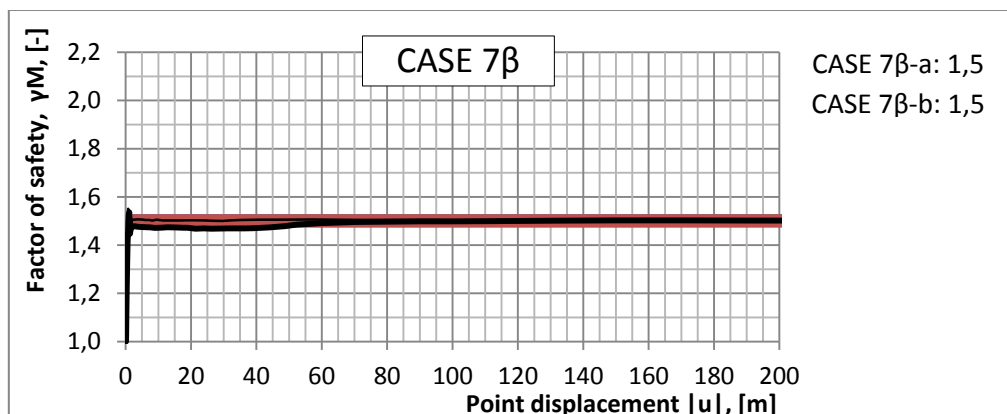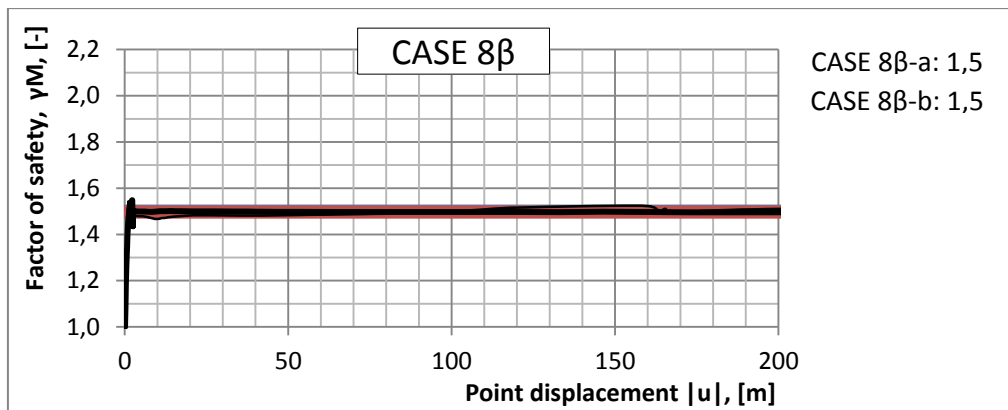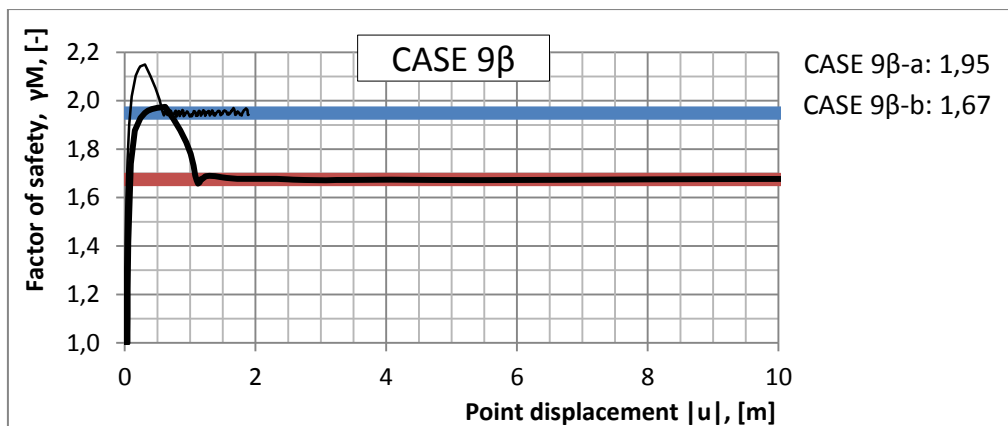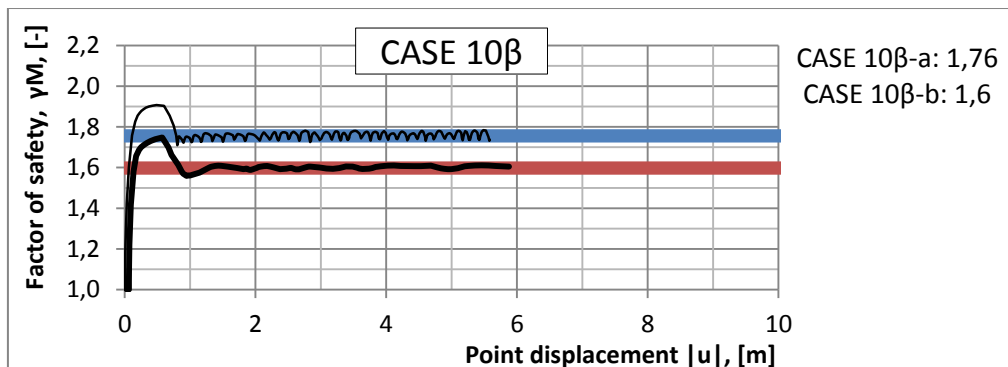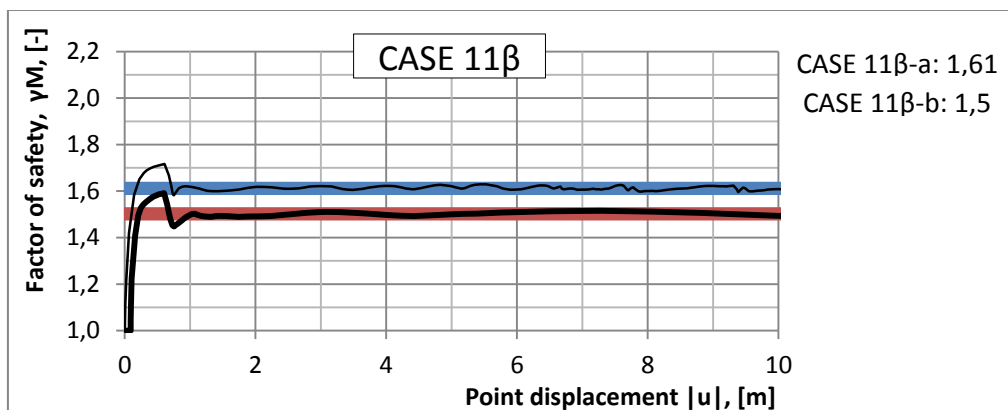
Figure 0.104: Results from PLAXIS run of case 3.

CASE 3-a: 1.52
CASE 3-b: 1.43
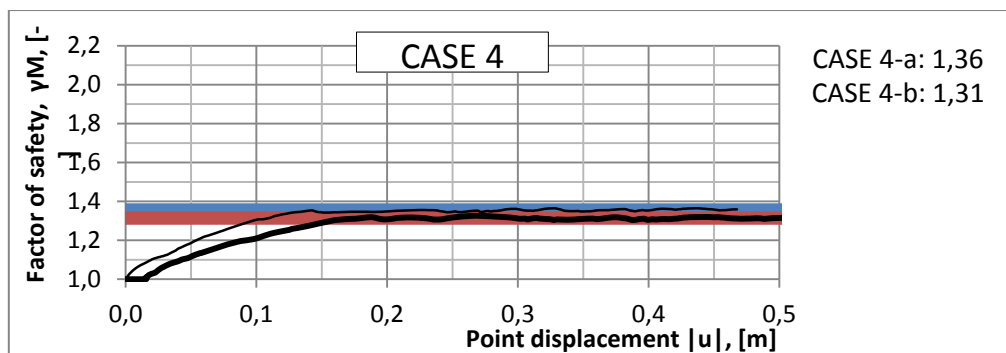
Figure 0.105: Results from PLAXIS run of case 4.

CASE 4-a: 1,36
CASE 4-b: 1,31
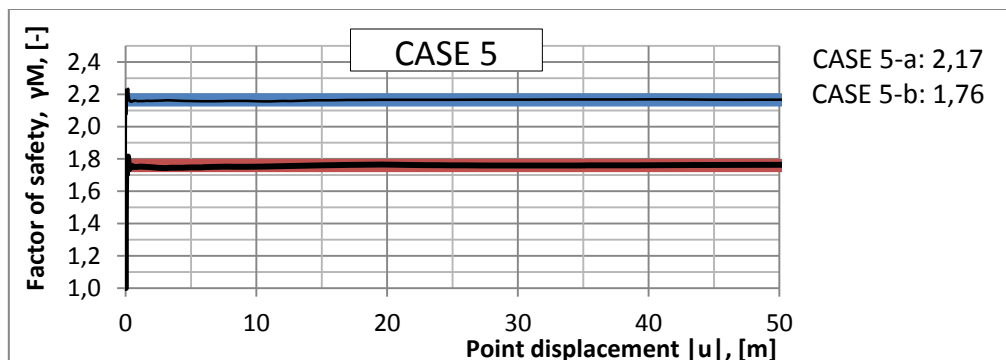
Figure 0.106: Results from PLAXIS run of case 5.

CASE 5-a: 2,17
CASE 5-b: 1,76
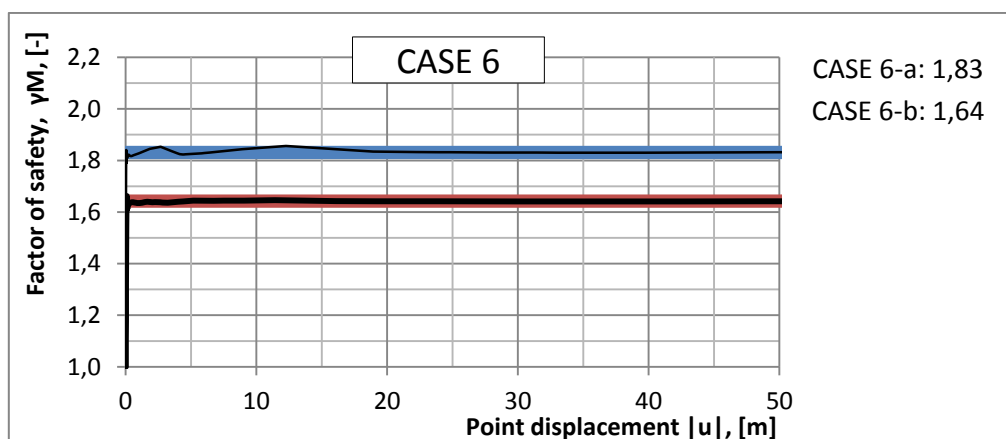
Figure 0.107: Results from PLAXIS run of case 6.

CASE 6-a: 1,83
CASE 6-b: 1,64

155
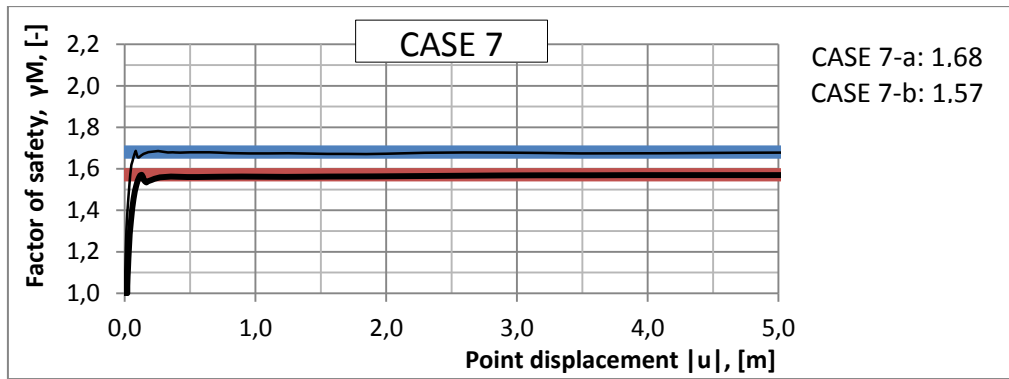
Figure 0.108: Results from PLAXIS run of case 7.
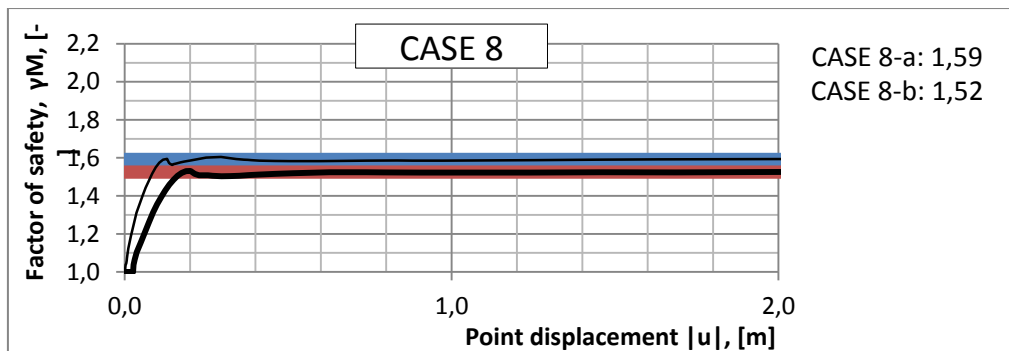
Figure 0.109: Results from PLAXIS run of case 8.
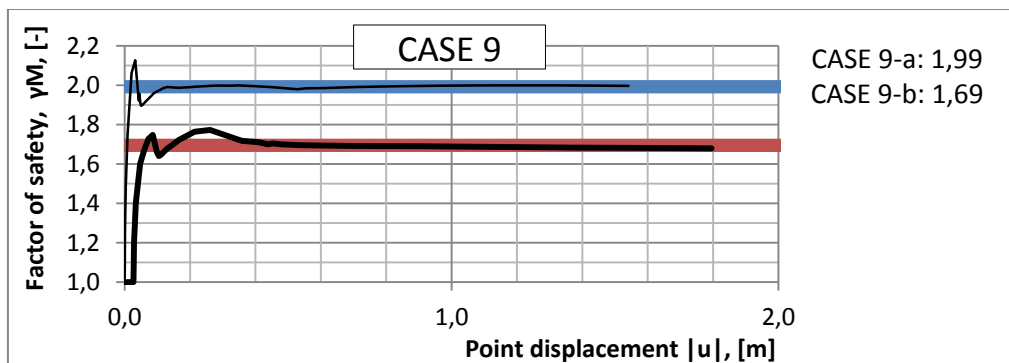
Figure 0.110: Results from PLAXIS run of case 9.
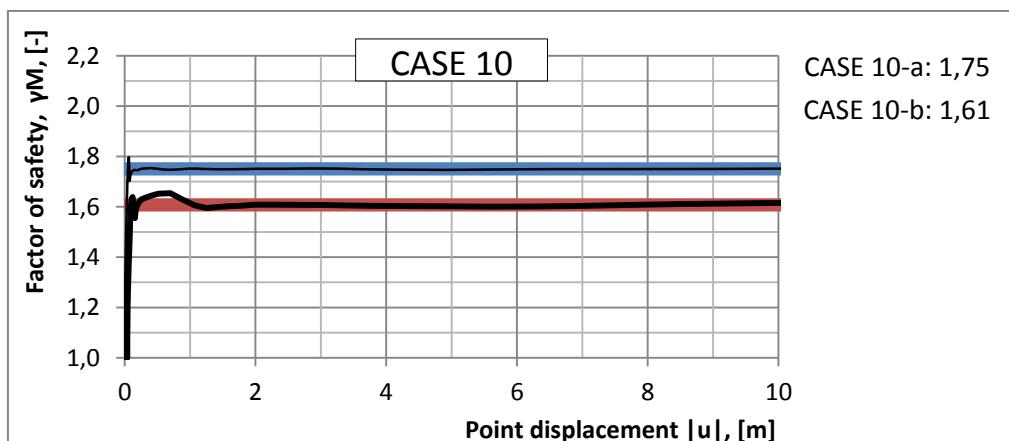
Figure 0.111: Results from PLAXIS run of case 10.

156
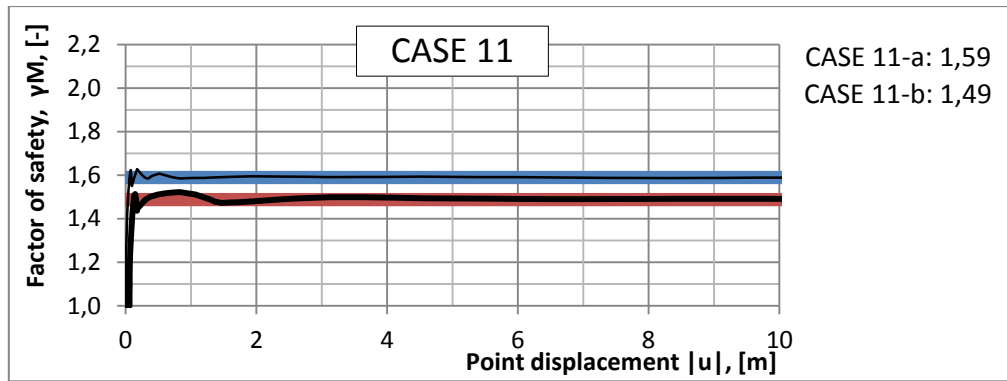
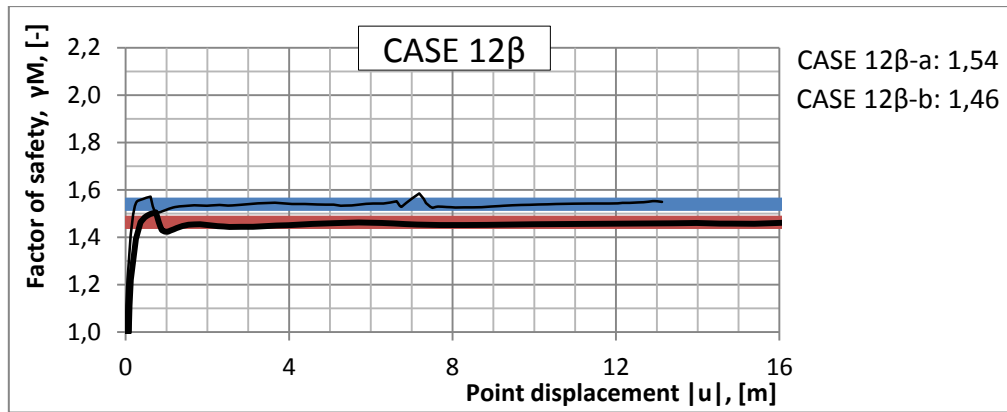*Figure 0.112: Results from PLAXIS run of case 11.*
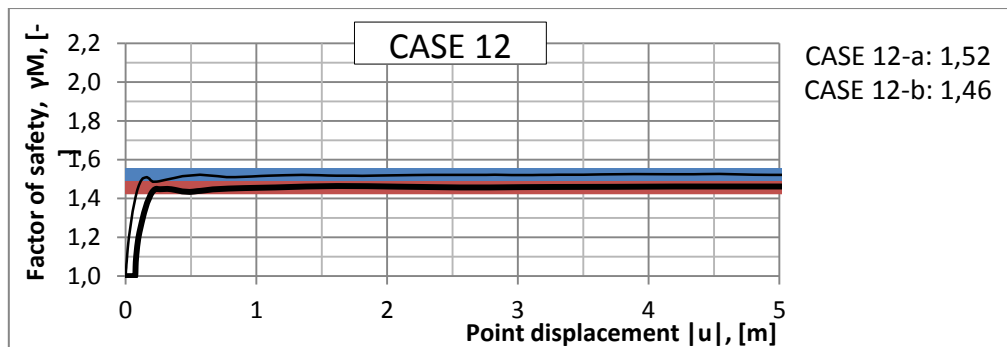
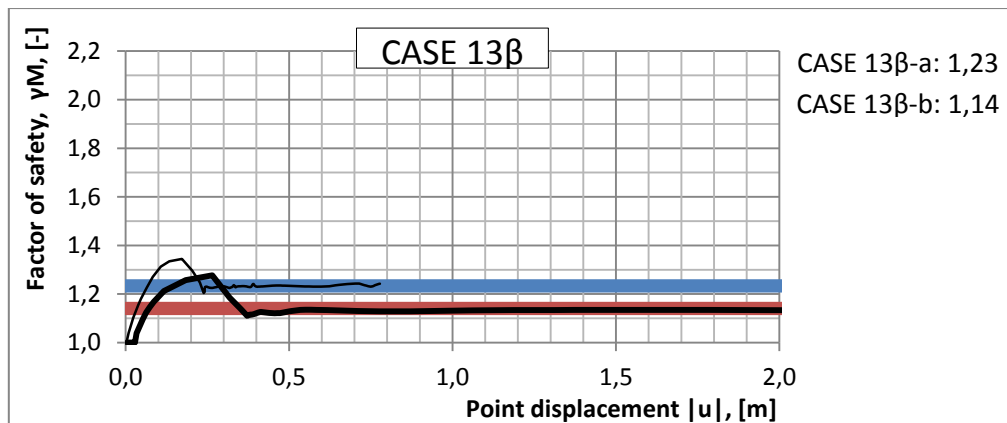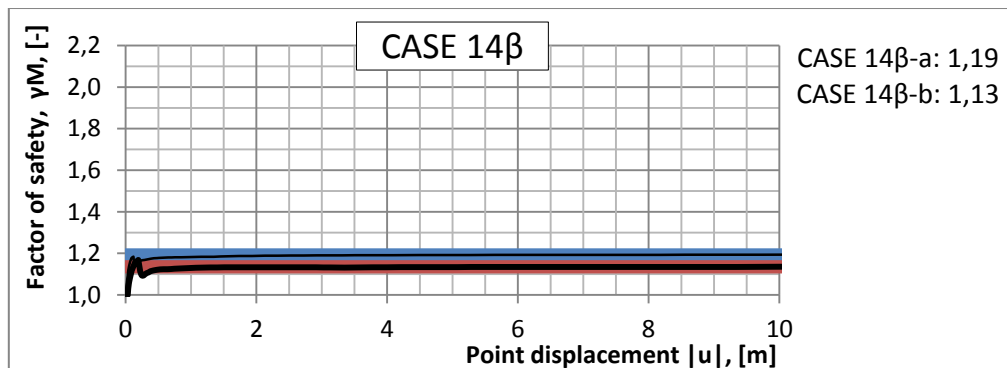*Figure 0.113: Results from PLAXIS run of case 12.*
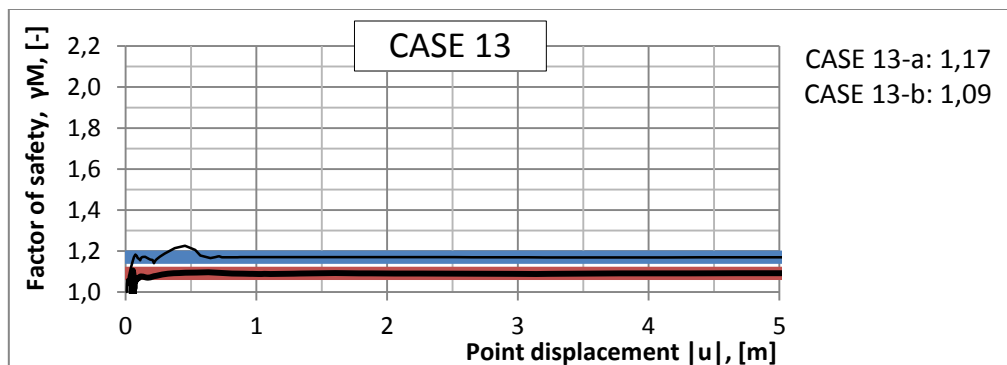
Figure 0.114: Results from PLAXIS run of case 13.
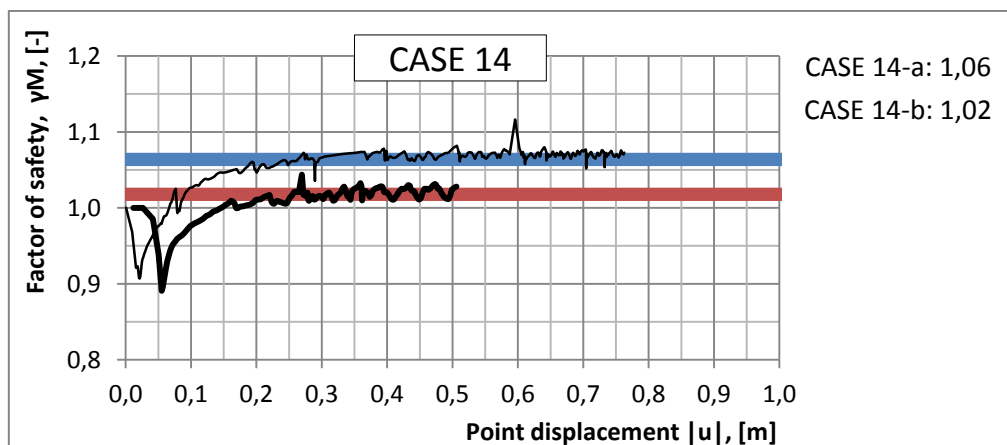
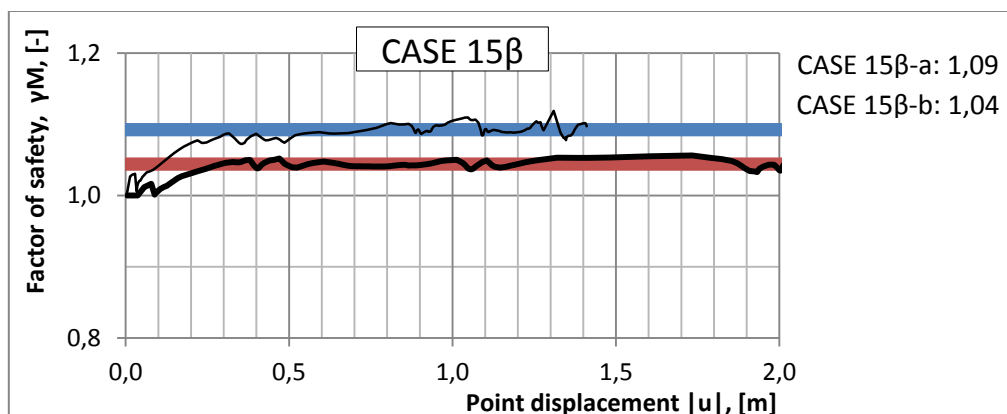*Figure 0.115: Results from PLAXIS run of case 14.*

157
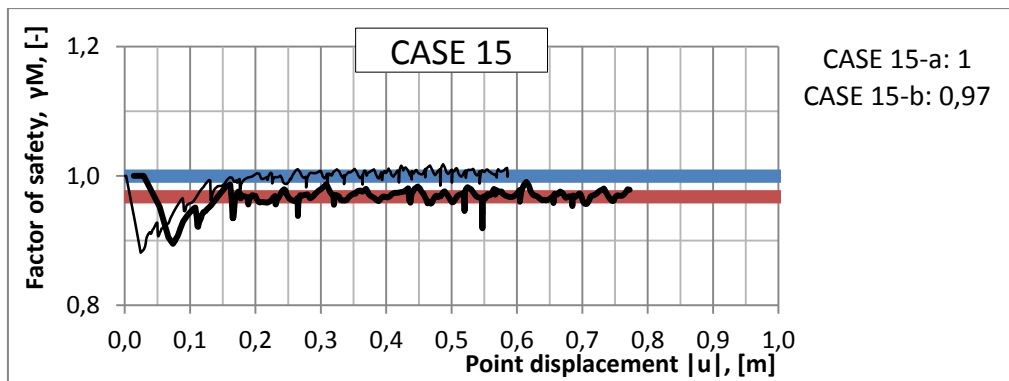
Figure 0.116: Results from PLAXIS run of case 15.
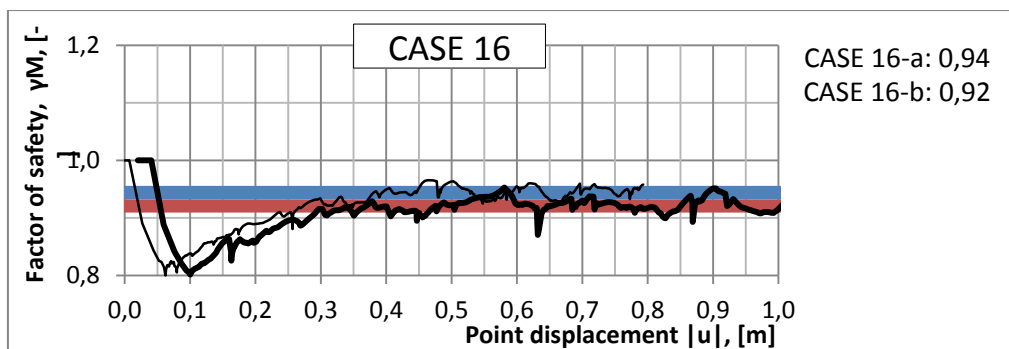
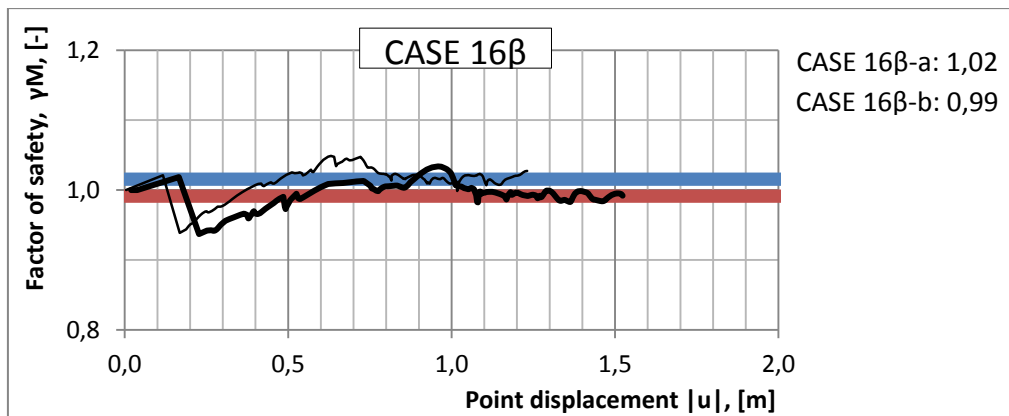*Figure 0.117: Results from PLAXIS run of case 16.*
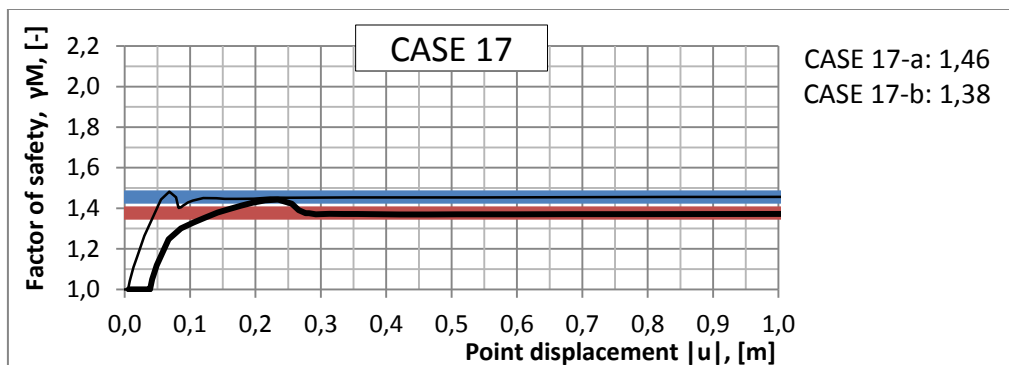
Figure 0.118: Results from PLAXIS run of case 17.
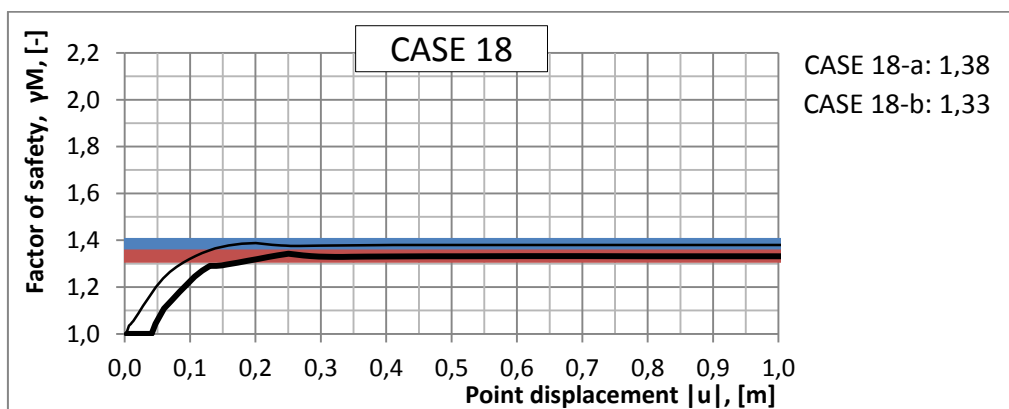
Figure 0.119: Results from PLAXIS run of case 18.

158
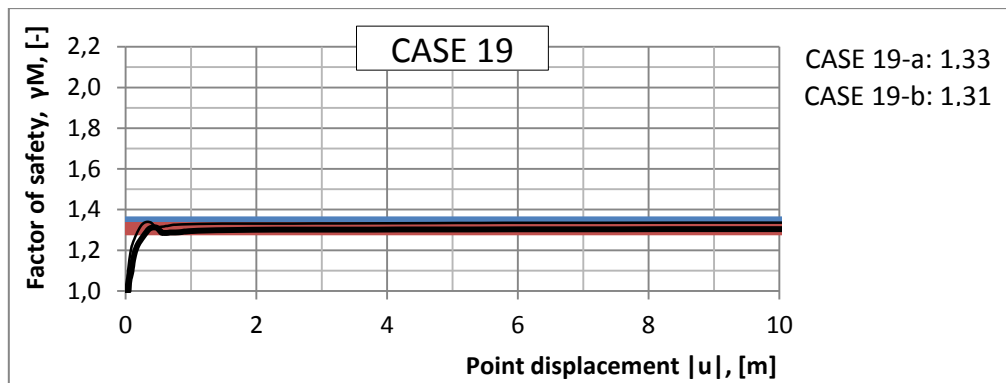
Figure 0.120: Results from PLAXIS run of case 19.
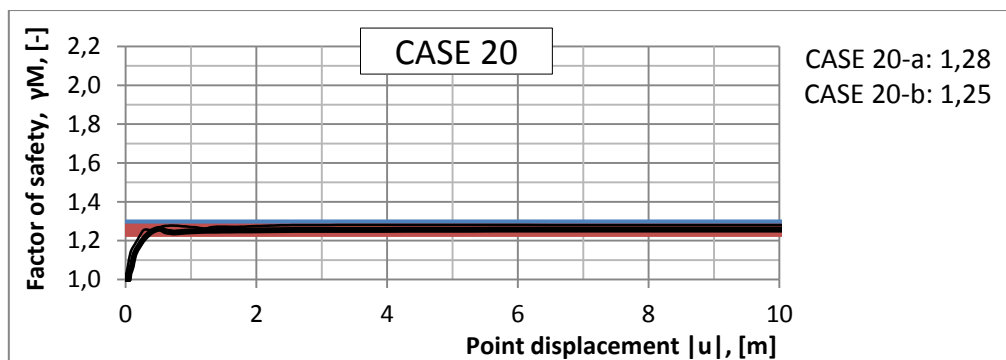
Figure 0.121: Results from PLAXIS run of case 20.
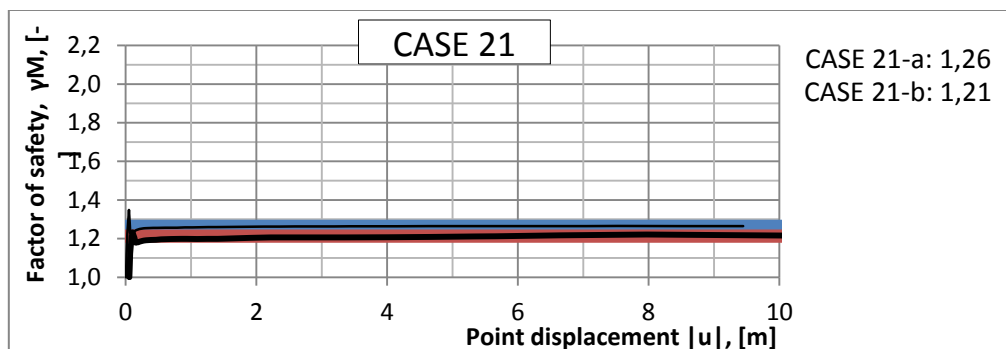
Figure 0.122: Results from PLAXIS run of case 21.
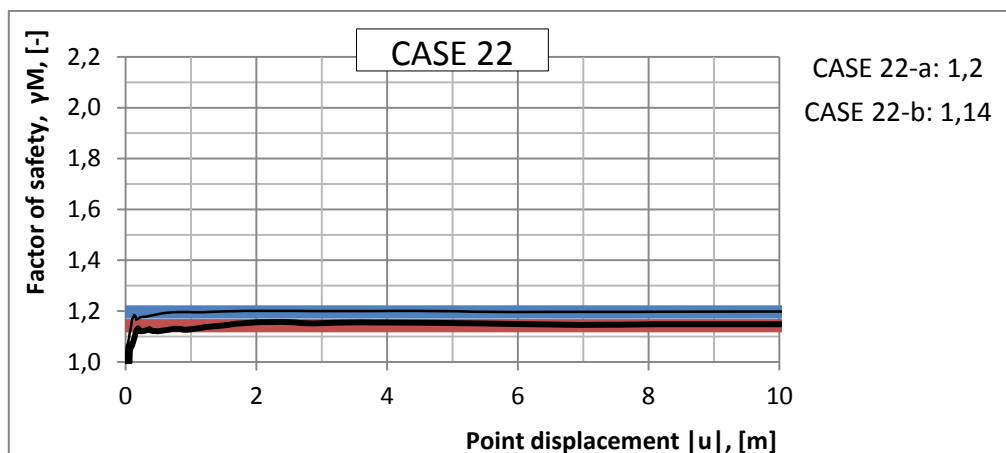
Figure 0.123: Results from PLAXIS run of case 22.
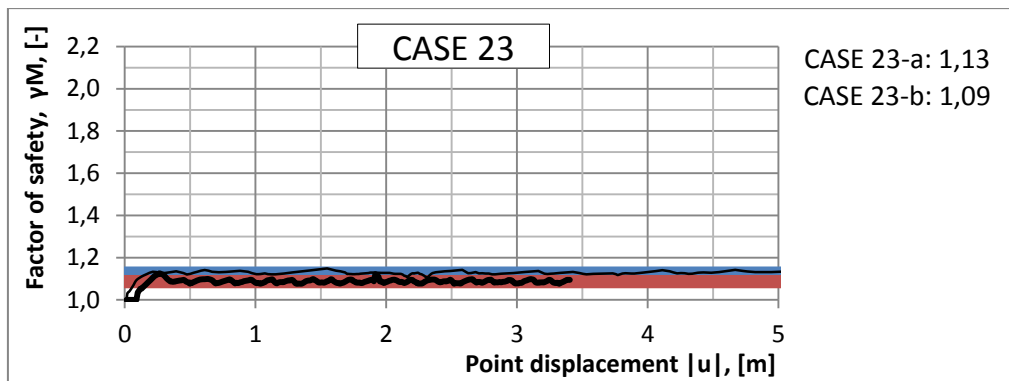
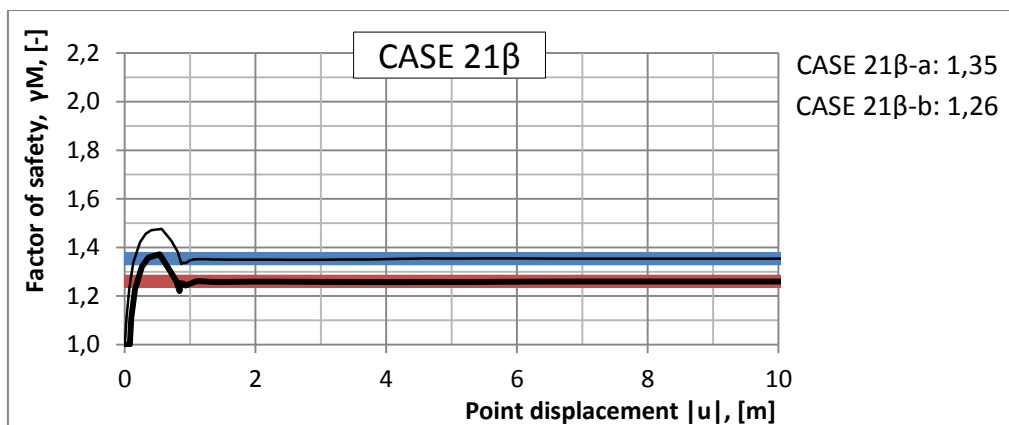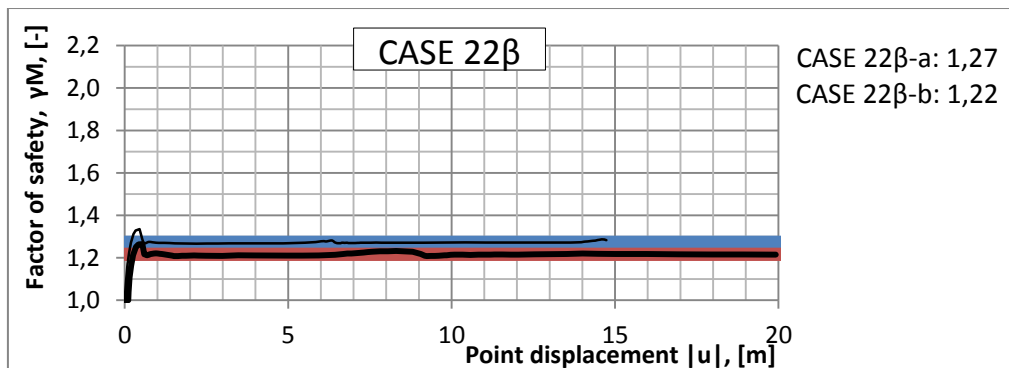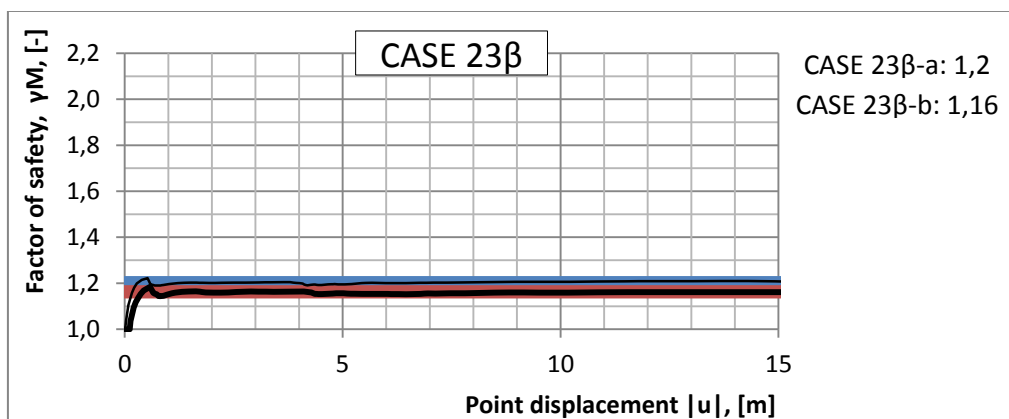*Figure 0.124: Results from PLAXIS run of case 23.*
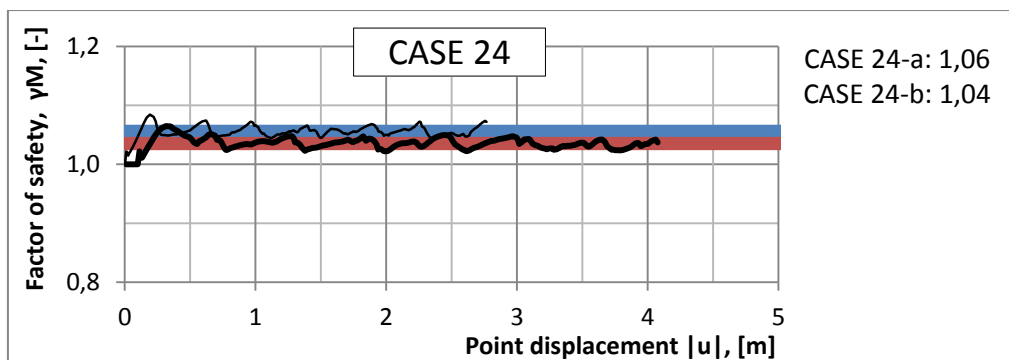
Figure 0.125: Results from PLAXIS run of case 24.
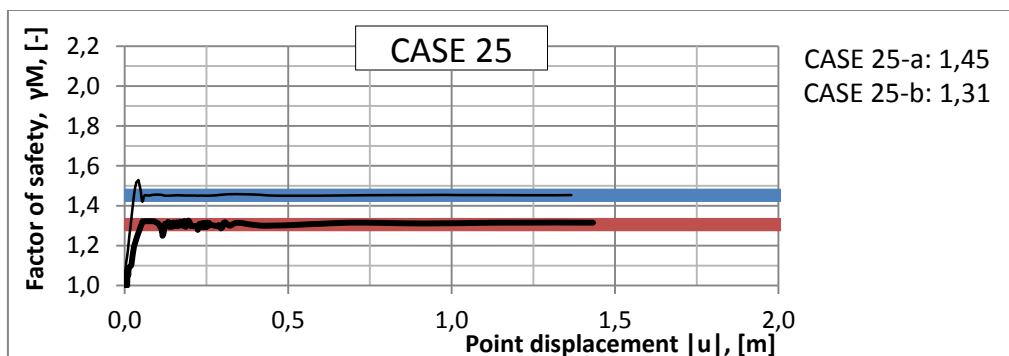
Figure 0.126: Results from PLAXIS run of case 25.
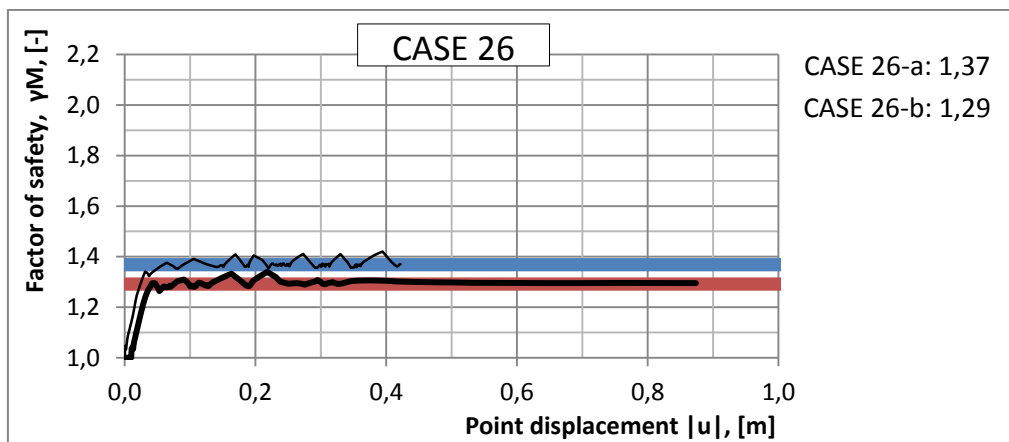
Figure 0.127: Results from PLAXIS run of case 26.

160

CASE 27-a: 1.25
CASE 27-b: 1.2
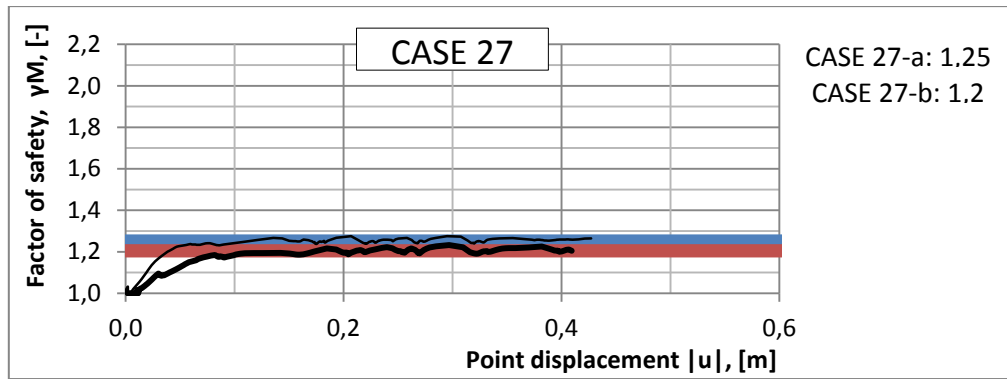
Figure 0.128: Results from PLAXIS run of case 27.

CASE 28-a: 1,19
CASE 28-b: 1,15
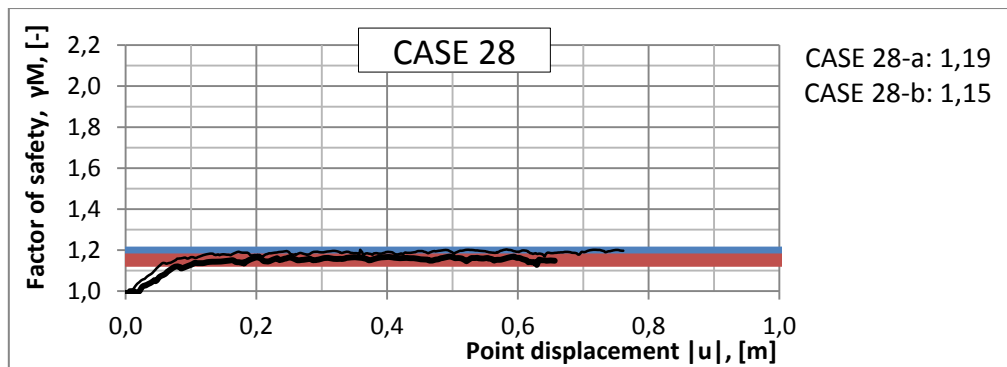
Figure 0.129: Results from PLAXIS run of case 28.

CASE 29-a: 2
CASE 29-b: 1,83
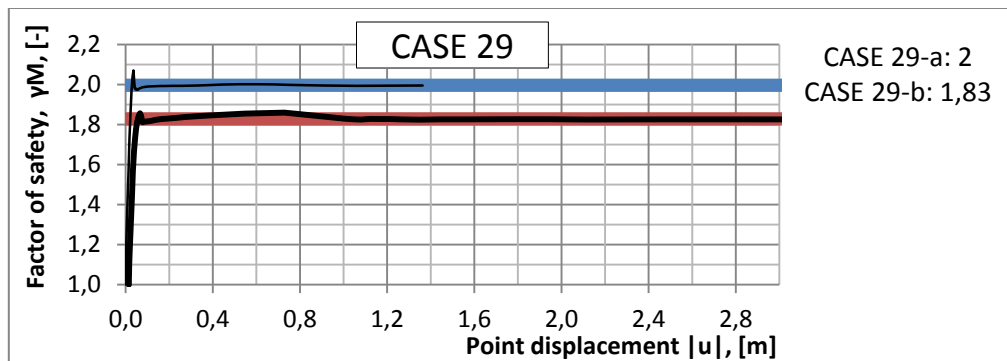
Figure 0.130: Results from PLAXIS run of case 29.

CASE 30-a: 1,88
CASE 30-b: 1,73
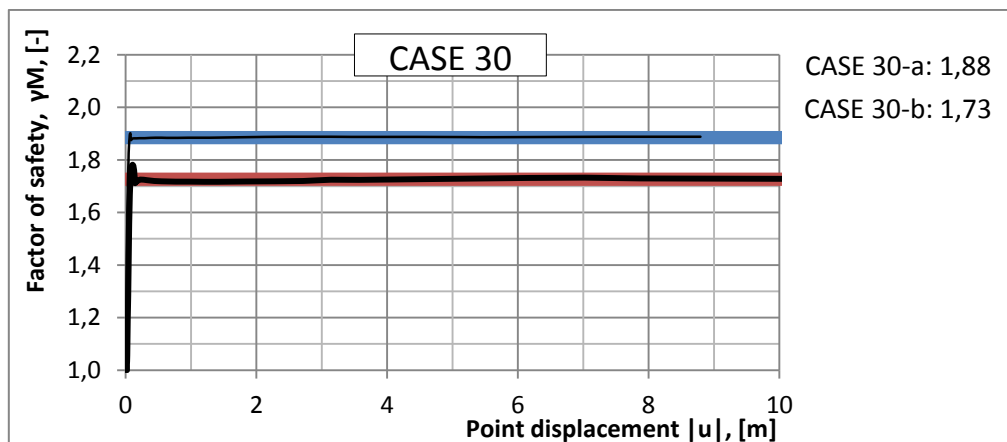
Figure 0.131: Results from PLAXIS run of case 30.

161
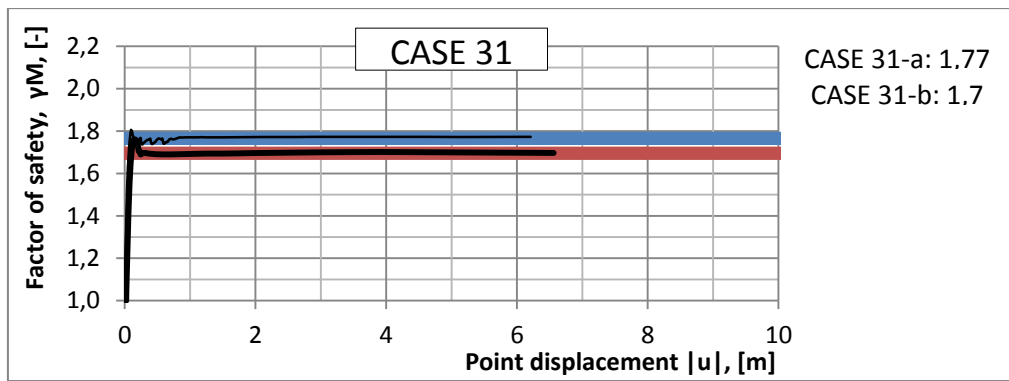
Figure 0.132: Results from PLAXIS run of case 31.
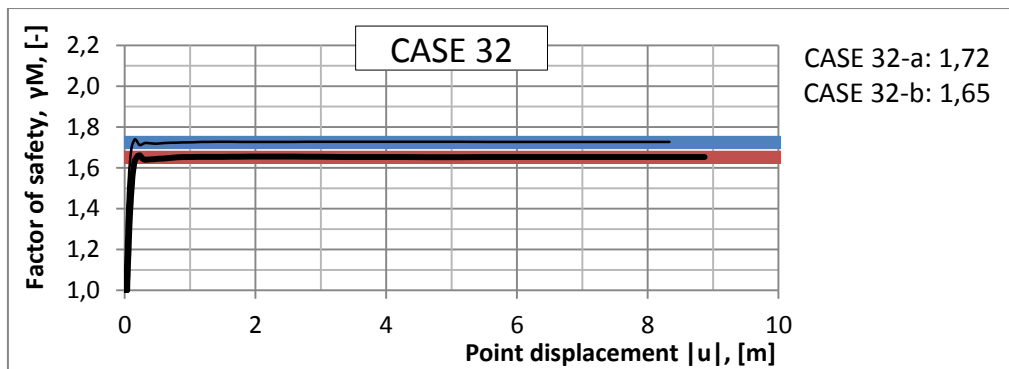
Figure 0.133: Results from PLAXIS run of case 32.
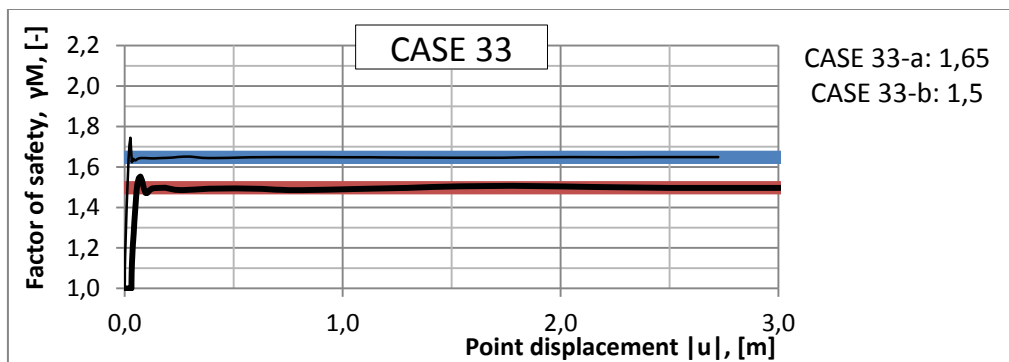
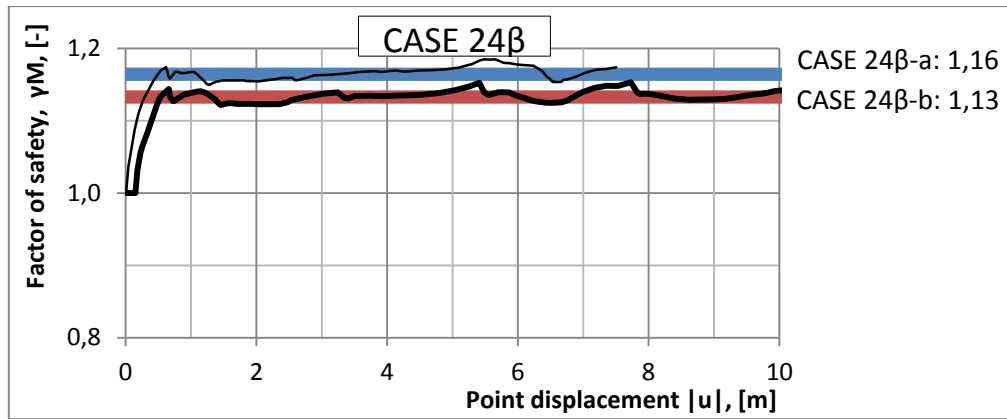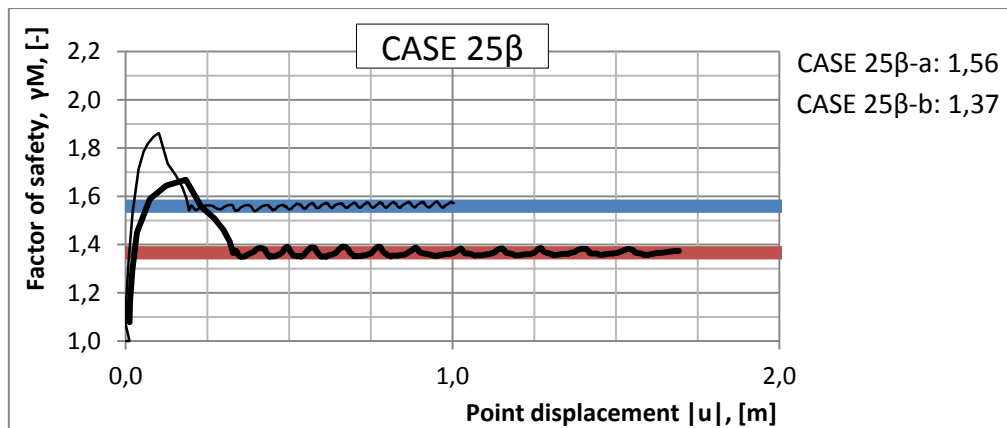*Figure 0.134: Results from PLAXIS run of case 33.*
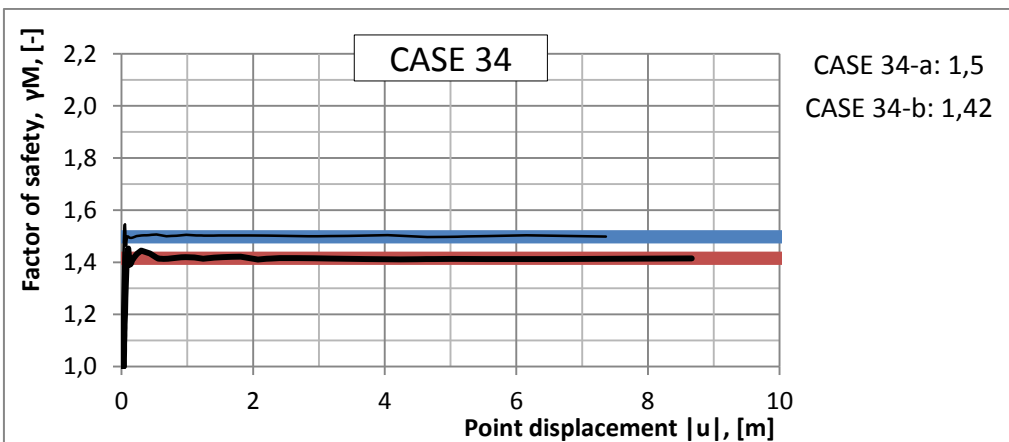
Figure 0.135: Results from PLAXIS run of case 34.
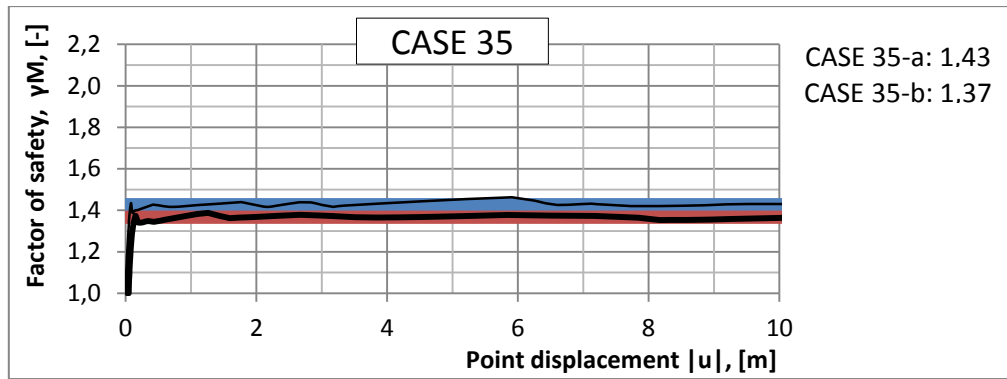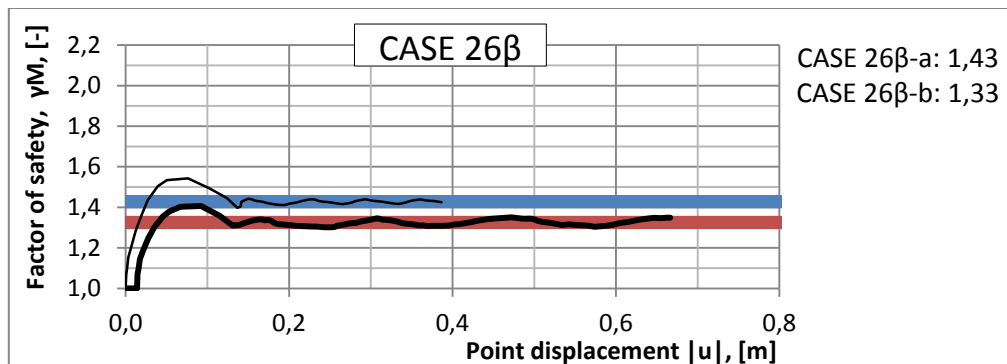
Figure 0.136: Results from PLAXIS run of case 35.
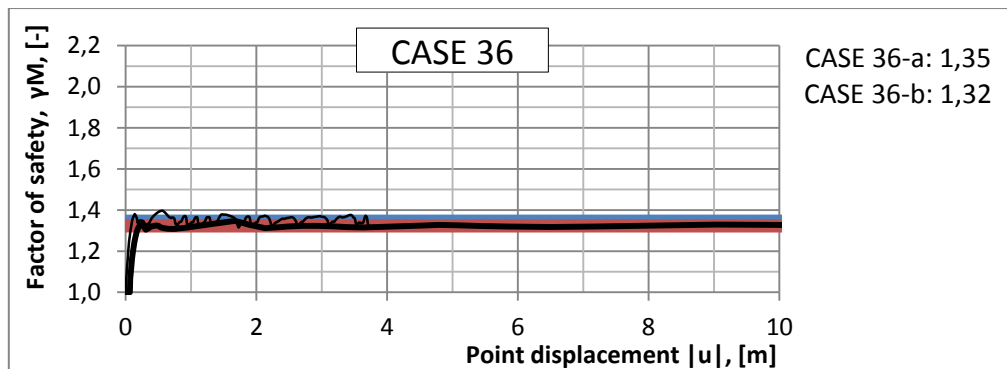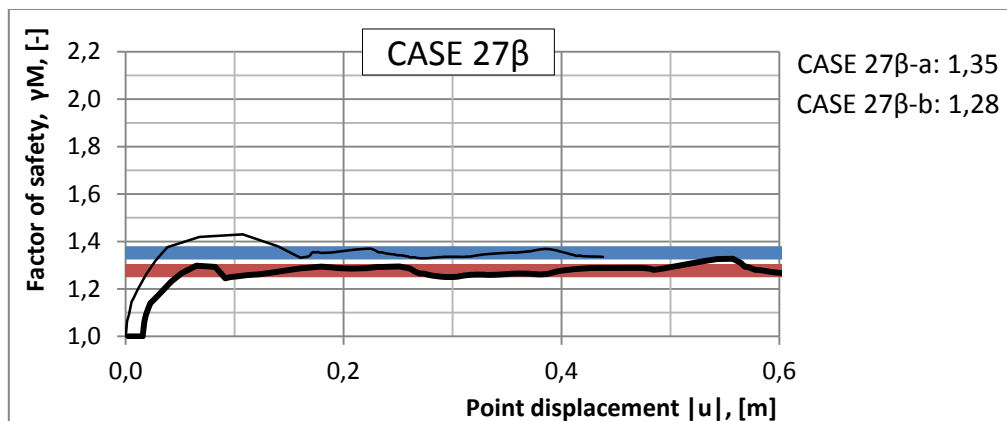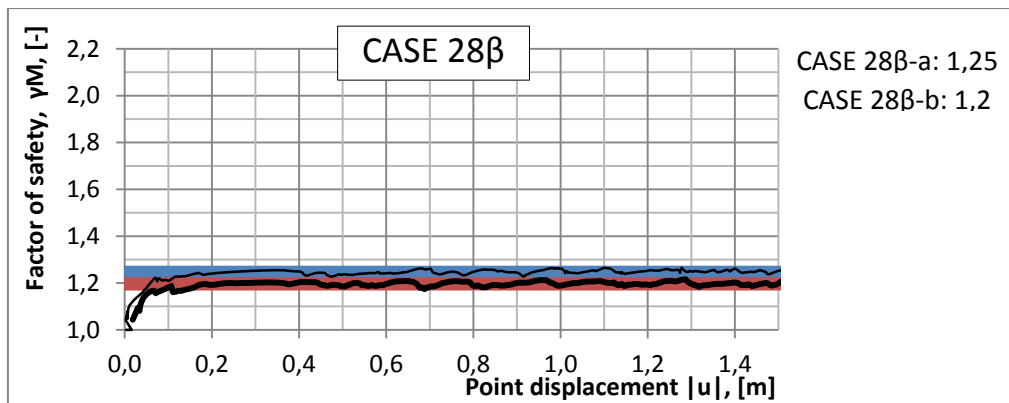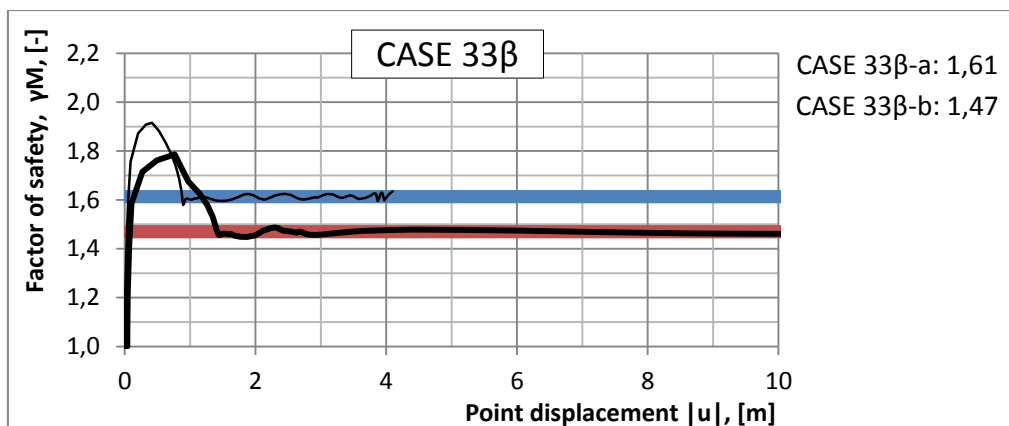

Figure 0.137: Results from PLAXIS run of case 36.

Locally refined mesh coarseness
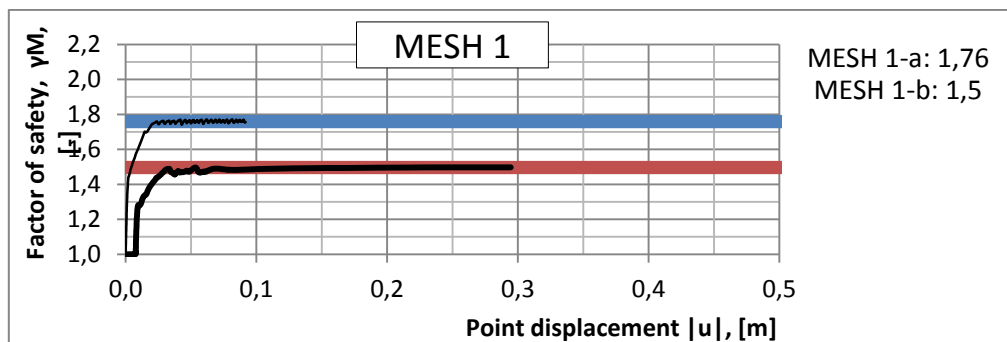
Figure 0.138: Results from PLAXIS run of case 1 with locally refined element mesh.
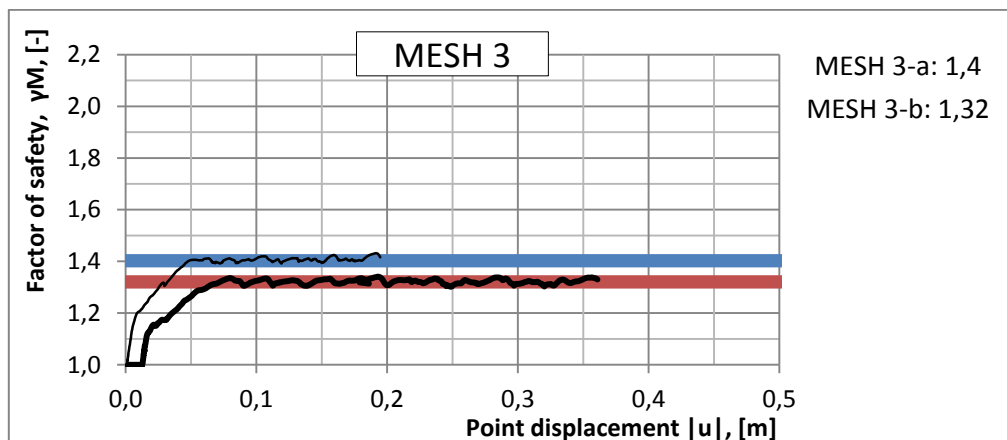
Figure 0.139: Results from PLAXIS run of case 3 with locally refined element mesh.

163
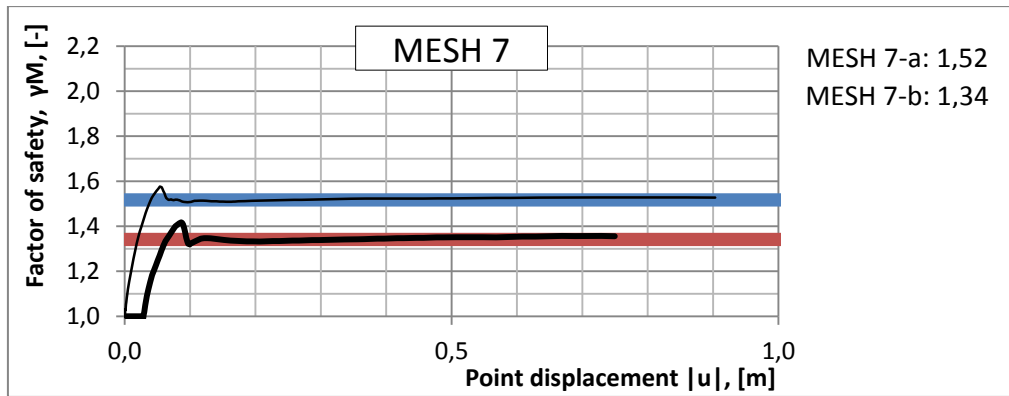
Figure 0.140: Results from PLAXIS run of case 7 with locally refined element mesh.
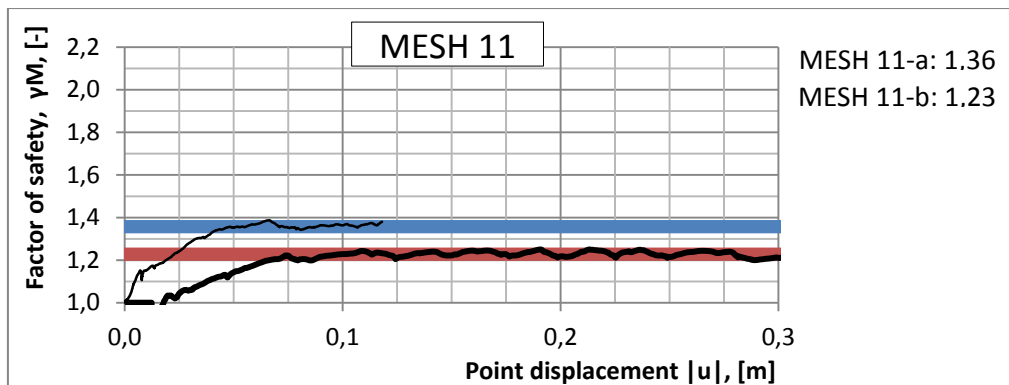
Figure 0.141: Results from PLAXIS run of case 11 with locally refined element mesh.
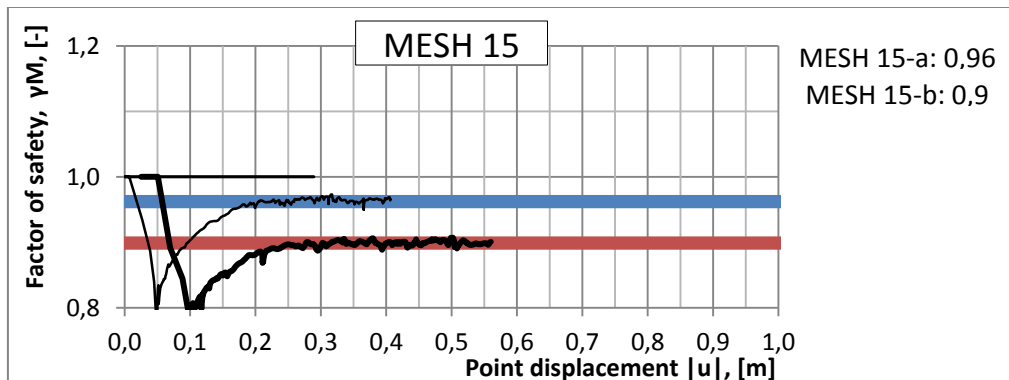
Figure 0.142: Results from PLAXIS run of case 15 with locally refined element mesh.
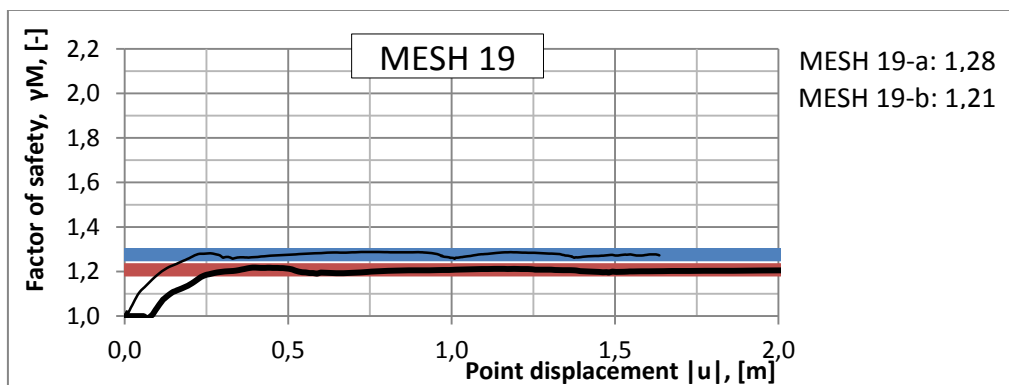
Figure 0.143: Results from PLAXIS run of case 19 with locally refined element mesh.

164
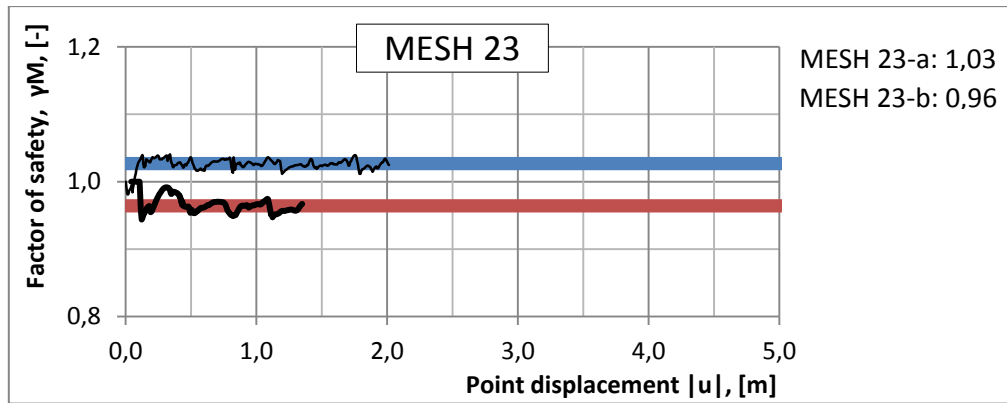
Figure 0.144: Results from PLAXIS run of case 23 with locally refined element mesh.
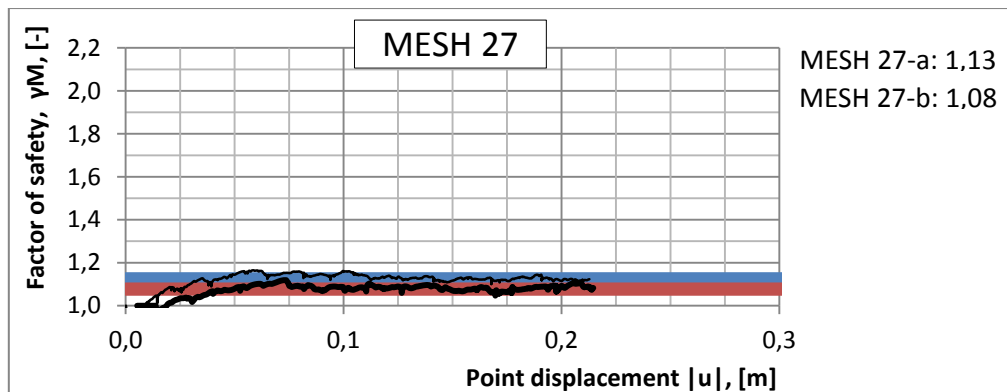
Figure 0.145: Results from PLAXIS run of case 27 with locally refined element mesh.
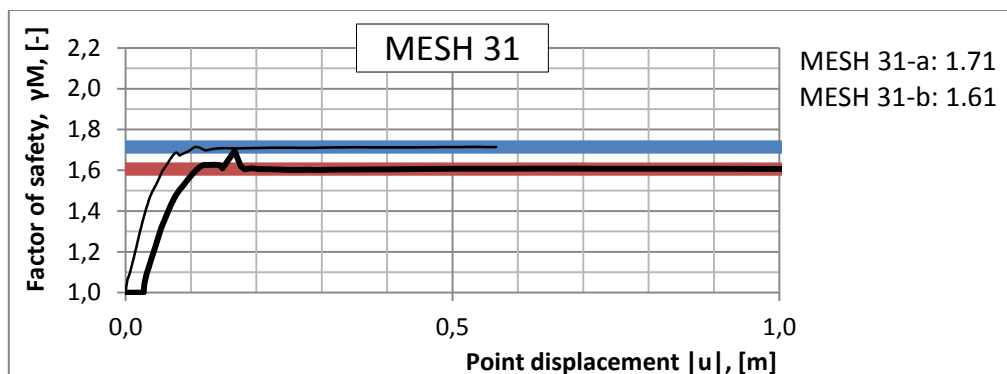
Figure 0.146: Results from PLAXIS run of case 31 with locally refined element mesh.
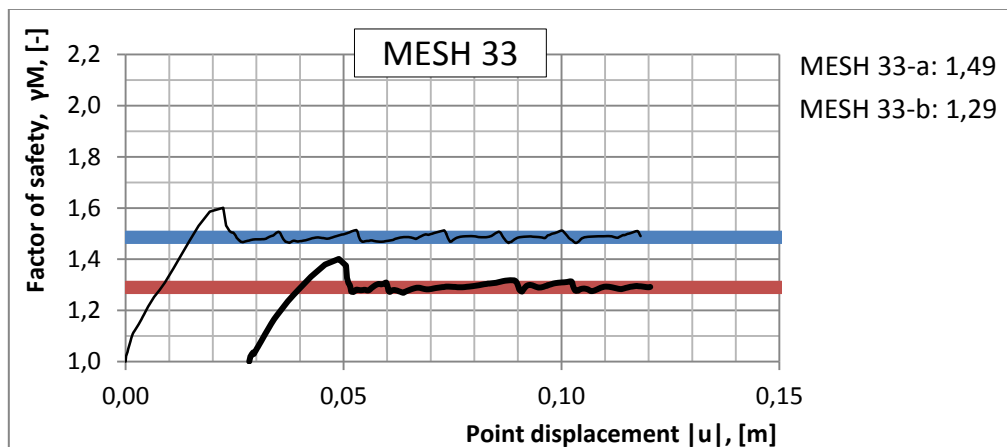
Figure 0.147: Results from PLAXIS run of case 33 with locally refined element mesh.

165
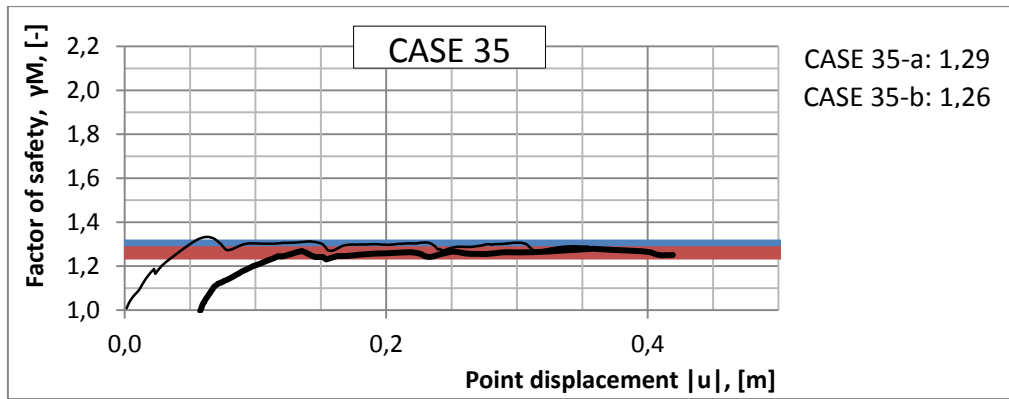
Figure 0.148: Results from PLAXIS run of case 35 with locally refined element mesh.

"Very fine" mesh coarseness – inclined backfill
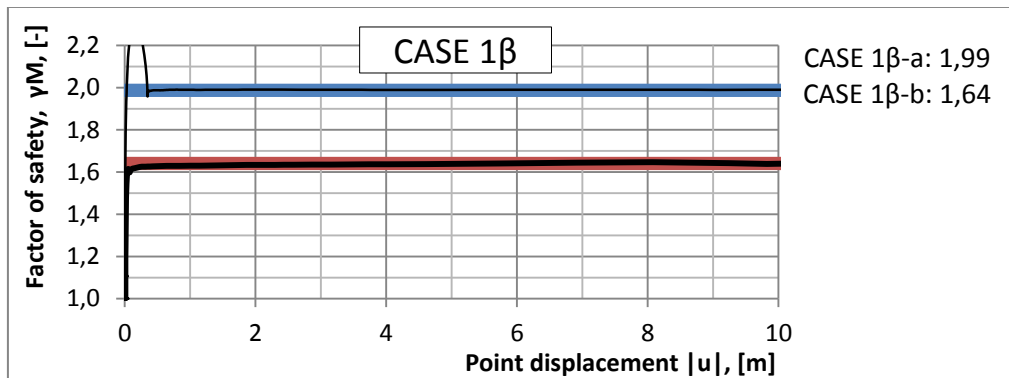
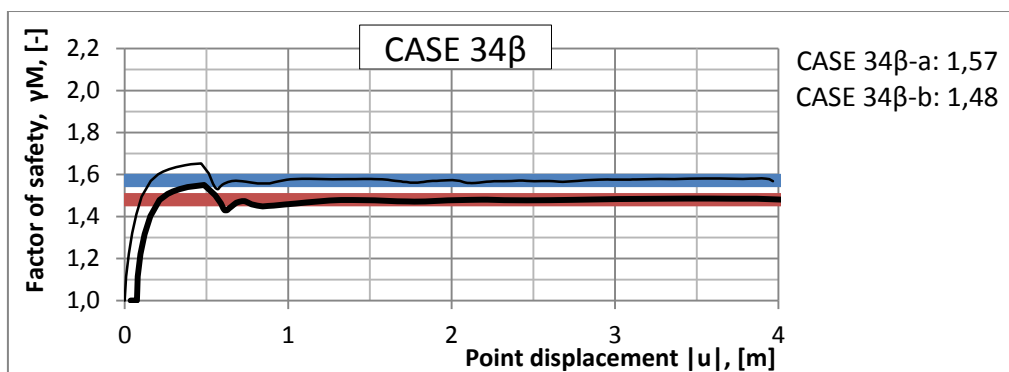
Figure 0.149: Results from PLAXIS run of case 1β.
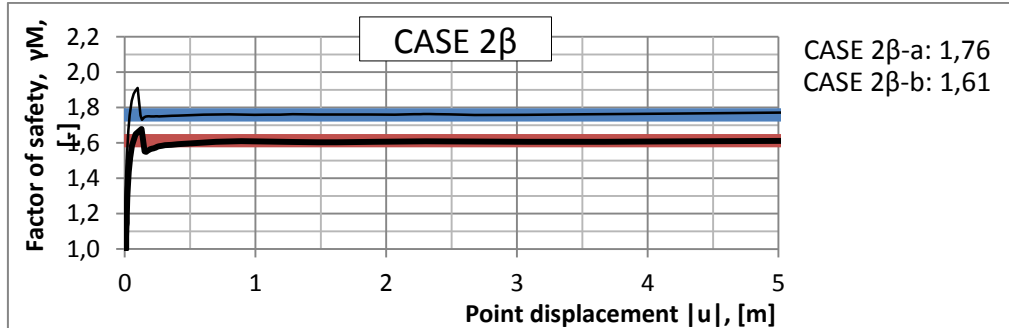
Figure 0.150: Results from PLAXIS run of case 2β.
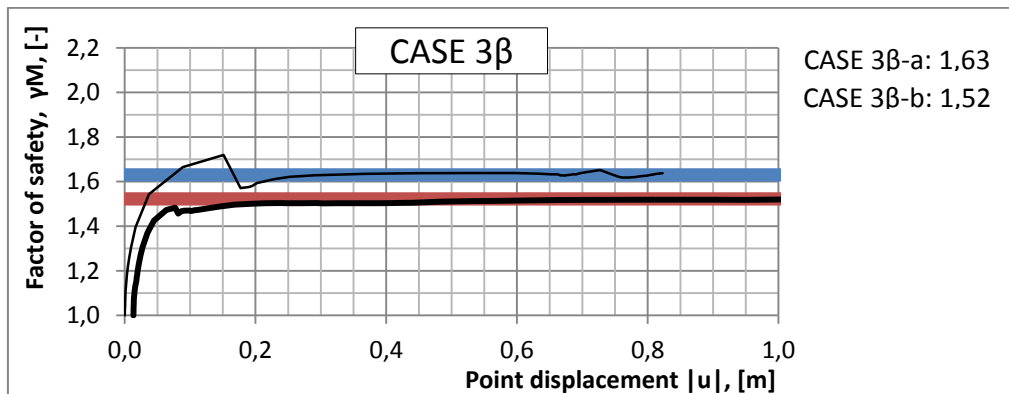
Figure 0.151: Results from PLAXIS run of case 3β.
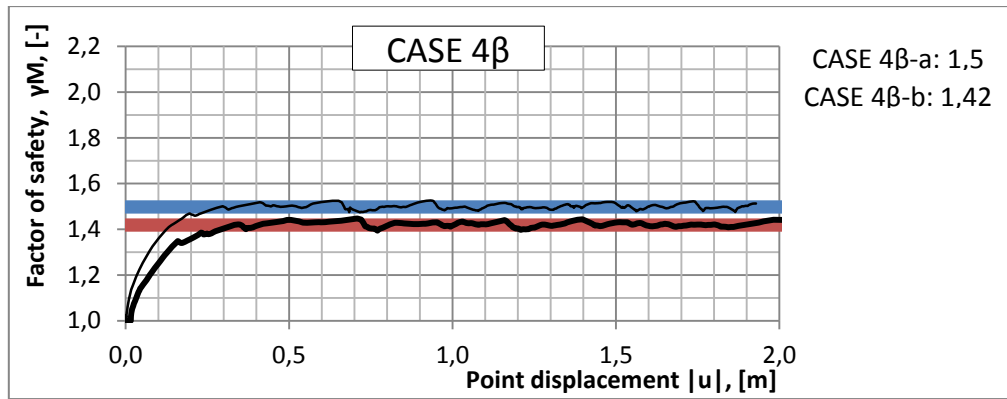
Figure 0.152: Results from PLAXIS run of case 4β.
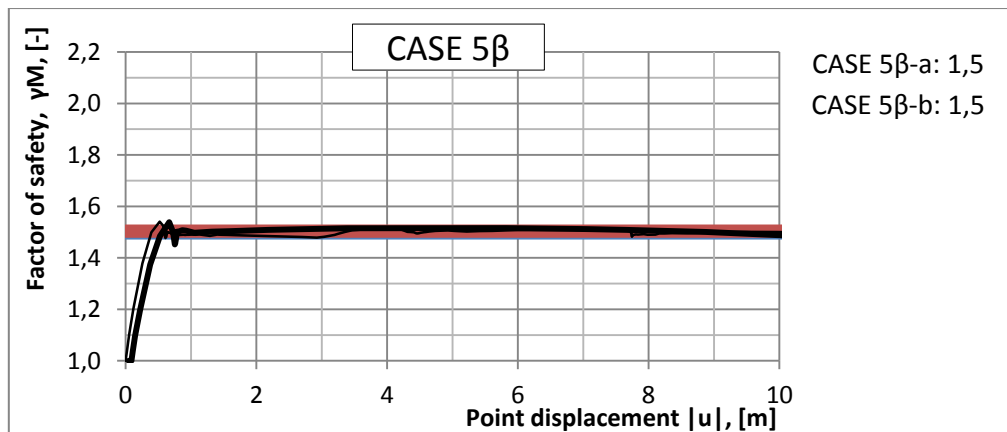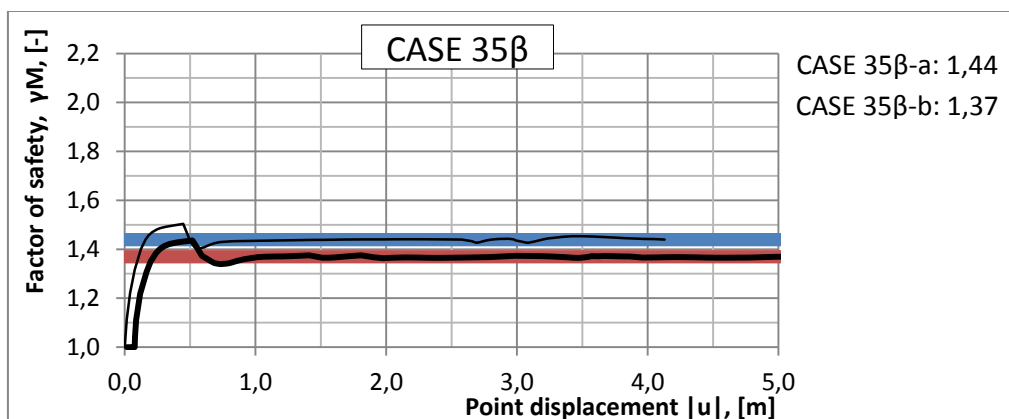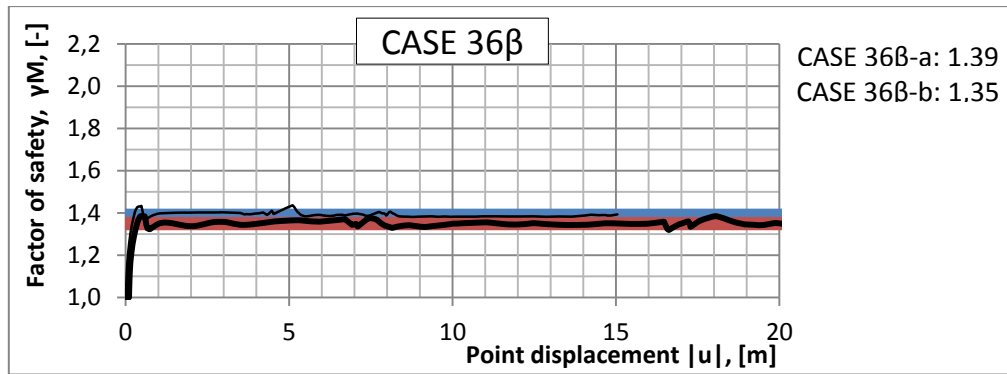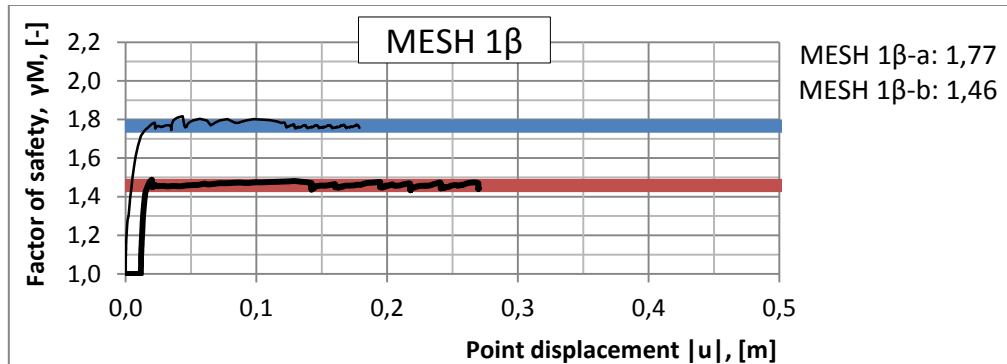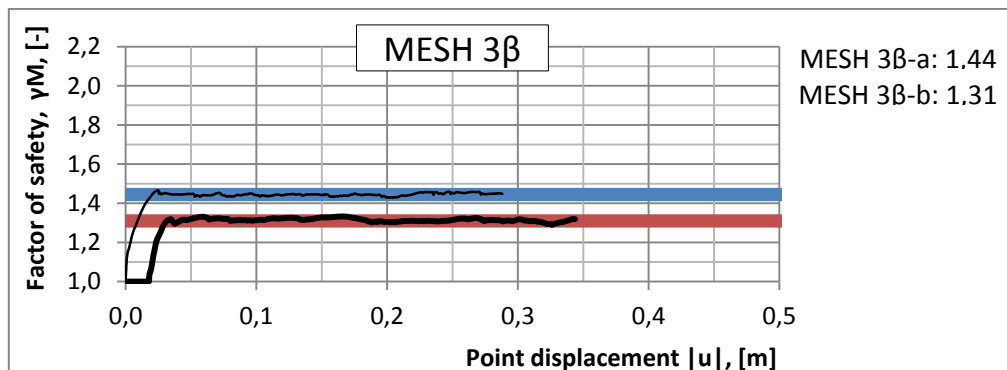

Figure 0.153: Results from PLAXIS run of case 5β.
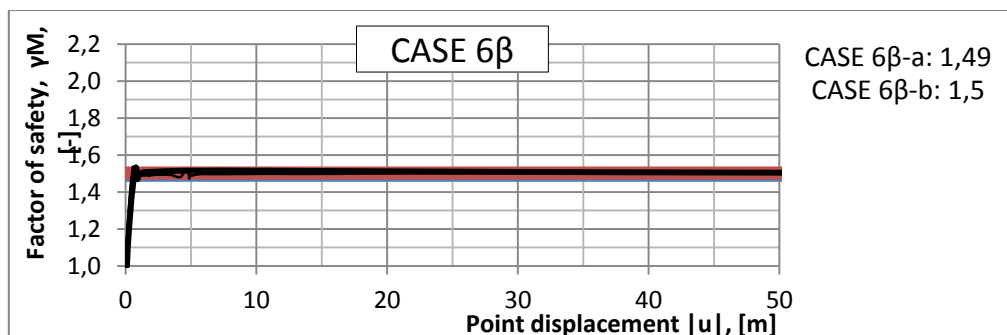
Figure 0.154: Results from PLAXIS run of case 6β.

Figure 0.155: Results from PLAXIS run of case 7β.

167

Figure 0.156: Results from PLAXIS run of case 8β.

Figure 0.157: Results from PLAXIS run of case 9β.

Figure 0.158: Results from PLAXIS run of case 10β.

Figure 0.159: Results from PLAXIS run of case 11β.

168

Figure 0.160: Results from PLAXIS run of case 12β.

Figure 0.161: Results from PLAXIS run of case 13β.

Figure 0.162: Results from PLAXIS run of case 14β.

Figure 0.163: Results from PLAXIS run of case 15β.

Figure 0.164: Results from PLAXIS run of case 16β.

Figure 0.165: Results from PLAXIS run of case 21β.

Figure 0.166: Results from PLAXIS run of case 22β.

Figure 0.167: Results from PLAXIS run of case 23β.

Figure 0.168: Results from PLAXIS run of case 24ß.

Figure 0.169: Results from PLAXIS run of case 25ß.

Figure 0.170: Results from PLAXIS run of case 26ß.

Figure 0.171: Results from PLAXIS run of case 27ß.

171

Figure 0.172: Results from PLAXIS run of case 28β.

Figure 0.173: Results from PLAXIS run of case 33β.

Figure 0.174: Results from PLAXIS run of case 34β.

Figure 0.175: Results from PLAXIS run of case 35β.

172

Figure 0.176: Results from PLAXIS run of case 36β.
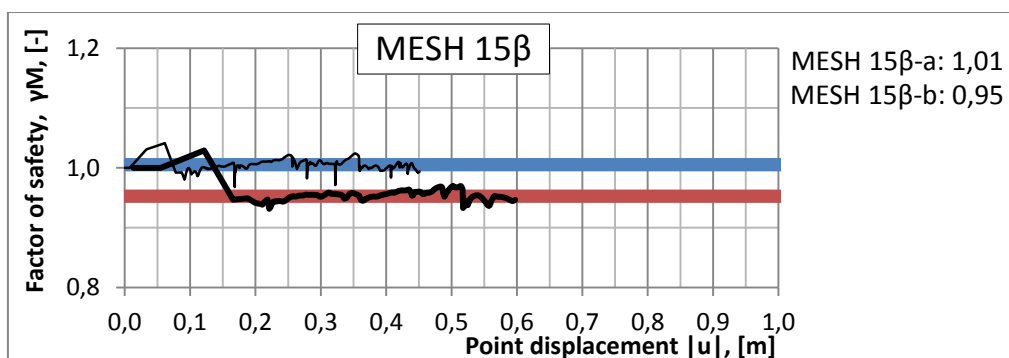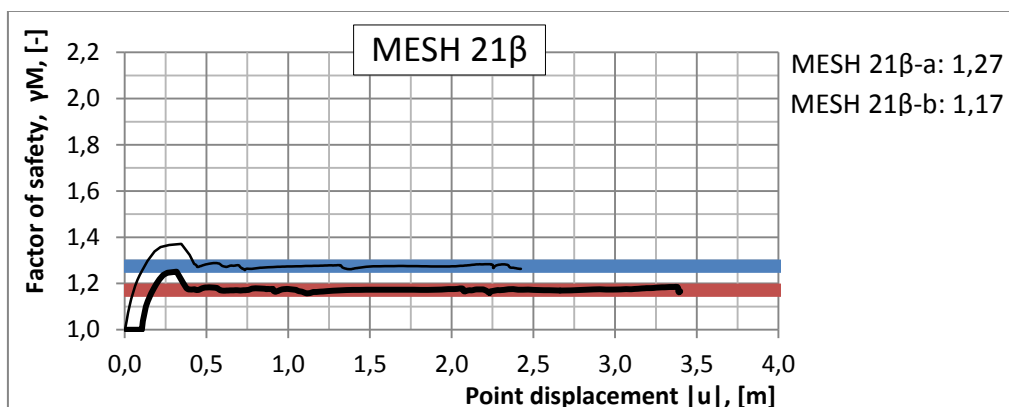
Locally refined mesh coarseness – inclined backfill

Figure 0.177: Results from PLAXIS run of case 1β with locally refined element mesh.

Figure 0.178: Results from PLAXIS run of case 3β with locally refined element mesh.
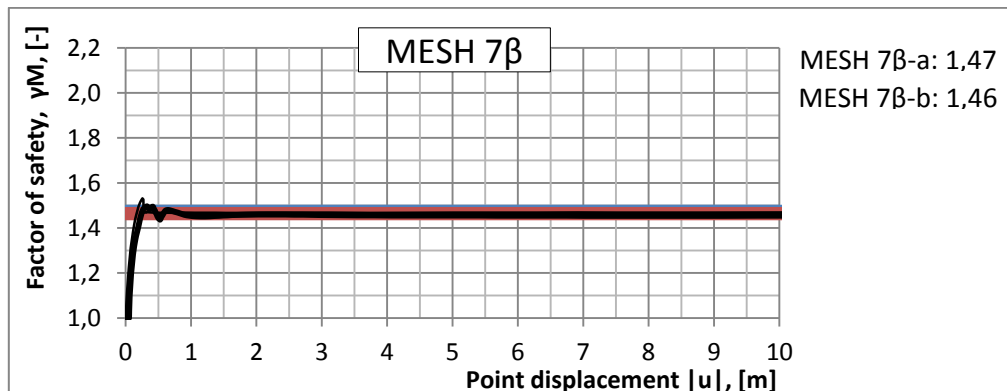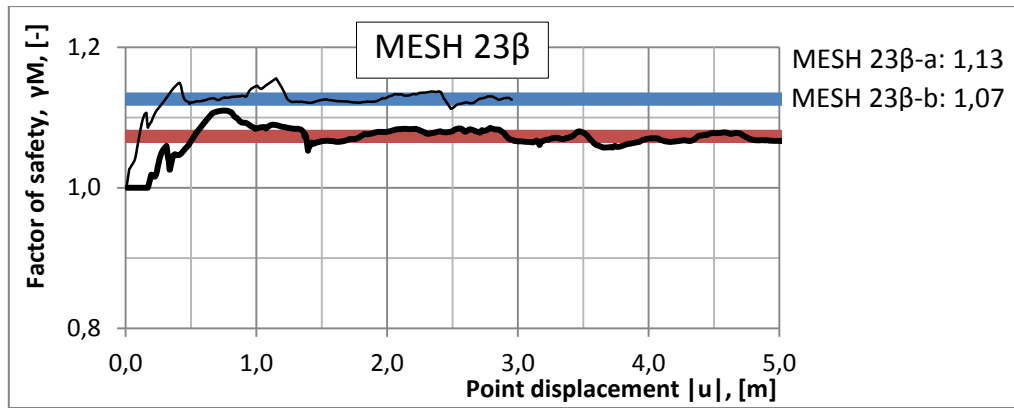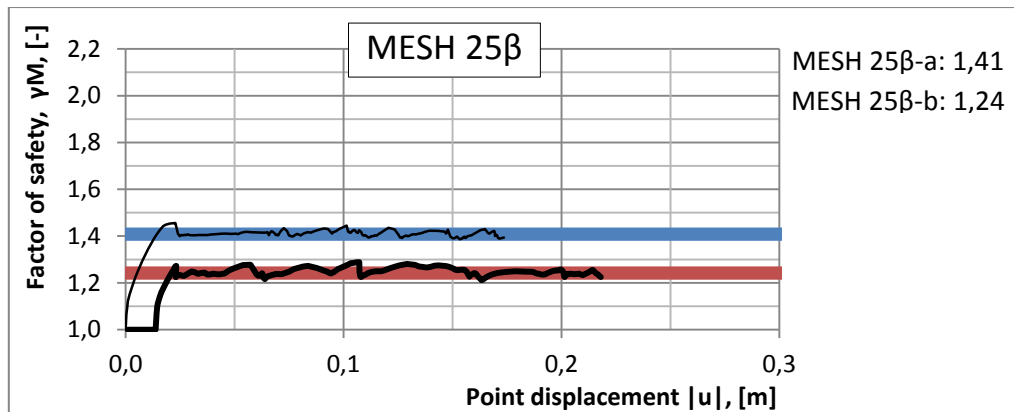

Figure 0.179: Results from PLAXIS run of case 7β with locally refined element mesh.
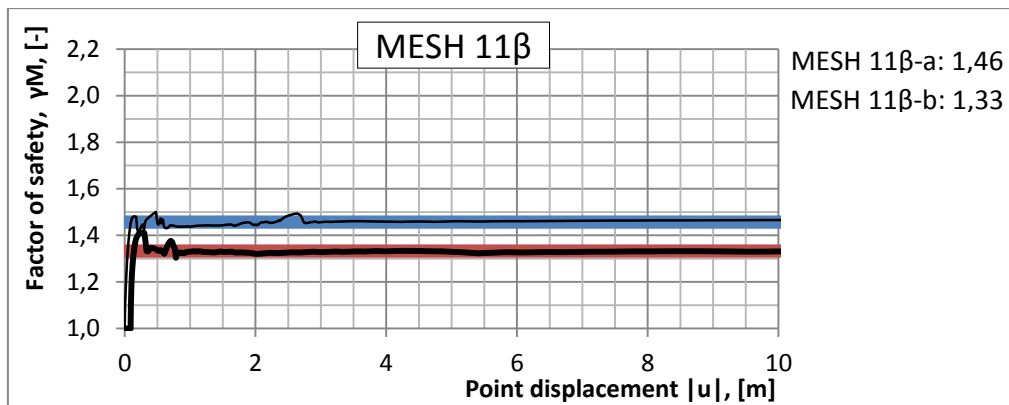
Figure 0.180: Results from PLAXIS run of case 11β with locally refined element mesh.
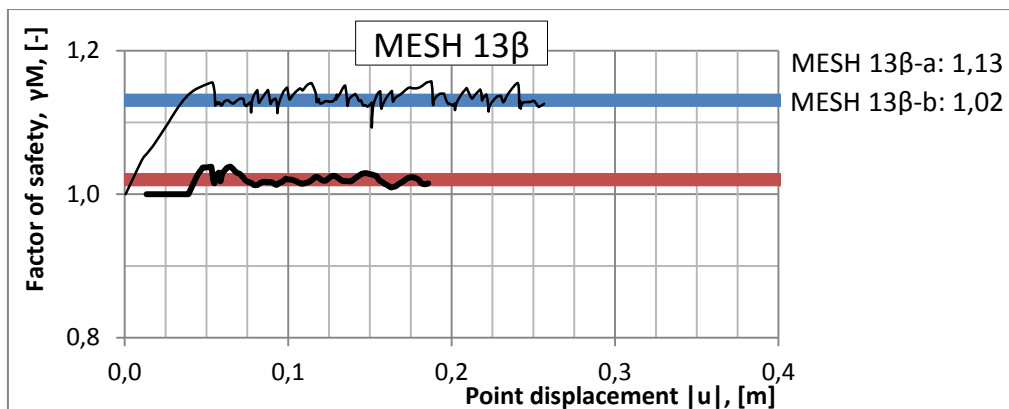
Figure 0.181: Results from PLAXIS run of case 13β with locally refined element mesh.

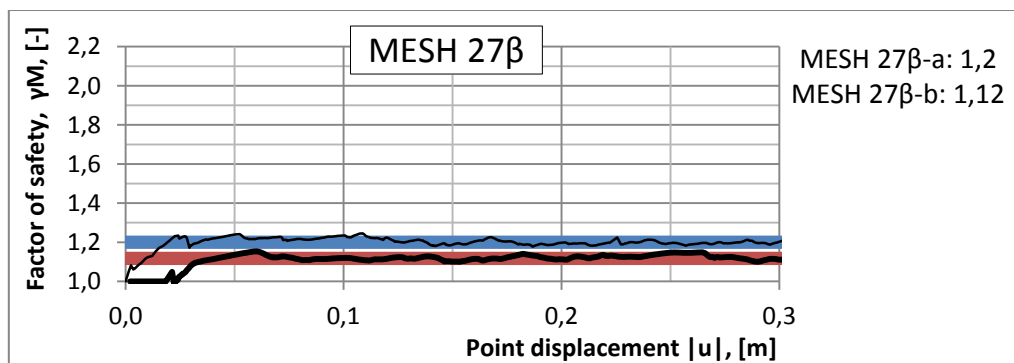*Figure 0.182: Results from PLAXIS run of case 15β with locally refined element mesh.*

Figure 0.183: Results from PLAXIS run of case 21β with locally refined element mesh.
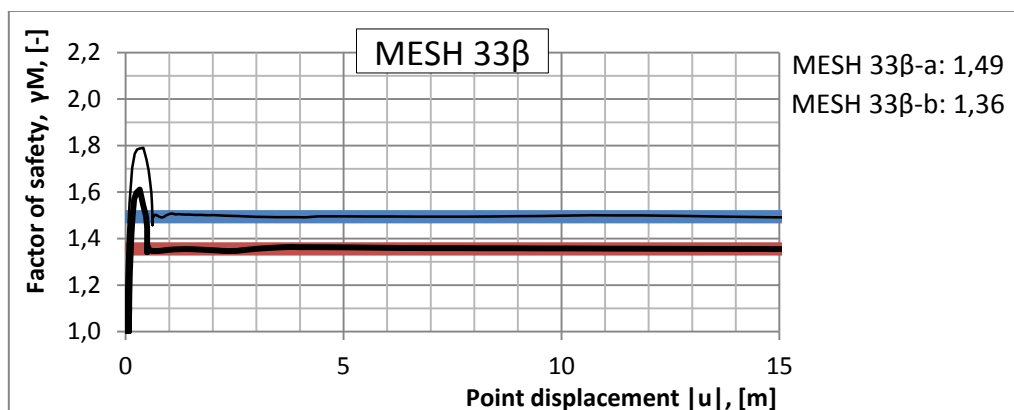
174

Figure 0.184: Results from PLAXIS run of case 23β with locally refined element mesh.

Figure 0.185: Results from PLAXIS run of case 25β with locally refined element mesh.

Figure 0.186: Results from PLAXIS run of case 27β with locally refined element mesh.

Figure 0.187: Results from PLAXIS run of case 33β with locally refined element mesh.
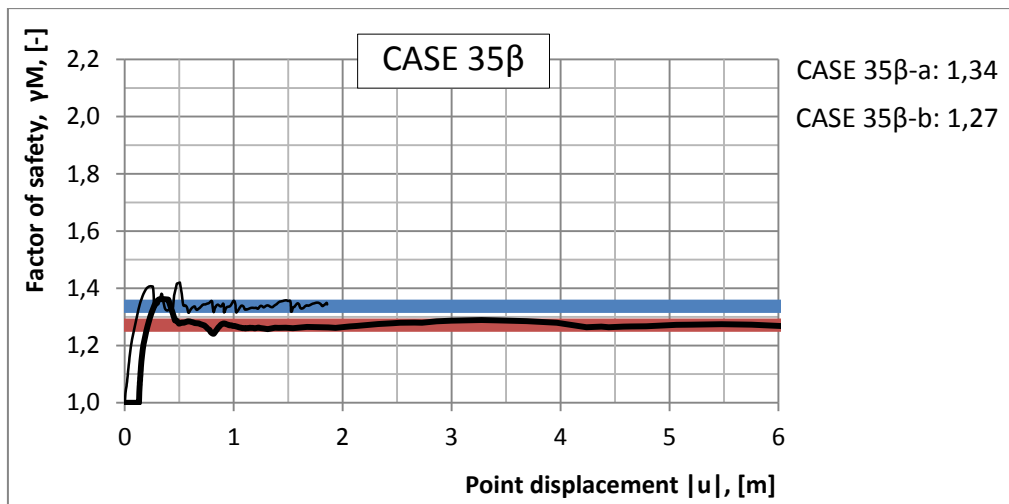
Figure 0.188: Results from PLAXIS run of case 35β with locally refined element mesh.

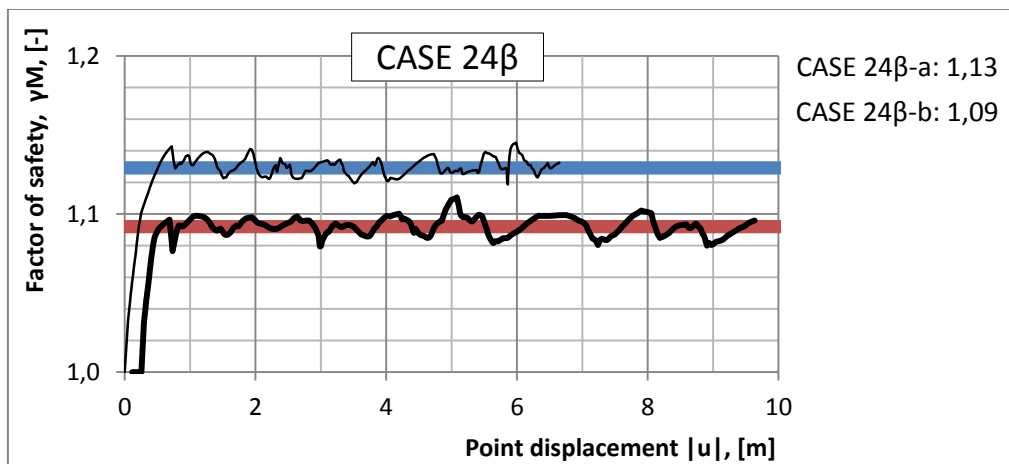## Enlarged models with locally refined mesh coarseness – inclined backfill

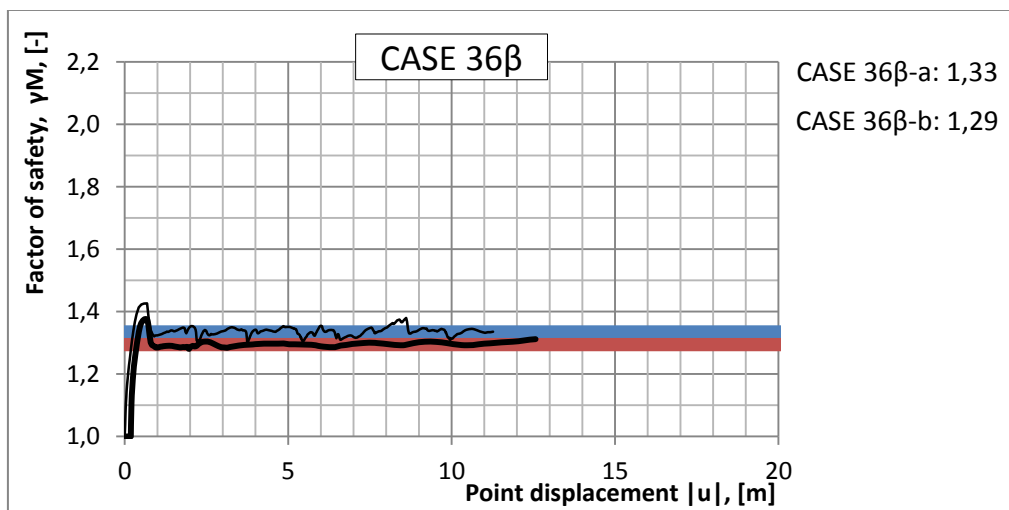*Figure 0.189: Results from PLAXIS run of case 35β with locally refined element mesh.*

Figure 0.190: Results from PLAXIS run of case 35β with locally refined element mesh.